

Mixed-dimensional finite element formulations for beam-to-solid interaction

Ivo Sebastian Steinbrecher

Vollständiger Abdruck der von der Fakultät für Bauingenieurwesen und Umweltwissenschaften
der Universität der Bundeswehr München zur Erlangung des akademischen Grades eines

Doktor-Ingenieurs (Dr.-Ing.)

genehmigten Dissertation.

- Gutachter:
1. Univ.-Prof. Dr.-Ing. Alexander Popp
 2. Univ.-Prof. Dr.-Ing. habil. Christian Hesch
Universität Siegen
 3. Assoz.Univprof. DI Dr.techn. Alexander Humer
Johannes Kepler Universität Linz

Die Dissertation wurde am 02. Juni 2022 bei der Universität der Bundeswehr München eingereicht
und durch die Fakultät für Bauingenieurwesen und Umweltwissenschaften am 03. September
2022 angenommen. Die mündliche Prüfung fand am 19. September 2022 statt.

Abstract

The interaction between slender fiber- or rod-like components, where one spatial dimension is much larger than the other two, with three-dimensional structures (solids) is an essential mechanism of mechanical systems in numerous fields of science, engineering and bio-mechanics. Examples include reinforced concrete, supported concrete slabs, fiber-reinforced composite materials and the impact of a tennis ball on the string bed of a tennis racket. Applications can also be found in medicine, where stent grafts are a commonly used device for endovascular aneurysm repair, and in many biological systems such as arterial wall tissue with collagen fibers. The different types of dimensionality of the interacting bodies, i.e., slender, almost one-dimensional fibers and general three-dimensional solids, pose a significant challenge for typical numerical simulation methods. Classical modeling techniques usually require a compromise between a detailed description of the one-dimensional structures and overall model complexity.

The main focus of this work is the development of novel computational approaches to simulate the interaction between fiber-like structures and three-dimensional solids. The key idea therein is to explicitly model the slender components as one-dimensional Cosserat continua based on the geometrically exact beam theory, which allows for an accurate and efficient description of the slender fibers (beams). Since the dimensions of the coupled differential equations are not equal, the resulting combined interaction problem is a mixed-dimensional beam-to-solid interaction problem. Not only the governing equations of the beam but also the developed interaction schemes are exclusively formulated along the one-dimensional beam centerline. From a mechanical point of view, the resulting mixed-dimensional interaction of nonlinear geometrically exact beam finite elements with classical continuum finite elements introduces a singular solution, similar to the problem of a concentrated line load acting on a three-dimensional continuum. As one of the main contributions of this thesis, theoretical considerations and numerical examples verify that this singularity does not affect the usability of the proposed methods within the envisioned application range.

Based on the considered applications, two different types of interacting geometry pairs can be identified: line-to-volume, e.g., beams embedded in solid volumes, and line-to-surface, e.g., beams tied or in contact with the surface of a solid volume. Within the present work, coupling (i.e., tying) of the beam centerline position to the underlying solid in line-to-volume problems is investigated first. As a next step, also the rotations of the Cosserat continua are coupled to the solid volume. This requires the construction of a suitable rotation (i.e., triad) field inside the solid (Boltzmann) continuum. For both, positional and rotational coupling, mortar-type methods, inspired by classical mortar methods from domain decomposition or surface-to-surface interface problems, are employed to discretize the coupling constraints. A penalty regularization is performed to eliminate the Lagrange multipliers from the global system of equations, which results in a robust coupling scheme. This is verified by several numerical examples, in which consistent spatial convergence behavior can be achieved and potential locking effects can be avoided. The second half of this thesis extends the previously developed algorithms for line-

to-volume coupling to line-to-surface coupling. This introduces the additional complexity of having to account for the surface normal vector in the positional coupling constraints. It is demonstrated that only a consistent handling of the surface normal vector leads to physically accurate results and guarantees fundamental mechanical properties such as conservation of angular momentum. Finally, a Gauss point-to-segment beam-to-solid surface contact scheme that allows for the modeling of unilateral contact between one-dimensional beams and two-dimensional solid surfaces is presented.

The previously mentioned building blocks constitute a novel mixed-dimensional beam-to-solid interaction framework, which is verified by theoretical discussions and numerical examples throughout this thesis. Possible extensions are outlined in this thesis and propose numerical and algorithmic improvements as well as the treatment of other physical effects such as delamination between embedded beams and the surrounding volume. However, already in the present state, the presented framework is an efficient, robust, and accurate tool for beam-to-solid interaction problems and can become a valuable tool in science and engineering.

Zusammenfassung

Die Wechselwirkung zwischen schlanken faser- oder stabartigen Komponenten mit dreidimensionalen Strukturen (Festkörpern) ist ein wesentlicher Mechanismus mechanischer Systeme in zahlreichen Bereichen der Wissenschaft, des Ingenieurwesens und der Biomechanik. Beispiele hierfür sind Stahlbeton, verstärkte Betonplatten, faserverstärkte Verbundwerkstoffe sowie der Aufprall eines Tennisballs auf die Schlagfläche eines Tennisschlägers. Anwendungen finden sich auch in der Medizin, wo Stentgrafts häufig verwendete Implantate für endovaskuläre Aortenreparatur sind, und in vielen biologischen Systemen wie zum Beispiel Arterienwandgewebe mit Kollagenfasern. Die unterschiedliche Dimensionalität der interagierenden Körper, d. h. schlanke, fast eindimensionale Fasern und allgemeine dreidimensionale Festkörper, stellt eine große Herausforderung für typische numerische Simulationsmethoden dar. Klassische Modellierungsverfahren erfordern in der Regel einen Kompromiss zwischen einer detaillierten Beschreibung der eindimensionalen Strukturen und der Gesamtkomplexität des Modells.

Der Schwerpunkt dieser Arbeit liegt auf der Entwicklung neuartiger Berechnungsansätze zur Simulation der Wechselwirkung zwischen faserartigen Strukturen und dreidimensionalen Festkörpern. Die Schlüsselidee ist, die schlanken Komponenten basierend auf der geometrisch exakten Balkentheorie explizit als eindimensionale Cosserat-Kontinua zu modellieren um eine genaue und effiziente Beschreibung der schlanken Fasern (Balken) zu ermöglichen. Da die Dimensionen der gekoppelten Differentialgleichungen nicht identisch sind, ist das resultierende kombinierte Interaktionsproblem ein gemischt-dimensionales Balken-Festkörper-Interaktionsproblem. Nicht nur die Balken beschreibenden Gleichungen, sondern auch die entwickelten Interaktionsschemata werden ausschließlich entlang der eindimensionalen Balkenmittellinie formuliert. Aus mechanischer Sicht führt die gemischt-dimensionale Interaktion von nichtlinearen geometrisch exakten finiten Balkenelementen mit klassischen finiten Kontinuumelementen zu einer singulären Lösung, ähnlich dem Problem einer konzentrierten Linienlast, welche auf ein dreidimensionales Kontinuum wirkt. Als einer der Hauptbeiträge dieser Arbeit wird anhand von theoretischen Überlegungen und numerischen Beispielen nachgewiesen, dass diese Singularität die Anwendbarkeit der vorgeschlagenen Methoden innerhalb des angestrebten Anwendungsbereichs nicht beeinträchtigt.

Basierend auf den betrachteten Anwendungen können zwei verschiedene Arten von interagierenden Geometriepaaren identifiziert werden: Linien-zu-Volumen, z.B. in Festkörpern eingebettete Balken, und Linien-zu-Flächen, z.B. an die Oberfläche eines Festkörpers verbundene oder mit ihr in Kontakt stehende Balken. Im Rahmen der vorliegenden Arbeit wird zunächst die fixe Kopplung der Position der Balkenmittellinie an den darunter liegenden Festkörper bei Linien-zu-Volumen-Problemen untersucht. In einem nächsten Schritt werden auch die Rotationen der Cosserat-Kontinua an das Festkörpervolumen gekoppelt. Dies erfordert die Konstruktion eines geeigneten Rotationsfeldes innerhalb des festen (Boltzmann-)Kontinuums. Sowohl für die Positions- als auch für die Rotationskopplung werden zur Diskretisierung der Kopplungsbedingungen mortarartige Methoden eingesetzt, die sich an den klassischen Mortar Methoden der Gebietszerlegung

oder von Kontaktproblemen orientieren. Es wird eine Strafterm-Regularisierung durchgeführt, um die Lagrange-Multiplikatoren aus dem globalen Gleichungssystem zu eliminieren, was zu einem robusten Kopplungsschema führt. Dies wird durch mehrere numerische Beispiele verifiziert, bei denen ein konsistentes räumliches Konvergenzverhalten erreicht und potentielle Versteifungseffekte vermieden werden können. In der zweiten Hälfte dieser Arbeit werden die zuvor entwickelten Algorithmen für die Linien-Volumen-Kopplung auf die Linien-Flächen-Kopplung erweitert. Dies bringt die zusätzliche Komplexität mit sich, dass der Oberflächennormalenvektor in den Kopplungsbedingungen berücksichtigt werden muss. Es wird gezeigt, dass nur eine konsistente Behandlung des Oberflächennormalenvektors zu physikalisch verwertbaren Ergebnissen führt und grundlegende mechanische Eigenschaften wie die Drehimpulserhaltung garantiert. Schließlich wird ein Gauß-Punkt-zu-Segment Linien-zu-Flächen Kontaktschema vorgestellt, das die Modellierung von Kontakt zwischen eindimensionalen Balken und zweidimensionalen Festkörperoberflächen ermöglicht.

Die zuvor beschriebenen Bausteine bilden einen neuartigen gemischt-dimensionalen Balken-Festkörper-Interaktionsansatz, welcher durch theoretische Diskussionen und numerische Beispiele in dieser Arbeit verifiziert wird. Mögliche Erweiterungen werden skizziert und versprechen numerische und algorithmische Verbesserungen sowie die Behandlung von weiteren physikalischen Effekten wie z.B. Delamination zwischen den eingebetteten Balken und dem umgebenden Volumen. Allerdings ist der vorgestellte Ansatz bereits in seinem jetzigen Zustand ein effizientes, robustes und genaues Werkzeug für Balken-Festkörper-Interaktionsprobleme und kann zu einem wertvollen Werkzeug in Wissenschaft und Technik werden.

Contents

1. Introduction	1
1.1. Motivation	1
1.2. Modeling approaches for beam-to-solid interaction problems	1
1.3. Research objective	4
1.3.1. Specification of requirements	4
1.3.2. Proposal for mixed-dimensional beam-to-solid interaction framework	5
1.4. Outline	6
2. Governing equations and finite element formulations	9
2.1. Solid mechanics	9
2.1.1. Kinematics	9
2.1.2. Variational formulation	11
2.2. Beam mechanics	11
2.2.1. Large rotations	12
2.2.2. Geometrically exact beam theory	13
2.3. Finite element formulations	17
2.3.1. Solid mechanics	17
2.3.2. Beam mechanics	18
2.4. Uncoupled beam and solid problem	22
2.5. Constrained beam-to-solid interaction problem	23
2.5.1. Lagrange multiplier method	23
2.5.2. Penalty regularization	25
3. Mixed-dimensional beam-to-solid interaction	27
3.1. Classification of beam-to-solid interaction problems	27
3.2. Modeling assumptions underlying mixed-dimensional models	29
3.2.1. Beam-to-solid volume coupling	29
3.2.2. Beam-to-solid surface coupling	32
3.2.3. Beam-to-solid surface contact	32
3.3. Positional and rotational coupling	33
3.4. Discretization strategies for beam-to-solid interaction problems	35
3.5. Overview	35
4. Positional beam-to-solid volume coupling	37
4.1. Problem formulation	37
4.2. Spatial discretization	39
4.2.1. Mortar-type coupling of positions	39
4.2.2. Discrete Lagrange multiplier spaces	41

4.2.3.	Penalty regularization	43
4.2.4.	Numerical integration	44
4.3.	Parallel evaluation of beam-to-solid pairs	45
4.4.	Examples	49
4.4.1.	Constant stress transfer	49
4.4.2.	Spatial convergence	53
4.4.3.	Influence of the penalty parameter	56
4.4.4.	Beam-to-solid element length ratio	57
4.4.5.	Fiber-reinforced composite plate	59
5.	Rotational beam-to-solid volume coupling	63
5.1.	Problem formulation	64
5.1.1.	Penalty potential	65
5.1.2.	Lagrange multiplier potential	66
5.1.3.	Objectivity of full beam-to-solid volume coupling	67
5.2.	Definition of solid triad field	67
5.2.1.	Motivation of the solid triad concept	68
5.2.2.	Polar decomposition of the deformation gradient	69
5.2.3.	Alternative solid triad definitions	72
5.2.4.	Variation of the solid rotation vector	73
5.3.	Spatial discretization	74
5.3.1.	Gauss point-to-segment coupling of cross-section rotations	74
5.3.2.	Mortar-type coupling of cross-section rotations	76
5.3.3.	Combined mortar-type coupling of positions and rotations	78
5.3.4.	Penalty regularization	79
5.4.	Examples	80
5.4.1.	Single element moment test	81
5.4.2.	Shear test	81
5.4.3.	Fiber-reinforced composite under shear loading	85
5.4.4.	Constant torque transfer	88
5.4.5.	Spatial convergence	89
5.4.6.	Plane cantilever bending	91
5.4.7.	Plate with embedded beam	92
5.4.8.	Fiber-reinforced pipe	93
5.4.9.	Twisted plate	96
6.	Beam-to-solid surface coupling	103
6.1.	Problem formulation	103
6.1.1.	Closest point projection	105
6.1.2.	Positional beam-to-solid surface coupling	106
6.1.3.	Rotational beam-to-solid surface coupling	109
6.2.	Surface triad field	110
6.3.	Spatial discretization	113
6.3.1.	Evaluation of solid surface normal field	113
6.3.2.	Mortar-type coupling of beam-to-solid surface normal distance	114

6.3.3.	Combined mortar-type coupling	117
6.3.4.	Penalty regularization	118
6.3.5.	Extended beam-to-solid volume coupling	122
6.4.	Examples	123
6.4.1.	Constant stress transfer	123
6.4.2.	Half-pipe with helix-shaped beam	127
6.4.3.	Supported plate	130
6.4.4.	Stented elastic artery	132
7.	Beam-to-solid surface contact	139
7.1.	Problem formulation	139
7.1.1.	Contact kinematics	139
7.1.2.	Variational formulation and finite element discretization	140
7.1.3.	Penalty laws	142
7.2.	Numerical examples	143
7.2.1.	Sliding spaghetti problem	143
7.2.2.	Four-point bending test	146
7.2.3.	Dynamic simulation of a tennis shot	147
8.	Summary and outlook	155
8.1.	Summary of achievements	155
8.2.	Outlook and future work	156
A.	Full 2D-3D coupling for beam-to-volume coupling problems	159
A.1.	Constraint enforcement strategies	159
A.1.1.	Penalty potential	159
A.1.2.	Lagrange multiplier potential	160
A.2.	Constraint discretization strategy for full 2D-3D coupling	160
A.2.1.	Gauss point-to-segment approach for full 2D-3D coupling	160
B.	L2-optimality for the polar decomposition of the deformation gradient	163
C.	Variation of the gap function in beam-to-solid surface contact	165

List of Figures

1.1. Occurrences of beam-to-solid interaction problems in real life applications and systems	2
1.2. Illustration of various beam-in-solid modeling techniques for the same physical problem of a material matrix with three straight embedded fibers	2
2.1. Kinematics of a solid continuum	10
2.2. Kinematics of a geometrically exact beam	14
2.3. Centerline degrees of freedom for a single beam element used in this thesis . .	19
2.4. Rotational degrees of freedom for a single beam element used in this thesis . .	20
3.1. Classification of beam-to-solid interaction problems based on the interacting geometries and the type of interaction	28
3.2. Illustration of the considered classes of beam-to-solid interaction problems . .	28
3.3. Two different types of mixed-dimensional coupling for an embedded fiber in an infinite solid	30
3.4. Schematic illustration of the solid displacement field for an embedded fiber in an infinite solid	30
3.5. Plane coupling problem of a single fiber with a solid finite element mesh	31
3.6. Truly 1D-2D coupling for beam-to-solid surface coupling problems	32
3.7. Plane coupling problem of a single fiber with a solid finite element surface . . .	33
3.8. Modeling assumptions for beam-to-solid surface contact	33
4.1. Notation of the finite deformation positional beam-to-solid volume coupling problem	38
4.2. Illustration of weak and strong discontinuities	45
4.3. Illustration of element-based and segment-based integration	46
4.4. Graph-based parallel distribution of a beam-to-solid volume coupling problem .	47
4.5. Binning-based parallel distribution for the evaluation of beam-to-solid pairs . .	48
4.6. Binning-based parallel distribution of a beam-to-solid volume coupling problem	49
4.7. Constant stress transfer test – problem setup	50
4.8. Constant stress transfer test – results for overlapping straight beams	52
4.9. Constant stress transfer test – results for overlapping helix-shaped beams	53
4.10. Strong discontinuities – Gauss point-to-segment and mortar-type approach . . .	54
4.11. Spatial convergence – problem setup of a coupled beam and solid structure . . .	54
4.12. Spatial convergence – error plots for various coupling methods	56
4.13. Spatial convergence – coupling interactions	57
4.14. Beam-to-solid element length ratio – L_2 -error for various parameter combinations and coupling schemes	58

4.15. Beam-to-solid element length ratio – L_2 -error for varying beam-to-solid element length ratios and linear interpolation of the Lagrange multipliers	59
4.16. Fiber-reinforced composite plate – problem setup	60
4.17. Fiber-reinforced composite plate – deformed configuration and coupling forces	60
4.18. Fiber-reinforced composite plate – deformed configurations of the mid-plane of the plate at various load values and for various modeling techniques	62
5.1. Employed notations and relevant kinematic quantities defining the 3D finite deformation full beam-to-solid volume coupling problem	64
5.2. Illustration of various solid triad definitions for an exemplary 2D problem setting	73
5.3. Single element moment test – problem setup	81
5.4. Single element moment test – resulting nodal loads for various solid triads	82
5.5. Shear test – problem setup	82
5.6. Shear test – deformed configurations	83
5.7. Shear test – resulting nodal loads for various solid triads	84
5.8. Shear test – relative displacement error $\ e\ _{L_2, \text{rel}}$ for various beam diameter to solid cube length ratios d/h	85
5.9. Fiber-reinforced composite under shear loading – problem setup	86
5.10. Fiber-reinforced composite under shear loading – deformed configurations	87
5.11. Constant torque transfer – problem setup	89
5.12. Constant torque transfer – deformed configuration	90
5.13. Spatial convergence – problem setup	90
5.14. Spatial convergence – convergence plot for various solid triads and the 2D-3D reference solution	91
5.15. Plane cantilever bending – problem setup and the deformed configuration	92
5.16. Plate with embedded beam – problem setup for variant A and B	93
5.17. Plate with embedded beam – deformed configurations for variant A	94
5.18. Plate with embedded beam – deformed configurations for variant B	94
5.19. Plate with embedded beam – deformed configurations of the edge indicated in Figure 5.16	95
5.20. Fiber-reinforced pipe – problem setup and deformed configuration	96
5.21. Twisted plate – problem setup	97
5.22. Twisted plate – deformed configurations at various load steps	98
5.23. Twisted plate – reaction moment at the fully clamped surface of the plate over the course of the simulation, with and without fiber-reinforcements	98
5.24. Twisted plate – closeup of deformed configuration at load step 100	99
5.25. Twisted plate – internal elastic fiber energies over the course of the simulation	100
5.26. Twisted plate – deformed configuration of a plate with an increased complexity	101
6.1. Notation of the finite deformation beam-to-solid surface coupling problem	104
6.2. Illustration of possible beam-to-solid surface coupling problems	106
6.3. Illustration of the three different positional beam-to-solid surface coupling variants	106
6.4. Illustration of the influence of out of plane solid deformations on the solid deformation gradient at the solid surface	112
6.5. Construction of the solid surface triad	112

6.6. Illustration of the constructed C^0 -continuous surface normal field	114
6.7. Projection of point \underline{p} to the parameter space of the solid finite element (e) with extended beam-to-solid volume coupling	122
6.8. Cautionary cases for extended beam-to-solid volume coupling	123
6.9. Constant stress transfer – problem setup	124
6.10. Constant stress transfer – results for straight beams and various coupling variants	124
6.11. Constant stress transfer – results for straight beams and various solid finite element discretizations	125
6.12. Constant stress transfer – results for curved beams and various coupling variants	126
6.13. Constant stress transfer – results for curved beams and various solid finite element discretizations	126
6.14. Half-pipe with helix-shaped beam – problem setup	127
6.15. Half-pipe with helix-shaped beam – finite element discretization of the beam-to-solid mesh and full 3D mesh	127
6.16. Half-pipe with helix-shaped beam – deformed configurations for the unloaded problem	129
6.17. Half-pipe with helix-shaped beam – deformed configurations for the loaded problem	129
6.18. Supported plate – problem setup	131
6.19. Supported plate – modeled weld line between the beam and the plate in the full 3D reference solution	131
6.20. Supported plate – deformed configurations for various modeling techniques . .	132
6.21. Supported plate – deformed configurations of the material line indicated in Figure 6.18 for various modeling techniques	133
6.22. Stented elastic artery – problem setup	133
6.23. Stented elastic artery – deformed configurations at various simulation times . .	135
6.24. Stented elastic artery – plot of the fluid velocity v_2 in channel direction along the centerline of the pipe	135
6.25. Stented elastic artery – negative coupling line loads for beam-to-solid surface coupling at various simulation times	136
7.1. Visualization of the quadratically regularized penalty law	143
7.2. Sliding spaghetti problem – problem setup	143
7.3. Sliding spaghetti problem – trajectories of the right hand tip of the beam over the course of the retraction process for the beam-to-solid surface contact method and the sliding-beam-formulation	145
7.4. Sliding spaghetti problem – deformed configurations at various retraction stages	145
7.5. Four-point bending test – problem setup	146
7.6. Four-point bending test – deformed configuration	147
7.7. Four-point bending test – quarter view of the deformed configuration	148
7.8. Four-point bending test – deformed configuration with the contact forces \underline{f}^c acting on the beams	148
7.9. Dynamic simulation of a tennis shot – problem setup	149
7.10. Dynamic simulation of a tennis shot – pre-stressed initial configuration of the racket	150

7.11. Dynamic simulation of a tennis shot – deformed configurations of tennis ball and racket at various time steps	152
7.12. Dynamic simulation of a tennis shot – average velocity of the tennis ball in \underline{e}_3 -direction over the course of the simulation	153
7.13. Dynamic simulation of a tennis shot – photo-realistic rendering of the tennis ball and racket $t = 1.5$ ms	154
A.1. Illustration of the discrete coupling points for 2D-3D coupling along a single cross-section	162

List of Tables

3.1. Overview over the investigated BTS interaction schemes in this thesis.	36
4.1. Listing of the various coupling methods investigated in Chapter 4	50
5.1. Listing of the various solid triad variants presented in Chapter 5	69
5.2. Shear test – numerical results	85
5.3. Fiber-reinforced composite under shear loading – numerical results.	87
6.1. Half-pipe with helix-shaped beam – numerical results for the unloaded problem	128
6.2. Half-pipe with helix-shaped beam – numerical results for energy and balance of moments	130
6.3. Half-pipe with helix-shaped beam – numerical displacements results	130
6.4. Stented elastic artery – problem parameters	134
7.1. Sliding spaghetti problem – geometric and material properties.	144

Nomenclature

Representation of scalars, tensors and other quantities

q, Q	Scalar quantity
$\underline{q}, \underline{Q}$	Tensor quantity of order one or higher
q_1, q_2, q_3	First, second and third component of a vector \underline{q} in Cartesian coordinates
\mathbf{q}	Discrete vector
\mathbf{Q}	Discrete matrix

Operators and symbols

\otimes	Dyadic product
\times	Vector product
\cdot	Inner product
$(\cdot)^T$	Transpose of a tensor, a vector, or a matrix
$(\cdot)^{-1}$	Inverse of a tensor or a matrix
$(\cdot)^{-T}$	Inverse of the transpose
\det	Determinant
cof	Cofactor
Lin	Linearization of a quantity
$\delta(\cdot)$	Variation of a quantity (additive in all cases unless mentioned otherwise)
$\delta_o(\cdot)$	Objective variation of a quantity
$\Delta(\cdot)$	Finite increment of a quantity (additive in all cases unless mentioned otherwise)
$(\cdot)'$	Derivative with respect to the beam arc-length parameter s
$(\cdot)_{,\xi}$	Derivative with respect to the solid surface parameter coordinate ξ^S
$(\cdot)_{,\eta}$	Derivative with respect to the solid surface parameter coordinate η^S
$\ (\cdot)\ $	Euclidean norm
$\text{rv}(\cdot)$	Extraction of rotation vector from rotation tensor
$\text{nl}(\cdot)$	Arbitrary function that depends on its arguments in a nonlinear manner
$\underline{\mathbf{I}}, \mathbf{I}$	Identity tensor, identity matrix

Superscripts and Subscripts

$(\cdot)^S$	Quantity associated with the solid structure
$(\cdot)^B$	Quantity associated with the beam structure
$(\cdot)^\nu$	Quantity resulting from positional beam-to-solid volume coupling

$(\cdot)^{\mathcal{R}}$	Quantity resulting from rotational beam-to-solid volume / surface coupling
$(\cdot)^{\mathcal{U}}$	Quantity resulting from positional beam-to-solid surface coupling
$(\cdot)^{\mathcal{C}}$	Quantity resulting from beam-to-solid surface contact
$(\cdot)_0$	Value in the reference configuration
$(\cdot)_{\text{int}}$	Internal
$(\cdot)_{\text{ext}}$	External
$(\cdot)_{\text{ref}}$	Reference value
$(\cdot)_{1\text{D-3D}}$	Interaction between the 1D beam centerline and a 3D volume
$(\cdot)_{2\text{D-3D}}$	Interaction between the 2D surface of a beam and a 3D volume
$(\cdot)_{\text{SR}}$	Simo–Reissner beam theory
$(\cdot)_{\text{KL}}$	Kirchhoff–Love beam theory
$(\cdot)_{\text{TF}}$	Torsion-free beam theory
$(\cdot)_{\text{REF}}$	REF variant of beam-to-solid surface coupling
$(\cdot)_{\text{DISP}}$	DISP variant of beam-to-solid surface coupling
$(\cdot)_{\epsilon}$	Penalty method
$(\cdot)_{\text{GP}}$	Gauss point
$(\cdot)_h$	Spatially discretized quantity
$(\cdot)_s$	Finite element vector or matrix associated with solid degrees of freedom
$(\cdot)_r$	Finite element vector or matrix associated with beam centerline degrees of freedom
$(\cdot)_{\theta}$	Finite element vector or matrix associated with rotational beam degrees of freedom
$(\cdot)_{\lambda}$	Finite element vector or matrix associated with positional or rotational Lagrange multiplier degrees of freedom
$(\cdot)^{[i]}$	Local finite element vector associated with the node i
$(\cdot)^{[i,j]}$	Local finite element matrix associated with the nodes i and j
$(\cdot)^{(e)}$	Quantity associated with the solid element e
$(\cdot)^{(f)}$	Quantity associated with the beam element f
$(\cdot)^{(e,f)}$	Quantity associated with the pairing of the solid element e and the beam element f
$(\cdot)^*$	Quantity transformed by an arbitrary rigid body rotation

Domains and boundaries

$\Omega_0^{\mathcal{S}}$	Solid reference configuration
$\Omega^{\mathcal{S}}$	Current solid configuration
$\partial\Omega_0^{\mathcal{S}}$	Solid boundary in reference configuration
$\partial\Omega^{\mathcal{S}}$	Solid boundary in current configuration
Γ_u	Dirichlet partition of the solid boundary in reference configuration
γ_u	Dirichlet partition of the solid boundary in current configuration
Γ_{σ}	Neumann partition of the solid boundary in reference configuration
γ_{σ}	Neumann partition of the solid boundary in current configuration
$\Omega_0^{\mathcal{B}}$	Reference beam arc-length domain
$\Omega^{\mathcal{B}}$	Current beam arc-length domain

Γ_{CS}	Boundary of a single beam cross-section
Γ_c	Coupling domain

Kinematics

$\underline{e}_1, \underline{e}_2, \underline{e}_3$	Cartesian basis vectors
$\underline{\mathbf{X}}$	Position in the reference configuration
$\underline{\mathbf{x}}$	Position in the current configuration
$\underline{\mathbf{u}}$	Displacement
$\underline{\dot{\mathbf{u}}}$	Velocity
$\underline{\mathbf{R}}^*$	Arbitrary rigid body rotation
$\delta \underline{\mathbf{u}}$	Constant virtual displacement
$\delta \phi$	Constant virtual rotation
$\underline{\mathbf{F}}$	Deformation gradient
J	Jacobian determinant, determinant of $\underline{\mathbf{F}}$
V_0, V	Reference and current volume
A_0, A	Reference and current surface area
$\underline{\mathbf{N}}, \underline{\mathbf{n}}$	Unit normal vector in reference and current configuration
$\underline{\mathbf{R}}, \underline{\mathbf{U}}, \underline{\mathbf{v}}$	Rotation tensor, material and spatial stretch tensors
$\underline{\mathbf{E}}$	Green–Lagrange strain tensor
s	Arc-length along initial beam centerline
L	Undeformed beam length
ζ	Slenderness ratio
R	Radius of circular cross-section
D	Diameter of circular cross-section
α, β	Beam cross-section coordinates
A	Cross-section area
A_2, A_3	Effective shear areas
I_2, I_3	Planar second moments of inertia
I_T	Polar second moment of inertia
$\underline{\mathbf{r}}_0$	Reference beam centerline position
$\underline{\mathbf{r}}$	Current beam centerline position
$\underline{\mathbf{t}}$	Current beam centerline tangent
$\underline{\mathbf{u}}_r^B$	Displacement of the beam centerline
$\underline{\mathbf{r}}_{CS}$	Position on a beam cross-section
φ	Twist along the beam centerline
$\underline{\mathbf{\Gamma}}$	Material deformation measure
$\underline{\mathbf{\Omega}}$	Material curvature vector
$\underline{\mathbf{\kappa}}$	Frenet–Serret vector
ϵ	Axial tension of the beam
κ	Scalar curvature
$\underline{\mathbf{x}}_r^S$	Solid material point coinciding with a corresponding beam centerline point
d	Distance function

d_c	Unilateral minimal distance value
ξ_c^S, η_c^S	Surface parameter coordinate at the closest point
g	Gap function

Stresses and constitutive laws

E	Young's modulus
ν	Poisson's ratio
G	Shear modulus
$\underline{\underline{S}}$	Second Piola–Kirchhoff stress tensor
Ψ	Strain energy function
$\underline{\underline{C}}_F, \underline{\underline{C}}_M$	Constitutive matrices in the Simo–Reissner beam theory
$\underline{\underline{F}}$	Material force resultants
$\underline{\underline{f}}$	Spatial force resultants
$\underline{\underline{M}}$	Material moment resultants
$\underline{\underline{m}}$	Spatial moment resultants

Large rotations

$(\cdot)_{21}$	Relative rotation from 1 to 2
$\underline{\underline{\Lambda}}, \underline{\underline{R}}$	Triad / rotation tensor with base vectors $\underline{\underline{g}}_1, \underline{\underline{g}}_2, \underline{\underline{g}}_3$
$\underline{\underline{\bar{\Lambda}}}$	Intermediate triad with base vectors $\underline{\underline{\bar{g}}}_1, \underline{\underline{\bar{g}}}_2, \underline{\underline{\bar{g}}}_3$
SO^3	Special orthogonal group
so^3	Set of skew symmetric tensors
$\underline{\underline{S}}(\underline{\underline{a}})$	Skew symmetric tensor with axial vector $\underline{\underline{a}}$
$\exp(\underline{\underline{S}}(\underline{\underline{a}}))$	Exponential map of rotation vector $\underline{\underline{a}}$ to a rotation tensor
$\underline{\underline{\psi}}$	Rotation (pseudo-)vector
ψ	Norm of rotation vector $\underline{\underline{\psi}}$
$\underline{\underline{e}}_\psi$	Normalized rotation vector $\underline{\underline{\psi}}$ representing the axis of rotation
$\Delta \underline{\underline{\psi}}$	Additive (finite) rotation vector increment
$\Delta \underline{\underline{\theta}}$	Multiplicative (finite) rotation vector increment
$\delta \underline{\underline{\psi}}$	Additive rotation vector variation
$\delta \underline{\underline{\theta}}$	Multiplicative rotation vector variation (spin vector)
$\underline{\underline{T}}$	Transformation matrix between the variations $\delta \underline{\underline{\theta}}$ and $\delta \underline{\underline{\psi}}$

Governing equations

t	Time
ρ	Reference mass density
Π	Potential
$\tilde{\Pi}$	Potential per unit length

W	Work
δW_λ	Variational form of the constraint equations
δW_c	Virtual work of the coupling forces
\underline{b}_0	Body force in reference configuration
\underline{t}_0	Prescribed surface traction in reference configuration
$\underline{\lambda}$	Lagrange multiplier vector
\underline{g}	Constraint vector

Finite element and mortar-type methods

e	Index for solid elements
f	Index for beam elements
k	Index for solid nodes
l	Index for beam nodes
j	Index for nodes carrying Lagrange multiplier degrees of freedom
n^S	Number of solid nodes
n_Γ^S	Number of solid surface nodes
n^B	Number of beam nodes carrying positional degrees of freedom
n_θ^B	Number of beam nodes carrying rotational degrees of freedom
n_{el}^S	Number of solid finite elements
n_{el}^B	Number of beam finite elements
$n_{dof}^{(e)}$	Number of discrete degrees of freedom of solid element e
$n_{adj,k}$	Number of solid surface elements adjacent to slave node k
ξ^S, η^S, ζ^S	Parametrization of solid finite element parameter space
N_k	Finite element shape function for solid node k
$\hat{\underline{X}}_k^S$	Reference position of solid node k
$\hat{\underline{x}}_k^S$	Current position of solid node k
$\hat{\underline{d}}_k^S$	Displacement of solid node k
$\underline{n}_{AVG,k}$	Averaged solid surface unit normal vector at node k
ξ^B	Parametrization of beam centerline finite element parameter space
H_l^r	Positional FE shape function for beam node l
H_l^t	Tangent FE shape function for beam node l
\mathbf{H}_l	Node-wise assembled beam centerline shape functions for beam node l
$\hat{\underline{r}}_l$	Current position of beam node l
$\hat{\underline{d}}_{r,l}^B$	Displacement of beam node l
$\hat{\underline{t}}_l$	Current centerline tangent at beam node l
$\hat{\underline{d}}_{t,l}^B$	Tangent increments at beam node l
$\hat{\underline{x}}_l^B$	Generalized nodal position vector for beam node l
$\hat{\underline{d}}_l^B$	Generalized nodal displacement vector for beam node l
$\tilde{\underline{I}}_l$	Generalized rotational shape function matrix for beam node l
$\tilde{\mathbf{I}}^{(f)}$	Element-wise assembled shape functions $\tilde{\underline{I}}_l$
L_l	Standard Lagrange polynomials at beam node l

$\mathbf{L}^{(f)}$	Element-wise assembled shape functions L_l
$\hat{\underline{\psi}}_l^{\mathcal{B}}$	Nodal rotation vector for beam node l
$\Delta \hat{\underline{\theta}}_l$	Multiplicative nodal rotation increments for beam node l
$\Delta \hat{\underline{\theta}}^{\mathcal{B}(f)}$	Element-wise assembled multiplicative rotation vector increments
$\delta \hat{\underline{\theta}}_l$	Multiplicative nodal rotation vector variation for beam node l
$\delta \hat{\underline{\theta}}^{\mathcal{B}(f)}$	Element-wise assembled multiplicative rotation vector variations
Φ_j	FE shape function for Lagrange multiplier node j
$\hat{\Phi}^{(f)}$	Element-wise assembled Lagrange multiplier shape functions
$\hat{\underline{\lambda}}_j$	Discrete Lagrange multiplier at node j
$\hat{\underline{\lambda}}^{(f)}$	Element-wise assembled Lagrange multipliers
\mathbf{K}	Tangent stiffness matrix
\mathbf{X}	Discrete reference positions
\mathbf{x}	Discrete current positions
\mathbf{d}	Discrete displacement
ψ	Discrete rotations
\mathbf{r}	Residuum vector
\mathbf{f}	Discrete force vector
χ	Mapping from beam to solid
\mathbf{D}	First mortar coupling matrix
\mathbf{M}	Second mortar coupling matrix
\mathbf{Q}	Coupling matrix
\mathbf{q}	Coupling vector
λ	Discrete Lagrange multiplier degrees of freedom
\mathbf{g}	Discrete constraint vector
$\tilde{\xi}_i^{\mathcal{B}}$	Beam parameter coordinate at Gauss point
\tilde{w}_i	Weighting factor for Gauss point
h	Characteristic finite element size

Solid triad construction

$\underline{g}_{1,0}^{\mathcal{S}}, \underline{g}_{2,0}^{\mathcal{S}}, \underline{g}_{3,0}^{\mathcal{S}}$	Basis vectors of solid reference triad $\underline{\Lambda}_0^{\mathcal{S}}$
$\underline{g}_i^{\mathcal{S}}$	Push forward of the reference solid triad base vectors $\underline{g}_{i,0}^{\mathcal{S}}$ for $i = 2, 3$
\underline{g}'_i	Normalized directors $\underline{g}_i^{\mathcal{S}}$ for $i = 2, 3$
$\tilde{\underline{g}}_1^{\mathcal{S}}, \tilde{\underline{g}}_2^{\mathcal{S}}, \tilde{\underline{g}}_3^{\mathcal{S}}$	Basis vectors of current solid triad $\underline{\Lambda}^{\mathcal{S}}$
$\underline{F}_{\underline{n}}$	Projection of the solid deformation gradient into the \underline{n} -plane
$\underline{R}_{\underline{n}}$	Pure rotation from $\underline{\Lambda}_0^{\mathcal{S}}$ onto $\underline{\Lambda}$
$\underline{F}_{2\text{D}}$	Quasi-2D in-plane deformation gradient
$\underline{R}_{2\text{D}}^{\mathcal{S}}, \underline{v}_{2\text{D}}$	Rotation tensor and stretch tensor obtained from the polar decomposition of $\underline{F}_{2\text{D}}$
$\underline{\Lambda}_{\text{POL}}^{\mathcal{S}}$	Solid triad obtained from polar decomposition
$\underline{\Lambda}_{\text{DIR}}^{\mathcal{S}}$	Solid triad fixed to material director

$\underline{\underline{\Lambda}}_{\text{AVG}}^S$	Solid triad fixed to averaged material director
$\underline{\underline{\Lambda}}_{\text{ORT}}^S$	Solid triad fixed to two orthogonal material directors
$\underline{\underline{g}}_{\text{AVG}}^S$	Averaged material director
$\underline{\underline{\Lambda}}_{\Gamma}^S$	Solid surface triad
$\underline{\underline{\Lambda}}_{\Gamma,0}^S$	Intermediate triad for the construction of the solid surface triad
θ	Orientation of arbitrary in-plane directors
θ_{diff}	Constant offset of θ
$\underline{\underline{G}}_{P2}, \underline{\underline{G}}_{P3}$	Material principle axes associated with the polar decomposition of $\underline{\underline{F}}_{2D}$
$\underline{\underline{g}}_{P2}, \underline{\underline{g}}_{P3}$	Spatial principle axes associated with the polar decomposition of $\underline{\underline{F}}_{2D}$

Penalty regularization and penalty method

ϵ	Penalty parameter
\mathbf{V}	Scaling matrix for penalty regularization
$\underline{\underline{c}}$	Penalty tensor for rotational cross-section interaction
f	Penalty law
\bar{g}	Regularization parameter for penalty law

Miscellaneous

A	Intermediate symbol to introduce abbreviations for matrices
b	Intermediate symbol to introduce abbreviations for vectors

Abbreviations

BTS	Beam-to-solid
BTSV	Beam-to-solid volume
BTSS	Beam-to-solid surface
BTSSC	Beam-to-solid surface contact
(·)-POS	Positional interaction
(·)-ROT	Rotational interaction
(·)-FULL	Positional and rotational interaction
(·)-CONS	Consistent variant of positional beam-to-surface coupling
(·)-REF	Forced reference configuration variant of positional beam-to-surface coupling
(·)-DISP	Displacement variant of positional beam-to-surface coupling
BTSV-POS-X	Extended positional beam-to-solid volume coupling
STR	Solid triad
STR-POL	Solid triad obtained from polar decomposition
STR-DIR	Solid triad fixed to material director
STR-AVG	Solid triad fixed to average of material directors
STR-ORT	Solid triad fixed to two orthogonal material directors

ABC	All-angle beam contact
CPU	Central processing unit
CT	computed tomography
CutFEM	Cut finite element method
FAD	Forward automatic differentiation
FSI	Fluid-structure interaction
FE	Finite element
FEM	Finite element method
GP	Gauss point
GPTS	Gauss point-to-segment
hex	Hexahedron
NTS	Node-to-segment
NURBS	Non-uniform rational B-splines
PID	Processor identification
SBF	Sliding-beam-formulation
SUPG	Streamline upwind Petrov–Galerkin
tet	Tetrahedron
XFEM	Extended finite element method

1. Introduction

1.1. Motivation

The interaction of fiber- or rod-like components with three-dimensional structures is omnipresent in our world. Often, these fiber components crucially determine the overall mechanical characteristics of the combined problem, such as the strength and stiffness properties. Applications can be found across several length scales from meters down to the range of nanometers as well as in various fields, see Figure 1.1 for exemplary illustrations. In civil engineering, steel reinforcements are embedded into concrete to improve its low tensile strength, or girders are used to support concrete slabs, cf. [33, 82, 125] and Figure 1.1(a). In mechanical engineering, fiber-reinforced composite materials based on carbon, glass, polymer or metal fibers embedded in a plastic, metal or ceramic matrix, make use of fibers with high stiffness embedded in softer matrix material for improved mechanical properties. This results in lightweight structures that are used in various applications, such as spacecrafts, planes, cars or boats [1, 74, 149]. Techniques such as tailored fiber placement, cf. [89, 90, 132], or additively manufactured components, cf. [104], allow for a very flexible and locally controlled reinforcement of the composite matrix, further enhancing the properties of the resulting structures [8, 10, 21]. Applications are not limited to embedded fibers. For example, the impact of a tennis ball on the string bed of a tennis racket, see Figure 1.1(b), is an application where the fibers not only improve the mechanical properties of the combined system but are vital for the functionality itself. In bio-mechanics, stent grafts, i.e., wire-like stent-structures fused with soft graft material, are a commonly used device for endovascular aneurysm repair, cf. [23, 40, 47, 56] and Figure 1.1(c). At a different length scale, fiber interactions play a key role for essential processes in countless biological systems, e.g., in the form of embedded networks (e.g., cytoskeleton, extracellular matrix, mucus), bundles (e.g., muscle, tendon, ligament) [4, 52, 88, 102], or in arterial wall tissue with collagen fibers, cf. [61, 62] and Figure 1.1(d). Computational models predicting the response of such structures are essential for a time- and cost-efficient design and development of technical products, but also to gain fundamental understanding of biological systems at length scales that are not accessible via experiments. In the context of computational modeling, as considered in this thesis, the embedded 1D structures will be referred to as *fibers* or *beams*, respectively, and the 3D structure as *solid*.

1.2. Modeling approaches for beam-to-solid interaction problems

Various modeling techniques exist to create a numerical model of the beam-to-solid (BTS) problem, almost all of them being based on the finite element method. Figure 1.2 exemplarily

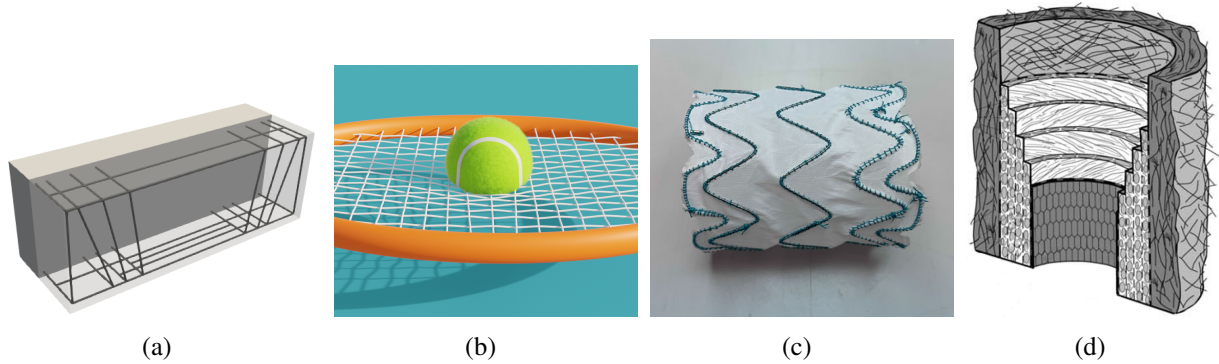


Figure 1.1.: Occurrences of beam-to-solid interaction problems in real life applications and systems – Steel reinforcements embedded inside a concrete structure (a), impact of a tennis ball on the string bed of a tennis racket (b), stent-graft employed for endovascular aneurysm repair (c), and collagen fibers inside arterial wall tissue (d). Figure (c) is reprinted from [54], permissions granted under the Creative Commons (CC BY) license. Figure (d) is reprinted from [62] by permission from Springer Nature Customer Service Centre GmbH.

illustrates three different modeling techniques on the basis of the same physical problem of three fibers being embedded inside a solid material matrix, with the modeling complexity increasing from left to right.

One common modeling approach is based on homogenized, anisotropic material models for the combined fiber-matrix structure [1, 149], cf. Figure 1.2(a). This widely used approach is appealing since, e.g., no additional degrees of freedom are required to model individual fibers, and existing simulation tools can be used as long as they support anisotropic material laws. However, such models cannot give detailed information about the interactions between fibers and surrounding matrix as, e.g., required to study mechanisms of failure. Moreover, the fiber distribution in the solid has to be sufficiently homogeneous and a separation of scales is required, i.e., the fiber size has to be sufficiently small as compared to the smallest dimension of the overall structure.

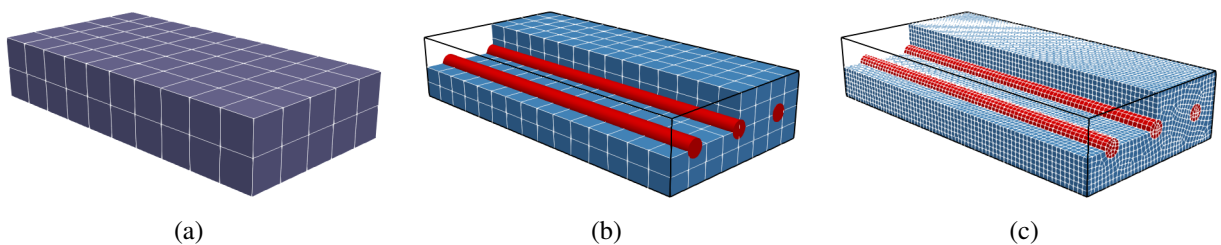


Figure 1.2.: Illustration of various beam-in-solid modeling techniques for the same physical problem of a material matrix with three straight embedded fibers – homogenized 3D model (a), 1D beams overlapping with 3D volume (b) and full 3D model (c). The modeling complexity increases from left to right. Figure is taken from the author's article [135], permissions granted under the Creative Commons (CC BY) license.

Eventually, when modeling new fiber arrangements, the homogenization step inherent to these continuum models requires sub-scale information, e.g., provided by a model with resolved fiber geometries. The main complexity in this approach lies in the accurate homogenization of the fibers and the matrix material. As the focus of this thesis lies on the development of BTS coupling schemes, where the beams are modeled explicitly, the homogenization approach will not be discussed in more detail.

Another modeling approach consists of fully describing the fibers and surrounding solid material as 3D continua, cf. Figure 1.2(c). This leads to a surface-to-surface coupling problem at the 2D interface between fiber surface and surrounding solid. In the context of the finite element method, these surfaces can be tied together by either applying fiber and solid discretizations that are conforming at the shared interface or via interface coupling schemes accounting for non-matching meshes, such as the mortar method [109, 111, 112, 115]. The creation of the finite element mesh with explicit boundaries at the interface between beam surface and solid can be a non-trivial task. Alternatively, extended finite element methods (XFEM) [101] or immersed finite element methods [86, 87, 120] can be used to represent 2D fiber surfaces embedded in an entirely independent background solid mesh. Therefore, a very simple, in many cases even structured Cartesian finite element mesh can be employed. While such fully resolved modeling approaches allow for studying local effects with high spatial resolution, the significant computational effort associated with these models prohibits their usage for large-scale systems with a large number of slender fibers.

The class of applications considered in this thesis typically involves very slender fibers. In this regime it is well justified, and highly efficient from a computational point of view, to model individual fibers as beams, e.g., based on the geometrically exact beam theory [19, 38, 96, 99, 117, 129–131], which is known to combine high model accuracy and computational efficiency [14, 119]. Based on the fundamental kinematic assumption of undeformable cross-sections, such beam models can be identified as 1D Cosserat continua embedded in 3D space with point-wise six degrees of freedom to describe the cross-section position (three positional degrees of freedom) and orientation (three rotational degrees of freedom). In some application cases, it can be beneficiary to impose additional constraints on the local deformation modes of the 1D Cosserat continua, e.g., vanishing shear or torsion deformations [96, 97, 99, 145]. Employing such 1D beam theories to model the fibers interacting with a 3D solid results in a *mixed-dimensional* interaction problem between 1D Cosserat continua and a 3D Boltzmann continuum, which is illustrated in Figure 1.2(b). A variety of mixed-dimensional interaction approaches exist in the literature, most of them investigating the application case of embedded fibers inside a solid volume. Early work on 1D fibers embedded in 3D structures has been carried out in the context of reinforced concrete in [105], with the restriction that the reinforcements have to align with a parameter coordinate of the solid element. In [34], this approach was extended to straight reinforcements with arbitrary directions relative to the solid elements, and in [44, 50, 116] also curved reinforcements are considered. All these works do not introduce additional degrees of freedom for the fibers, but instead incorporate the fiber stiffness contributions into the stiffness matrices of the solid elements. Alternatively, each fiber can be described by its own set of degrees of freedom, which introduces the need for kinematic coupling constraints acting on the fibers and solid. In [72], a cut finite element method (CutFEM) approach is employed to embed 1D fiber reinforcements into a 3D matrix material. All of the previously mentioned works on 1D-3D interaction involve truss / string models, i.e., 1D structural models accounting only for internal elastic energy contributions

from axial tension. Work on the mixed-dimensional interaction between beams, i.e., full Cosserat continua, and solids is much rarer. In [43], collocation along the beam centerline is applied to couple beams with a surrounding solid material. In a very recent approach [73], the *full* mixed-dimensional BTS coupling problem involving positions *and* rotations has been addressed for the first time. In this contribution, the coupling constraints between the 1D beam and the 3D solid volume are formulated on the surface of the beam and are subsequently projected onto the beam centerline considering a Taylor series expansion of the solid displacement field. The coupling of the two directors spanning the (undeformable) beam cross-section with the underlying solid continuum together with the coupling of the cross-section centroids results in a total of nine coupling constraints. One specific focus of this interesting contribution is a static condensation strategy, which allows to eliminate the associated Lagrange multipliers and the beam balance equations from the final, discrete system of equations. The requirement of a C^1 -continuous spatial discretization of the solid domain, as resulting from the proposed condensation strategy, is satisfied by employing NURBS-based test and trial functions. The approach recently presented in [85] combines the techniques from Figure 1.2(b) and Figure 1.2(c) by using a 3D representation of the beams in zones of interest and 1D structural models otherwise. A 1D beam to 2D surface contact scheme is presented in [77], however, there the solid surfaces are assumed to be rigid, which heavily limits the applicability within real life engineering problems. Moreover, mixed-dimensional coupling can also be found in multi-physics scenarios, e.g., between beams and a surrounding fluid field, as relevant for fluid-structure-interaction (FSI) problems, which has been considered in some recent contributions [53, 144]. Another interesting application for mixed-dimensional coupling has been presented in [79], where vascular tumor growth is simulated by coupling the 1D vasculature to the surrounding 3D tissue.

1.3. Research objective

Structural beam theories feature very desirable properties for modeling the slender fibers involved in the typical application cases considered in this thesis. Therefore, this thesis aims at developing mixed-dimensional finite element interaction schemes for BTS interaction problems, where the beams are explicitly modeled using 1D beam finite elements, while the solid is modeled using 3D continuum finite elements. As outlined in Section 1.2, this topic has been part of scientific and industrial applications for many years. However, a truly general and robust framework for large deformation mixed-dimensional BTS interactions is still missing.

1.3.1. Specification of requirements

This section lists the most important requirements for the development of a general BTS interaction framework, where the beams are modeled using 1D beam finite elements.

Clear definition of the modeling assumptions and application range As with almost every mathematical model of a physical problem, the modeling assumptions have to be clearly stated. This is especially important in the considered case of BTS problems, as the mixed-dimensional nature of the considered interactions between 1D beams and 3D solid limits the application range compared to a classical full 3D continuum representation for beams and solid.

Accuracy The inevitable introduction of modeling errors due to the mixed-dimensional coupling shall not degrade the ability of the developed finite element schemes to accurately predict the quantity of interest.

Numerical and model creation efficiency Employing a 1D beam theory increases the numerical efficiency compared to a full 3D description of the beams. The developed BTS interaction algorithms have to be designed and implemented in such a way that they do not offset this increased numerical efficiency. Furthermore, efficiency also refers to a drastically simplified model creation process, compared to full 3D surface coupled models. To allow for a flexible mesh creation process, the proposed algorithms shall exhibit the capabilities to deal with general configurations of the beams and solid, i.e., the placement of the beam finite elements shall not be restricted to align with solid element edges.

Handling of non-matching discretizations The previous requirement already states that the BTS interaction algorithms have to be able to handle general, i.e., non-matching, discretizations of the beams and solid. In the case of BTS coupling (mesh tying) applications, this allows for a flexible mesh creation process. Even more importantly, this is a requirement to allow for application cases where the beams are in contact with the solid, i.e., the configurations change relative to each other over the course of the simulation, thus resulting in inevitably non-matching grids.

Compatibility The developed BTS interaction methods shall be compatible with various finite element formulations for the beams and the solid, e.g., mixed / hybrid elements or isogeometric discretizations based on non-uniform rational B-splines (NURBS). This allows for the employment of modern finite element technologies developed for pure beam or pure solid problems in combination with each other.

Flexibility The developed finite element procedure and code framework should consist of clearly distinguishable logical units that can be combined for specific requirements of the considered applications. This includes that parts of the developed code framework can also be used for other mixed-dimensional interaction applications, e.g., embedded beams in an incompressible fluid field.

1.3.2. Proposal for mixed-dimensional beam-to-solid interaction framework

This thesis describes novel mixed-dimensional interaction schemes between 1D beam finite elements and 3D solid finite elements, addressing all of the aforementioned requirements. To the author's knowledge, this distinguishes the proposed formulations from all existing approaches available in the literature. The most important novel scientific contributions of the presented approaches include:

- the first successful implementation of line-to-volume mortar-type coupling approaches for embedded 1D fibers inside a 3D solid volume.
 - See Chapter 4 and [135] for the positional coupling constraints, i.e., a coupling of the beam centerline positions to the underlying solid volume.

- See Chapter 5 and [138] for the positional *and* rotational coupling constraints, i.e., a coupling of all deformation modes of the 1D Cosserat continua representing the beam to the underlying solid volume. This is also the first time, that mortar-type methods are employed to discretize rotational coupling constraints.
- an elaborate discussion and analysis of the modeling assumptions introduced by a mixed-dimensional coupling in solid mechanics, see Chapter 3 and [135, 138]. This includes an analysis of possibly singular solutions as well as a clear definition of the envisioned application range.
- the first successful implementation of line-to-surface mortar-type coupling approaches for consistent coupling of 1D fibers to the 2D surface of a 3D volume, see Chapter 6. This includes a novel analysis of the conservation of momentum properties for line-to-surface coupling problems where, in the continuous setting, the line is offset from the surface in surface normal direction. This can also be easily adapted to similar surface-to-surface mesh tying problems.

Summing up, the methods proposed in this thesis combine existing finite element discretization techniques for beam and solid formulations by applying existing ideas from other applications such as surface-to-surface mesh tying / contact. This allows for a more efficient and general treatment of a broad range of BTS interaction problems, thus for the first time tapping the full potential of a truly general mixed-dimensional BTS interaction framework.

1.4. Outline

The methods and algorithms in this thesis are organized in a way to systematically present the building blocks for a general BTS interaction framework. Thus, the remainder of this thesis is organized as follows.

In Chapter 2, the relevant governing equation of nonlinear solid mechanics and structural beam theories are outlined. This includes an overview on the mathematical treatment of finite rotations as required for the employed beam theories. In addition, the basic concepts of the finite element method for the considered beam and solid formulations are reviewed in a very general manner. Furthermore, the general procedure of combining the individual beam and solid problem, by adding constraints via the Lagrange multiplier method, is presented.

Chapter 3 presents a general classification of BTS interaction problems, which will also be used to split the presented methods and remaining structure of this thesis. Moreover, an elaborated discussion regarding the modeling assumptions and envisioned application range of the presented BTS interaction methods is given.

The application case of fibers embedded inside a solid volume is presented in Chapter 4. In this chapter only positional coupling between the beam centerline and the solid volume is considered. The numerical integration procedure (as will also be used for all other presented BTS cases) is outlined and investigated. Furthermore, some important aspects of parallel evaluation of the BTS coupling terms are presented. Finally, the proposed methods are validated and illustrated with several numerical examples.

Chapter 5 presents an additional building block for BTS coupling problems, the enforcement of constrained rotations between the beam cross-section and the solid. The theoretical and numerical considerations in this chapter are presented based on beams embedded inside a solid volume, i.e., the extension of the previous chapter to couple positions *and* rotations between the beams and the surrounding solid. Rotational coupling requires a suitable orthonormal triad field to be defined within the solid volume. Various variants to construct this triad field are investigated and compared to each other. Selected numerical examples are presented, to verify the proposed methods.

In Chapter 6, the case of beams tied to a solid surface is considered. The presented method employs several of the building blocks presented in the previous two chapters and extends them to account for the surface normal distance between the beam and the solid surface. Various variants of the coupling equations are presented and compared by investigating some basic mechanical principals such as conservation of angular momentum. Furthermore, this chapter includes a definition of a suitable solid surface triad field to couple rotations of the beam cross-section to the solid surface. Again, numerical examples are presented to validate the proposed approach and illustrate its applicability to multi-physics problems.

In Chapter 7, an unilateral contact formulation between 1D beams and 3D solids is presented. This topic is part of ongoing research, however, the presented examples verify and illustrate a maturity of the presented BTS contact scheme.

Finally, Chapter 8 concludes this thesis by summarizing the most important results and accomplishments. Furthermore, an outlook on extensions and further improvements of the presented BTS interaction schemes is presented.

2. Governing equations and finite element formulations

In this chapter, the governing equations for the employed solid and beam formulations are reviewed. Moreover, a recapitulation of the basics of the finite element discretization of both the solid formulation and the beam formulation, as well as general interactions between them, is given. As the focus of this thesis is the development of BTS interaction schemes, the purpose of this chapter is to give the reader a general understanding of the underlying physics and discretization techniques and to introduce an appropriate theoretical basis for the proposed BTS interactions. The references throughout this chapter refer the interested reader to more extensive literature on the aforementioned topics.

All presented BTS interaction schemes in this thesis are time-independent, i.e., the interaction conditions and discretized interaction terms are equal for dynamic and quasi-static problems. Therefore, without loss of generality, only the quasi-static governing equations are stated in this chapter and throughout this thesis. For the dynamic governing equations of the solid and beam formulations the interested reader is again referred to the corresponding literature.

2.1. Solid mechanics

A brief introduction to classical continuum solid mechanics is given in this section. This section is not intended to give an elaborate review of continuum mechanics, but rather give insight to the necessary theoretical basics for the proposed BTS interaction schemes. The interested reader is referred to the corresponding literature, e.g., [9, 27, 60, 80, 128].

2.1.1. Kinematics

The basic kinematic relationships describing the deformation of the considered solid bodies are visualized in Figure 2.1. A Cartesian frame $[\underline{e}_1, \underline{e}_2, \underline{e}_3]$ is employed as a fixed frame of reference. The solid is modeled as a 3D Boltzmann continuum, represented by the open set $\Omega_0^S \subset \mathbb{R}^3$ in the reference (material) configuration and by $\Omega^S \subset \mathbb{R}^3$ in the deformed (current / spatial) configuration. Throughout this thesis, the subscript $(\cdot)_0$ indicates a quantity in the reference configuration. In the reference configuration, a material point on the solid can be identified by its reference position $\underline{X}^S \in \mathbb{R}^3$. The current position $\underline{x}^S \in \mathbb{R}^3$ is related to the reference position through the displacement field $\underline{u}^S \in \mathbb{R}^3$ via

$$\underline{x}^S(\underline{X}^S) = \underline{X}^S + \underline{u}^S(\underline{X}^S). \quad (2.1)$$

The (material) deformation gradient $\underline{F} \in \mathbb{R}^{3 \times 3}$ serves as a fundamental measure of deformation

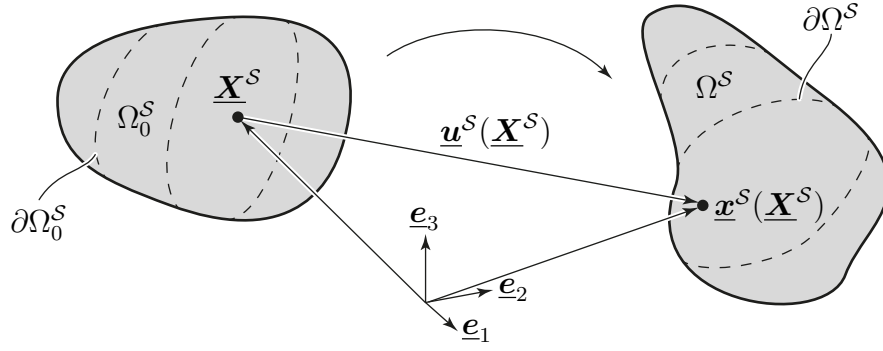


Figure 2.1.: Kinematics of a solid continuum, the reference (left) and current (right) configuration.

and strain in the solid continuum. It is defined as the partial derivative of the current configuration with respect to the spatial configuration, i.e.,

$$\underline{F} = \frac{\partial \underline{x}^S}{\partial \underline{X}^S}. \quad (2.2)$$

The deformation gradient is a so-called two-point tensor (or *push-forward* operator), i.e., it represents a mapping of the reference configuration to the current configuration. This can be interpreted in a geometric way: an infinitesimal line element $\Delta \underline{X}^S$ in the reference configuration corresponds to the current line element $\Delta \underline{x}^S$ via

$$\Delta \underline{x}^S = \underline{F} \Delta \underline{X}^S. \quad (2.3)$$

Assuming bijectivity and smoothness of the deformation, the inverse of the deformation gradient \underline{F}^{-1} is well-defined. This guarantees a positive determinant of the deformation gradient, i.e., $J = \det \underline{F} > 0$. The determinant of the deformation gradient, also referred to as the *Jacobian* determinant of the deformation, represents the relation between an infinitesimal volume element in the reference and the current configuration, i.e.,

$$dV = \det \underline{F} dV_0 = J dV_0. \quad (2.4)$$

Finally, the mapping between infinitesimal oriented area elements is described by

$$d\underline{A} = J \underline{F}^{-T} d\underline{A}_0 = \text{cof} \underline{F} d\underline{A}_0. \quad (2.5)$$

Here, the infinitesimal oriented area elements are interpreted as vectors $d\underline{A}_0 = dA_0 \underline{N}$ and $d\underline{A} = dA \underline{n}$, where \underline{N} and \underline{n} denote the unit normal vectors of the area element in the reference and current configuration, respectively. Furthermore, $\text{cof} \underline{F}$ denotes the cofactor of \underline{F} . Equation (2.5) is commonly referred to as Nanson's formula.

The polar decomposition theorem can be applied to split the deformation gradient into a volume-preserving rigid body motion part and a volume-changing part, i.e.,

$$\underline{F} = \underline{R} \underline{U} = \underline{v} \underline{R}. \quad (2.6)$$

Here $\underline{U} \in \mathbb{R}^{3 \times 3}$ and $\underline{v} \in \mathbb{R}^{3 \times 3}$ are symmetric positive definite second-order tensors also referred to as the right (material) and left (spatial) stretch tensors, respectively. Furthermore, $\underline{R} \in SO^3$ is

a second-order rotation tensor. For a more detailed discussion on the properties of rotation tensors see Section 2.2.1 and the references therein.

In the variational formulation for the solid continuum, the Green–Lagrange strain tensor $\underline{\mathbf{E}}$ is used as strain measure and is defined as

$$\underline{\mathbf{E}} = \frac{1}{2} (\underline{\mathbf{F}}^T \underline{\mathbf{F}} - \underline{\mathbf{I}}), \quad (2.7)$$

with $\underline{\mathbf{I}} \in \mathbb{R}^{3 \times 3}$ being the 3D second-order identity tensor. The Green–Lagrange strain tensor is objective, i.e., it is invariant with respect to an arbitrary rigid body motion.

2.1.2. Variational formulation

The variational formulation of the quasi-static balance equations serves as a basis for the finite element method, resulting in the solid contribution δW^S to the total virtual work. A Lagrangian formulation is used, i.e., all field variables refer to the reference configuration. Hence, the integration of the field variables is performed over the reference volume Ω_0^S and its boundary $\partial\Omega_0^S$. The reference surface $\partial\Omega_0^S$ of the solid volume can be divided into the Dirichlet and Neumann boundary surfaces, Γ_u and Γ_σ , respectively. In the current configuration they are denoted as γ_u and γ_σ . Since the variation along the Dirichlet boundary Γ_u vanishes, the only remaining surface integral in the variational formulation is over the Neumann boundary Γ_σ . The virtual work δW^S of the solid is given by

$$\delta W^S = \underbrace{\int_{\Omega_0^S} \underline{\mathbf{S}} : \delta \underline{\mathbf{E}} dV_0}_{-\delta W_{\text{int}}^S} - \underbrace{\int_{\Omega_0^S} \underline{\mathbf{b}}_0 \cdot \delta \underline{\mathbf{u}}^S dV_0 + \int_{\Gamma_\sigma} \underline{\mathbf{t}}_0 \cdot \delta \underline{\mathbf{u}}^S dA_0}_{-\delta W_{\text{ext}}^S}, \quad (2.8)$$

where δ denotes the variation of a quantity and $\underline{\mathbf{S}} \in \mathbb{R}^{3 \times 3}$ represents the second Piola–Kirchhoff stress tensor, which is the energy-conjugate to the Green–Lagrange strain tensor. Contributions to the external virtual work δW_{ext}^S result from the prescribed body load $\underline{\mathbf{b}}_0 \in \mathbb{R}^3$ and surface traction $\underline{\mathbf{t}}_0 \in \mathbb{R}^3$, both defined in the reference configuration. For simplicity, a hyperelastic material with the strain energy function $\Psi(\underline{\mathbf{E}})$ is assumed. The strain energy function relates to the second Piola–Kirchhoff stress tensor as follows:

$$\underline{\mathbf{S}} = \frac{\partial \Psi(\underline{\mathbf{E}})}{\partial \underline{\mathbf{E}}}. \quad (2.9)$$

Throughout this thesis a hyperelastic material model is employed for the solid, although this is not a requirement of the presented BTS interaction schemes. Other material models (e.g., elasto-plastic solids) can be directly used in combination with the presented BTS interaction schemes.

2.2. Beam mechanics

The main aspect of this thesis is to develop interaction algorithms between 3D solid (Boltzmann) continua and 1D Cosserat continua. A Boltzmann continuum has three local degrees of freedom,

i.e., the position of a material point in a suitable 3D coordinate system. Cosserat continua, on the other hand, have six local degrees of freedom, three positional ones and three rotational ones. The three positional degrees of freedom can be interpreted similar to the degrees of freedom in a Boltzmann continuum, as they describe the spatial position of a material point. The additional three rotational degrees of freedom describe the spatial orientation of a material point. Thin slender structures, i.e., beams, can be efficiently modeled as Cosserat continua based on structural beam theories. The considered 3D large deformation beam theories, as well as the BTS rotational coupling interactions, require a consistent treatment of finite rotations. Therefore, in the next section a short overview on the theory of large rotations is given. Furthermore, an overview of the beam theories employed in this thesis is given in Section 2.2.2.

2.2.1. Large rotations

This section gives a brief overview of the mathematical treatment of finite rotations as required by the employed beam theories and the formulation of rotational coupling constraints in Chapter 5. For a more comprehensive treatment of this topic, the interested reader is referred to the literature, e.g., [18, 31, 63, 68, 99, 118, 130].

Let us consider a rotation tensor

$$\underline{\Lambda} = [\underline{g}_1, \underline{g}_2, \underline{g}_3] \in SO^3, \quad (2.10)$$

where SO^3 is the special orthogonal group and the base vectors \underline{g}_i form an orthonormal triad, mapping the Cartesian basis vectors \underline{e}_i onto \underline{g}_i . In the following, a rotation pseudo-vector $\underline{\psi}$ is used for its parametrization, i.e., $\underline{\Lambda} = \underline{\Lambda}(\underline{\psi})$. The rotation vector describes a rotation by an angle $\psi = \|\underline{\psi}\|$ around the rotation axis $\underline{e}_\psi = \underline{\psi} / \|\underline{\psi}\|$. The parametrization can be given by the well-known Rodrigues formula [11]

$$\underline{\Lambda}(\underline{\psi}) = \exp(\underline{S}(\underline{\psi})) = \underline{I} + \sin \psi \underline{S}(\underline{e}_\psi) + (1 - \cos \psi) \underline{S}^2(\underline{e}_\psi), \quad (2.11)$$

where $\exp(\cdot)$ is the exponential map. Furthermore, $\underline{S} \in so^3$ is a skew-symmetric tensor, where so^3 represents the set of skew-symmetric tensors with $\underline{S}(\underline{a}) \underline{b} = \underline{a} \times \underline{b} \forall \underline{a}, \underline{b} \in \mathbb{R}^3$. The inverse of the Rodrigues formula (2.11), i.e., the rotation vector as a function of the rotation tensor, will be denoted as $\underline{\psi}(\underline{\Lambda}) = \text{rv}(\underline{\Lambda})$ in the remainder of this thesis. In practice, Spurrier's algorithm [133] can be used for the extraction of the rotation vector.

Two triads $\underline{\Lambda}_1(\underline{\psi}_1)$ and $\underline{\Lambda}_2(\underline{\psi}_2)$, with their respective rotation vectors $\underline{\psi}_1$ and $\underline{\psi}_2$, can be related by the relative rotation $\underline{\Lambda}_{21}(\underline{\psi}_{21})$. The relative rotation is given by

$$\underline{\Lambda}_2(\underline{\psi}_2) = \underline{\Lambda}_{21}(\underline{\psi}_{21}) \underline{\Lambda}_1(\underline{\psi}_1) \Leftrightarrow \underline{\Lambda}_{21}(\underline{\psi}_{21}) = \underline{\Lambda}_2(\underline{\psi}_2) \underline{\Lambda}_1(\underline{\psi}_1)^T, \quad (2.12)$$

with the identity $\underline{\Lambda}^T = \underline{\Lambda}^{-1}$ for all elements of SO^3 . Thus, the (non-additive) rotation vector $\underline{\psi}_{21} = \text{rv}(\underline{\Lambda}_{21}) \neq \underline{\psi}_2 - \underline{\psi}_1$ describes the relative rotation between $\underline{\Lambda}_1$ and $\underline{\Lambda}_2$.

In a next step, the infinitesimal variations of the rotation tensor shall be considered, which can be expressed either by an infinitesimal additive variation $\delta \underline{\psi}$ of the rotation vector

$$\delta \underline{\Lambda} = \left. \frac{d}{d\epsilon} \right|_{\epsilon=0} \underline{\Lambda}(\underline{\psi} + \epsilon \delta \underline{\psi}) = \frac{\partial \underline{\Lambda}(\underline{\psi})}{\partial \underline{\psi}} \delta \underline{\psi}, \quad (2.13)$$

or by a infinitesimal multiplicative rotation variation $\delta\boldsymbol{\underline{\theta}}$, also denoted as the spin vector:

$$\delta\boldsymbol{\underline{\Lambda}} = \left. \frac{d}{d\epsilon} \right|_{\epsilon=0} \boldsymbol{\underline{\Lambda}}(\epsilon\delta\boldsymbol{\underline{\theta}}) \boldsymbol{\underline{\Lambda}}(\boldsymbol{\underline{\psi}}) = \boldsymbol{\underline{S}}(\delta\boldsymbol{\underline{\theta}}) \boldsymbol{\underline{\Lambda}}(\boldsymbol{\underline{\psi}}). \quad (2.14)$$

While the definition of the multiplicative rotation variation (2.14) can often be found in literature, e.g., in [38, 68, 131], the notation introduced for the additive rotation variation (2.13) simply represents the standard definition of partial differentiation, which is based on additive increments. With the relation above and the definition of $\boldsymbol{\underline{S}}$, the variations of the triad basis vectors $\delta\boldsymbol{\underline{g}}_i$ read

$$\delta\boldsymbol{\underline{g}}_i = \delta\boldsymbol{\underline{\theta}} \times \boldsymbol{\underline{g}}_i. \quad (2.15)$$

The infinitesimal additive and multiplicative rotation vector variations can be related according to

$$\delta\boldsymbol{\underline{\psi}} = \boldsymbol{\underline{T}}(\boldsymbol{\underline{\psi}})\delta\boldsymbol{\underline{\theta}}, \quad (2.16)$$

where the transformation matrix $\boldsymbol{\underline{T}}(\boldsymbol{\underline{\psi}})$ [131] is defined as

$$\boldsymbol{\underline{T}}(\boldsymbol{\underline{\psi}}) = \frac{1}{\psi^2} \boldsymbol{\underline{\psi}} \boldsymbol{\underline{\psi}}^T - \frac{1}{2} \boldsymbol{\underline{S}}(\boldsymbol{\underline{\psi}}) + \frac{\psi}{2 \tan(\frac{\psi}{2})} \left(\boldsymbol{\underline{I}} - \frac{1}{\psi^2} \boldsymbol{\underline{\psi}} \boldsymbol{\underline{\psi}}^T \right). \quad (2.17)$$

In [94], the objective variation δ_o of a spatial quantity defined in a moving frame $\boldsymbol{\underline{\Lambda}}_1$ is defined as the difference between the total variation and the variation of the base vectors of the moving frame. In the context of rotational coupling constraints this will be required when expressing the objective variation of a relative rotation vector $\boldsymbol{\underline{\psi}}_{21}$:

$$\delta_o \boldsymbol{\underline{\psi}}_{21} = \delta \boldsymbol{\underline{\psi}}_{21} - \delta \boldsymbol{\underline{\theta}}_1 \times \boldsymbol{\underline{\psi}}_{21} = \boldsymbol{\underline{T}}(\boldsymbol{\underline{\psi}}_{21})(\delta \boldsymbol{\underline{\theta}}_2 - \delta \boldsymbol{\underline{\theta}}_1). \quad (2.18)$$

For a detailed derivation of this expression for the objective variation the interested reader is referred to [94].

Remark 2.1. Via right-multiplication of (2.17) with the rotation vector $\boldsymbol{\underline{\psi}}$ it can easily be shown that $\boldsymbol{\underline{\psi}}$ is an eigenvector (with eigenvalue 1) of $\boldsymbol{\underline{T}}$ and also of $\boldsymbol{\underline{T}}^T$, i.e., $\boldsymbol{\underline{T}}\boldsymbol{\underline{\psi}} = \boldsymbol{\underline{\psi}}$ and $\boldsymbol{\underline{T}}^T\boldsymbol{\underline{\psi}} = \boldsymbol{\underline{\psi}}$. This property will be beneficial for derivations presented in subsequent sections. Every vector parallel to $\boldsymbol{\underline{\psi}}$ is also an eigenvector of $\boldsymbol{\underline{T}}$. This can be interpreted in a geometrical way: If the additive increment $\delta\boldsymbol{\underline{\psi}}$ to a rotation vector $\boldsymbol{\underline{\psi}}$ is parallel to the rotation vector, i.e., $\delta\boldsymbol{\underline{\psi}} = \delta\psi \boldsymbol{\underline{e}}_{\boldsymbol{\underline{\psi}}}$ and $\boldsymbol{\underline{\psi}} = \psi \boldsymbol{\underline{e}}_{\boldsymbol{\underline{\psi}}}$, the resulting compound rotation $\boldsymbol{\underline{\psi}} + \delta\boldsymbol{\underline{\psi}} = (\psi + \delta\psi) \boldsymbol{\underline{e}}_{\boldsymbol{\underline{\psi}}}$ is still defined around the rotation axis $\boldsymbol{\underline{e}}_{\boldsymbol{\underline{\psi}}}$. In this case, the rotation increment is a plane rotation relative to $\boldsymbol{\underline{\Lambda}}(\boldsymbol{\underline{\psi}})$, and the multiplicative and additive rotational increments are equal to each other, $\delta\boldsymbol{\underline{\psi}} = \delta\boldsymbol{\underline{\theta}}$.

Remark 2.2. In addition to $\boldsymbol{\underline{\Lambda}}$, the symbol $\boldsymbol{\underline{R}}$ will also be used in this thesis to represent rotation tensors.

2.2.2. Geometrically exact beam theory

The beams employed in this thesis are modeled as 1D Cosserat continua embedded in 3D space based on the so-called *geometrically exact* beam theory, e.g., [19, 38, 96, 99, 117, 129–131], which in turn builds upon the kinematic assumption of plane, rigid cross-sections. Figure 2.2

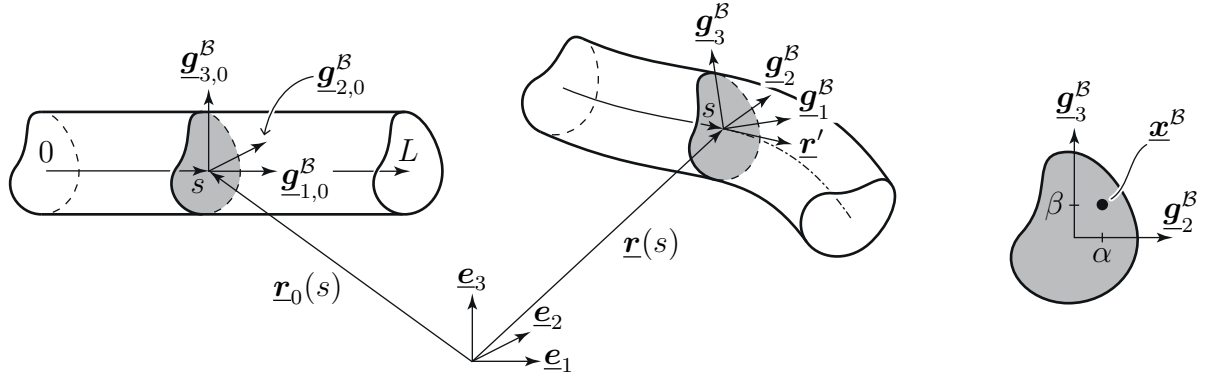


Figure 2.2.: Kinematics of a geometrically exact beam. Figure is taken from the author's article [135], permissions granted under the Creative Commons (CC BY) license.

shows the reference and current configuration of a beam without any additional kinematic assumptions, i.e., a general shear and torsion deformable beam. For illustration purposes, the reference configuration shows a straight beam, but unless stated otherwise, the presented beam theories can also be applied to beams with initial curvature. The complete beam kinematics can be defined by a centerline curve $\underline{r}(s) \in \mathbb{R}^3$ connecting the cross-section centroids, and a field of right-handed orthonormal triads $\underline{\Lambda}^B(s) := [\underline{g}_1^B(s), \underline{g}_2^B(s), \underline{g}_3^B(s)] = \underline{\Lambda}^B(\underline{\psi}^B(s)) \in SO^3$ defining the orientation of the cross-sections. Here $s \in [0, L] =: \Omega_0^B \subset \mathbb{R}$ is the arc-length along the undeformed beam centerline and $\underline{\Lambda}^B(\underline{\psi}^B(s))$ is a rotation tensor, which maps the global Cartesian basis vectors \underline{e}_i onto the local cross-section basis vectors $\underline{g}_i^B(s) = \underline{\Lambda}^B \underline{e}_i$ for $i = 1, 2, 3$. Therein, $\underline{\psi}^B \in \mathbb{R}^3$ is the rotation pseudo-vector chosen as parametrization for the triad, which defines the triad based on the formula (2.11). The triad field in the reference configuration is denoted as $\underline{\Lambda}_0^B(s) := [\underline{g}_{1,0}^B(s), \underline{g}_{2,0}^B(s), \underline{g}_{3,0}^B(s)] = \underline{\Lambda}_0^B(\underline{\psi}_{B,0}(s))$, and the relative rotation between the triads in reference and current configuration is denoted as $\underline{R}^B := \underline{\Lambda}^B(\underline{\Lambda}_0^B)^T$. According to the fundamental kinematic assumption of undeformable cross-sections, the kinematic quantities $\underline{X}^B, \underline{x}^B, \underline{u}^B \in \mathbb{R}^3$, i.e., reference position, current position and displacement of an arbitrary point within the cross-section, are functions of the centerline coordinate s as well as the cross-section coordinates $\alpha, \beta \in \mathbb{R}$:

$$\underline{X}^B(s, \alpha, \beta) = \underline{r}_0(s) + \alpha \underline{g}_{2,0}^B(s) + \beta \underline{g}_{3,0}^B(s), \quad (2.19)$$

$$\underline{x}^B(s, \alpha, \beta) = \underline{r}(s) + \alpha \underline{g}_2^B(s) + \beta \underline{g}_3^B(s), \quad (2.20)$$

$$\underline{u}^B(s, \alpha, \beta) = \underline{u}_r^B(s) + \alpha \left(\underline{g}_2^B(s) - \underline{g}_{2,0}^B(s) \right) + \beta \left(\underline{g}_3^B(s) - \underline{g}_{3,0}^B(s) \right), \quad (2.21)$$

where $\underline{u}_r^B = \underline{r} - \underline{r}_0$ is the displacement of the beam centerline.

In this thesis, three different geometrically exact beam theories are employed: the Simo–Reissner beam theory, which describes a general shear and torsion deformable beam, the Kirchhoff–Love beam theory for shear-stiff beams, and a torsion-free beam theory for beams with negligible shear and torsion. For many envisaged applications the Kirchhoff–Love and torsion-free beam theories are of particular interest as they are an efficient and accurate model for thin fibers. However, the torsion-free beam theory can only be applied if the considered beam problem satisfies certain properties, cf. Section 2.2.2.3. The internal elastic energy $\Pi_{\text{int},(\cdot)}^B$ for each beam

theory will be stated in the following subsections. The beam contribution to the global virtual work reads

$$\delta W_{(\cdot)}^{\mathcal{B}} = \underbrace{\delta \Pi_{\text{int},(\cdot)}^{\mathcal{B}}}_{-\delta W_{\text{int}}^{\mathcal{B}}} - \delta W_{\text{ext}}^{\mathcal{B}}. \quad (2.22)$$

Here, the virtual work of external forces and moments is summarized in $\delta W_{\text{ext},(\cdot)}^{\mathcal{B}}$. To improve readability of the following equations, derivatives with respect to the beam centerline coordinate s will be represented by $(\cdot)' := \partial(\cdot)/\partial s$ throughout this section.

2.2.2.1. Simo–Reissner beam theory

Of the three beam theories considered in this thesis, the Simo–Reissner (SR) beam theory describes the most general case. It does not introduce additional kinematic constraints on the beam, besides the assumption of rigid cross-sections. This results in shear-deformable beams capturing six modes of deformation: axial strain, two bending modes, torsion and two shear modes. The cross-section kinematics can be described with six degrees of freedom: the spatial position of the cross-section $\underline{\mathbf{r}}(s)$ and its rotation vector $\underline{\psi}^{\mathcal{B}}(s)$. Based on a hyperelastic stored-energy function according to

$$\Pi_{\text{int},\text{SR}}^{\mathcal{B}} = \int_{\Omega_0^{\mathcal{B}}} \tilde{\Pi}_{\text{int},\text{SR}}^{\mathcal{B}} \, ds, \quad (2.23)$$

with

$$\tilde{\Pi}_{\text{int},\text{SR}}^{\mathcal{B}} = \frac{1}{2} (\underline{\Gamma}^T \underline{\mathbf{C}}_F \underline{\Gamma} + \underline{\Omega}^T \underline{\mathbf{C}}_M \underline{\Omega}), \quad (2.24)$$

the material force stress resultants and moment stress resultants can be derived, i.e., $\underline{\mathbf{F}} = \partial \tilde{\Pi}_{\text{int},\text{SR}}^{\mathcal{B}} / \partial \underline{\Gamma}$ and $\underline{\mathbf{M}} = \partial \tilde{\Pi}_{\text{int},\text{SR}}^{\mathcal{B}} / \partial \underline{\Omega}$. Axial tension and shear strains are represented by the material deformation measure $\underline{\Gamma} := \underline{\Gamma}(\underline{\psi}^{\mathcal{B}}, \underline{\mathbf{r}}') = \underline{\Lambda}^{\mathcal{B}^T} \underline{\mathbf{r}}' - \underline{\mathbf{e}}_1 \in \mathbb{R}^3$. Torsion and bending strains are represented by the material curvature vector $\underline{\Omega} \in \mathbb{R}^3$, which in turn follows from $\underline{\Omega} \times \underline{\mathbf{a}} = \underline{\Lambda}^{\mathcal{B}^T} \underline{\Lambda}^{\mathcal{B}'} \underline{\mathbf{a}} \, \forall \, \underline{\mathbf{a}} \in \mathbb{R}^3$. This implies that $\underline{\Lambda}^{\mathcal{B}^T} \underline{\Lambda}^{\mathcal{B}'} \in so^3$ which holds true for all $\underline{\Lambda}^{\mathcal{B}} \in SO^3$. For a more detailed derivation of the strain resultants within the Simo–Reissner beam theory the interested reader is referred to [93, 99]. Using the rotation vector parameterization of the triad field $\underline{\Lambda}^{\mathcal{B}}(\underline{\psi}^{\mathcal{B}}(s))$, as discussed above, the resulting curvature vector can be formulated as a function of $\underline{\psi}^{\mathcal{B}}$ and $\underline{\psi}^{\mathcal{B}'}$, i.e., $\underline{\Omega} = \underline{\Omega}(\underline{\psi}^{\mathcal{B}}, \underline{\psi}^{\mathcal{B}'})$. The constitutive matrices $\underline{\mathbf{C}}_F \in \mathbb{R}^{3 \times 3}$ and $\underline{\mathbf{C}}_M \in \mathbb{R}^{3 \times 3}$ are defined as

$$\underline{\mathbf{C}}_F = \begin{bmatrix} EA & 0 & 0 \\ 0 & GA_2 & 0 \\ 0 & 0 & GA_3 \end{bmatrix} \quad \text{and} \quad \underline{\mathbf{C}}_M = \begin{bmatrix} GI_T & 0 & 0 \\ 0 & EI_2 & 0 \\ 0 & 0 & EI_3 \end{bmatrix}, \quad (2.25)$$

where $E^{\mathcal{B}}$ is the Young's modulus, $G^{\mathcal{B}}$ the shear modulus, A the cross-section area, A_2 and A_3 the effective shear areas, and I_T, I_2, I_3 are the polar and planar second moments of area, respectively.

2.2.2.2. Kirchhoff–Love beam theory

The Kirchhoff–Love (KL) theory introduces an additional kinematic constraint, restraining the shear deformation of the beam. This is equivalent to the requirement that the first cross-section

basis vector \underline{g}_1^B is parallel to the centerline tangent \underline{r}' , or

$$\underline{g}_2^B \cdot \underline{r}' \equiv 0 \quad \wedge \quad \underline{g}_3^B \cdot \underline{r}' \equiv 0. \quad (2.26)$$

While the position of the cross-section is described in the same manner as for the Simo–Reissner beam, the additional constraints reduce the number of independent rotations to one, thus a total of four degrees of freedom remain to fully describe the cross-section. The sole remaining rotational degree of freedom $\varphi(s) \in \mathbb{R}$ describes the twist rotation of the cross-section around the tangent vector \underline{r}' measured with respect to a properly defined reference triad $\underline{\Lambda}_{\text{ref,KL}}(\underline{r}')$, such that the cross-section triad can be described as a function of the centerline tangent and the twist, $\underline{\Lambda}^B(s) = \underline{\Lambda}^B(\underline{r}'(s), \varphi(s))$. A detailed overview of parametrization techniques for the twist degree of freedom can be found in [99]. The curvature of the beam centerline is described with the Frenet–Serret vector

$$\underline{\kappa} = \frac{\underline{r}' \times \underline{r}''}{\|\underline{r}'\|^2}, \quad (2.27)$$

which only depends on the beam centerline. The definition of the curvature contains second derivatives of the beam centerline, therefore resulting in the smoothness requirement of C^1 -continuous beam centerlines. Defining the material curvature vector $\underline{\Omega}$ identical to the Simo–Reissner case above, it can be formulated as a function of φ , φ' , \underline{r}' and $\underline{\kappa}$ for the Kirchhoff–Love case [99], i.e., $\underline{\Omega} = \underline{\Omega}(\varphi, \varphi', \underline{r}', \underline{\kappa})$. The internal energy for the Kirchhoff–Love beam is

$$\Pi_{\text{int,KL}}^B = \frac{1}{2} \int_{\Omega_0^B} EA\epsilon^2 + \underline{\Omega}^T \underline{C}_M \underline{\Omega} \, ds. \quad (2.28)$$

Therein, $\epsilon = \|\underline{r}'\| - 1$ is the axial tension of the beam.

2.2.2.3. Torsion-free beam theory

The torsion-free (TF) beam formulation considered in this thesis was first proposed in [97] and extended in [98]. It represents a special case of the Kirchhoff–Love beam theory. For certain properties of the problem, i.e., straight undeformed beams with axisymmetric cross-sections and no external torsional moments, it can be shown that the static equilibrium configurations resulting from the Kirchhoff–Love beam theory are characterized by (exactly) vanishing torsion [97]. The application of this type of beam element formulation is justified and motivated as these requirements are fulfilled in many practically relevant systems, as well as many of the examples considered in this thesis. Compared to the Kirchhoff–Love beam, the twist degree of freedom is no longer present and the beam can be completely described by its centerline position, i.e., three degrees of freedom per cross-section. Since the discrete representation and algorithmic treatment of large rotations remains the main complexity of geometrically nonlinear beam theories, the employed torsion-free beam theory is particularly appealing and easy to handle, as it completely abstains from any rotational degrees of freedom. The internal energy of the torsion-free beam reads

$$\Pi_{\text{int,TF}}^B = \frac{1}{2} \int_{\Omega_0^B} EA\epsilon^2 + EI\kappa^2 \, ds, \quad (2.29)$$

with the scalar curvature $\kappa = \|\underline{\kappa}\|$.

2.3. Finite element formulations

In this thesis, spatial discretization of the beam, solid and interaction terms will be exclusively based on the finite element method. As was the case with the previous sections, this section is not intended to give a detailed introduction to all aspects and mathematical properties of the finite element method. Only the basic ideas and notations needed for the presented discretized BTS interaction problem are given here. For a more detailed survey of the finite element method in solid mechanics the reader is referred to the corresponding literature, e.g., [13, 16, 36, 64, 153, 155]. These references are mostly concerned with general 3D solid mechanics, for detailed literature on the finite element method for structural beam theory the reader is referred to, e.g., [69, 99, 126, 130, 131, 145].

2.3.1. Solid mechanics

The basic concept of the finite element method is to find a numerical solution of the variational formulation (or weak form) of the balance equations (2.8) based on discrete points, so-called *nodes*. The finite *elements* connect the nodes to approximate the solid domain Ω_0^S , spanning a so-called *mesh*. The solid reference position is approximated by

$$\underline{\mathbf{X}}^S \approx \underline{\mathbf{X}}_h^S = \sum_{k=1}^{n^S} N_k(\xi^S, \eta^S, \zeta^S) \hat{\underline{\mathbf{X}}}_k^S. \quad (2.30)$$

Here, n^S is the total number of solid finite element nodes, $N_k \in \mathbb{R}$ and $\hat{\underline{\mathbf{X}}}_k^S \in \mathbb{R}^3$ are the finite element shape function and reference position of the solid node k , respectively. Furthermore, $\xi^S, \eta^S, \zeta^S \in \mathbb{R}$ are the 3D coordinates of the solid finite element parameter space. In the following and throughout this thesis, a subscript $(\cdot)_h$ refers to an interpolated field quantity. It is assumed, without loss of generality, that the solid parameter coordinates are chosen such that the third parameter coordinate ζ^S is constant at the solid surface, i.e., the discretized solid surface $\partial\Omega_{0,h}^S$ can be parameterized with only the first two solid parameter coordinates ξ^S and η^S . The solid domain is discretized with an isoparametric finite element approach, i.e., position, displacement and virtual displacement field are discretized with the same interpolation, i.e., spatial interpolation of the solid displacement and virtual displacement fields is given by

$$\underline{\mathbf{u}}^S \approx \underline{\mathbf{u}}_h^S = \sum_{k=1}^{n^S} N_k(\xi^S, \eta^S, \zeta^S) \hat{\underline{\mathbf{d}}}_k^S, \quad (2.31)$$

and

$$\delta \underline{\mathbf{u}}^S \approx \delta \underline{\mathbf{u}}_h^S = \sum_{k=1}^{n^S} N_k(\xi^S, \eta^S, \zeta^S) \delta \hat{\underline{\mathbf{d}}}_k^S. \quad (2.32)$$

Here, $\hat{\underline{\mathbf{d}}}_k^S \in \mathbb{R}^3$ and $\delta \hat{\underline{\mathbf{d}}}_k^S \in \mathbb{R}^3$ are the reference displacement and virtual displacement of node k , respectively. According to (2.1) the current position of a solid node evaluates to $\hat{\underline{\mathbf{x}}}_k^S = \hat{\underline{\mathbf{X}}}_k^S + \hat{\underline{\mathbf{d}}}_k^S$.

Inserting the finite element approximations into the variational formulation of the equilibrium equations (2.8) yields the discretized virtual work of the solid, which now only depends on the

(unknown) nodal displacements and nodal variations, i.e.,

$$\delta W^S \approx \delta W_h^S(\mathbf{d}^S, \delta \mathbf{d}^S). \quad (2.33)$$

Here, $\mathbf{d}^S \in \mathbb{R}^{3n^S}$ is the global displacement vector, which contains all nodal displacements, i.e., $\mathbf{d}^S = [(\underline{\mathbf{d}}_1^S)^T, (\underline{\mathbf{d}}_2^S)^T, \dots, (\underline{\mathbf{d}}_{n^S}^S)^T]^T$. Similarly, $\delta \mathbf{d}^S \in \mathbb{R}^{3n^S}$ is the global vector of virtual displacements. With the chosen finite element approximation, (2.33) can be reformulated as

$$\delta W_h^S(\mathbf{d}^S, \delta \mathbf{d}^S) = \delta \mathbf{d}^{S^T} \mathbf{r}^S(\mathbf{d}^S), \quad (2.34)$$

with the solid residual vector $\mathbf{r}^S \in \mathbb{R}^{3n^S}$. To illustrate the meaning of this residual vector, let us consider a pure solid problem. In this case the virtual work of the solid domain has to vanish, i.e., $\delta W_h^S = 0$. Since (2.34) has to hold for arbitrary non-zero virtual displacements $\delta \mathbf{d}^S$, the only way to fulfill condition (2.34) is by solving the system of non-linear equations $\mathbf{r}^S(\mathbf{d}^S) = \mathbf{0}$. In other words, \mathbf{r}^S represents the non-linear equilibrium equations of the discretized solid problem.

Remark 2.3. In this section classical node-based finite element discretizations for the solid domain are presented. The shape functions N_k are typically Lagrange polynomials. However, all presented BTS interaction schemes are also directly compatible with other discretization schemes, such as C^1 -continuous (or higher) isogeometric solid discretizations based on non-uniform rational B-splines (NURBS), cf. [37, 65, 106]. Due to the higher order continuity provided by such discretization techniques, the evaluation of the BTS interaction terms simplifies in beam-to-solid surface (coupling and contact) problems, as no averaged surface normal field has to be constructed.

2.3.2. Beam mechanics

As presented in Section 2.2.2, the beam centerline position $\underline{\mathbf{r}}$ and the cross-section orientation $\underline{\mathbf{A}}^B$ arise as the two primary fields of unknowns in the beam domain. In this thesis, the employed finite element methods for the Simo–Reissner, Kirchhoff–Love and torsion-free beam theories use the same spatial discretization of the beam centerline. The interpolation of the beam triad field only influences the rotational BTS coupling, cf. Chapter 5, which is only considered in combination with the Simo–Reissner beam theory. Therefore, the triad interpolation is only stated for the Simo–Reissner beam theory. For details on the triad interpolation within the Kirchhoff–Love beam theory, the reader is referred to the literature, e.g., [93, 96, 97, 145]. There is no triad field in the torsion-free beam theory, therefore, there is also no need for a rotational interpolation.

2.3.2.1. Centerline interpolation

Kirchhoff–Love and torsion-free beam elements require a C^1 -continuous centerline interpolation in order to represent the Frenet–Serret vector (2.27), which is realized with third-order Hermite polynomials [99, 145]. Due to its superior numerical properties, this discretization scheme is also used for the Simo–Reissner beam element, as derived in [95]. Each beam centerline node l holds six local degrees of freedom, i.e., the nodal position $\hat{\mathbf{r}}_l \in \mathbb{R}^3$ and the nodal centerline tangent vector $\hat{\mathbf{t}}_l \in \mathbb{R}^3$. The resulting beam finite elements have two centerline nodes each, cf. Figure 2.3.

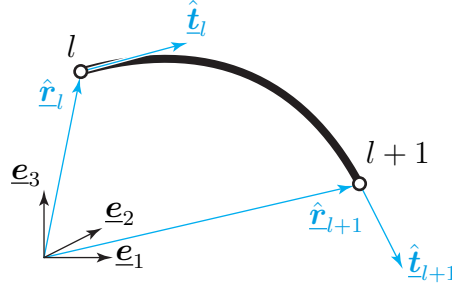


Figure 2.3.: Centerline degrees of freedom for a single beam element used in this thesis. The element exemplarily connects the centerline nodes l and $l + 1$.

The beam centerline position is interpolated by

$$\underline{r} \approx \underline{r}_h = \sum_{l=1}^{n^B} H_l^r(\xi^B) \hat{\underline{r}}_l + H_l^t(\xi^B) \hat{\underline{t}}_l. \quad (2.35)$$

Here, n^B is the number of beam centerline nodes, $H_l^r \in \mathbb{R}$ and $H_l^t \in \mathbb{R}$ denote the Hermite shape functions for the positional and tangential degrees of freedom for the beam node l . Both shape functions are a function of the scalar beam centerline parameter coordinate ξ^B . At this point it is important to note that the positional Hermite shape functions fulfill the partition of unity property, i.e., $\sum_{l=1}^{n^B} H_l^r \equiv 1$. The tangential Hermite shape functions H_l^t contain a scaling factor dependent on the reference geometry of the element. For more details on the definition of this factor the reader is referred to the literature, e.g., [93].

The beam centerline displacement and variation are interpolated by

$$\underline{u}_r^B \approx \underline{u}_{r,h}^B = \sum_{l=1}^{n^B} H_l^r(\xi^B) \hat{\underline{d}}_{r,l}^B + H_l^t(\xi^B) \hat{\underline{d}}_{t,l}^B, \quad (2.36)$$

and

$$\delta \underline{r} = \delta \underline{u}_r^B \approx \delta \underline{r}_h = \sum_{l=1}^{n^B} H_l^r(\xi^B) \delta \hat{\underline{d}}_{r,l}^B + H_l^t(\xi^B) \delta \hat{\underline{d}}_{t,l}^B, \quad (2.37)$$

where the discrete vectors, $\hat{\underline{d}}_{r,l}^B$ and $\hat{\underline{d}}_{t,l}^B$, are the nodal displacements and tangent increments, respectively. Furthermore, $\delta \hat{\underline{d}}_{r,l}^B$ and $\delta \hat{\underline{d}}_{t,l}^B$ are the respective variations. To improve readability of the beam centerline interpolations, (2.35) to (2.37) are redefined in the following way

$$\underline{r}_h = \sum_{l=1}^{n^B} \mathbf{H}_l(\xi^B) \hat{\mathbf{x}}_l^B, \quad (2.38)$$

$$\underline{u}_{r,h}^B = \sum_{l=1}^{n^B} \mathbf{H}_l(\xi^B) \hat{\mathbf{d}}_l^B, \quad (2.39)$$

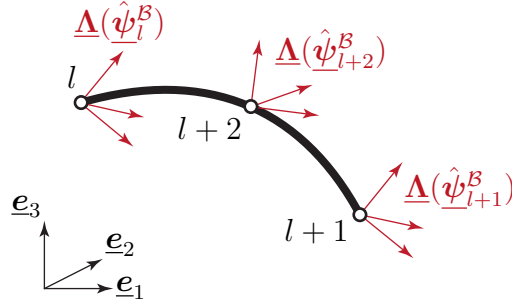


Figure 2.4.: Rotational degrees of freedom for a single beam element used in this thesis. The element exemplarily connects the rotational nodes l , $l + 1$ and $l + 2$.

and

$$\delta \underline{r}_h = \sum_{l=1}^{n^B} \mathbf{H}_l(\xi^B) \delta \hat{\mathbf{d}}_l^B, \quad (2.40)$$

with

$$\mathbf{H}_l = [\mathbf{H}_l^r \mathbf{I}^{3 \times 3} \quad \mathbf{H}_l^t \mathbf{I}^{3 \times 3}] \in \mathbb{R}^{3 \times 6}, \quad (2.41)$$

$$\hat{\mathbf{x}}_l^B = \begin{bmatrix} \hat{\mathbf{r}}_l \\ \hat{\mathbf{t}}_l \end{bmatrix} \in \mathbb{R}^6, \quad \hat{\mathbf{d}}_l^B = \begin{bmatrix} \hat{\mathbf{d}}_{r,l}^B \\ \hat{\mathbf{d}}_{t,l}^B \end{bmatrix} \in \mathbb{R}^6 \quad \text{and} \quad \delta \hat{\mathbf{d}}_l^B = \begin{bmatrix} \delta \hat{\mathbf{d}}_{r,l}^B \\ \delta \hat{\mathbf{d}}_{t,l}^B \end{bmatrix} \in \mathbb{R}^6. \quad (2.42)$$

Here, \mathbf{H}_l is the matrix with the node-wise assembled beam centerline shape functions, and $\hat{\mathbf{x}}_l^B$, $\hat{\mathbf{d}}_l^B$ and $\delta \hat{\mathbf{d}}_l^B$ are the corresponding generalized nodal vectors for position, displacement and virtual displacement, respectively.

Remark 2.4. The Simo–Reissner beam theory only requires a C^0 -continuous centerline interpolation. Employing C^1 -continuous centerline interpolations for the Simo–Reissner beam elements constrains the solution space and prohibits kinks in the beam centerline. Kinks occur when concentrated loads act on the beam centerline. For the considered BTS interaction problems, the interaction forces are smooth along the beam centerline, thus resulting in a C^1 -continuous centerline solution and justifying the employed C^1 -continuous centerline interpolation also for the Simo–Reissner beam theory.

Remark 2.5. All presented examples in this thesis employ a C^1 -continuous centerline representation for the beam elements. However, this is not a restriction of the presented BTS interaction methods, which can also directly be applied to C^0 -continuous centerline interpolation.

2.3.2.2. Interpolation of the triad field

A triad interpolation scheme based on nodal rotation vectors $\hat{\psi}^B$ is utilized, cf. [38]. Each beam finite element contains three nodes carrying rotational degrees of freedom, i.e., the third node is located in between the two centerline nodes of the element and carries no positional degrees of freedom, only rotational ones, cf. Figure 2.4. The nodal rotation vectors serve as primal degrees of freedom for the interpolated rotation field along the beam centerline. Each rotation vector has

three degrees of freedom, thus resulting in a total of 9 rotational degrees of freedom per beam finite element.

The interpolation of the beam cross-section triad along the beam centerline is a non-trivial task and requires an orthonormal interpolation scheme for the interpolated triad $\underline{\mathbf{A}}_h^{\mathcal{B}}(\xi^{\mathcal{B}})$ to guarantee that the interpolated triad field is still a member of the rotational group SO^3 . Furthermore, objectivity of the discrete beam deformation measures has to be preserved by the interpolation, which is a challenging task if rotational degrees of freedom are involved. In this thesis the interpolated triad field will be referred to as an abstract nonlinear function of the beam parameter coordinate and the nodal rotation vectors, i.e., $\underline{\mathbf{A}}_h^{\mathcal{B}}(\xi^{\mathcal{B}}) = \text{nl}(\xi^{\mathcal{B}}, \hat{\underline{\boldsymbol{\psi}}}_1^{\mathcal{B}}, \hat{\underline{\boldsymbol{\psi}}}_2^{\mathcal{B}}, \dots, \hat{\underline{\boldsymbol{\psi}}}_{n_{\theta}^{\mathcal{B}}}^{\mathcal{B}})$, where $n_{\theta}^{\mathcal{B}}$ is the total number of beam nodes carrying rotational degrees of freedom. The discretized rotation vector of a beam cross-section is calculated via $\underline{\boldsymbol{\psi}}_h^{\mathcal{B}}(\xi^{\mathcal{B}}) = \text{rv}(\underline{\mathbf{A}}_h^{\mathcal{B}}(\xi^{\mathcal{B}}))$. The corresponding interpolated field of multiplicative rotation vector increments $\Delta \underline{\boldsymbol{\theta}}_h^{\mathcal{B}}(\xi^{\mathcal{B}})$ has been consistently derived in [38] and reads:

$$\Delta \underline{\boldsymbol{\theta}}_h^{\mathcal{B}} = \sum_{l=1}^{n_{\theta}^{\mathcal{B}}} \tilde{\mathbf{I}}_l(\xi^{\mathcal{B}}) \Delta \hat{\underline{\boldsymbol{\theta}}}_l. \quad (2.43)$$

Therein, $\tilde{\mathbf{I}}_l \in \mathbb{R}^{3 \times 3}$ for $l = 1, \dots, n_{\theta}^{\mathcal{B}}$ are generalized shape function matrices for the multiplicative nodal rotation increments $\Delta \hat{\underline{\boldsymbol{\theta}}}_l$. It should be pointed out that $\tilde{\mathbf{I}}_l$ are nonlinear functions of the beam parameter coordinate and the nodal rotation vectors of the beam element, i.e., these rotational shape functions are deformation-dependent. The beam finite elements employed in this thesis follow a Petrov–Galerkin discretization approach as suggested in [71], i.e., the interpolation of the spin vector differs from the interpolation of the multiplicative rotation vector increments. Standard Lagrange shape functions are used to interpolate the discretized nodal spin vectors:

$$\delta \underline{\boldsymbol{\theta}}_h^{\mathcal{B}} = \sum_{l=1}^{n_{\theta}^{\mathcal{B}}} L_l(\xi^{\mathcal{B}}) \delta \hat{\underline{\boldsymbol{\theta}}}_l. \quad (2.44)$$

Here, $L_l \in \mathbb{R}$ for $l = 1, \dots, n_{\theta}^{\mathcal{B}}$ are standard second-order Lagrange polynomials, and $\delta \hat{\underline{\boldsymbol{\theta}}}_l$ are the nodal spin vectors. For a more detailed discussion on the rotational interpolation and the Petrov–Galerkin discretization of the employed Simo–Reissner beam finite elements the interested reader is referred to [71, 93, 99]. In Chapter 5 the rotational BTS coupling terms are derived on element pair level. It is advantageous to reformulate (2.43) and (2.44) in an element-wise manner, i.e.,

$$\Delta \underline{\boldsymbol{\theta}}_h^{\mathcal{B}(f)} = \tilde{\mathbf{I}}^{(f)}(\xi^{\mathcal{B}}) \Delta \underline{\boldsymbol{\theta}}^{\mathcal{B}(f)} \quad (2.45)$$

$$\delta \underline{\boldsymbol{\theta}}_h^{\mathcal{B}(f)} = \mathbf{L}^{(f)}(\xi^{\mathcal{B}}) \delta \underline{\boldsymbol{\theta}}^{\mathcal{B}(f)}. \quad (2.46)$$

Here, $\Delta \underline{\boldsymbol{\theta}}_h^{\mathcal{B}(f)}$ is the multiplicative rotation vector increment field in the beam element (f) . Accordingly, $\tilde{\mathbf{I}}^{(f)} \in \mathbb{R}^{3 \times 9}$ and $\Delta \underline{\boldsymbol{\theta}}^{\mathcal{B}(f)} \in \mathbb{R}^9$ are the corresponding element-wise assembled shape functions and nodal values, respectively. Furthermore, $\mathbf{L}^{(f)} \in \mathbb{R}^{3 \times 9}$ and $\delta \underline{\boldsymbol{\theta}}^{\mathcal{B}(f)} \in \mathbb{R}^9$ are the element-wise assembled quantities for the spin vector field.

2.3.2.3. Beam residual vectors

In this paragraph, the residual contributions of the geometrically exact beam theory are stated in abstract form, based on the previously introduced beam finite element interpolations. For

the detailed derivation in the context of the employed geometrically exact beam theories, the reader is referred to the aforementioned literature. Similar to the procedure in the solid domain, cf. Section 2.3.1, the beam finite element approximations (2.35) to (2.37) can be inserted into the weak form of the beam balance equations (2.22) and written in general form as

$$\delta W_{(\cdot)}^B \approx \delta W_{(\cdot),h}^B = \delta W_{(\cdot),h}^B(\mathbf{d}^B, \delta \mathbf{d}^B, \boldsymbol{\psi}^B, \delta \boldsymbol{\theta}^B). \quad (2.47)$$

Here, $\mathbf{d}^B \in \mathbb{R}^{6n^B}$ is the global beam centerline displacement vector which simply contains all discrete positional beam degrees of freedom, i.e., $\mathbf{d}^B = [(\hat{\mathbf{d}}_1^B)^T, (\hat{\mathbf{d}}_2^B)^T, \dots, (\hat{\mathbf{d}}_{n^B}^B)^T]^T$, and $\boldsymbol{\psi}^B = [(\hat{\boldsymbol{\psi}}_1^B)^T, (\hat{\boldsymbol{\psi}}_2^B)^T, \dots, (\hat{\boldsymbol{\psi}}_{n^B}^B)^T]^T \in \mathbb{R}^{3n_\theta^B}$ is the global vector containing all nodal rotation vectors. Furthermore, $\delta \mathbf{d}^B$ and $\delta \boldsymbol{\theta}^B$ are the global virtual displacement vector and global spin vector, respectively. Equation (2.47) can be rewritten as

$$\delta W_{(\cdot),h}^B(\mathbf{d}^B, \delta \mathbf{d}^B, \boldsymbol{\psi}^B, \delta \boldsymbol{\theta}^B) = \delta \mathbf{d}^{B^T} \mathbf{r}_r^B(\mathbf{d}^B, \boldsymbol{\psi}^B) + \delta \boldsymbol{\theta}^{B^T} \mathbf{r}_\theta^B(\mathbf{d}^B, \boldsymbol{\psi}^B), \quad (2.48)$$

where $\mathbf{r}_r^B \in \mathbb{R}^{6n^B}$ and $\mathbf{r}_\theta^B \in \mathbb{R}^{3n_\theta^B}$ are the beam residual vectors for the positional and rotational beam degrees of freedom, respectively.

2.4. Uncoupled beam and solid problem

In the previous sections the individual discretizations of the beam and solid domain are presented. For the BTS interaction problems considered in this thesis, the balance equations for beam and solid have to be united. This is done by adding the virtual work contributions of the individual beam and solid problem together, yielding the variational formulation of the (uncoupled) beam and solid problem, i.e.,

$$\delta W^S + \delta W_{(\cdot)}^B = 0. \quad (2.49)$$

With (2.34) and (2.48), the residual of the combined problem reads

$$\begin{bmatrix} \mathbf{r}^S(\mathbf{d}^S) \\ \mathbf{r}_r^B(\mathbf{d}^B, \boldsymbol{\psi}^B) \\ \mathbf{r}_\theta^B(\mathbf{d}^B, \boldsymbol{\psi}^B) \end{bmatrix} = \mathbf{0}. \quad (2.50)$$

Here, the solid residuum \mathbf{r}^S is independent of the beam residuals \mathbf{r}_r^B and \mathbf{r}_θ^B , i.e., the two domains are uncoupled. This can be seen even more clearly in the linearized system of the nonlinear equilibrium equations (2.50),

$$\begin{bmatrix} \mathbf{K}_{ss}^S & \mathbf{0} & \mathbf{0} \\ \mathbf{0} & \mathbf{K}_{rr}^B & \mathbf{K}_{r\theta}^B \\ \mathbf{0} & \mathbf{K}_{\theta r}^B & \mathbf{K}_{\theta\theta}^B \end{bmatrix} \begin{bmatrix} \Delta \mathbf{d}^S \\ \Delta \mathbf{d}^B \\ \Delta \boldsymbol{\theta}^B \end{bmatrix} = \begin{bmatrix} -\mathbf{r}^S \\ -\mathbf{r}_r^B \\ -\mathbf{r}_\theta^B \end{bmatrix}, \quad (2.51)$$

as there are no coupling terms between the beam and solid degrees of freedom. In (2.51), Δ represents an increment to the state vectors, $\mathbf{K}_{ss}^S \in \mathbb{R}^{3n^S \times 3n^S}$ is the solid tangent stiffness matrix and $\mathbf{K}_{rr}^B \in \mathbb{R}^{6n^B \times 6n^B}$, $\mathbf{K}_{r\theta}^B \in \mathbb{R}^{6n^B \times 3n_\theta^B}$, $\mathbf{K}_{\theta r}^B \in \mathbb{R}^{3n_\theta^B \times 6n^B}$ and $\mathbf{K}_{\theta\theta}^B \in \mathbb{R}^{3n_\theta^B \times 3n_\theta^B}$ are the beam tangent stiffness matrices. The discrete rotational degrees of freedom are multiplicative

increments, therefore, the update of the rotation state has to be preformed according accordingly, cf. [99]. This system serves as a starting point for all considered BTS interaction problems, as the interaction terms are simply added to this uncoupled system. The theoretical background of discretizing and solving the constrained system, i.e., the beam-to-solid system, is outlined in the following section.

Remark 2.6. It should be mentioned, that due to the Petrov–Galerkin finite element discretization of the beams rotational degrees of freedom, the corresponding tangent stiffness matrices are non-symmetric in general, i.e., $\mathbf{K}_{r\theta}^B \neq (\mathbf{K}_{\theta r}^B)^T$ and $\mathbf{K}_{\theta\theta}^B \neq (\mathbf{K}_{\theta\theta}^B)^T$.

2.5. Constrained beam-to-solid interaction problem

The main focus of this thesis is the development of BTS interaction methods, i.e., the addition of coupling constraints between the beam and the solid finite element formulations. For the considerations in this section, the strong form of the coupling constraints can be written in abstract form as

$$\underline{\mathbf{g}} = \underline{\mathbf{g}}(\underline{\mathbf{x}}^S, \underline{\mathbf{r}}, \underline{\Lambda}^B) = \underline{\mathbf{0}} \quad \text{on} \quad \Gamma_c. \quad (2.52)$$

Here, $\underline{\mathbf{g}}$ is a (pseudo) tensor-valued function of the kinematic beam and solid fields, and Γ_c is the coupling domain. In the following, the general procedure of adding constraints to the variational formulation, based on the Lagrange multiplier method, is presented, as is a penalty regularization of the resulting system of equations.

2.5.1. Lagrange multiplier method

The Lagrange multiplier method introduces an additional field of unknowns $\underline{\Lambda}$, the so-called *Lagrange multiplier* field, defined on the coupling domain Γ_c . The dimension of the Lagrange multiplier field is the same as the dimension of the coupling constraints, i.e., $\dim(\underline{\mathbf{g}}) = \dim(\underline{\Lambda})$. A global Lagrange multiplier potential is defined as

$$\Pi_\lambda = \int_{\Gamma_c} \underline{\Lambda}^T \underline{\mathbf{g}} \, ds. \quad (2.53)$$

Variation of the global Lagrange multiplier potential leads to the coupling contributions to the variational formulation, i.e.,

$$\delta \Pi_\lambda = \underbrace{\int_{\Gamma_c} \delta \underline{\Lambda}^T \underline{\mathbf{g}} \, ds}_{\delta W_\lambda} + \underbrace{\int_{\Gamma_c} \underline{\Lambda}^T \delta \underline{\mathbf{g}} \, ds}_{-\delta W_c}, \quad (2.54)$$

where δW_λ and δW_c are the variational form of the coupling constraints and the virtual work of the generalized coupling forces, respectively. The resulting variational formulation of the constrained BTS coupling problem, the so-called *mixed formulation*, reads:

$$\delta W^S + \delta W_{(\cdot)}^B + \delta W_\lambda - \delta W_c = 0. \quad (2.55)$$

2. Governing equations and finite element formulations

Throughout this thesis a mortar-type approach for discretizing the Lagrange multiplier field is employed. A more detailed explanation on this topic is given in the respective sections, e.g., Sections 4.2.2, 5.3.2 and 6.3.2, or in the literature, e.g., [109, 112, 150]. For the purpose of this section, it is sufficient to consider a general form of the discretized variational formulation, i.e.,

$$\begin{aligned}
 0 = & \underbrace{\delta \mathbf{d}^S \mathbf{r}^S(\mathbf{d}^S) + \delta \mathbf{d}^B \mathbf{r}_r^B(\mathbf{d}^B, \psi^B) + \delta \theta^B \mathbf{r}_\theta^B(\mathbf{d}^B, \psi^B)}_{\delta W_{\lambda, h}} \\
 & + \underbrace{\delta \boldsymbol{\lambda}^T \mathbf{g}(\mathbf{d}^S, \mathbf{d}^B, \psi^B)}_{-\delta W_{c, h}} \\
 & + \delta \mathbf{d}^S \mathbf{Q}_{s\lambda}(\mathbf{d}^S, \mathbf{d}^B, \psi^B) \boldsymbol{\lambda} + \delta \mathbf{d}^B \mathbf{Q}_{r\lambda}(\mathbf{d}^S, \mathbf{d}^B, \psi^B) \boldsymbol{\lambda} + \delta \theta^B \mathbf{Q}_{\theta\lambda}(\mathbf{d}^S, \mathbf{d}^B, \psi^B) \boldsymbol{\lambda}.
 \end{aligned} \tag{2.56}$$

Here, $\mathbf{g} \in \mathbb{R}^{n_{\text{const}}}$ is the global discretized constraint vector and $\boldsymbol{\lambda} \in \mathbb{R}^{n_{\text{const}}}$ is the global vector of discrete Lagrange multiplier unknowns with n_{const} being the number of discretized constraint equations. Furthermore, $\mathbf{Q}_{s\lambda}$, $\mathbf{Q}_{r\lambda}$ and $\mathbf{Q}_{\theta\lambda}$ are the coupling matrices that project the global Lagrange multiplier vector onto the nodal force contributions for solid degrees of freedom, positional beam degrees of freedom and rotational beam degrees of freedom, respectively. For improved readability, the explicit dependency of the residual contributions on the discrete unknowns will be omitted going further. From (2.56) follows the vector with the constrained nonlinear balance equations of the BTS interaction problem as

$$\begin{bmatrix} \mathbf{r}^S + \mathbf{Q}_{s\lambda} \boldsymbol{\lambda} \\ \mathbf{r}_r^B + \mathbf{Q}_{r\lambda} \boldsymbol{\lambda} \\ \mathbf{r}_\theta^B + \mathbf{Q}_{\theta\lambda} \boldsymbol{\lambda} \\ \mathbf{g} \end{bmatrix} = \mathbf{0}. \tag{2.57}$$

Employing a Newton–Raphson algorithm, the residual vector is linearized with respect to the solid and beam degrees of freedom, thus resulting in the global linear system of equations

$$\begin{bmatrix} \mathbf{K}_{ss}^S + \mathbf{Q}_{ss} & \mathbf{Q}_{sr} & \mathbf{Q}_{s\theta} & \mathbf{Q}_{s\lambda} \\ \mathbf{Q}_{rs} & \mathbf{K}_{rr}^B + \mathbf{Q}_{rr} & \mathbf{K}_{r\theta}^B + \mathbf{Q}_{r\theta} & \mathbf{Q}_{r\lambda} \\ \mathbf{Q}_{\theta s} & \mathbf{K}_{\theta r}^B + \mathbf{Q}_{\theta r} & \mathbf{K}_{\theta\theta}^B + \mathbf{Q}_{\theta\theta} & \mathbf{Q}_{\theta\lambda} \\ \mathbf{Q}_{\lambda s} & \mathbf{Q}_{\lambda r} & \mathbf{Q}_{\lambda\theta} & \mathbf{0} \end{bmatrix} \begin{bmatrix} \Delta \mathbf{d}^S \\ \Delta \mathbf{d}^B \\ \Delta \theta^B \\ \boldsymbol{\lambda} \end{bmatrix} = \begin{bmatrix} -\mathbf{r}^S \\ -\mathbf{r}_r^B \\ -\mathbf{r}_\theta^B \\ -\mathbf{g} \end{bmatrix}. \tag{2.58}$$

Here, $\mathbf{Q}_{(\cdot)(\cdot)}$ are the coupling matrices, representing the coupling between the beam, solid and Lagrange multiplier degrees of freedom.

Directly solving the linearized system (2.58) results in an exact fulfillment of the constraint equations $\mathbf{g} = \mathbf{0}$. However, some drawbacks occur when (2.58) is solved directly. Compared to the uncoupled system, the coupled system has an increased system size, because the Lagrange multipliers are introduced as additional unknowns. Furthermore, the linearized system (2.58) shows a zero matrix block on the diagonal, i.e., the system exhibits a saddle point structure. This limits the applicability of some linear solvers. These drawbacks can be at least partially overcome by various approaches, e.g., by the augmented Lagrangian method, cf. [3], or the so-called dual Lagrange multiplier approach, cf. [108, 110, 150]. The augmented Lagrangian method allows for an exact enforcement of the constraint equations in combination with a penalty-like regularization

of (2.58) for an easier numerical treatment. The resulting linear system still exhibits a saddle point structure, which can be overcome by employing the well-known Uzawa algorithm. The main idea behind the dual Lagrange multiplier approach is the definition of the discrete coupling variables based on a biorthogonality condition with the primary unknowns. This allows for a trivial condensation of the Lagrange multipliers (and their primal counterparts) from the linear system of equations, eliminating its saddle point structure. However, as argued in Section 4.2.3 an exact fulfillment of the BTS constraint equations is not required from a physical point of view. Therefore, (2.58) will not be solved directly to obtain solutions to the coupled BTS problem. Instead, a penalty regularization is employed to obtain approximate solutions of (2.58).

2.5.2. Penalty regularization

In this thesis, the discretized coupled BTS problems such as (2.58) will be exclusively solved using a penalty regularization. The main idea behind the employed penalty regularization is to remove the constraint equations from the discretized system of equations, i.e., the last row in (2.58), and instead penalize violations of the constraint equations. In other words, the spatial discretization of the constraint equations is performed before the penalty regularization. The resulting formulation is purely based on beam and solid degrees of freedom and does not contain any additional variables.

It is important to note that the employed penalty regularization is not a penalty method in the classical sense. In classical penalty methods a *space continuous* penalty potential is defined as $\Pi_\epsilon = \frac{\epsilon}{2} \int_{\Gamma_c} \underline{\mathbf{g}}^T \underline{\mathbf{g}} \, ds$, cf. [152]. The constraint equations $\underline{\mathbf{g}} = \underline{\mathbf{0}}$ are no longer fulfilled exactly, but are approximated by penalizing constraint violations with the scalar penalty parameter $\epsilon \in \mathbb{R}^+$. Variation of the penalty potential yields the coupling contributions to the total weak form. In the space continuous setting, the solution of the penalty method converges towards the solution of the Lagrange multiplier method for $\epsilon \rightarrow \infty$. However, in the discretized setting this is no longer the case. Common discretization strategies for the penalty method are the node-to-segment (NTS) and the Gauss point-to-segment (GPTS) scheme. In both cases, the variation of the penalty potential is evaluated at discrete points (i.e., the finite element nodes or the Gauss points) on one of the coupling interfaces. This local characteristic of the penalty method is fundamentally different from the employed penalty regularized Lagrange multiplier method, where the constraint equations are formulated in a weighted sense. Therefore, the discrete solutions of the two approaches will not match.

The relaxation of the discretized coupling constraints $\underline{\mathbf{g}} = \underline{\mathbf{0}}$ can be stated in the general form of

$$\underline{\lambda} = \epsilon \mathbf{V}^{-1} \underline{\mathbf{g}}. \quad (2.59)$$

Herein, the Lagrange multipliers are no longer independent variables, but well-defined functions of the beam and solid displacements. They can subsequently be removed from the global system of equations. Again, $\epsilon \in \mathbb{R}^+$ is the scalar penalty parameter and it is clear that for $\epsilon \rightarrow \infty$, (2.59) becomes equivalent to the last row in (2.57). Furthermore, $\mathbf{V} \in \mathbb{R}^{n_{\text{const}} \times n_{\text{const}}}$ is a scaling matrix to account for different weighting of the individual constraint equations. An adequately scaling of the constraint equations in the penalty relaxation is required to pass basic consistency tests, see Sections 4.4.1, 5.4.4 and 6.4.1. Inserting (2.59) into (2.58), and eliminating all dependent degrees

of freedom, yields the penalty regularized global system of equations:

$$\left(\begin{bmatrix} \mathbf{K}_{ss}^S + \mathbf{Q}_{ss} & \mathbf{Q}_{sr} & \mathbf{Q}_{s\theta} \\ \mathbf{Q}_{rs} & \mathbf{K}_{rr}^B + \mathbf{Q}_{rr} & \mathbf{K}_{r\theta}^B + \mathbf{Q}_{r\theta} \\ \mathbf{Q}_{\theta s} & \mathbf{K}_{\theta r}^B + \mathbf{Q}_{\theta r} & \mathbf{K}_{\theta\theta}^B + \mathbf{Q}_{\theta\theta} \end{bmatrix} + \epsilon \begin{bmatrix} \mathbf{Q}_{s\lambda} \\ \mathbf{Q}_{r\lambda} \\ \mathbf{Q}_{\theta\lambda} \end{bmatrix} \begin{bmatrix} \mathbf{V}^{-1} & \mathbf{0} & \mathbf{0} \\ \mathbf{0} & \mathbf{V}^{-1} & \mathbf{0} \\ \mathbf{0} & \mathbf{0} & \mathbf{V}^{-1} \end{bmatrix} \begin{bmatrix} \mathbf{Q}_{\lambda s} & \mathbf{Q}_{\lambda r} & \mathbf{Q}_{\lambda\theta} \end{bmatrix} \right) \cdot \begin{bmatrix} \Delta \mathbf{d}^S \\ \Delta \mathbf{d}^B \\ \Delta \boldsymbol{\theta}^B \end{bmatrix} = \begin{bmatrix} -\mathbf{r}^S - \epsilon \mathbf{Q}_{s\lambda} \mathbf{V}^{-1} \mathbf{g} \\ -\mathbf{r}^B - \epsilon \mathbf{Q}_{r\lambda} \mathbf{V}^{-1} \mathbf{g} \\ -\mathbf{r}_\theta^B - \epsilon \mathbf{Q}_{\theta\lambda} \mathbf{V}^{-1} \mathbf{g} \end{bmatrix}. \quad (2.60)$$

Here, the number of global unknowns is the same as in the uncoupled case, i.e., the system is only solved for the solid and beam degrees of freedom. An additional effect of the penalty-regularized version of (2.58) is the elimination of the saddle point structure in the stiffness matrix. However, there are some drawbacks of the penalty approach. The constraint equations are violated by definition, which can only be reduced with higher penalty parameters. This in turn leads to an ill-conditioned tangential system matrix. Therefore, it is desirable to choose a penalty parameter that results in a sufficiently accurate solution of the constraint equations, but also limits unwanted numerical effects.

Remark 2.7. For the penalty regularization, an inversion of the (global) scaling matrix \mathbf{V} is required, which is not feasible for a general structure of the scaling matrix. In practice, the scaling matrix is defined in such a way, that it is diagonal, which allows for a trivial inversion *and* the passing of basic consistency tests, e.g., constant stress transfer tests.

Remark 2.8. The presented derivation of the penalty regularized global system of equations can also be interpreted in an algebraic way, cf. [155], by adding the term $\delta \boldsymbol{\lambda}^T \frac{1}{\epsilon} \mathbf{V} \boldsymbol{\lambda}$ to the variational formulation (2.56), which obviously vanishes for $\epsilon \rightarrow \infty$. By adding this term, the Lagrange multipliers can be condensed from the last row of (2.58) yielding (2.60).

3. Mixed-dimensional beam-to-solid interaction

This chapter gives an overview over some of the most important aspects to consider when developing a general mixed-dimensional BTS interaction framework. It is not intended as a complete summary of all the complex details of mixed-dimensional interactions. The goal is to provide the reader with a general understanding of the important classifications and methodological building blocks before the detailed investigations are presented in the subsequent chapters.

3.1. Classification of beam-to-solid interaction problems

The general classification of BTS interaction problems, within this thesis is illustrated in Figure 3.1. This classification is based on the type of interaction and the interacting geometries. Based on the two possible geometry pairings, i.e., line-to-volume and line-to-surface, and the two considered interaction types, i.e., coupling and contact, three different categories can be identified. Figure 3.2(a) illustrates the first main category of considered cases, a beam embedded inside a solid volume. From a geometric point of view this is a line-to-volume (1D-3D) problem. The embedded beam is fixed relative to the solid, i.e., this will be referred to as a 1D-3D beam-to-solid volume (BTSV) coupling problem. The next considered case is visualized in Figure 3.2(b), where the beam is also coupled to the solid, however, instead of being embedded inside the solid volume, the beam is coupled to the surface of the solid volume. Geometrically, this is a line-to-surface (1D-2D) problem and will be referred to as a 1D-2D beam-to-solid surface (BTSS) coupling problem. Finally, Figure 3.2(c) illustrates the third category considered in this thesis, a beam in unilateral contact with the surface of a solid volume. The involved geometries are the same as in the BTSS coupling problem. However, in this case the interactions between the beam and the surface are described by unilateral contact constants instead of tied coupling constraints. This will be referred to as 1D-2D beam-to-solid contact (BTSSC) in this thesis.

Remark 3.1. In this thesis, the term *coupling* denotes a tie between the beams and the solid. The equivalent in surface-to-surface problems is commonly referred to as mesh tying or tied contact. Since the interacting finite element meshes in BTS problems are not equidimensional, the term mesh tying is slightly misleading as the procedure can more accurately be described as the embedding of a mesh in a higher dimensional background mesh. The term tied contact can also be confusing since there is no "untied" contact in BTSV problems.

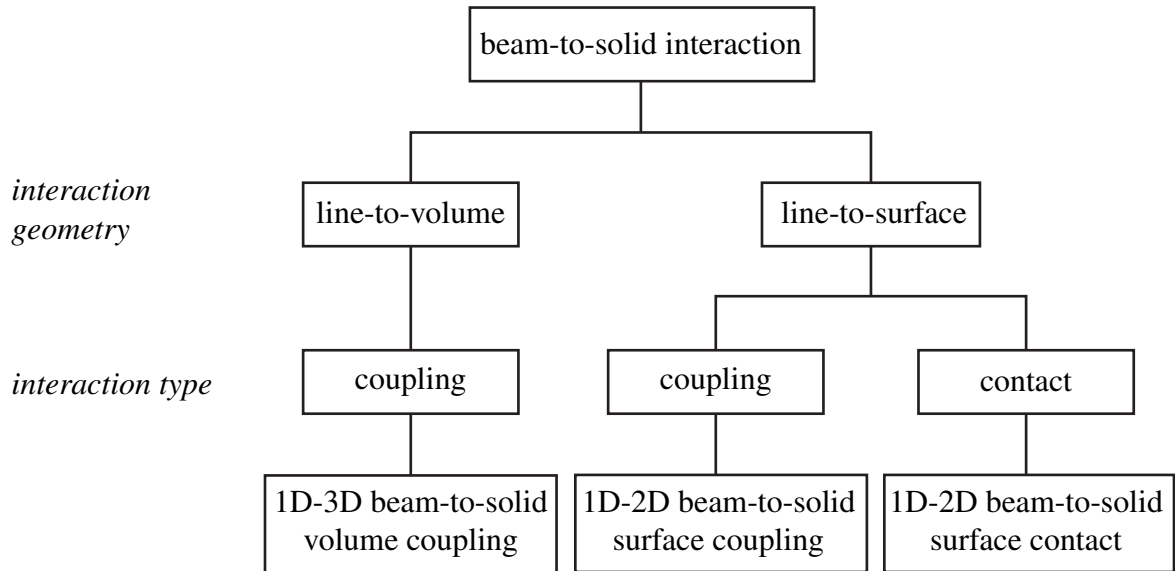


Figure 3.1.: Classification of BTS interaction problems based on the interacting geometries and the type of interaction.

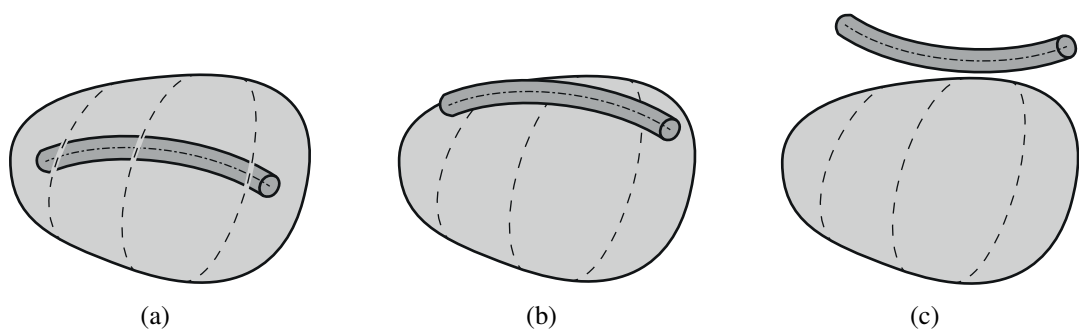


Figure 3.2.: Illustration of the considered classes of BTS interaction problems – beam embedded inside a solid volume (a), beam coupled to the surface of a solid volume (b) and beam in contact with the surface of a solid volume (c).

3.2. Modeling assumptions underlying mixed-dimensional models

In this section, the main modeling assumptions generally underlying the considered mixed-dimensional interaction schemes will be discussed.

3.2.1. Beam-to-solid volume coupling

The considered class of BTSV coupling schemes is based on the assumption that the fiber material is stiff compared to the solid material, and local fiber cross-section dimensions are small compared to the global solid dimensions. Thus, the solid may be discretized without subtracting the fiber volume, formally resulting in overlapping solid and fiber domains. This introduces a modeling error, since in the physical problem no two material points can share the same spatial position. This modeling error is proportional to the fiber volume fraction as well as the stiffness ratio of fiber and matrix. The high fiber stiffness compared to the matrix stiffness in the considered cases reduces the influence of this modeling error. Furthermore, in cases with a high fiber volume fraction, the modeling error can be counteracted by scaling the stiffness of the matrix material to account for the missing volume occupied by the fibers. Based on the assumption of overlapping volumes, two different types of coupling are possible: a truly 1D-3D coupling approach, where the coupling conditions are exclusively defined along the beam centerline, thus preserving the computational advantages of the dimensionally reduced beam models, cf. Figure 3.3(a). And secondly, 2D-3D coupling of the fiber surface (described by a 1D centerline) with the solid volume, cf. Figure 3.3(b). Consistent 2D-3D coupling on the fiber surface would allow for high-resolution stress field predictions in the direct vicinity of the 2D fiber-solid interface. However, such approaches require an evaluation of coupling constraints on a 2D interface and a sufficient discretization resolution of the solid with mesh sizes smaller than the fiber cross-section dimensions, thus in large parts deteriorating the advantages provided by a reduced dimensional description of the fibers. Therefore, the developed BTSV coupling schemes in this thesis are based on truly 1D-3D coupling, i.e., a line-to-volume coupling problem. For comparison and verification purposes of the 1D-3D coupling method, a 2D-3D coupling scheme is also presented.

Truly 1D-3D coupling approaches inevitably introduce a modeling error as compared to the 2D-3D coupling, i.e., the *surface* tractions on the 2D beam-solid interface are approximated by localized resultant *line* forces and moments acting on the beam centerline. Therefore, from a mechanical point of view, the line-to-volume coupling is equivalent to a line load acting on an 3D solid continuum. This is a generalized version of the Kelvin problem, cf. [46, 107, 141] and Figure 3.3(a), which consists of an infinite solid loaded with an embedded line load. It is well known and studied, that the analytical solutions to the Kelvin problem contain singularities in the stress and displacement fields close to the point of action of the line load, cf. [46, 107, 141]. This is schematically visualized in Figure 3.4, where the analytical solid displacement field is plotted along the indicated line. The far-field displacements of the 1D-3D and 2D-3D coupling approaches are very similar. The difference between the two displacement fields can be observed close to the singularity. This singularity in the analytical solution prevents the finite element discretization of the truly 1D-3D coupling method to achieve spatial mesh convergence in the fine

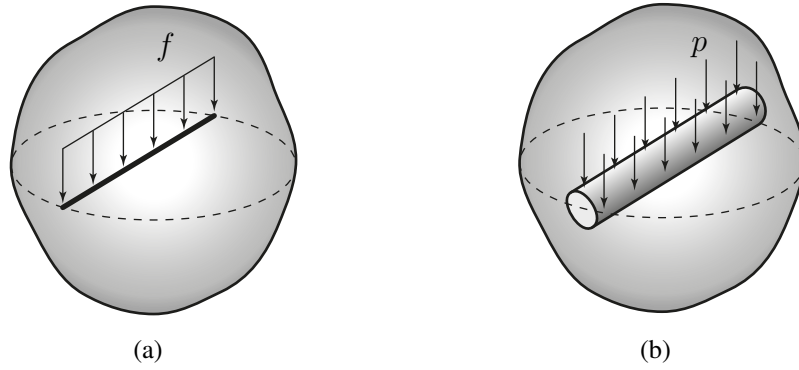


Figure 3.3.: Two different types of mixed-dimensional coupling for an embedded fiber in an infinite solid. Truly 1D-3D coupling (a) and 2D-3D coupling (b). Figure (a) is adapted from the author's article [135], permissions granted under the Creative Commons (CC BY) license.

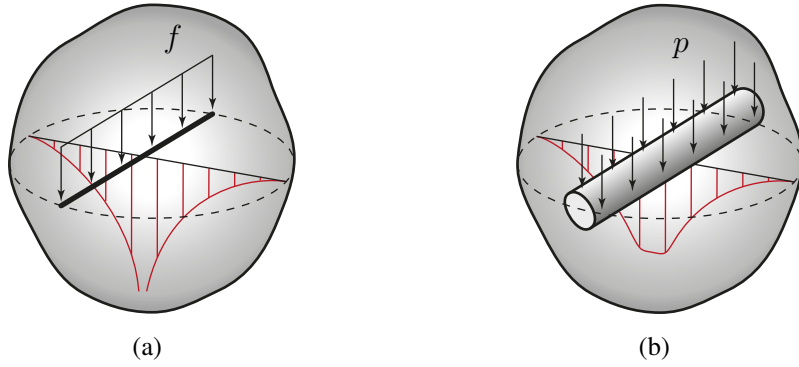


Figure 3.4.: Schematic illustration of the solid displacement field for an embedded fiber in an infinite solid – truly 1D-3D coupling (a) and 2D-3D coupling (b).

mesh limit. However, for mesh sizes in the range of the beam cross-section dimensions or larger, which are well within the range of real life engineering applications, the presented positional *and* rotational coupling methods converge towards the exact solution, i.e., the one if the beam were modeled with continuum elements. This is a crucial property for the applicability of the considered mixed-dimensional BTS coupling problems.

To verify this statement, a plane problem of a loaded beam cross-section coupled to a solid finite element is considered as depicted in Figure 3.5. As long as the cross-section diameter is smaller than the solid finite element mesh size, the resulting discrete nodal forces F_S acting on the solid are independent of the employed coupling approach, i.e., either truly 1D-3D coupling with the associated force F^B (Figure 3.5, left) or 2D-3D coupling with associated coupling surface load f^B (Figure 3.5, right). Obviously this is an idealized setting, but this still underlines and nicely illustrates the validity of a 1D-3D coupling approach down to a solid element size of about the cross-section diameter. For more practical discussion of this topic the reader is referred to Section 5.4.5.

In the presented BTS coupling methods, the solid and beam domains can be discretized

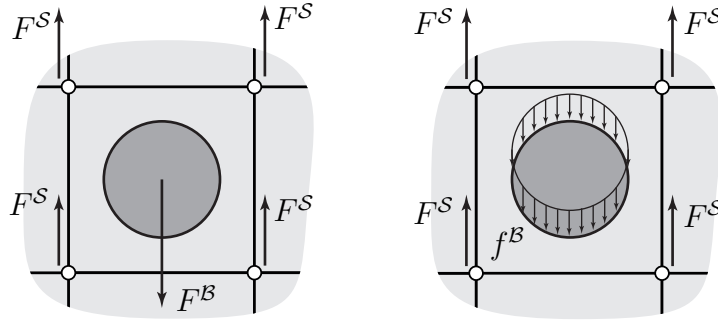


Figure 3.5.: Plane coupling problem of a single fiber with a solid finite element mesh – 1D-3D coupling (left), 2D-3D coupling (right). Figure is taken from the author’s article [135], permissions granted under the Creative Commons (CC BY) license.

independently from each other. It is important to note that the two finite element meshes have to satisfy certain conditions relative to each other. Throughout this thesis, embedded fibers with relatively high slenderness ratios $\zeta_{\text{fiber}} := l_{\text{fiber}}/D_{\text{fiber}} \gg 1$ are considered. Herein, l_{fiber} is the physical length of a fiber and D_{fiber} is a representative cross-section dimension. Moreover, a powerful third-order geometrically exact beam finite element formulation is employed, which typically allows to achieve practically relevant discretization error levels at comparatively coarse spatial discretizations, thus leading to large beam element slenderness ratios $\zeta^B := h^B/D_{\text{fiber}} \gg 1$. Herein, h^B is a characteristic beam finite element length. Due to the previously discussed singularities, the beam cross-section dimensions should be smaller than the characteristic solid finite element size h^S . Based on these consideration, the following two assumptions are made with respect to beam and solid finite element size: (i) $h^S \geq D_{\text{fiber}}$ and (ii) $h^S \leq h^B$. These requirements arise from basic considerations concerning the envisaged applications and the employed finite element methods. As seen in the numerical examples, these assumptions prevent a potential deterioration of spatial convergence rates either due to force localization effects (i) or due to contact locking (ii).

Remark 3.2. The mechanical considerations in the previous section show that the exact analytical solution of the 1D-3D line-to-volume problem has a singularity and is therefore not relevant for the BTSV coupling methods developed in this thesis. The 1D-3D BTSV coupling methods in this thesis are based upon either a zero-order (Chapter 4) or first-order (Chapter 5) Taylor series expansion of the 2D-3D coupling constraints around the beam centerline. If higher-order Taylor series expansions are considered, as is done in [73], second gradient coupling terms are introduced in the solid volume and the solid can be interpreted as a *higher gradient material*. In such a case, the previously discussed singularity does not occur. However, from a mathematical point of view, the existence of such a solution is still not guaranteed. A detailed mathematical analysis of this topic is part of ongoing research and beyond the scope of the present thesis. The interested reader is referred to [81], which is one of the few works in literature that discusses the existence of solutions for higher gradient materials.

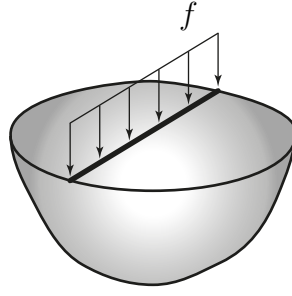


Figure 3.6.: Truly 1D-2D coupling for BTSS coupling problems.

3.2.2. Beam-to-solid surface coupling

The BTSS coupling schemes considered in this thesis are based on the assumption that the beam material is relatively stiff compared to the solid material and the beam cross-section dimensions are small compared to the overall solid dimensions. Furthermore, the connection between the beam and the solid surface is assumed to be sufficiently stiff, so that it can be modeled as a rigid connection. Therefore, the solid may be discretized without exactly modeling the connection between the beam and the solid, thus resulting in a smooth representation of the solid surface. Based on this assumption, only a truly 1D-2D coupling approach is possible for the considered BTSS coupling schemes, i.e., geometrically they all can be classified as line-to-surface coupling schemes, cf. Figure 3.6. This again has a significant impact on the analytical solution of the problem. In an idealized setting, the truly 1D-2D BTSS coupling problem is equal to the Flamant problem of a line load acting on an infinite half space, cf. Figure 3.6, which is well known to exhibit singular stress and displacement fields, cf. [46, 107]. Thus, convergence of the 1D-2D solution towards the exact solution is not expected. However, in regard of the envisioned applications, the primary interest is in global system responses rather than in local stress distributions in the direct vicinity of the fibers. Thus, practically relevant solid element sizes are considered that are larger than the fiber cross-section dimensions. This is illustrated in Figure 3.7. As long as the cross-section diameter is smaller than the solid finite element mesh size, the resulting solid surface nodal forces are independent of the employed coupling approach, as well as the exact geometry of the connection between the solid surface and the fiber. In this regime of mesh resolutions, the inherent modeling error of truly 1D-2D approaches can typically be neglected. Furthermore, the considerations regarding the BTS finite element length ratio for BTSS coupling also hold in the case of BTSS coupling, i.e., the characteristic solid finite element length should be smaller than the beam finite element length.

3.2.3. Beam-to-solid surface contact

The presented BTSSC scheme is based on the assumption that the beam material is relatively stiff compared to the solid material and that all considered beams have circular cross-sections. Furthermore, it is assumed that the thickness of the contact area is small compared to the beam cross-section dimensions. Therefore, contact between the solid surface and a single beam cross-section can be modeled via *one* point-wise contact condition, cf. Figure 3.8. According to this assumption, the contact area can be accurately represented as a 1D line running along the surface

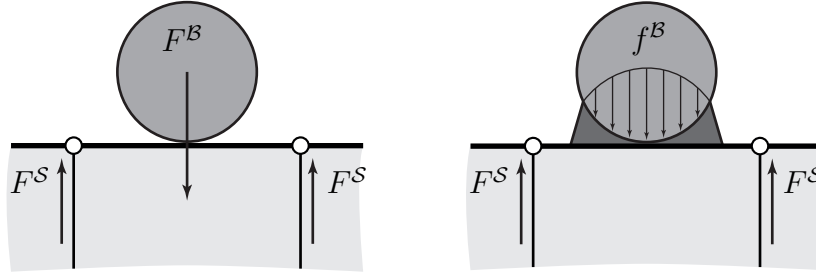


Figure 3.7.: Plane coupling problem of a single fiber with a solid finite element surface – 1D-2D coupling with idealized surface geometry (left), exact coupling interactions and geometry (right).



Figure 3.8.: Modeling assumptions for BTSSC – exact contact pressure p between beam cross-section and solid surface (left) and idealized concentrated point-wise contact force F between beam cross-section and solid surface (right).

of the beam. The BTSSC conditions can be formulated along the beam centerline when the radius of the rigid beam cross-section is taken into account. The resulting truly 1D-2D contact approach shows close similarities with the previously discussed BTSS coupling scheme. This introduces a singular analytical solution to the 1D-2D contact problem. As long as the solid element sizes are large enough not to fully resolve the contact area, the modeling error due to the truly 1D-2D contact can typically be neglected. Contrary to the BTSS coupling case, where the interaction between beam and solid surface occurs over the whole beam cross-section, in the case of BTSSC the assumed contact area is small compared to the beam cross-section dimensions. Therefore, also solid element discretizations with element sizes smaller than the beam cross-section dimensions can be employed.

3.3. Positional and rotational coupling

The primary interest of this thesis lies in the development of truly 1D-2D and 1D-3D coupling schemes, i.e., coupling schemes where the coupling conditions are exclusively defined along the 1D beam centerline. The formulation of the constraint equations along the beam centerline brings about an advantageous property of the developed methods: the coupling constraints of the *positional* and *rotational* fields along the 1D Cosserat continua (representing the beams) can be formulated completely independent of each other. This finding has several important implications for the proposed coupling schemes, as well as the structure of this thesis. First, positional and rotational coupling can be viewed as separate building blocks in the developed BTS framework.

This allows to employ a single positional coupling scheme for different types of considered beam theories. For example, the same positional coupling scheme can be employed for the torsion-free beam theory as well as Simo–Reissner beam theory, even though the former carries three (positional) point-wise degrees of freedom, while the latter carries six (three positional and three rotational) point-wise degrees of freedom. Furthermore, a rotational coupling scheme can be employed in combination with a positional coupling scheme to couple all six point-wise degrees of freedom along the Simo–Reissner centerline. The combination of positional and rotational coupling will be referred to as *full* coupling throughout this thesis. For didactic purposes, the positional and rotational coupling constraints will be presented in individual chapters of this thesis. This allows for a thorough analysis of some important mechanical and algorithmic aspects of positional BTS coupling without having to deal with the complexity of finite rotations right away. Moreover, the derivation of the rotational coupling constraints can be presented with some prior knowledge on the mechanical and algorithmic aspects of mixed-dimensional coupling. All presented rotational interaction schemes in this thesis are developed for BTS coupling problems. A detailed investigation of contact interactions between cross-section rotations and the contacting solid surface is beyond the scope of this thesis as this inherently requires frictional contact. An outlook on the basic steps towards frictional BTSSC is given in Remark 7.3.

To differentiate the scope of validity of purely positional coupling and full coupling (positional and rotational), two application scenarios are discussed.

- (i) First, systems are considered that contain only transversely isotropic fibers (e.g., circular cross-section shape *and* initially straight) and whose global system response is dominated by the axial and bending stiffness of the fibers, i.e., the torsional contribution is negligible. Positional BTS coupling schemes can be considered as a reasonable mechanical model in this case, since local (twist / torsional) rotations of the fibers with respect to their straight axes will rarely influence the global system response. Torsion-free beam models [97] represent an elegant mechanical description of the fibers for such applications.
- (ii) Second, systems are considered that contain transversely anisotropic fibers (e.g., non-circular cross-section shape *or* initially curved). It is clear that twist rotations of the fiber cross-sections with respect to the centerline tangent (even if not possible in their simplest form as rigid body rotations) will change the global system response, since such fibers exhibit distinct directions of maximal / minimal bending stiffness or initial curvature. Additionally, due to the inherent two-way coupling of bending and torsion in initially curved beams [97], bending deformation will inevitably induce torsion in such application scenarios, i.e., the global system stiffness is approximated as *too soft* if these torsional rotations are not transferred to the matrix by a proper coupling scheme. Thus, a unique and consistent mechanical solution for this scenario can only be guaranteed by full BTS coupling schemes.

Remark 3.3. Both aforementioned application scenarios might lead to non-unique static solutions if rotational coupling is neglected. For transversely isotropic fibers the non-uniqueness only occurs at the local fiber level, i.e., the twist orientation of the fibers is not uniquely defined, which does not influence the global system response. The locally non-unique fiber orientation is typically only an issue from a numerical point of view (e.g., linear solvers), and can be effectively circumvented by employing, e.g., torsion-free beam models not exhibiting the relevant rotational degrees of freedom. For transversely anisotropic fibers, such local twist rotations will change

the global system response. This gives rise to non-unique static solutions on the global level and, thus, has significant implications from a physical point of view.

3.4. Discretization strategies for beam-to-solid interaction problems

Spatial discretization of the investigated BTS interaction problems results in inevitably non-matching grids, thus requiring an interaction discretization strategy for non-matching grids. This is a well studied topic for 2D-2D surface-to-surface mesh tying and contact interaction between 3D bodies [152]. One general approach are Gauss point-to-segment (GPTS) methods, where the coupling constraints are enforced strongly, i.e., point-wise, at designated points. An elaborate overview of this topic can be found in [151]. Recently, penalty based GPTS schemes have been employed successfully for beam-to-beam contact, cf. [95, 98]. In this thesis, 1D-2D and 1D-3D GPTS schemes are developed to discretize the mixed-dimensional BTS interaction problems. Furthermore, a 2D-3D GPTS method is developed to generate reference solutions for comparison purposes, cf. Appendix A.

A conceptually alternative approach is the so-called mortar finite element method, which can be interpreted as a special kind of segment-to-segment method, cf. [57–59, 109, 111–115, 150]. The mortar finite element approach was originally introduced in the context of discretization schemes based on the domain decomposition techniques for non-matching grids. The main feature of the mortar method is the formulation of the interaction constraints in a weak (weighted) sense. In classical computational mechanics, mortar methods refer to discretization techniques between interface conforming, i.e., non-overlapping and non-immersed, domains. This also implies, that the dimensions of the interfaces are the same. Additionally, the discretization of the Lagrange multiplier field has to match one of the two interface discretizations, i.e., the Lagrange multiplier field is discretized equal to one of the interface displacement fields. Obviously, these aspects are not fulfilled by the considered mixed-dimensional BTS interaction problems. Since there is a close resemblance of the presented methods to classical mortar methods in solid mechanics, e.g., [112–114], the term *mortar-type* will be used for the developed weak constraint enforcement methods in this thesis. The mortar method defines a Lagrange multiplier field on one of the interacting surfaces, which can be identified as the surface tractions between the interfaces. The weighted nature of the mortar methods has been proven to be preferable over GPTS methods. In recent years, mortar methods have become well established and the preferred choice for robust finite element discretization in domain decomposition and computational contact mechanics. This thesis proposes mortar-type approaches to model embedded 1D-3D BTSV coupling and 1D-2D BTSS coupling problems between beam and solid finite elements. A line load represented by a Lagrange multiplier field is defined along the beam centerline to enforce the coupling constraints, thus resulting in a constraint formulation in a weak variational sense.

3.5. Overview

To conclude this chapter, Table 3.1 presents an overview over the investigated BTS interaction variants in this thesis. Not all combinations of the various topics discussed in this chapter are

3. Mixed-dimensional beam-to-solid interaction

Table 3.1.: Overview over the investigated BTS interaction schemes in this thesis.

BTS interaction type	BTS discretization	BTS dimension	coupled fields	chapter
beam-to-volume coupling (BTSV)	mortar-type	1D-3D	pos	4
			pos + rot	5
	GPTS	1D-3D	pos	4
			pos + rot	5
		2D-3D	pos	4
			pos + rot	5
beam-to-surface coupling (BTSS)	mortar-type	1D-2D	pos + rot	6
beam-to-surface contact (BTSSC)	GPTS	1D-2D	pos	7

investigated. The ordering of the chapters in this thesis is chosen such that the interested reader (with certain prior knowledge on computational mechanics) is able to comprehend the individual presented building blocks as part of a general mixed-dimensional BTS interaction framework. For example, the rotational coupling constraints are presented and analyzed in combination with BTSV coupling problems. However, the findings are almost directly applicable to rotational coupling for BTSS coupling problems as well, and therefore, will not be presented again.

4. Positional beam-to-solid volume coupling

In this chapter, positional beam-to-solid volume (BTSV-POS) coupling is presented as a first building block towards a general BTS interaction framework. The coupling terms are exclusively formulated as line-to-volume interactions through the beam centerline position, which decouples the beam cross-section orientations (rotations) from the solid deformations, thus resulting in a purely *positional* coupling of the beam centerline to the underling solid. At first glance, not coupling the beam cross-section rotations might be considered as a rather coarse approximation for certain physical systems such as fiber-reinforced composite materials, where fibers are e.g., molded / glued into a matrix such that all modes of relative motion are blocked. However, the BTSV-POS coupling scheme presented in this chapter can still be applied to applications, where the main contributions to the internal energy of the beams and the mechanical resistance of the overall structure stem from bending and axial tension of the fibers, therefore justifying the choice to neglect the coupling of cross-section rotations. In such applications, it is desirable to employ a torsion-free beam theory, which does not carry any rotational degrees of freedom, and therefore, can only be used in combination with the purely positional BTSV-POS coupling scheme. Moreover, apart from being considered as a standalone coupling scheme, the presented BTSV-POS coupling formulation will be used in combination with rotational coupling to formulate a full consistent coupling of positions *and* rotations, cf. Chapter 5. Most of the content of this chapter has previously been published in the author's article [135].

4.1. Problem formulation

In this chapter a 3D finite deformation BTSV-POS problem, as shown in Figure 4.1, is considered. The principle of virtual work serves as basis for the employed finite element method. Contributions to the total virtual work of the system can be split into solid, beam and coupling terms, where the solid and beam terms are independent of the coupling constraint. Therefore, well-established formulations for the solid as well as the beam can be used without modifications. Without loss of generality, only quasi-static problems are considered in this thesis. This only impacts the virtual work contributions from the solid and the beam, but the coupling terms for the BTSV-POS problem hold also for time-dependent problems.

In the BTSV-POS problem shown in Figure 4.1, the beam is embedded inside the solid volume. The solid volume overlapping with the beam volume is not subtracted from the solid volume, thus resulting in overlapping volumes. However, the numerical examples in Section 4.4 demonstrate that this does not impact the accuracy of the presented method.

If the embedded beam is considered as a 3D body, the most natural choice for the coupling conditions is to couple the beam surface to the solid volume. However, there is no explicit surface

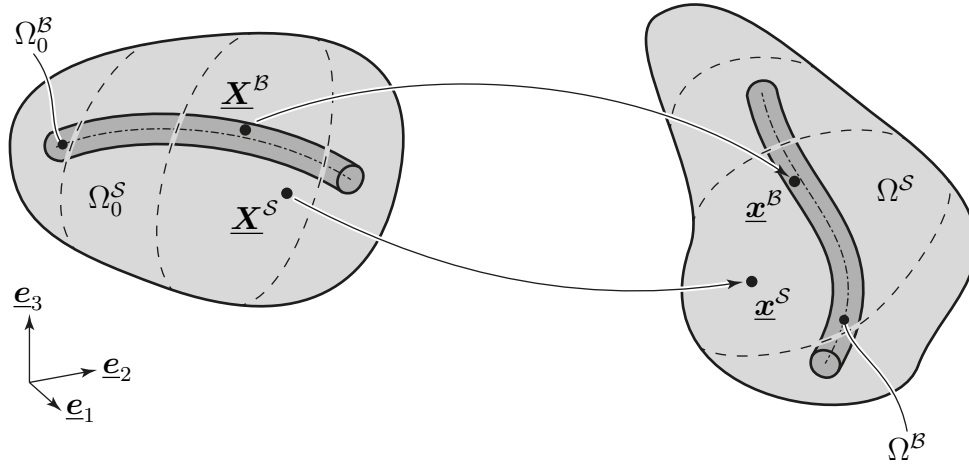


Figure 4.1.: Notation of the finite deformation BTSV-POS coupling problem. Figure is taken from the author's article [135], permissions granted under the Creative Commons (CC BY) license.

in the solid domain, to define the coupling conditions on. Therefore, this is a surface-to-volume (2D-3D) coupling problem, i.e., the beam surface is embedded into the background solid volume. The coupling constraints read

$$\underline{x}^B - \underline{x}^S = \underline{0} \quad \text{on} \quad \Gamma_{c,2D-3D}, \quad (4.1)$$

where $\Gamma_{c,2D-3D}$ is the 2D-3D coupling surface, i.e., the part of the beam surface that lies within the solid volume. The Lagrange multiplier method is employed to impose the coupling constraint. Therefore, a Lagrange multiplier vector field $\underline{\lambda}_{2D-3D}(s, \alpha, \beta) \in \mathbb{R}^3$ is defined on $\Gamma_{c,2D-3D}$, which can be interpreted as the negative interface tractions acting on the beam surface. The total Lagrange multiplier potential reads

$$\Pi_{\lambda,2D-3D} = \int_{\Gamma_{c,2D-3D}} \underline{\lambda}_{2D-3D}^T (\underline{x}^B - \underline{x}^S) \, dA_0. \quad (4.2)$$

In the following, let \underline{x}_r^S denote the line of material solid points that coincide with the beam centerline in the current configuration, i.e., $\underline{x}_r^S = \underline{r}$. The 2D-3D coupling conditions (4.1) can now be expanded via a Taylor series around the beam centerline, i.e.,

$$\underline{r} - \underline{x}_r^S + \mathcal{O}(R) = \underline{0}. \quad (4.3)$$

The 1D-3D coupling strategy underlying the proposed BTSV-POS scheme relies on the basic assumption of slender beams, i.e., $R \ll L$, where R is a characteristic cross-section dimension (e.g., the radius of circular cross-sections). In this chapter the Taylor series is truncated after the constant term. The remaining terms only depend on the positional degrees of freedom of the beam and solid at the beam centerline. The error introduced by this approximation is of order $\mathcal{O}(R)$. Moreover, the approximation changes the physical coupling dimensionality applied to the BTSV-POS model from surface-to-volume (2D-3D) to a line-to-volume (1D-3D) coupling. This is a significant change in the mathematical description of the mechanical model, cf. Chapter 3.

In Chapter 5 the linear term of the Taylor series will also be considered, thus resulting in positional *and* rotational coupling. The approximation (4.3) inserted in the coupling potential (4.2) gives

$$\Pi_{\lambda,2D-3D} \approx \Pi_{\lambda,1D-3D}^{\mathcal{V}} = \int_{\Gamma_{c,2D-3D}} \underline{\lambda}_{2D-3D}^T (\underline{r} - \underline{x}_r^S) \, dA_0. \quad (4.4)$$

The surface integral in (4.4) can be split up in an integral along the part of the beam centerline that lies within the solid volume, i.e., $\Gamma_{c,1D-3D} = \Omega_0^S \cap \Omega_0^B$, and an integral over the circumference of the cross-section Γ_{CS} . This yields

$$\Pi_{\lambda,1D-3D}^{\mathcal{V}} = \int_{\Gamma_{c,1D-3D}} \int_{\Gamma_{CS}} \underline{\lambda}_{2D-3D}^T (\underline{r} - \underline{x}_r^S) \, d\Gamma_{CS} \, ds. \quad (4.5)$$

The positions \underline{r} and \underline{x}_r^S can be extracted from the inner integral because they are only dependent on the beam parameter coordinate s . The remaining integral over the circumference of the cross-section only contains the Lagrange multiplier field, and the following abbreviation is introduced

$$\underline{\lambda}_{1D-3D}(s) = \int_{\Gamma_{CS}} \underline{\lambda}_{2D-3D}(s, \alpha, \beta) \, d\Gamma_{CS}. \quad (4.6)$$

Here, $\underline{\lambda}_{1D-3D}(s) \in \mathbb{R}^3$ represents the resultants of the 2D-3D Lagrange multiplier field acting on a single cross-section. It is important to point out that $\underline{\lambda}_{2D-3D}$ and $\underline{\lambda}_{1D-3D}$ have different physical dimensionality and, accordingly, also different units: the first one is a surface load, while the latter one represents a line load. The final approximated total Lagrange multiplier potential can be stated as

$$\Pi_{\lambda,1D-3D}^{\mathcal{V}} = \int_{\Gamma_{c,1D-3D}} \underline{\lambda}_{1D-3D}^T (\underline{r} - \underline{x}_r^S) \, ds. \quad (4.7)$$

Variation of this Lagrange multiplier potential yields the coupling contributions to the total virtual work

$$\delta \Pi_{\lambda,1D-3D}^{\mathcal{V}} = \underbrace{\int_{\Gamma_{c,1D-3D}} \underline{\lambda}_{1D-3D} (\delta \underline{r} - \delta \underline{x}_r^S) \, ds}_{-\delta W_{c,1D-3D}^{\mathcal{V}}} + \underbrace{\int_{\Gamma_{c,1D-3D}} \delta \underline{\lambda}_{1D-3D} (\underline{r} - \underline{x}_r^S) \, ds}_{\delta W_{\lambda,1D-3D}^{\mathcal{V}}}, \quad (4.8)$$

with the coupling interface contributions $\delta W_{c,1D-3D}^{\mathcal{V}}$ and the variational form of the coupling constraints $\delta W_{\lambda,1D-3D}^{\mathcal{V}}$. This leads to the final saddle point-type weak formulation of the 1D-3D BTSV-POS problem:

$$\delta W^S + \delta W^B - \delta W_{c,1D-3D}^{\mathcal{V}} + \delta W_{\lambda,1D-3D}^{\mathcal{V}} = 0. \quad (4.9)$$

For improved readability, the subscript 1D-3D for the line-to-volume coupling terms will be omitted from now on. Furthermore, the positional 1D-3D Lagrange multiplier field will be referred to as $\underline{\lambda}^{\mathcal{V}}$.

4.2. Spatial discretization

4.2.1. Mortar-type coupling of positions

Employing a mortar-type coupling approach, the Lagrange multipliers are approximated with a finite element interpolation [17, 110, 150]. The continuous Lagrange multiplier field $\underline{\lambda}^{\mathcal{V}}$ is defined

along the beam centerline. Therefore, the Lagrange multiplier interpolation is defined along the 1D beam elements. All subsequent integration is performed on the coupling domain $\Gamma_{c,h}$, which is the projection of the continuous coupling domain Γ_c onto the beam finite element function space. In the nomenclature of classical computational contact mechanics, the beam would be considered the slave side, and the solid the master side. The approximated Lagrange multiplier field reads

$$\underline{\lambda}_h^\nu = \sum_{j=1}^{n^\nu} \Phi_j^\nu(\xi^B) \hat{\underline{\lambda}}_j^\nu, \quad (4.10)$$

where $\Phi_j^\nu \in \mathbb{R}$ is the shape function for the discrete Lagrange multiplier vector $\hat{\underline{\lambda}}_j^\nu \in \mathbb{R}^3$ at node j . The total number of discrete Lagrange multiplier nodes is n^ν , which is not necessarily equal to n^B . The shape functions Φ_j^ν are a function of the scalar beam centerline parameter coordinate ξ^B . Note that even though the Lagrange multipliers are defined along the beam centerline domain, the beam centerline shape functions H_l^r and H_l^t will not be used to interpolate the Lagrange multiplier field. An adequate choice of Lagrange multiplier shape functions will be discussed in Section 4.2.2. The nodal discrete Lagrange multiplier unknowns $\hat{\underline{\lambda}}_j^\nu$ are assembled into the global vector $\underline{\lambda}^\nu$.

In what follows, all coupling terms are evaluated on the beam centerline. This requires the projection of points along the beam centerline parameter space into the solid element parameter space, all in the reference configuration, which in turn is achieved by solving the set of nonlinear equations $\underline{\mathbf{X}}_h^S(\xi^S, \eta^S, \zeta^S) = \underline{\mathbf{r}}_{0,h}(\xi^B)$, for a given ξ^B . Going further, the mapping operator χ_h will be used to represent this projection from a point on the beam centerline to the corresponding point in the solid volume. To improve readability, the dependency on parameter coordinates will not be stated explicitly. Insertion of the finite element approximations (2.31), (2.36) and (4.10) into the variational form of the coupling constraints (4.8) gives

$$\delta W_{\lambda,h}^\nu = \sum_{l=1}^{n^B} \sum_{j=1}^{n^\nu} \delta \hat{\underline{\lambda}}_j^{\nu T} \left(\int_{\Gamma_{c,h}} \Phi_j^\nu \mathbf{H}_l \, ds \right) \delta \hat{\mathbf{d}}_l^B - \sum_{k=1}^{n^S} \sum_{j=1}^{n^\nu} \delta \hat{\underline{\lambda}}_j^{\nu T} \left(\int_{\Gamma_{c,h}} \Phi_j^\nu (N_k \circ \chi_h) \, ds \right) \hat{\underline{\mathbf{d}}}_k^S. \quad (4.11)$$

In the previous equation, two local matrices with mass matrix-like structure can be identified:

$$\mathbf{D}^{\nu[j,l]} = \int_{\Gamma_{c,h}} \Phi_j^\nu \mathbf{H}_l \, ds \in \mathbb{R}^{3 \times 6}, \quad (4.12)$$

$$\mathbf{M}^{\nu[j,k]} = \int_{\Gamma_{c,h}} \Phi_j^\nu (N_k \circ \chi_h) \, ds \mathbf{I}^{3 \times 3} \in \mathbb{R}^{3 \times 3}. \quad (4.13)$$

There, $\mathbf{D}^{\nu[j,l]}$ describes the coupling between the Lagrange multiplier node j and the beam node l and $\mathbf{M}^{\nu[j,k]}$ describes the coupling between the Lagrange multiplier node j and the solid node k . They can be assembled into global, so-called mortar matrices $\mathbf{D}^\nu \in \mathbb{R}^{3n^\nu \times 6n^B}$ and $\mathbf{M}^\nu \in \mathbb{R}^{3n^\nu \times 3n^S}$, which are in general both rectangular. A similar expression containing \mathbf{D}^ν and \mathbf{M}^ν can also be derived for the virtual work $\delta W_{c,h}^\nu$ of the coupling forces. All in all, the

coupling contributions to the weak form can now be stated in global matrix form

$$-\delta W_{c,h}^\nu = \delta \mathbf{d}^{\mathcal{B}^T} \underbrace{\mathbf{D}^{\nu^T} \boldsymbol{\lambda}^\nu}_{\mathbf{r}_r^\nu(\boldsymbol{\lambda}^\nu)} - \delta \mathbf{d}^{\mathcal{S}^T} \underbrace{\mathbf{M}^{\nu^T} \boldsymbol{\lambda}^\nu}_{-\mathbf{r}_s^\nu(\boldsymbol{\lambda}^\nu)}, \quad (4.14)$$

$$\delta W_{\lambda,h}^\nu = \delta \boldsymbol{\lambda}^{\nu^T} \mathbf{D}^\nu \mathbf{d}^\mathcal{B} - \delta \boldsymbol{\lambda}^{\nu^T} \mathbf{M}^\nu \mathbf{d}^\mathcal{S} = \delta \boldsymbol{\lambda}^{\nu^T} \underbrace{\begin{bmatrix} -\mathbf{M}^\nu & \mathbf{D}^\nu \end{bmatrix} \begin{bmatrix} \mathbf{d}^\mathcal{S} \\ \mathbf{d}^\mathcal{B} \end{bmatrix}}_{\mathbf{g}^\nu(\mathbf{d}^\mathcal{S}, \mathbf{d}^\mathcal{B})}. \quad (4.15)$$

Here, \mathbf{r}_s^ν and \mathbf{r}_r^ν are the vectors with the discretized coupling forces acting on the solid and positional beam degrees of freedom, respectively. The vector \mathbf{g}^ν contains the discretized constraint equations and its entries can be interpreted as the relative displacement between beam centerline and solid weighted with the Lagrange multiplier shape functions. Inserting all discretized variables into (4.9) gives the discrete nonlinear system of equations for the quasi-static BTSV-POS problem:

$$\mathbf{r}^\mathcal{S}(\mathbf{d}^\mathcal{S}) + \mathbf{r}_s^\nu(\boldsymbol{\lambda}^\nu) = \mathbf{0}, \quad (4.16)$$

$$\mathbf{r}_r^\mathcal{B}(\mathbf{d}^\mathcal{B}) + \mathbf{r}_r^\nu(\boldsymbol{\lambda}^\nu) = \mathbf{0}, \quad (4.17)$$

$$\mathbf{g}^\nu(\mathbf{d}^\mathcal{S}, \mathbf{d}^\mathcal{B}) = \mathbf{0}. \quad (4.18)$$

Here, $\mathbf{r}^\mathcal{S}$ and $\mathbf{r}_r^\mathcal{B}$ are the solid and beam residual vectors, respectively. The Newton–Raphson algorithm is used to obtain solutions to the system of nonlinear equations. Therefore, a linearization of equations (4.16) to (4.18) with respect to the global unknowns $\mathbf{d}^\mathcal{S}$ and $\mathbf{d}^\mathcal{B}$ has to be derived. The linearized system of equations with saddle point structure reads:

$$\begin{bmatrix} \mathbf{K}_{ss}^\mathcal{S} & \mathbf{0} & -\mathbf{M}^{\nu^T} \\ \mathbf{0} & \mathbf{K}_{rr}^\mathcal{B} & \mathbf{D}^{\nu^T} \\ -\mathbf{M}^\nu & \mathbf{D}^\nu & \mathbf{0} \end{bmatrix} \begin{bmatrix} \Delta \mathbf{d}^\mathcal{S} \\ \Delta \mathbf{d}^\mathcal{B} \\ \boldsymbol{\lambda}^\nu \end{bmatrix} = \begin{bmatrix} -\mathbf{r}^\mathcal{S} \\ -\mathbf{r}_r^\mathcal{B} \\ -\mathbf{g}^\nu \end{bmatrix}, \quad (4.19)$$

where $\mathbf{K}_{ss}^\mathcal{S}$ and $\mathbf{K}_{rr}^\mathcal{B}$ are the tangent stiffness matrices associated with the solid degrees of freedom and positional beam degrees of freedom, respectively.

Remark 4.1. For BTSV-POS problems, the coupling matrices \mathbf{D}^ν and \mathbf{M}^ν only depend on the reference configuration, i.e., they are evaluated once at the beginning of the simulation and are stored for further load steps.

Remark 4.2. As a consequence of purely positional coupling, no coupling terms arise between the beams rotational degree of freedom and the rest of the BTS system. Thus, the rotation of beam fibers around their centerline might be unconstrained, possibly yielding a singular linear system to solve. As a remedy, one can impose Dirichlet boundary conditions on at least one of the twist degrees of freedom. This discussion also underlines an advantage coming with the torsion-free beam theory: the corresponding beam finite elements do not have any rotational degrees of freedom, and consequently, such rigid body modes cannot occur.

4.2.2. Discrete Lagrange multiplier spaces

The choice of discrete Lagrange multiplier spaces and associated shape functions is important for the mathematical properties of the discretized system, since the discrete Lagrange multiplier shape

functions, must fulfill an inf-sup condition with the displacement field [24]. In the context of surface-to-surface contact or mesh tying in solid mechanics, this is a well studied-topic. However, in the considered mixed-dimensional BTSV-POS problem, Hermite polynomials are employed as primary shape functions for the slave side, i.e., the beam, which is unusual compared to the standard surface-to-surface case. Additionally, BTSV-POS coupling is an embedded 1D-3D coupling problem, i.e., there is no explicit curve representation in the solid mesh to match the beam centerline, which can lead to stability issues [122]. The numerical experiments in Section 4.4.2 and 4.4.3 carefully evaluate the influence of different Lagrange multiplier bases on the numerical properties of the BTSV-POS problem.

Since the Lagrange multipliers are defined on the beam centerline, a natural choice in the spirit of the mortar method would be to use the same shape functions as for the beam elements, i.e., third-order C^1 -continuous Hermite polynomials. However, the integral over the Hermite shape functions associated with the tangential degrees of freedom becomes zero for neighboring beam elements with equal length. This can lead to numerical difficulties in the penalty-based constraint enforcement. Therefore, in this thesis, standard Lagrangian shape functions are used to interpolate the Lagrange multiplier field. Three different types of shape functions will be compared: linear, quadratic and cubic. In surface-to-surface mortar methods, the use of stable lower order interpolations for the Lagrange multipliers compared to the displacement interpolation order was already successfully explored in [111, 115].

From a mathematical point of view, the BTSV-POS problem is an embedded mesh problem and the discrete multiplier space must satisfy a uniform inf-sup condition to guarantee stability. In the literature some appealing approaches are available together with a deep mathematical analysis. For example, in [15] the so-called vital vertex method is introduced, which defines Lagrange multipliers at the intersections between the coupled meshes, i.e., at the intersections between the beam centerline and the solid elements in the BTSV-POS problem considered here. Another interesting approach, the so-called MorteX method, is presented in [2]. The MorteX method was developed for mesh tying along embedded interfaces, and introduces a coarse-grained interpolation of the Lagrange multipliers. This coarsening is an approach to overcome spurious mesh locking effects, which are a known issue of mixed formulations. Other approaches include Nitsche's method [42, 55, 123] or discontinuous Galerkin formulations [55, 122]. A deep mathematical analysis is beyond the scope of the present thesis, but it is important to point out that in this thesis the mixed formulation, i.e., the saddle-point system, is exclusively solved using a penalty regularization, thus circumventing the inf-sup condition. In principle this is similar to how Nitsche's method sidesteps possible inf-sup stability issues. The penalty regularization of a not inf-sup stable system might lead to locking phenomena, i.e., the coupling discretization becomes to stiff. However, the examples presented in Section 4.4 show that the presented BTSV-POS method with a linear interpolation of the Lagrange multipliers is locking-free for typical BTS length ratios and penalty parameters. This is also confirmed by other numerical investigations on embedded mesh methods, cf. [122], where classical mortar-type Lagrange multiplier ideas are also formally unstable, but only cause locking problems in certain situations (i.e. if the embedded mesh is finer than the background mesh).

Remark 4.3. The previous derivations are given for the case, where the constraint equations are fulfilled in a truly weak (variational) sense. In Section 4.4, this mortar-type coupling will be compared to a classical Gauss point-to-segment (GPTS) coupling approach. In the GPTS

coupling, the strong form of the constraint equations (4.1) is fulfilled at each Gauss point along the beam, i.e., a discrete Lagrange multiplier vector $\hat{\underline{\lambda}}_{\text{GP},i}^{\mathcal{V}} \in \mathbb{R}^3$ is defined at each Gauss point in the sense of a collocation method. However, GPTS coupling can also be interpreted as a special case of the mortar-type coupling, namely if the Lagrange multiplier field is interpolated as

$$\underline{\lambda}_{\text{GP},h}^{\mathcal{V}} = \sum_i^{n_{\text{GP}}^{\mathcal{V}}} \tilde{w}_i \delta(\tilde{\xi}_i^{\mathcal{B}} - \xi^{\mathcal{B}}) \hat{\underline{\lambda}}_{\text{GP},i}^{\mathcal{V}}.$$

Here, δ is the Dirac delta distribution with the property $\int_{\Gamma_{c,h}} \delta(\alpha - \xi^{\mathcal{B}}) f(\xi^{\mathcal{B}}) \text{d}s = f(\alpha)$. The position and weight of the i -th Gauss point are denoted with $\tilde{\xi}_i^{\mathcal{B}}$ and \tilde{w}_i , respectively.

4.2.3. Penalty regularization

The constraint equations (4.1) are discretized with a mortar coupling approach using Lagrange multipliers, thus resulting in a mixed formulation. However, due to certain drawbacks, e.g., an increased system size compared to the uncoupled problem and a saddle point structure, (4.19) will not be solved directly to obtain solutions to the BTSV-POS problem. Instead, a penalty regularization is used to obtain approximate solutions of (4.19). This results in a formulation that is purely displacement-based and does not contain any additional variables, cf. Section 2.5.2. The main idea is to allow a relaxation of the discretized coupling constraints $\mathbf{g}^{\mathcal{V}} = \mathbf{0}$ in the form

$$\underline{\lambda}^{\mathcal{V}} = \epsilon^{\mathcal{V}} (\mathbf{V}^{\mathcal{V}})^{-1} \mathbf{g}^{\mathcal{V}}(\mathbf{d}^{\mathcal{S}}, \mathbf{d}^{\mathcal{B}}). \quad (4.20)$$

Herein, $\epsilon^{\mathcal{V}} \in \mathbb{R}^+$ is the penalty parameter and it is clear that for $\epsilon^{\mathcal{V}} \rightarrow \infty$, (4.20) becomes equivalent to (4.18). The entries in the weighted relative displacement vector $\mathbf{g}^{\mathcal{V}}$ are proportional to the support of the corresponding Lagrange multiplier shape function, i.e., they depend on the beam element length. If unaccounted for, this dependency would result in a violation of the basic consistency tests presented in Section 4.4.1. To resolve this problem, the relaxation of the constraints in (4.20) is additionally multiplied with the inverse of the diagonal nodal scaling matrix $\mathbf{V}^{\mathcal{V}}$, similar to the approach in [154]. The local scaling matrix for the Lagrange multiplier node j is defined by

$$\mathbf{V}^{\mathcal{V}[j,j]} = \int_{\Gamma_{c,h}} \Phi_j^{\mathcal{V}} \text{d}s \mathbf{I}^{3 \times 3}, \quad (4.21)$$

and is assembled into the global scaling matrix $\mathbf{V}^{\mathcal{V}}$. It is important to note, that $\mathbf{V}^{\mathcal{V}}$ is a diagonal matrix and its inversion is therefore trivial. With the penalty regularization, the coupling residual contributions $\mathbf{r}_s^{\mathcal{V}}$ and $\mathbf{r}_r^{\mathcal{V}}$ can be stated as,

$$-\mathbf{r}_s^{\mathcal{V}}(\mathbf{d}^{\mathcal{S}}, \mathbf{d}^{\mathcal{B}}) = \epsilon^{\mathcal{V}} \mathbf{M}^{\mathcal{V}^T} (\mathbf{V}^{\mathcal{V}})^{-1} [-\mathbf{M}^{\mathcal{V}} \quad \mathbf{D}^{\mathcal{V}}] \begin{bmatrix} \mathbf{d}^{\mathcal{S}} \\ \mathbf{d}^{\mathcal{B}} \end{bmatrix} \quad (4.22)$$

$$\mathbf{r}_r^{\mathcal{V}}(\mathbf{d}^{\mathcal{S}}, \mathbf{d}^{\mathcal{B}}) = \epsilon^{\mathcal{V}} \mathbf{D}^{\mathcal{V}^T} (\mathbf{V}^{\mathcal{V}})^{-1} [-\mathbf{M}^{\mathcal{V}} \quad \mathbf{D}^{\mathcal{V}}] \begin{bmatrix} \mathbf{d}^{\mathcal{S}} \\ \mathbf{d}^{\mathcal{B}} \end{bmatrix}. \quad (4.23)$$

With this the final global system of equations (4.19) becomes:

$$\begin{bmatrix} \mathbf{K}_{ss}^{\mathcal{S}} + \epsilon^{\mathcal{V}} \mathbf{M}^{\mathcal{V}^T} (\mathbf{V}^{\mathcal{V}})^{-1} \mathbf{M}^{\mathcal{V}} & -\epsilon^{\mathcal{V}} \mathbf{M}^{\mathcal{V}^T} (\mathbf{V}^{\mathcal{V}})^{-1} \mathbf{D}^{\mathcal{V}} \\ -\epsilon^{\mathcal{V}} \mathbf{D}^{\mathcal{V}^T} (\mathbf{V}^{\mathcal{V}})^{-1} \mathbf{M}^{\mathcal{V}} & \mathbf{K}_{rr}^{\mathcal{B}} + \epsilon^{\mathcal{V}} \mathbf{D}^{\mathcal{V}^T} (\mathbf{V}^{\mathcal{V}})^{-1} \mathbf{D}^{\mathcal{V}} \end{bmatrix} \begin{bmatrix} \Delta \mathbf{d}^{\mathcal{S}} \\ \Delta \mathbf{d}^{\mathcal{B}} \end{bmatrix} = \begin{bmatrix} -\mathbf{r}_s^{\mathcal{S}}(\mathbf{d}^{\mathcal{S}}) - \mathbf{r}_s^{\mathcal{V}}(\mathbf{d}^{\mathcal{S}}, \mathbf{d}^{\mathcal{B}}) \\ -\mathbf{r}_r^{\mathcal{B}}(\mathbf{d}^{\mathcal{B}}) - \mathbf{r}_r^{\mathcal{V}}(\mathbf{d}^{\mathcal{S}}, \mathbf{d}^{\mathcal{B}}) \end{bmatrix}. \quad (4.24)$$

The penalty regularization introduces an additional system parameter ϵ^ν . This leaves the important question on how to choose that parameter. Obviously, choosing too high penalty parameters can lead to an ill-conditioned system matrix and subsequent issues with the numerical solution procedure, as well as to contact locking effects, cf. Section 4.4.3. Moreover, also from a mechanical point of view, an infinitely large penalty parameter is not desirable. This is because in the real physical problem the beam cross-section itself is flexible, however, the employed beam theories introduce the assumption of rigid cross-sections. Therefore, the penalty parameter is no longer a pure mathematical tool of constraint enforcement, but it also has a physical meaning, representing the beam cross-section stiffness. Similar observations can be made in the case of beam-to-beam contact, cf. [98]. Going further, one could define the penalty parameter based on continuum mechanical analysis of the cross-section deformation and stiffness. However, since the primary interest is the regularization of (4.19), the following rule of thumb for choosing the penalty parameter can be given: the positional penalty parameter should be in the range of the beams' Young's modulus, i.e., $\epsilon^\nu \approx E^B$. In practice this does not lead to an unphysically large violation of the positional coupling constraints, and contact locking has not been observed in combination with a linear interpolation of the Lagrange multiplier field.

4.2.4. Numerical integration

The BTSV-POS contributions to the global system of equations are all calculated via integration over the beam domain in the reference configuration, cf. (4.12) and (4.13). Numerical integration, namely a Gauss–Legendre quadrature, is used to evaluate the coupling matrices \mathbf{D}^ν and \mathbf{M}^ν and the scaling matrix \mathbf{V}^ν during the finite element simulation. An accurate numerical evaluation of the coupling integrals is absolutely essential to pass basic consistency tests, cf. Section 4.4.1. The integrands in \mathbf{D}^ν and \mathbf{V}^ν solely contain fields defined along the beam centerline, namely the beam displacements and the Lagrange multipliers. If the Jacobian $\|\partial \underline{\mathbf{r}}_{0,n}/\partial s\|$ along the beam element is constant, the integrand is of polynomial form and the numerical integration is exact, if enough quadrature points are used. In the cases considered in this thesis, the maximal polynomial degree of the integrand in \mathbf{D}^ν and \mathbf{V}^ν is 6, i.e., third-order beam shape functions and third-order Lagrange multiplier shape functions. Therefore, 4 Gauss–Legendre points are needed for the numerical integration to be exact. The integrand of \mathbf{M}^ν contains fields defined along the beam centerline as well as the solid volume. In Figure 4.2, it can be seen that the evaluation of the solid shape functions along the beam centerline results in a general nonlinear function which contains so-called weak discontinuities, i.e., kinks at the points where the beam crosses between solid elements, and strong discontinuities, i.e., jumps at points where the beam sticks out of the solid volume. Moreover, the continuous parts of the integrand in \mathbf{M}^ν are not of polynomial degree. To still guarantee high accuracy of numerical integration for the integrand in \mathbf{M}^ν , two different algorithms will be investigated and compared, cf. Figure 4.3. Element-based integration uses a fixed number of Gauss points per beam element. The only exception occurs at strong discontinuities, where the integration is only performed for the part of the beam element inside the solid volume. In segment-based integration, the integration domain along the beam element is split into multiple segments, such that the integrand in the individual segments does not contain any kinks. Each segment is then integrated with a fixed number of Gauss points.

The global coupling matrices only depend on the initial configuration of the BTSV-POS problem, i.e., they remain constant over the course of the simulation. From a computational point

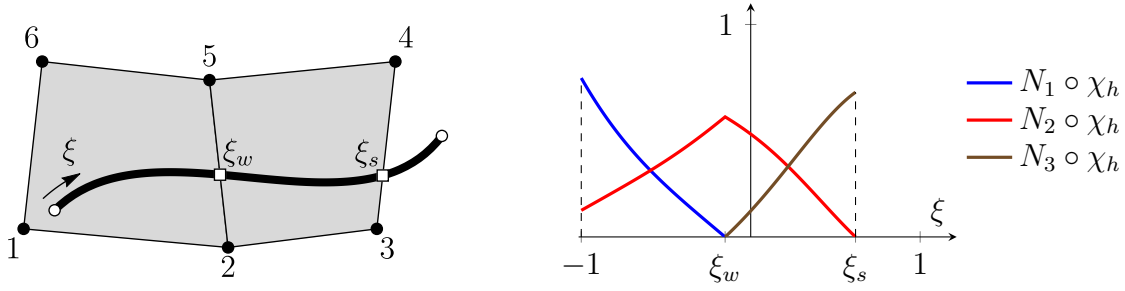


Figure 4.2.: Illustration of weak and strong discontinuities – patch of two solid elements and one beam element with a weak discontinuity at ξ_w and a strong discontinuity at ξ_s (left) and the projection of selected solid shape functions onto the beam centerline (right). Figure is taken from the author’s article [135], permissions granted under the Creative Commons (CC BY) license.

of view, it makes sense to evaluate the coupling matrices \mathbf{D}^ν , \mathbf{M}^ν and \mathbf{V}^ν once and store them for subsequent Newton iterations and time steps. Nevertheless, it is important to address the impact of the two different numerical integration schemes with regard to computational performance and accuracy. Independent of the integration scheme used, each Gauss point evaluation requires the solution of a local nonlinear system of equations, i.e., the projection of the point on the beam centerline into the solid finite element parameter space. For element-based integration, the evaluation time for the coupling terms is more or less proportional to the number of Gauss points used. Since the integrand contains kinks, a relatively high number of Gauss points is necessary to obtain a sufficiently accurate numerical integration. On the other hand, segment-based integration requires calculation of the intersections of the beam elements with the solid surfaces. This intersection operation also requires the solution of local nonlinear systems. The total number of intersections, which have to be calculated, depends on the mesh configuration and cannot be quantified in a general manner. The advantage of the segment-based integration is that the integrands over a segment are smooth, see the left part of Figure 4.2, and an acceptable integration error can be obtained with a reasonable number of Gauss points. Unless stated otherwise, all the examples in this thesis use 6 Gauss points per integration segment. A direct comparison of the two integration schemes regarding evaluation time is difficult, as the times depend on the mesh configuration of the individual problem. In [45], an elaborate comparison of various numerical integration algorithms for mortar methods is given. It should be stated that, in general, due to the non-polynomial integrand in \mathbf{M}^ν both integration schemes cannot integrate \mathbf{M}^ν exactly. Nevertheless, the segment-based integration has clear advantages: the accuracy of its numerical integration is independent of the BTS element length ratio and a higher accuracy can be achieved with the same global number of Gauss points.

4.3. Parallel evaluation of beam-to-solid pairs

A detailed analysis of the implementation and software design associated with the proposed BTS finite element methods is not the main focus of this thesis. Nevertheless, a short discussion of

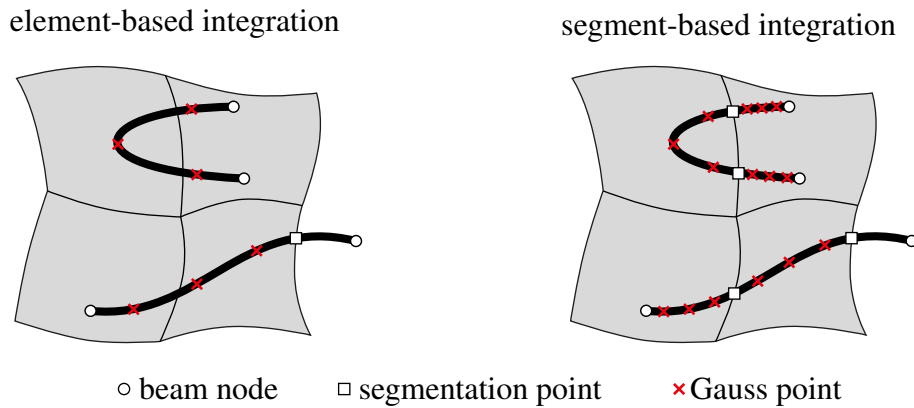


Figure 4.3.: Illustration of element-based and segment-based integration. Figure is taken from the author's article [135], permissions granted under the Creative Commons (CC BY) license.

the broad aspects regarding the parallel implementation of the presented beam-to-solid (BTS) interaction algorithms is given in the following section.

All examples considered in this thesis are simulated with the in-house parallel finite element solver BACI [12], which heavily relies on the Trilinos software package [143]. The BTS coupling algorithms in this thesis are designed to be used on modern many core computer systems (clusters) with distributed memory. Without going into too much detail concerning the specific hardware configuration, the term *processor* refers to a single processing unit in the remainder of this thesis. In most cases, the number of processors is equal to the number of central processing units (CPUs) assigned to a specific simulation. To efficiently run large finite element simulations a distribution of the global problem, i.e., nodes and finite elements, but also global vectors and matrices, to the individual processors is required. Within BACI, the standard domain decomposition functionality for uncoupled beam and solid problems is provided by the third-party library Zoltan [25]. Therein, a graph based parallel distribution, based on the nodal connectivity of the finite element mesh, is performed. This allows for an efficient evaluation of the tangent stiffness and internal force vectors of the beam and solid finite elements. However, in the case of coupled BTS problems, this graph-based parallel distribution can lead to a significant performance bottleneck. Consider a BTSV coupling problem of a thin plate modeled with 81,000 eight-noded hexahedral finite elements and 65×41 unconnected fiber-reinforcements consisting of a total of 8480 beam finite elements. Figure 4.4 illustrates the parallel partitioning of the problem for eight processors. It can be seen that the solid elements are distributed on seven different processors, while one processor mainly carries all the beam finite elements. This is because the graph-based partitioning algorithm does not have any information about the connectivity between the beam and solid elements. Since all BTS coupling terms are defined along the beam centerline, it makes sense that the processor owning a specific beam element also performs the evaluation of the corresponding BTS pairs. The term *beam-to-solid pair* refers to the pairing of a single beam and a single solid element interacting with each other. With the parallel distribution shown in Figure 4.4, one processor would carry almost the entire workload regarding the BTS coupling evaluation, i.e., search of possible BTS coupling pairs and the numerical integration of the coupling terms. Obviously, this would result in a considerable decrease of parallel efficiency. Additionally, in this case the

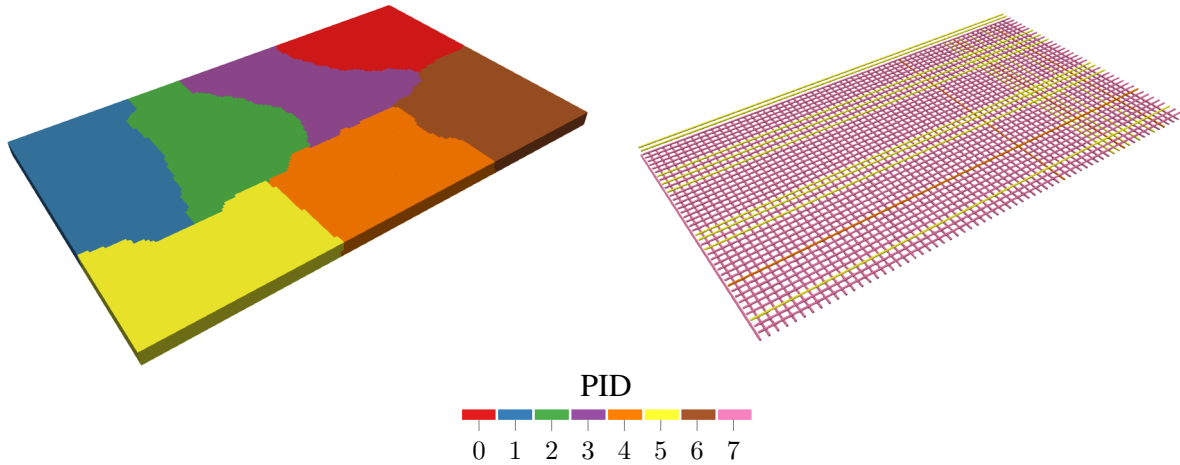


Figure 4.4.: Graph-based parallel distribution of a BTSV coupling problem – Coloring indicates the owning processor identification number (PID).

evaluating processor requires information of the entire solid mesh, resulting in a massive amount of (expensive) parallel communication and possibly one might also run into memory issues as a copy of the entire solid mesh has to be stored for each processor.

To circumvent the previously described issues, in this thesis, the parallel evaluation of the BTS pairs is exclusively based on a so-called *binning* strategy. Therein, the parallel distribution of the global finite element problem is not performed on a graph-based method but rather a geometrically inspired method. The procedure is exemplary illustrated in Figure 4.5. First, the domain of the BTS problem, cf. Figure 4.5(a), is divided into axis aligned *bins*, cf. Figure 4.5(b). In a next step, a weighted parallel distribution of the bins is performed, exemplary shown in Figure 4.5(c) for two processors. Therein, also the ghosted, i.e., not locally owned but locally available bins, are illustrated. The parallel distribution of the finite element mesh is then performed accordingly, cf. Figure 4.5(d). Finally, the evaluation of the BTS pairs is illustrated in Figure 4.5(e). It can be seen that all information required to evaluate the pairs is already locally available, i.e., no additional parallel communication for the pair evaluation is required. However, in some cases a pair provides contributions to two processors, i.e., if the beam element and solid element are not owned by the same processor, cf. the interaction of beams with ghosted solid elements in Figure 4.5(e). In such cases, the so-called *off processor terms* are stored locally and their parallel communication to the other processors is performed once at the end of the pair evaluation phase. Figure 4.6 illustrates the binning strategy applied to the plate example. Now the geometric distribution of the beam and solid elements is geometrically motivated, which reduces the inter-processor communication and provides parallel scalability. The quality of the resulting parallel distribution obtained with the binning strategy obviously depends on the considered problem. However, for all numerical examples considered in this thesis, a binning-based parallel distribution has proven to be sufficient in order to avoid drastic performance bottlenecks during the pair evaluation stage.

Remark 4.4. The BTSV-POS method presented in this chapter yields constant coupling matrices which are only evaluated once at the beginning of the simulation and stored for all subsequent load steps. Therefore, the binning-based parallel distribution is only performed once at the beginning

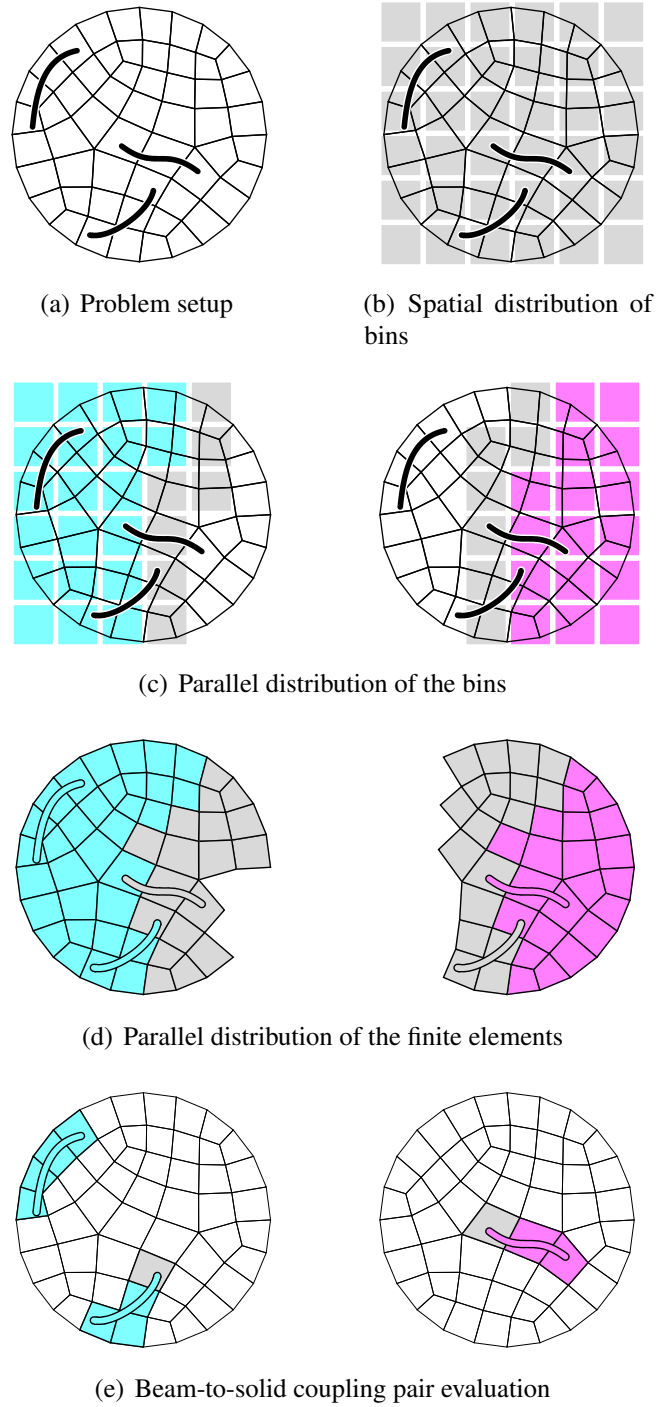


Figure 4.5.: Binning-based parallel distribution for the evaluation of BTS pairs, involving two independent processors. Bins and elements owned by processor 1 and processor 2 are shown in cyan and magenta, respectively. Furthermore, gray colored bins or elements are ghosted by the respective processor. Figure is adapted from the author's article [136], permissions granted under the Creative Commons non-commercial (CC BY-NC) license.

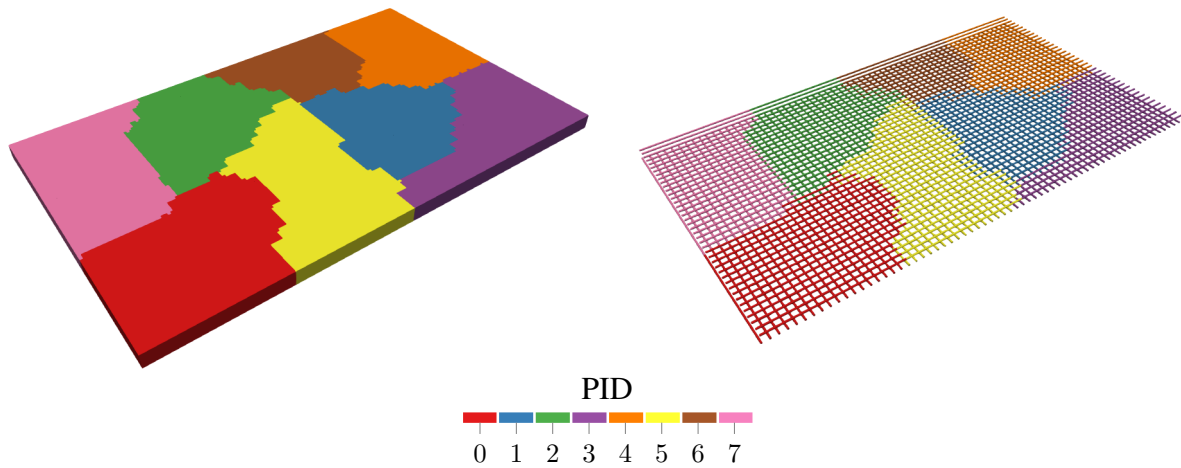


Figure 4.6.: Binning-based parallel distribution of a BTSV coupling problem – Coloring indicates the owning processor identification number (PID).

of the simulation. The BTS coupling methods presented in Chapters 5 and 6 result in deformation dependent coupling terms, i.e., they have to be reevaluated in each Newton–Raphson iteration. There, a parallel redistribution is also not required since all coupling integrals are evaluated on the fixed coupling domain in the reference configuration. In other words, coupling (mesh tying) problems do not necessitate a parallel redistribution over the course of the simulation. However, in the case of BTS contact problems parallel redistributions are required over the course of the simulation. This ensures that, even for large relative motions, all relevant contact pairs are found by the contact algorithm. The recurring parallel redistributions also result in a better distribution of the evaluation workload over the individual processors. In [92] an elaborate discussion on this topic, in the case of surface-to-surface contact problems, is given.

4.4. Examples

The following examples are chosen to evaluate the various BTSV-POS methods proposed in this chapter, cf. Table 4.1, and to demonstrate their accuracy and robustness for the simulation of challenging engineering applications. All numerical examples are set up using the open source beam finite element pre-processor MeshPy [137] and are simulated with the in-house parallel multi-physics research code BACI [12].

4.4.1. Constant stress transfer

The first examples serve as basic consistency tests of the BTSV-POS coupling methods and their ability to transfer constant stress states. The examples are inspired by classical patch tests, which are a well-established tool to investigate the consistency of finite element formulations [140].

4. Positional beam-to-solid volume coupling

Table 4.1.: Listing of the various coupling methods investigated in this chapter. Table is taken from the author's article [135], permissions granted under the Creative Commons (CC BY) license.

coupling discretization	coupling type	Lagrange multiplier shape function	numerical integration
GPTS	1D-3D	–	element + segment based
	2D-3D	–	element based
mortar	1D-3D	linear	element + segment based
		quadratic	element + segment based
		cubic	element + segment based

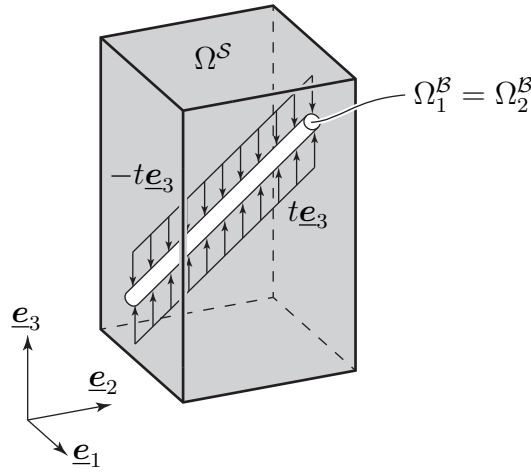


Figure 4.7.: Constant stress transfer test – problem setup. Both beams Ω_1^B and Ω_2^B occupy the same spatial position. Figure is taken from the author's article [135], permissions granted under the Creative Commons (CC BY) license.

4.4.1.1. Beams inside a solid volume

Figure 4.7 shows the first constant stress transfer test presented here. It consists of a solid cuboid Ω^S with two embedded straight beams B1 and B2, where Ω_1^B and Ω_2^B , i.e., the domains of the two beams, occupy the same spatial position. No surface loads or body forces are applied on the solid, while constant line loads with a magnitude t act in opposite directions $\pm \underline{e}_3$ on the beams. Therefore, the opposing loads on the two beams cancel each other out and in sum the two beams transfer no loads to the solid. This gives the trivial solution for the solid displacement field $\underline{u}^S = \underline{0}$ and the constant solution $-\underline{u}_1^B = \underline{u}_2^B = \underline{e}_3 t / \epsilon^\nu$ for the beam displacements, where ϵ^ν is the penalty parameter, cf. (4.20). This test uses the proposed BTSV-POS method to couple both beams to the solid. By doing so, all interactions between the beams are transferred via the solid domain. This test case will be used to assess the influence of discretization and integration error on the performance of the proposed BTSV-POS method.

The dimensions of the cube are $1 \text{ m} \times 1 \text{ m} \times 2 \text{ m}$ and a compressible Neo-Hookean material law with Young's modulus $E^S = 10 \text{ N/m}^2$ and Possion's ratio $\nu^S = 0.3$ is employed as constitutive

model. The penalty stiffness of the BTSV-POS is $\epsilon^V = 10^4 \text{ N/m}^2$. Both beams align along the space diagonal of the cuboid and have a length of $0.7\sqrt{5} \text{ m}$. Their cross-sections are circular with a radius of 0.05 m and the constitutive parameters are $E^B = 100 \text{ N/m}^2$, $\nu^B = 0$. The solid is discretized with $4 \times 4 \times 7$ eight-noded, first-order hexahedral elements (*hex8*). Simo–Reissner beam elements are used to represent both beams $B1$ and $B2$, which are discretized with 5 and 7 equidistant elements, respectively. Mortar coupling is applied between the beam centerline and the solid, with a linear interpolation of the Lagrange multiplier field $\underline{\lambda}^V$ along the beam elements. To circumvent numerical problems in the solution of the resulting linear system of equations, the solid is constrained such that all six rigid body modes of the system are eliminated. Additionally, any rotation of the first nodes of the two beams is constrained to prevent a rigid body rotation of the beams around their axes. The magnitude of the line loads on the beams is $t = 5 \text{ N/m}$.

For the given geometry, there is no discretization error, since the chosen shape functions for the beams and the solid are able to exactly represent both geometry and numerical solution. To assess the numerical integration error, the problem is solved once with element-based integration of the mortar coupling terms and once with segment-based integration. Figure 4.8(a) shows the result obtained with element-based integration and 6 Gauss points per beam element. Clearly, the solution is not exact, as the solid is not stress-free and the deformation of the beams is not constant, thus resulting in non-vanishing curvatures along the beams. Figure 4.8(b) shows the results obtained with segment-based integration of the mortar coupling terms, where each segment is integrated with 6 Gauss points. In this case, the numerical results exactly match the analytical solution up to machine precision, which confirms the vanishing integration error for segment-based integration.

A second constant stress transfer test is set up similar to the first one, with the straight beams being replaced by two helix-shaped beams. The helix has the following geometrical parameters: a radius of 0.45 m , three turns with a pitch of $9/5 \text{ m}$ and a right handed screw type. In this case, the beams $B1$ and $B2$ are discretized with 23 and 31 elements, respectively. The employed C^1 -continuous Hermite polynomials used for the beam centerline interpolation can not represent the helix geometry exactly, which results in two slightly different geometries of the beams and different arc lengths of the two helices, thus introducing a discretization error. In order for the two beams to be in equilibrium, the load t on beam $B2$ is scaled with a factor of 0.999318 , to correct for the different beam lengths. In this case, the beams can not perform a rigid body motion when coupled to the solid. Therefore, only the six rigid body modes of the solid are constrained. All other parameters are equal to the previously described example. Figure 4.9(a) shows the results with element-based integration of the mortar coupling terms. Similar to the previous scenario, one can see non-vanishing stresses in the solid and curvature oscillations in the beams. In this case, also the result with segment-based integration, shown in Figure 4.9(b), does not match the analytical results up to machine precision, because of the previously described discretization error. However, when comparing the quantitative results, one can see that the influence of the numerical integration error for element-based integration is about one order of magnitude larger than the discretization error, which confirms that element-based integration introduces a significant additional integration error.

The presented results were all calculated with the mortar-type BTSV-POS coupling approach and first-order interpolation of the Lagrange multipliers. Quantitatively, the results change only slightly if a GPTS (1D-3D) approach is used or if a different interpolation scheme for the Lagrange multipliers is applied. Therefore, the conclusions obtained from the shown examples, i.e., the

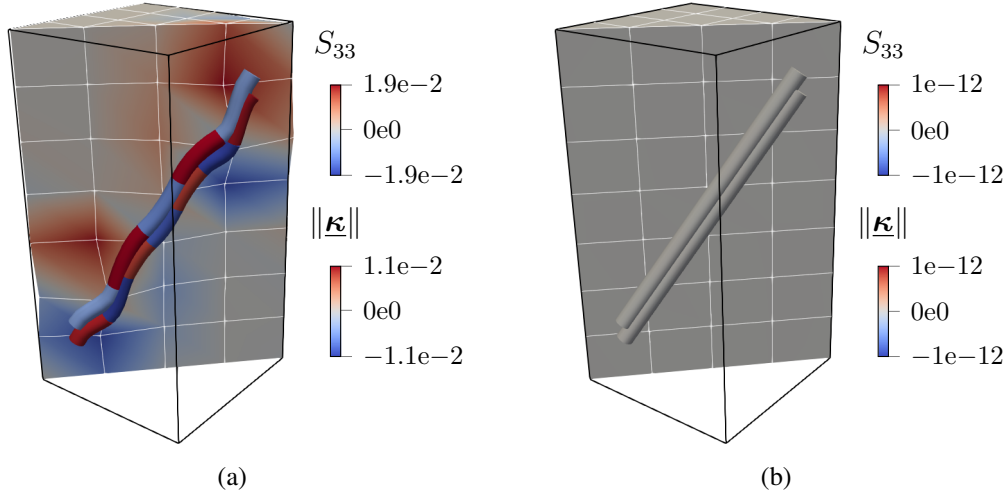


Figure 4.8.: Constant stress transfer test – results for overlapping straight beams. Deformed configurations are shown for element-based integration (a) and segment-based integration (b). The second Piola-Kirchhoff stress S_{33} is shown in the solid and the curvature κ at the middle of each beam element. Displacements of beams and solid are scaled with a factor of 100. Note that both beams Ω_1^B and Ω_2^B occupy the same spatial domain in the undeformed reference configuration. Figure is taken from the author’s article [135], permissions granted under the Creative Commons (CC BY) license.

importance of an accurate numerical integration of the BTSV-POS terms and the superiority of segment- over element-based integration, can be applied to all aforementioned cases.

4.4.1.2. Strong discontinuities

To check the ability of the proposed methods to handle strong discontinuities, i.e., a beam sticking out of a solid domain, two more consistency tests are introduced. Both problems consist of a solid cube and a straight beam which starts inside of the cube and ends outside of it. In the first case, the beam intersects a face of the solid, in the second one it intersects an edge. All solid degrees of freedom are constrained and a constant line load $-t\mathbf{e}_3 = -1 \text{ N/m } \mathbf{e}_3$ is applied only to the part of the beam inside of the cube. Similar to the previous consistency test the analytical solution for the beam displacement is $\mathbf{u}^B = -t/\epsilon^\nu \mathbf{e}_3$. Furthermore, the beam can only be in equilibrium if the coupling interface traction is $\mathbf{\lambda}^\nu = t\mathbf{e}_3 = 1 \text{ N/m } \mathbf{e}_3$. For reasons of simplicity, the solid cube is discretized with a single *hex8* element, the beam with a single Simo–Reissner element. In this case, segment- and element-based integration are identical to each other, as both schemes will result in the same integration points and weights. Segmentation has to be performed at the point where the beam exits the solid volume. The consistency tests are analyzed once with a GPTS approach and once with mortar-type coupling using a linear interpolation of the Lagrange multipliers. Figure 4.10 shows the results. For the Gauss point-to-segment method, the coupling forces at the integration points are illustrated and it can be observed that they are exact up to machine precision. The same holds true for the Lagrange multiplier interface tractions in the

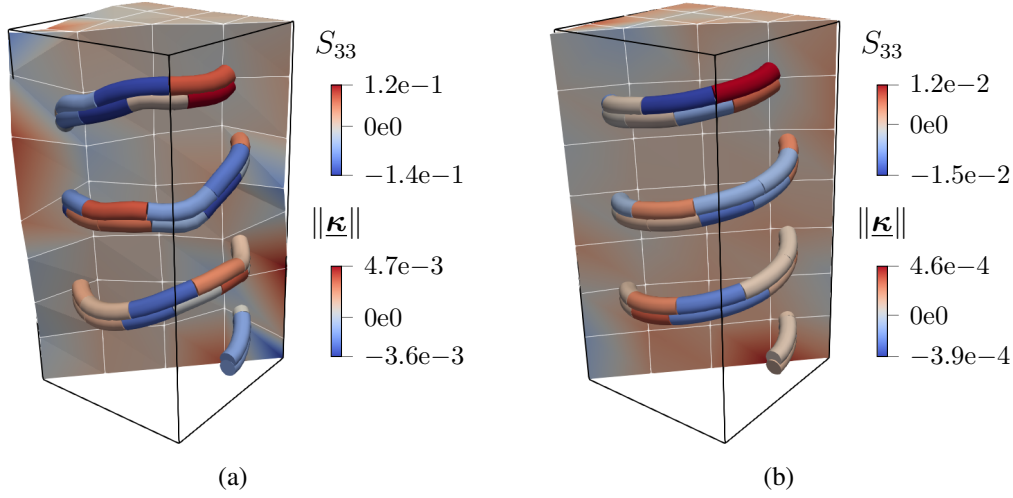


Figure 4.9.: Constant stress transfer test – results for overlapping helix-shaped beams. Deformed configurations are shown for element-based integration (a) and segment-based integration (b). The second Piola-Kirchhoff stress S_{33} is shown in the solid and the curvature κ at the middle of each beam element. Displacements of beams and solid are scaled with a factor of 50. Note that both beams Ω_1^B and Ω_2^B occupy the same spatial domain in the undeformed reference configuration. Figure is taken from the author’s article [135], permissions granted under the Creative Commons (CC BY) license.

mortar case. The discrete Lagrange multipliers should not be confused with discrete nodal loads on the beam element, as the Lagrange multiplier field is only integrated on the beam segment that resides inside the solid. This underlines the importance of segmentation at solid surfaces, i.e., proper treatment of strong discontinuities.

4.4.2. Spatial convergence

The following numerical example investigates the spatial convergence properties of the BTSV-POS method as well the validity of the evaluation of the coupling terms along the beam centerline instead of the beam surface, i.e., the fundamental mixed-dimensional 1D-3D modeling assumption. The considered problem is shown in Figure 4.11. It consists of a solid block with the dimensions $5\text{ m} \times 1\text{ m} \times 1\text{ m}$ and a hyperelastic Saint Venant–Kirchhoff material model ($E^S = 10\text{ N/m}^2$, $\nu^S = 0.0$). Embedded inside the solid block is a rod with the length 5 m . The beam is modeled as a torsion-free beam ($E^B = 4346\text{ N/m}^2$) with circular cross-section (radius $R = 0.125\text{ m}$). The parameters are chosen such that the rod and solid have the same bending stiffness around the \underline{e}_2 and \underline{e}_3 axes. At the left end surface of the solid block, displacements are fixed as are the rod displacements and rotations. At the right end, the rod is loaded with a moment $\underline{M} = -0.025\text{ Nm } \underline{e}_2$. No external loads are applied to the solid block.

The spatial convergence behavior of the various coupling methods will be analyzed with respect

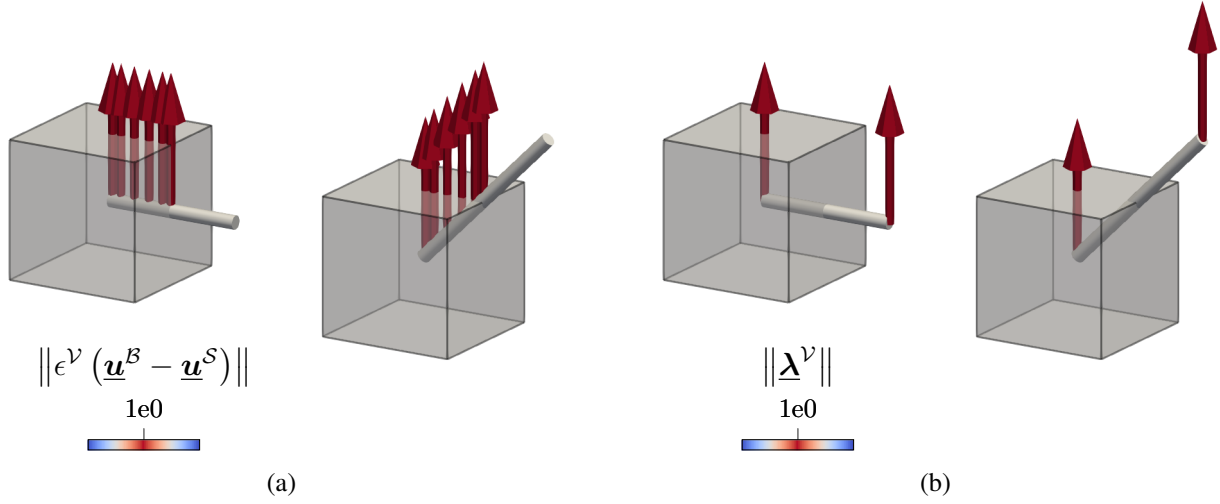


Figure 4.10.: Strong discontinuities – Gauss point-to-segment and mortar-type approach. Gauss point-to-segment approach with the negative coupling forces at the integration points (a) and mortar-type coupling with the negative discrete Lagrange multiplier traction vectors (b). Figure is taken from the author's article [135], permissions granted under the Creative Commons (CC BY) license.

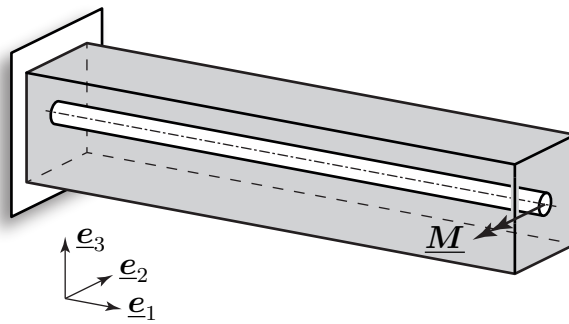


Figure 4.11.: Spatial convergence – problem setup of a coupled beam and solid structure. Figure is taken from the author's article [135], permissions granted under the Creative Commons (CC BY) license.

to the L_2 displacement error

$$\|e\|_{L_2} = \frac{1}{V_0} \sqrt{\int_{\Omega_0^S} \|\underline{\mathbf{u}}_h^S - \underline{\mathbf{u}}_{\text{ref}}^S\|^2 dV_0} + \frac{1}{L} \sqrt{\int_{\Omega_0^B} \|\underline{\mathbf{u}}_{r,h}^B - \underline{\mathbf{u}}_{r,\text{ref}}^B\|^2 ds}. \quad (4.25)$$

Here, $V_0 = 5 \text{ m}^3$ is the solid volume in the reference configuration and $L = 5 \text{ m}$ is the reference length of the beam. The error is computed relative to a reference finite element solution obtained with 2D-3D (surface-to-volume) coupling, cf. Appendix A. In all of the following results obtained with 2D-3D coupling, 6 Gauss–Legendre point in axial direction and 128 integration points in circumferential direction are used. This ensures a sufficiently accurate numerical evaluation of the 2D-3D coupling terms in order to hold as reference solution, and the chosen penalty parameter does not lead to unwanted stiffening effects. Since the derivations presented in Appendix A are stated for the general case of a Simo–Reissner beam, a slight modification has to be applied to deal with the torsion-free beam theory employed in this example, as the torsion-free beam theory inherently does not provide a unique beam cross-section triad. Considering that the present example exhibits a symmetry around the $\underline{\mathbf{e}}_1 - \underline{\mathbf{e}}_3$ plane, a unique beam triad can be constructed in a straight forward manner via $\underline{\mathbf{\Lambda}}^B = [\underline{\mathbf{t}}, \underline{\mathbf{e}}_2, \underline{\mathbf{t}} \times \underline{\mathbf{e}}_2]$, where $\underline{\mathbf{t}}$ is the normalized beam centerline tangent, i.e., $\underline{\mathbf{t}} = \underline{\mathbf{r}}' / \|\underline{\mathbf{r}}'\|$.

The solid block is meshed with first-order *hex8* solid elements, with an element size h^S . The rod is discretized with torsion-free beam finite elements with a length of $h^B = 2.5h^S$. The penalty parameter for all 1D-3D coupling methods is 100 N/m^2 , for 2D-3D GPTS coupling it is 100 N/m^3 . Additionally to the previously described integration rule for 2D-3D coupling, all 1D-3D coupling schemes in this example are evaluated with segment-based integration and 6 Gauss points per segment. The penalty parameter and the number of Gauss points are chosen according to Section 4.4.3 in order to avoid unwanted contact locking effects. For models purely consisting of either first-order solid or third-order beam elements, the expected convergence rate of the L_2 -error is $\mathcal{O}(h^2)$ and $\mathcal{O}(h^4)$, respectively. The expected optimal convergence rate for the coupled problem is thus the lower of the two, i.e., $\mathcal{O}(h^2)$. Figure 4.12 shows the convergence plot of the coupled structure with various coupling methods. The 2D-3D GPTS coupling scheme exhibits the expected optimal convergence rate of $\mathcal{O}(h^2)$ for the entire dataset. All 1D-3D coupling schemes behave very similar to each other. For coarse meshes, the expected optimal convergence order $\mathcal{O}(h^2)$ can be observed. At around $h^S = 0.12 \text{ m}$ the convergence behavior of all 1D-3D coupling methods has a kink, and for smaller element sizes the error does not decrease any further, it even slightly increases. The bottom right part of Figure 4.12 illustrates the solid mesh size compared to the beam cross-section at three different points in the convergence plot. In the case of a coupling along the beam surface (2D-3D), the beam interacts with all solid elements along its surface. In truly 1D-3D BTSV coupling, the beam only interacts with the solid elements along its centerline. For finer discretizations, the influence of the different interaction types becomes more evident, which materializes in the kink in the convergence plot. This behavior is expected, as the coupling interactions in the 1D-3D scheme represent a singular line load, which results in non-converging solutions for spatial mesh refinement [155]. This result gives rise to a very important finding, namely that the 1D-3D BTSV-POS coupling scheme is valid down to a certain element size, i.e., up to the kink in the convergence plot. Exemplarily, the beam tip displacement of the 2D-3D reference solution is 0.19009 m . With the 1D-3D BTSV-POS coupling method the tip displacement at the kink in the convergence plot (mesh B from Figure 4.12) is 0.18895 m ,

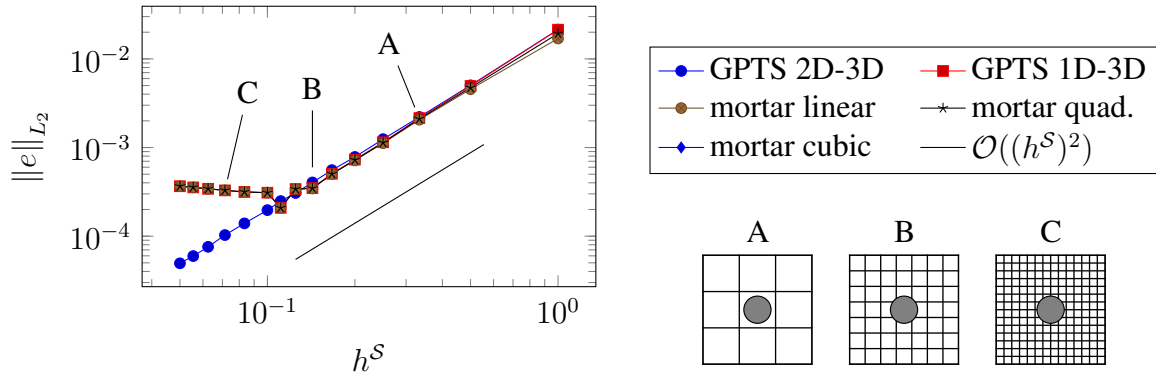


Figure 4.12.: Spatial convergence – error plots for various coupling methods. The details A-C illustrate the solid element size compared to the beam cross-section diameter at certain data points. Figure is taken from the author’s article [135], permissions granted under the Creative Commons (CC BY) license.

which amounts to a relative error of approximately 0.5%. The coupling interactions of the 2D-3D and 1D-3D schemes are shown in Figure 4.13. The critical solid element size, i.e., up to which the 1D-3D coupling is accurate, depends on a number of different parameters and can not be given in closed form. However, for the problems considered in this work, i.e., rather stiff beams and soft solids, a rule of thumb can be given: the solid element size should not be smaller than the beam cross-section diameter, cf. Section 3.2. Keeping in mind the envisaged applications, one can conclude that this does not pose any restrictions on the BTSV-POS methods, but is perfectly in line with their modeling goal.

4.4.3. Influence of the penalty parameter

In this example the analyzed problem is the same as in Section 4.4.2, now with a fixed solid element length $h^S = 0.25$ m. The model is simulated with various penalty parameters and BTS element length ratios. To quantify the differences between results obtained with various parameters, the L_2 -errors relative to the same reference solution as used in Section 4.4.2 are compared. The results are shown in Figure 4.14. Each of the four plots represents a fixed BTS element length ratio. The penalty parameter is plotted on the abscissa. The line style identifies the employed coupling scheme. For both element and segment-based integration, 6 integration points are used per element and segment, respectively. The desired behavior for an increasing penalty parameter is a convergence towards the exact fulfillment of the constraint equations, i.e., the solution of (4.19). In the presented plots, this corresponds to a horizontal line for high penalty parameters. For all element length ratios, the GPTS scheme with segment-based integration exhibits an increasing error for increasing penalty parameters. The GPTS scheme with element-based integration behaves better for high element length ratios, but as the beam length gets closer to the solid element size, the same behavior can be observed. This effect is sometimes referred to as contact locking and occurs due to an over-constraining of the system, i.e., too many discrete coupling constraints are enforced, and as a result, the coupling discretization becomes too stiff. Mathematically, this is related to a violation of the discrete inf-sup condition [24]. This

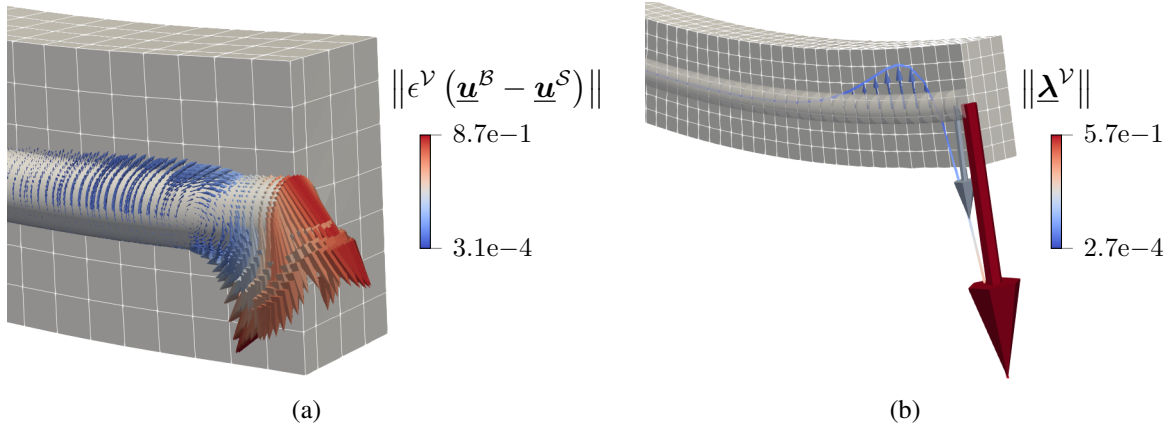


Figure 4.13.: Spatial convergence – coupling interactions. Gauss point coupling forces are shown for 2D-3D coupling (a) and the negative Lagrange multiplier field is shown for 1D-3D mortar-type (linear interpolation) coupling (b). The shown plots are for $h^S = 0.14$ m. Figure is taken from the author’s article [135], permissions granted under the Creative Commons (CC BY) license.

effect is especially distinct for GPTS schemes, where each Gauss point represents three coupling constraints, i.e., the number of discrete coupling constraints depends on the integration scheme used. A smaller number of Gauss points can usually improve the contact locking properties for GPTS schemes, but this in turn can lead to the non-fulfillment of the basic consistency tests given in Section 4.4.1. The BTSV-POS mortar schemes behave better: for element length ratios of 10 and 5 no locking can be observed at all. For smaller element length ratios the schemes with quadratic and cubic interpolation also show signs of contact locking. Linear interpolations of the Lagrange multipliers do not show such behavior for the considered element length ratios. By using a lower order interpolation of the Lagrange multipliers, the number of constraints is reduced, which explains the better behavior of the lower-order Lagrange multiplier interpolations regarding contact locking. The employed numerical integration scheme does not affect the contact locking behavior of mortar-type BTSV-POS coupling methods, as the number of coupling constraints is independent of the number of Gauss points used.

The results show that a GPTS-based coupling discretization tends to be prone to spurious contact locking effects. A linear interpolation of the Lagrange multipliers within a mortar-based coupling discretization, as suggested in this contribution, is the most robust coupling scheme regarding the choice of the penalty parameter.

4.4.4. Beam-to-solid element length ratio

In this example, the influence of the BTS element length ratio is investigated. Again, the analyzed problem setup is the same as in Section 4.4.2, but now with a fixed solid element length $h^S = 0.14$ m. The penalty parameter is 1000 N/m^2 , which, in combination with the linear interpolation of the Lagrange multipliers along the beam elements, does not lead to unwanted locking effects, cf. Section 4.4.3. The L_2 -error is computed compared to the same reference solution as used in Section 4.4.2. Figure 4.15 depicts the L_2 -error for various BTS element length

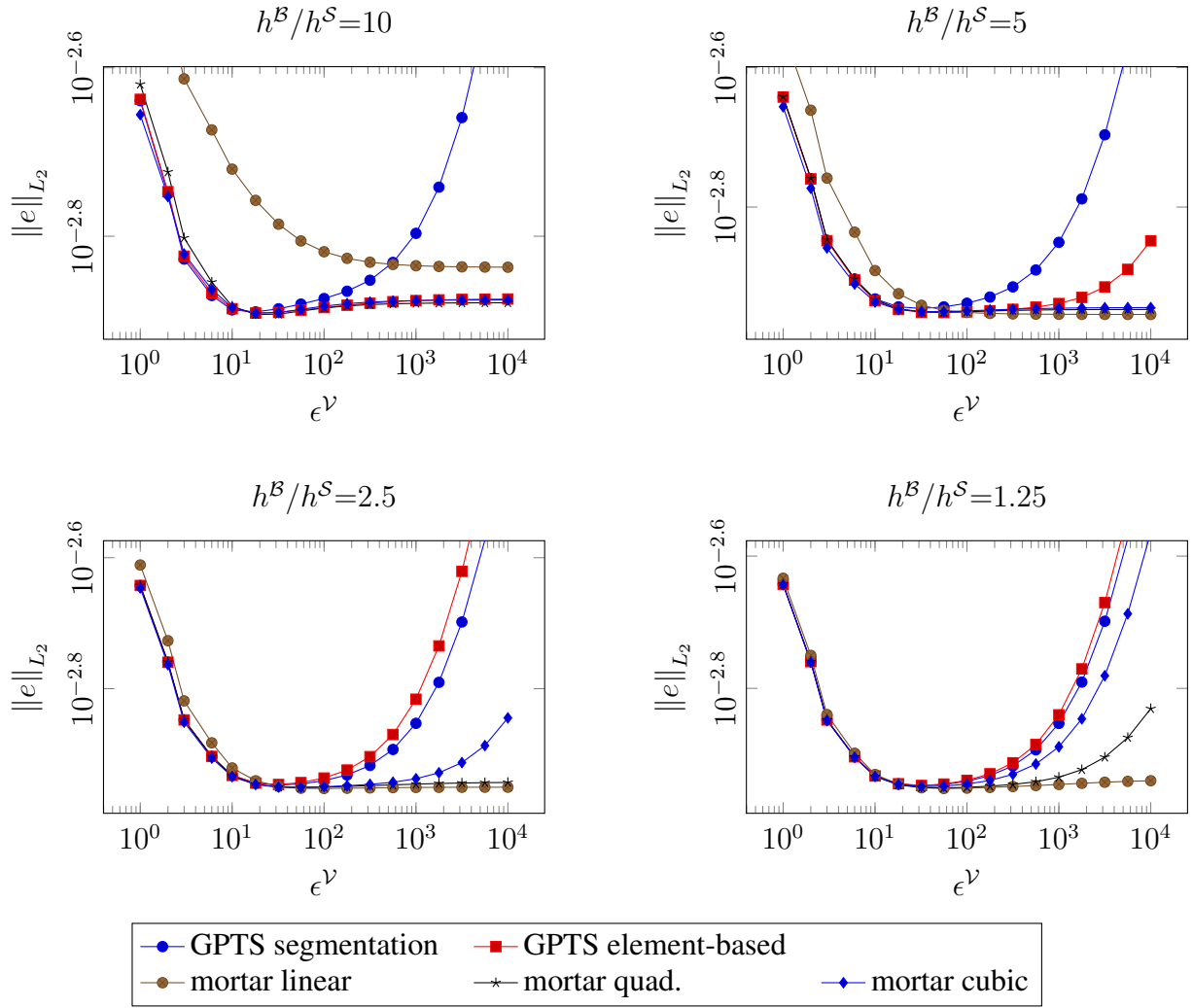


Figure 4.14.: Beam-to-solid element length ratio – L_2 -error for various parameter combinations and coupling schemes. Figure is taken from the author’s article [135], permissions granted under the Creative Commons (CC BY) license.

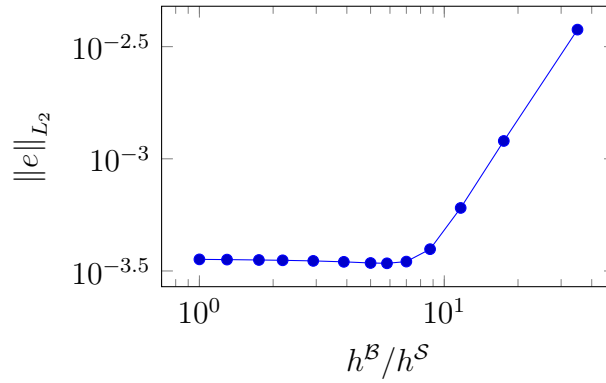


Figure 4.15.: Beam-to-solid element length ratio – L_2 -error for varying BTS element length ratios and linear interpolation of the Lagrange multipliers ($h^S = 0.14$ m). Figure is taken from the author’s article [135], permissions granted under the Creative Commons (CC BY) license.

ratios, and it can be seen that the error decreases for decreasing BTS element length ratios of about 5. For smaller ratios, i.e., even more beam elements, the error does not decrease any further. Thus, $h^B/h^S \approx 5$ can be interpreted as the tipping point, where the beam mesh is fine enough and the solid mesh has to be refined to further improve the solution. Moreover, this example illustrates the remarkable robustness of a linear interpolation of the Lagrange multipliers, since even for small BTS element length ratios, i.e., more constraint equations, no spurious locking can be observed. Obviously, this result is problem-dependent, nevertheless it allows for giving a first meaningful recommendation regarding the range of desirable BTS element length ratios for the BTSV-POS method, which should approximately be $h^B/h^S \in [2.5, 5.0]$.

4.4.5. Fiber-reinforced composite plate

In this final numerical example, a fiber-reinforced composite plate is modeled with the proposed BTSV-POS method and the results are compared to a homogenized approach, which employs a transversely isotropic material law as is common for laminate theory, cf. [149]. Figure 4.16 shows the problem setup of a two-layer composite plate. The plate has a length and width of 2 m and 1 m, respectively. The layer buildup is asymmetric: it consists of two layers with fiber directions of 45° and -45° , each with a thickness of 0.02 m. A hyperelastic Saint Venant–Kirchhoff material model ($E^S = 10$ N/m², $\nu^S = 0.3$) is used to model the matrix material. The fibers are modeled as torsion-free beams ($E^B = 1000$ N/m²) with circular cross-sections (radius $R = 0.045$ m). Figure 4.16 shows the fiber placement in the layers, which results in a fiber volume ratio of 0.25. At one of its short ends the plate is clamped in \underline{e}_1 and \underline{e}_3 direction, and a surface Neumann load p in \underline{e}_1 direction of 2.5 N/m² is applied at the other short end. The matrix is modeled with 288 eight-noded solid-shell elements [20, 147] and the fibers with 1498 torsion-free beam elements, respectively. On average, the BTS element length ratio is about 2.5. Mortar coupling with linear interpolation of the Lagrange multiplier shape functions and a penalty parameter of 1000 N/m is used to couple the beams to the solid. Segment-based integration is used to evaluate the coupling terms. All boundary conditions are exclusively applied to the solid-shell elements.

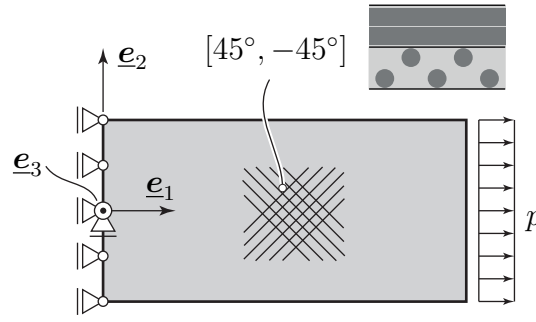


Figure 4.16.: Fiber-reinforced composite plate – problem setup. Figure is taken from the author’s article [135], permissions granted under the Creative Commons (CC BY) license.

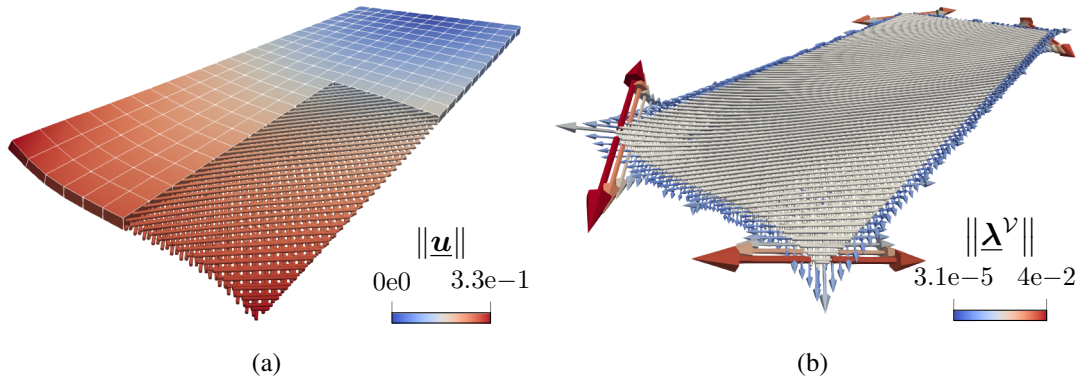


Figure 4.17.: Fiber-reinforced composite plate – deformed configuration (a) and negative discrete mortar coupling tractions (b) Figure is taken from the author’s article [135], permissions granted under the Creative Commons (CC BY) license.

Figure 4.17(a) shows the deformed plate, where for illustration purposes only three quarters of the solid elements are visualized. Due to its asymmetric layer buildup, the plate deforms out of the $e_1 - e_2$ plane, even though all applied loads and boundary conditions are exclusively in-plane. Figure 4.17(b) shows only the beam elements and a vector plot of the negative discrete nodal values of the coupling tractions calculated with (4.20). The largest coupling tractions occur at the boundary of the plate, especially at the corners. These coupling tractions will be used to gain insight on fiber pull-out and related composite damage phenomena in future research. Such information cannot be obtained at all from a homogenized theory.

The same plate is also modeled using a homogenized approach. Each layer is modeled with a transversely isotropic material, thus representing a homogenization of the fibers and matrix in that layer. As is common practice, the material properties for the transversely isotropic material are calculated according to a homogenization approach for linear strains, cf. [149]. For the nonlinear simulation of the plate, a combination of a purely isotropic hyperelastic material and a transversely orthotropic hyperelastic material is employed, cf. [26]. Each layer is modeled with 288 eight-noded solid-shell elements, thus resulting in a total of 576 finite elements for the homogenized model. In Figure 4.18, the deformations of the mid-plane at the right end ($e_1 = 2$ m) are compared to the results obtained with the BTSV-POS method. Only for larger loads, there is a

tiny discrepancy between the various methods, which can be attributed to a number of factors, e.g., the different strain measurements used in the beam and the homogenized solid, or small scale effects in the composite that can not be resolved by the continuum model. Nevertheless, the results are in excellent agreement with each other, which underlines the general applicability of the BTSV-POS method to fiber-reinforced composites.

Remark 4.5. The presented BTSV-POS model of the composite plate consists of 1,950 solid degrees of freedom and 10,992 (torsion-free) beam finite element degrees of freedom. This example can also be modeled with Kirchhoff–Love beam elements, which yields the same numerical results up to machine precision, due to exactly vanishing torsion [97]. However, the number of beam degrees of freedom for the Kirchhoff–Love model increases by about 30% to 14,322, thus justifying and encouraging the application of torsion-free beam element formulations if the underlying assumptions are met.

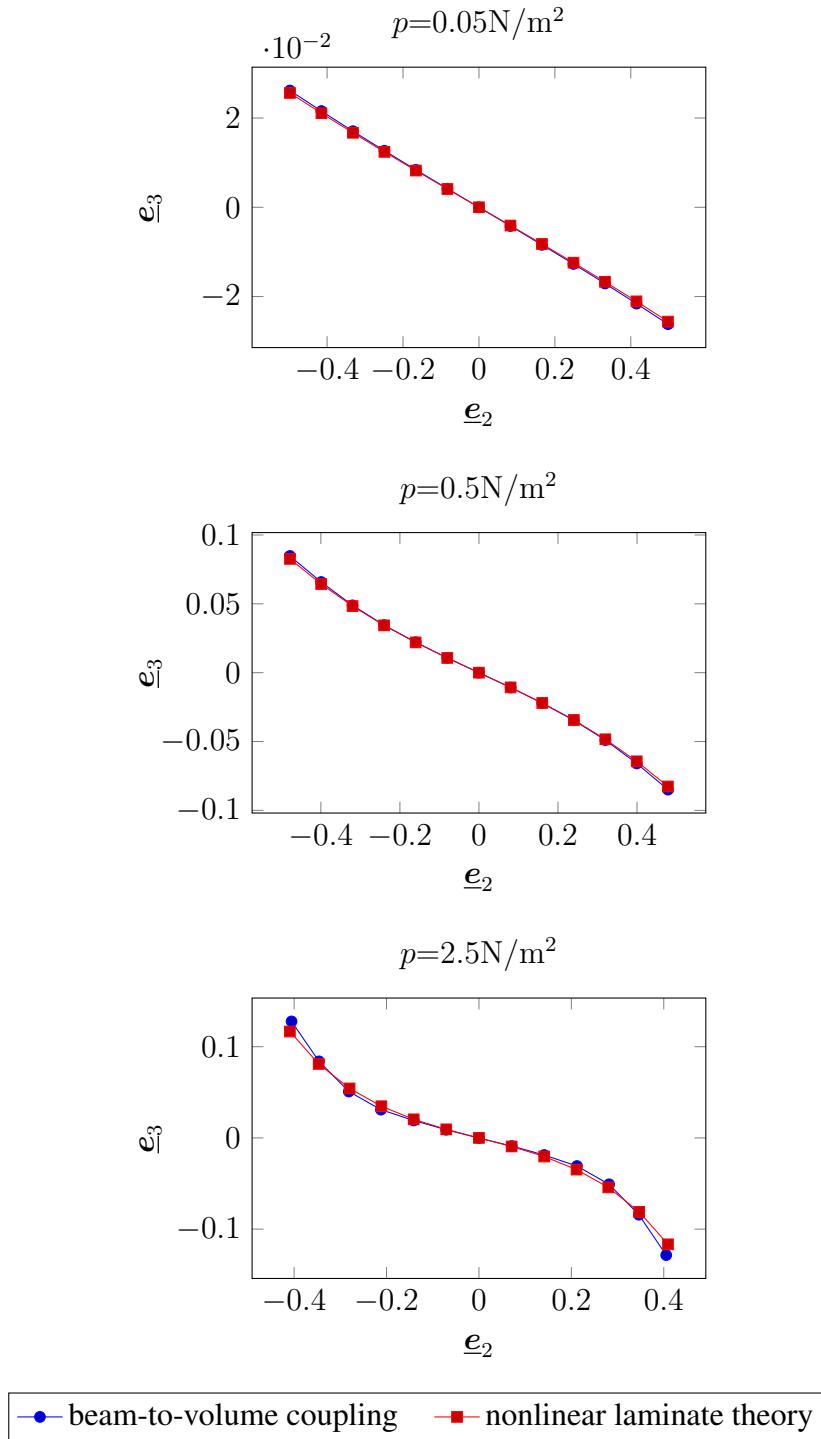


Figure 4.18.: Fiber-reinforced composite plate – deformed configurations of the mid-plane of the plate at various load values and for various modeling techniques. Figure is taken from the author’s article [135], permissions granted under the Creative Commons (CC BY) license.

5. Rotational beam-to-solid volume coupling

The class of applications considered in this thesis typically involves very slender fibers, which are modeled using the geometrically exact beam theory. Based on the fundamental kinematic assumption of undeformable cross-sections, such beam models can be identified as 1D Cosserat continua with six degrees of freedom defined at each centerline point to describe the cross-section position (three positional degrees of freedom) and orientation (three rotational degrees of freedom). In this chapter, the importance of rotational coupling, i.e., coupling between the orientation of a beam cross-section and the solid continuum, will be motivated. In the previous chapter the positional 1D-3D coupling (BTSV-POS) coupling scheme is presented, where only the beam centerline positions, but not the cross-section orientations, are coupled to the solid. In such models, an embedded fiber can still perform local twist/torsional rotations, i.e., cross-section rotations with respect to its centerline tangent vector, relative to the solid. While this simplified coupling procedure can reasonably describe the mechanics of certain problem classes where such relative rotations will rarely influence the global system response, e.g., embedding of straight fibers with circular cross-section shape, for many practical applications a more realistic description of the physical problem requires to also couple the rotations of beam and solid. The present chapter proposes a *full* 1D-3D beam-to-solid volume (BTSV-FULL) coupling approach, based on six, i.e., three positional *and* three rotational, coupling constraints between the cross-sections of 1D beams and a 3D solid. Most of the content of this chapter has previously been published in the author's article [138].

Consistently deriving the *full 1D-3D coupling* on the beam centerline from a *2D-3D coupling* formulation on the beam surface via a first-order Taylor series expansion of the solid displacement field would require to fully couple the two orthonormal directors spanning the (undeformable) beam cross-section with the (in-plane projection of the) solid deformation gradient evaluated at the cross-section centroid position. It is demonstrated that such an approach, which suppresses all in-plane deformation modes of the solid at the coupling point, might result in severe locking effects in the practically relevant regime of coarse solid mesh sizes. Therefore, various definitions of orthonormal triads are proposed that are representative for the orientation of material directions of the 3D continuum in an average sense, without additionally constraining in-plane deformation modes when coupled to the beam cross-section. It is shown that the rotation tensor defined by the polar decomposition of the (in-plane projection of the) deformation gradient appears as a natural choice for this purpose, which even represents the average orientation of material directions of the 3D continuum in a L_2 -optimal manner. Moreover, several alternative solid triad definitions are investigated that potentially allow for a more efficient numerical evaluation. Once these solid triads have been defined, objective (i.e., frame-invariant) rotational coupling constraints in the form of relative rotations are formulated for each pair of triads representing the beam and solid orientation. Their variationally consistent enforcement either based on a penalty potential

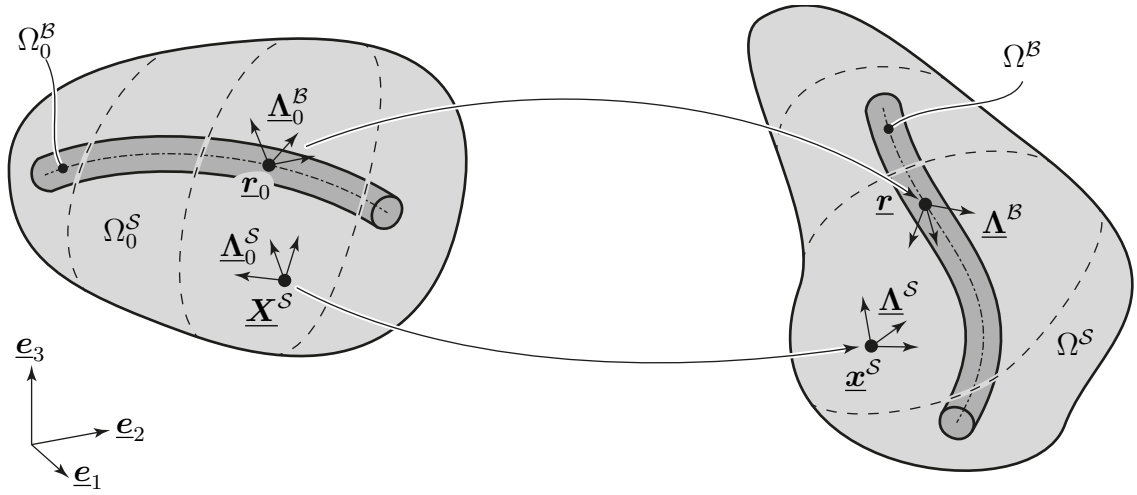


Figure 5.1.: Employed notations and relevant kinematic quantities defining the 3D finite deformation BTSV-FULL coupling problem. Figure is taken from the author's article [138], permissions granted under the Creative Commons (CC BY) license.

or a Lagrange multiplier potential, with an associated Lagrange multiplier field representing a distributed coupling moment along the beam centerline, is shown.

From a mechanical point of view, it is not desirable to only couple the beam cross-section orientations, i.e., for almost all types of applications, rotational coupling only makes sense in combination with positional coupling. In this thesis, rotational coupling is applied for beam-to-solid volume (BTSV) and beam-to-solid surface (BTSS) coupling problems. Without loss of generality, this chapter only considers BTSV coupling problems. However, the presented rotational coupling constraints can also be directly used in combination with positional BTSS coupling presented in the next chapter. Therein a modified construction of the solid triad field, taking advantage of the kinematic description of the solid surface, is advantageous and is resented in Section 6.2.

5.1. Problem formulation

We consider a 3D finite deformation full beam-to-solid volume (BTSV-FULL) coupling problem as shown in Figure 5.1. In the proposed BTSV-FULL method, the point-wise six degrees of freedom associated with the beam centerline positions and cross-section triads are coupled to the surrounding solid, i.e.,

$$\underline{\mathbf{r}} - \underline{\mathbf{x}}_r^S = \underline{\mathbf{0}} \quad \text{on} \quad \Gamma_c \quad (5.1)$$

$$\underline{\psi}_{SB} = \underline{\mathbf{0}} \quad \text{on} \quad \Gamma_c. \quad (5.2)$$

Herein, $\Gamma_c = \Omega_0^S \cap \Omega_0^B$ is the one-dimensional coupling domain between the beam centerline and the solid volume, i.e., the part of the beam centerline that lies within the solid. Furthermore, let us recall the definition of $\underline{\mathbf{x}}_r^S$ from the previous chapter, which denotes the line of material solid points that coincide with the beam centerline in the current configuration, i.e., $\underline{\mathbf{x}}_r^S = \underline{\mathbf{r}}$. The rotational

coupling between beam cross-section and solid as presented in this section is in close analogy to the generalized cross-section interaction laws proposed in [94]. The rotation vector $\underline{\psi}_{SB}$ describes the relative rotation between a beam cross-section triad $\underline{\Lambda}^B$ and a corresponding triad $\underline{\Lambda}^S$ associated with the current solid configuration,

$$\underline{\psi}_{SB} = \text{rv} \left(\underline{\Lambda}^S \underline{\Lambda}^{B^T} \right). \quad (5.3)$$

Opposite to $\underline{\Lambda}^B$, which is well defined along the beam centerline, there is no obvious or unique definition for $\underline{\Lambda}^S$ in the solid domain. In Section 5.2, various definitions of the solid triad $\underline{\Lambda}^S$ are presented and investigated. However, for the derivation of the coupling equations, it is sufficient to assume the general form $\underline{\Lambda}^S = \underline{\Lambda}^S(\underline{F})$, i.e., formulating the solid triad as a general function of the solid deformation gradient in the current configuration.

The formulation of the constraint equations along the beam centerline brings about an advantageous property of the BTSV-FULL method: the positional (5.1) and rotational (5.2) coupling constraints are completely decoupled. Therefore, the rotational coupling equations (5.2) can be interpreted as a direct extension to the BTSV-POS method, which only couples the beam centerline positions to the solid as derived and thoroughly discussed in Chapter 4. Thus, the total virtual work of the BTSV-FULL problem is

$$\delta W^S + \delta W_{SR}^B + \delta \Pi_\lambda^\nu + \delta \Pi_{(\cdot)}^\mathcal{R} = 0, \quad (5.4)$$

where δW^S and δW_{SR}^B are the virtual work of the solid domain and beam domain, respectively. It is important to point out, that in this thesis only the Simo–Reissner beam theory is considered in combination with rotational coupling. The positional coupling constraints are added to the total virtual work via the variation of the positional Lagrange multiplier potential $\delta \Pi_\lambda^\nu$, cf. (4.8). Finally, $\delta \Pi_{(\cdot)}^\mathcal{R}$ is the virtual work contribution of the rotational coupling constraints. In what follows, two different constraint enforcement strategies for the rotational coupling conditions will be presented.

5.1.1. Penalty potential

Let us consider a quadratic space-continuous penalty potential between beam cross-section triads and solid triads defined along the beam centerline:

$$\Pi_\epsilon^\mathcal{R} = \int_{\Gamma_c} \tilde{\Pi}_\epsilon^\mathcal{R} \, ds = \int_{\Gamma_c} \frac{1}{2} \underline{\psi}_{SB}^T \underline{c} \underline{\psi}_{SB} \, ds, \quad (5.5)$$

with the cross-section coupling potential $\tilde{\Pi}_\epsilon^\mathcal{R} = \tilde{\Pi}_\epsilon^\mathcal{R}(s)$ and the symmetric penalty tensor $\underline{c} \in \mathbb{R}^{3 \times 3}$. Variation of the penalty potential leads to the following contribution to the weak form:

$$\delta \Pi_\epsilon^\mathcal{R} = \int_{\Gamma_c} \frac{\partial \tilde{\Pi}_\epsilon^\mathcal{R}}{\partial \underline{\psi}_{SB}} \delta_o \underline{\psi}_{SB} \, ds = \int_{\Gamma_c} \left(\delta_o \underline{\psi}_{SB} \right)^T \underline{c} \underline{\psi}_{SB} \, ds. \quad (5.6)$$

Therein, $\delta_o \underline{\psi}_{SB}$ is the objective variation of the rotation vector $\underline{\psi}_{SB}$. Making use of (2.18), the variation of the total potential becomes, cf. [94],

$$\delta \Pi_\epsilon^\mathcal{R} = \int_{\Gamma_c} (\delta \underline{\theta}^S - \delta \underline{\theta}^B)^T \underline{T}^T(\underline{\psi}_{SB}) \underline{c} \underline{\psi}_{SB} \, ds, \quad (5.7)$$

where $\delta\theta^S$ and $\delta\theta^B$ are multiplicative variations associated with the solid and beam triad, respectively. In this section, penalty tensors of the form $\underline{c} = \epsilon^R \underline{I}$ with a scalar penalty parameter $\epsilon^R \in \mathbb{R}^+$ with physical unit Nm/m are considered. With this definition and the identity $\underline{T}^T(\underline{\psi})\underline{\psi} = \underline{\psi}$ (cf. Remark 2.1) the variation of the penalty potential simplifies to

$$\delta\Pi_\epsilon^R = \epsilon^R \int_{\Gamma_c} (\delta\theta^S - \delta\theta^B)^T \underline{\psi}_{SB} ds. \quad (5.8)$$

It is well-known from the geometrically exact beam theory that the (multiplicative) virtual rotations $\delta\theta^B$ are work-conjugated to the moment stress resultants. Therefore, $\epsilon^R \underline{\psi}_{SB}$ can be directly interpreted as the (negative) coupling moment acting on the beam cross-section.

5.1.2. Lagrange multiplier potential

Alternatively, the Lagrange multiplier method can be employed to impose the rotational coupling constraints. A Lagrange multiplier field $\underline{\lambda}^R = \underline{\lambda}^R(s) \in \mathbb{R}^3$ is therefore defined on the coupling curve Γ_c . For now, this field is a purely mathematical construct in the sense of generalized coupling forces associated with the coupling conditions (5.2). The Lagrange multiplier potential for the rotational coupling is

$$\Pi_\lambda^R = \int_{\Gamma_c} \underline{\lambda}^{RT} \underline{\psi}_{SB} ds. \quad (5.9)$$

Variation of the Lagrange multiplier potential again leads to a constraint contribution to the weak form, i.e.,

$$\delta\Pi_\lambda^R = \underbrace{\int_{\Gamma_c} \delta\underline{\lambda}^{RT} \underline{\psi}_{SB} ds}_{\delta W_\lambda^R} + \underbrace{\int_{\Gamma_c} \underline{\lambda}^{RT} \delta_o \underline{\psi}_{SB} ds}_{-\delta W_c^R}. \quad (5.10)$$

Therein, δW_λ^R and δW_c^R are the variational form of the coupling constraints and the virtual work of the generalized coupling forces $\underline{\lambda}^R$, respectively. With (2.18) the virtual work of the generalized coupling forces becomes

$$-\delta W_c^R = \int_{\Gamma_c} (\delta\theta^S - \delta\theta^B)^T \underline{T}^T(\underline{\psi}_{SB}) \underline{\lambda}^R ds. \quad (5.11)$$

Since the multiplicative rotation variations $\delta\theta^B$ are work-conjugated to the moment stress resultants of the beam, the term $-\underline{T}^T(\underline{\psi}_{SB}) \underline{\lambda}^R$ can be interpreted as a distributed coupling moment acting along the beam centerline.

Remark 5.1. For a vanishing relative rotation $\underline{\psi}_{SB} = \underline{0}$, as enforced in the space-continuous problem setting according to (5.2), the identity $-\underline{T}^T(\underline{\psi}_{SB}) = \underline{I}$ holds true and the rotational Lagrange multipliers exactly represent the coupling moments along the beam centerline. However, for the discretized problem this is only an approximation.

5.1.3. Objectivity of full beam-to-solid volume coupling

As indicated above, the solid triad field depends on the solid deformation gradient \underline{F} . It can easily be shown, that the presented solid triad definitions STR-POL, STR-AVG and STR-ORT, in Section 5.2 are objective with respect to an arbitrary rigid body rotation $\underline{R}^* \in SO^3$, i.e.,

$$\underline{\Lambda}^{\mathcal{S}*} = \underline{\Lambda}^{\mathcal{S}}(\underline{R}^* \underline{F}) = \underline{R}^* \underline{\Lambda}^{\mathcal{S}}(\underline{F}). \quad (5.12)$$

The geometrically exact beam model employed in this thesis is also objective [96, 99], i.e.,

$$\underline{\Lambda}^{\mathcal{B}*} = \underline{R}^* \underline{\Lambda}^{\mathcal{B}}. \quad (5.13)$$

Equations (5.12) and (5.13) inserted into the definition of the relative beam-to-solid rotation vector according to (5.3) gives the rotated relative rotation vector,

$$\underline{\psi}_{SB}^* = \text{rv}(\underline{R}^* \underline{\Lambda}^{\mathcal{S}} \underline{\Lambda}^{\mathcal{B}\text{T}} \underline{R}^{*\text{T}}) = \underline{R}^* \underline{\psi}_{SB}, \quad (5.14)$$

where the identity $\text{rv}(\underline{R}^* \underline{\Lambda} \underline{R}^{*\text{T}}) = \underline{R}^* \text{rv}(\underline{\Lambda})$ has been used. Thus, the rotational coupling conditions (5.2) in combination with the proposed solid triad definitions and the employed geometrically exact beam models are objective. As shown in [94], in this case also an associated penalty potential of type (5.5) or an associated Lagrange multiplier potential of type (5.9) is objective.

The previous considerations show objectivity of the proposed (space-continuous) 1D-3D coupling approaches. However, in the realm of the finite element method, cf. Section 5.3, it is important to demonstrate that objectivity is preserved also in the discrete problem setting. It is well known that the discretized deformation gradient, as required for the definition of solid triads, is objective as long as standard discretization schemes (e.g., via Lagrange polynomials) are applied to the displacement field of the solid. Also the employed beam finite element formulation based on the geometrically exact beam theory is objective, even though this topic is not trivial and the interested reader is referred to [96, 99]. Therefore, it can be concluded that the proposed 1D-3D coupling schemes are objective for the space-continuous as well as for the spatially discretized problem setting.

Remark 5.2. Objectivity is the main reason for formulating the rotational coupling constraints in (5.2) based on the relative rotation vector, i.e., $\underline{\psi}_{SB} = \underline{0}$, cf. [94]. As alternative choice for the rotational coupling constraints the difference between the beam and solid triad rotation vectors, i.e., $\underline{\psi}^{\mathcal{B}} - \underline{\psi}^{\mathcal{S}} = \underline{0}$, could be considered. However, such coupling constraints would result in a non-objective coupling formulation [94].

5.2. Definition of solid triad field

One of the main aspects of the present chapter is the definition of a suitable right-handed orthonormal triad field $\underline{\Lambda}^{\mathcal{S}}$ in the solid, which is required for the coupling constraint (5.2). This is by no means a straightforward choice, and different triad definitions will lead to different properties of the resulting numerical coupling scheme. In the following, a brief motivation will be given for the concept of solid triads before various solid triad definitions will be proposed.

5.2.1. Motivation of the solid triad concept

If the embedded beam is considered as a 3D body, a consistent 2D-3D coupling constraint between the 2D beam surface and the surrounding 3D solid can be formulated as

$$\underline{\mathbf{x}}^B - \underline{\mathbf{x}}^S = \underline{\mathbf{0}} \quad \text{on} \quad \Gamma_{c,2D-3D}. \quad (5.15)$$

Therein, $\Gamma_{c,2D-3D}$ is the 2D-3D coupling surface, i.e., the part of the beam surface that lies within the solid volume. In the following, $\underline{\mathbf{\Lambda}}_0^S = [\underline{\mathbf{g}}_{1,0}^S, \underline{\mathbf{g}}_{2,0}^S, \underline{\mathbf{g}}_{3,0}^S]$ shall represent material directions of the solid that coincide with the beam triad in the reference configuration according to

$$\underline{\mathbf{\Lambda}}_0^S = \underline{\mathbf{\Lambda}}_0^B. \quad (5.16)$$

The corresponding triad in the deformed configuration is denoted as $\underline{\mathbf{\Lambda}}^S$. Let us now expand the position field in the solid as Taylor series around $\underline{\mathbf{x}}_r^S$, i.e.,

$$\underline{\mathbf{x}}^S = \underline{\mathbf{x}}_r^S + \underline{\mathbf{F}} \Delta \underline{\mathbf{X}} + \mathcal{O}(R^2), \quad (5.17)$$

where $\underline{\mathbf{F}}$ is the deformation gradient of the solid according to (2.2). The 1D-3D coupling strategy underlying the proposed BTSV-FULL scheme relies on the basic assumption of slender beams, i.e., $R \ll L$, where R is a characteristic cross-section dimension (e.g., the radius of circular cross-sections). Therefore, it only small increments $\Delta \underline{\mathbf{X}} = \alpha \underline{\mathbf{g}}_{2,0}^S + \beta \underline{\mathbf{g}}_{3,0}^S$, with $\alpha, \beta \leq R$, are considered:

$$\underline{\mathbf{x}}^S \approx \underline{\mathbf{x}}_r^S + \alpha \underline{\mathbf{g}}_2^S + \beta \underline{\mathbf{g}}_3^S. \quad (5.18)$$

Here, the directors $\underline{\mathbf{g}}_2^S$ and $\underline{\mathbf{g}}_3^S$, which are not orthonormal in general, represent the push-forward of the solid directions $\underline{\mathbf{g}}_{2,0}^S$ and $\underline{\mathbf{g}}_{3,0}^S$, i.e.,

$$\underline{\mathbf{g}}_i^S := \underline{\mathbf{F}} \underline{\mathbf{g}}_{i,0}^S \quad \text{for} \quad i = 2, 3. \quad (5.19)$$

In the previous chapter, the Taylor expansion of (5.15) is truncated after the constant term, thus resulting in purely positional coupling. In this chapter, the Taylor series is truncated after the linear term which results in an error of order $\mathcal{O}(R^2)$. It follows from (2.20) and (5.18) that the 2D-3D coupling conditions (5.15) between the beam surface and the expanded solid position field are exactly fulfilled if the following 1D-3D coupling constraints are satisfied:

$$\underline{\mathbf{x}}_r^S = \underline{\mathbf{r}}, \quad (5.20)$$

$$\underline{\mathbf{g}}_2^S = \underline{\mathbf{g}}_2^B, \quad \underline{\mathbf{g}}_3^S = \underline{\mathbf{g}}_3^B. \quad (5.21)$$

Coupling constraints of the form (5.21) enforce that the material fibers $\underline{\mathbf{g}}_2^S$ and $\underline{\mathbf{g}}_3^S$ of the solid remain orthonormal during deformation, thus enforcing vanishing in-plane strains of the solid at the coupling point $\underline{\mathbf{x}}_r^S = \underline{\mathbf{r}}$. In Section 5.4, it will be demonstrated that constraints of this type lead to severe locking effects when applied to finite element discretizations that are relevant for the proposed BTSV-FULL scheme, i.e., solid mesh sizes that are larger than the beam cross-section dimensions. It will be demonstrated that such locking effects can be avoided if the solid triad field is defined in a manner that only captures the purely rotational contributions to the local solid deformation at $\underline{\mathbf{x}}_r^S = \underline{\mathbf{r}}$ without additionally constraining the solid directors in the deformed

Table 5.1.: Listing of the various solid triad variants presented in this chapter.

solid triad	description
STR-POL	obtained from the polar decomposition of the solid deformation gradient
STR-DIR _{2/3}	fix one chosen solid material direction to the solid triad
STR-AVG	fix average of two solid material directions to the solid triad
STR-ORT	orthogonal solid material directions stay orthogonal

configuration. As will be demonstrated in the next sections, the rotation tensor defined by the polar decomposition of the deformation gradient is an obvious choice for this purpose, but also alternative solid triad definitions are possible. Table 5.1 gives an overview of the solid triad variants proposed in the following.

All of these solid triad definitions $\underline{\Lambda}^S = [\tilde{\underline{g}}_1^S, \tilde{\underline{g}}_2^S, \tilde{\underline{g}}_3^S]$ will be a function of the solid deformation gradient \underline{F} , i.e., $\underline{\Lambda}^S = \underline{\Lambda}^S(\underline{F})$. Moreover, all solid triad definitions will be constructed in a manner such that the associated orthonormal base vectors $\tilde{\underline{g}}_2^S$ and $\tilde{\underline{g}}_3^S$ represent the effective rotation of the non-orthonormal directors \underline{g}_2^S and \underline{g}_3^S in an average sense. Thus, it will be required that $\tilde{\underline{g}}_2^S$ and $\tilde{\underline{g}}_3^S$ lie within a plane defined by the normal vector

$$\underline{n} = \frac{\underline{g}_2^S \times \underline{g}_3^S}{\|\underline{g}_2^S \times \underline{g}_3^S\|}, \quad (5.22)$$

in the following denoted as the \underline{n} -plane. Eventually, in the examples in Section 5.4, two desirable properties of the solid triad field for the proposed BTSV-FULL method are identified:

- (i) The solid triad should be invariant, i.e., symmetric / unbiased with respect to the reference in-plane beam cross-section basis vectors $\underline{g}_{2,0}^B$ and $\underline{g}_{3,0}^B$.
- (ii) The resulting BTSV-FULL method should not lead to locking effects in the spatially discretized coupled problem.

These properties will be investigated for the following solid triad definitions.

5.2.2. Polar decomposition of the deformation gradient

In [127], variational formulations for classical non-linear elasticity are presented, where the rotational field is considered as an independent variable. For three-dimensional solids, the rotational field is defined as the rotation tensor from the polar decomposition of the solid deformation gradient. Based on polar decomposition (2.6), the deformation gradient of the solid problem can be split into a product $\underline{F} = \underline{v}\underline{R}^S = \underline{R}^S\underline{U}$ consisting of a rotation tensor $\underline{R}^S \in SO^3$ and a (spatial or material) positive definite symmetric tensor \underline{v} or \underline{U} , respectively, which describes the stretch. An explicit calculation rule for the rotation tensor, e.g., based on \underline{v} , can be stated as:

$$\underline{v}^2 = \underline{F}\underline{F}^T, \quad (5.23)$$

$$\underline{R}^S = \underline{v}^{-1}\underline{F}. \quad (5.24)$$

As mentioned above, it is desirable that the orthonormal base vectors $\tilde{\underline{g}}_2^S$ and $\tilde{\underline{g}}_3^S$ of the solid triad $\underline{\Lambda}^S$ lie in a plane with normal vector \underline{n} according to (5.22). It can easily be verified that the rotation tensor \underline{R}^S associated with the total deformation gradient \underline{F} according to (5.24) will in general not satisfy this requirement. Thus, a modification will be presented in the following to preserve this property.

5.2.2.1. Construction of polar decomposition-based solid triad

Since the sought-after solid triad shall be uniquely defined already by the two in-plane directors \underline{g}_2^S and \underline{g}_3^S , a modified version of the deformation gradient will be considered,

$$\underline{F}_{\underline{n}} = \underline{n} \otimes \underline{g}_{1,0}^S + \underline{g}_2^S \otimes \underline{g}_{2,0}^S + \underline{g}_3^S \otimes \underline{g}_{3,0}^S, \quad (5.25)$$

which consists of the projection of the total deformation gradient \underline{F} into the \underline{n} -plane extended by the additional term $\underline{n} \otimes \underline{g}_{1,0}^S$. This modified deformation gradient ensures that the two relevant in-plane basis vectors are correctly mapped, i.e., $\underline{g}_2^S = \underline{F}_{\underline{n}} \underline{g}_{2,0}^S$ and $\underline{g}_3^S = \underline{F}_{\underline{n}} \underline{g}_{3,0}^S$, while the third basis vector, which is not relevant for the proposed coupling procedure, is mapped onto the normal vector of the \underline{n} -plane, i.e., $\underline{n} = \underline{F}_{\underline{n}} \underline{g}_{1,0}^S$. This specific definition of a deformation gradient allows for the following multiplicative split:

$$\underline{F}_{\underline{n}} = \underline{F}_{2D} \underline{R}_{\underline{n}}, \quad (5.26)$$

where $\underline{R}_{\underline{n}}$ describes the (pure) rotation from the initial solid triad $\underline{\Lambda}_0^S$ onto a (still to be defined) orthonormal intermediate triad $\bar{\underline{\Lambda}} = [\bar{\underline{g}}_1, \bar{\underline{g}}_2, \bar{\underline{g}}_3]$, whose base vectors $\bar{\underline{g}}_2$ and $\bar{\underline{g}}_3$ lie within the \underline{n} -plane, and \underline{F}_{2D} represents a (quasi-2D) in-plane deformation between $\bar{\underline{g}}_2$ and $\bar{\underline{g}}_3$ and the non-orthonormal base vectors \underline{g}_2^S and \underline{g}_3^S . Now, by applying the polar decomposition only to the in-plane deformation, i.e.,

$$\underline{F}_{2D} = \underline{v}_{2D} \underline{R}_{2D}^S, \quad (5.27)$$

a solid triad can be defined from the initial triad $\underline{\Lambda}_0^S$ as:

$$\underline{\Lambda}_{\text{POL}}^S = \underline{R}_{2D}^S \underline{R}_{\underline{n}} \underline{\Lambda}_0^S. \quad (5.28)$$

Once an intermediate triad $\bar{\underline{\Lambda}}$ is defined, the required rotation tensors \underline{R}_{2D}^S and $\underline{R}_{\underline{n}}$ can be calculated as follows:

1. $\underline{R}_{\underline{n}} = \bar{\underline{\Lambda}} (\underline{\Lambda}_0^S)^T$,
2. $\underline{F}_{2D} = \underline{F}_{\underline{n}} (\underline{R}_{\underline{n}})^T$,
3. $(\underline{v}_{2D})^2 = \underline{F}_{2D} (\underline{F}_{2D})^T$,
4. $\underline{R}_{2D}^S = (\underline{v}_{2D})^{-1} \underline{F}_{2D}$.

The last remaining question is the definition of the triad $\bar{\underline{\Lambda}}$. It can be shown that the choice of this triad is arbitrary and does not influence the result, since a corresponding in-plane rotation offset would be automatically considered/compensated (in the sense of a superposed rigid body rotation) via the rotational part \underline{R}_{2D}^S of the in-plane polar decomposition (5.27). For example, a simple choice is given by $\bar{\underline{g}}_1 = \underline{n}$, $\bar{\underline{g}}_2 = \underline{g}_2^S / \|\underline{g}_2^S\|$ and $\bar{\underline{g}}_3 = \underline{n} \times \bar{\underline{g}}_2$, which coincides with the solid triad definition later discussed in Section 5.2.3.1.

Remark 5.3. It can be verified that $\underline{\mathbf{R}}^S = \underline{\mathbf{R}}_{2D}^S \underline{\mathbf{R}}_n$ is fulfilled for quasi-2D deformation states, e.g., for pure torsion load cases where the beam axis remains straight during the entire deformation (see example in Section 5.4.5). In this case, the (simpler) polar decomposition of the total deformation gradient $\underline{\mathbf{F}}$ according to (5.24) can be exploited.

5.2.2.2. Properties of polar decomposition-based solid triad

In contrast to alternative solid triad definitions that will be investigated in the following sections, the definition according to (5.28), referred to as STR-POL or by the subscript $(\cdot)_{\text{POL}}$, is not biased by an ad-hoc choice of material directors in the solid that are coupled to the beam. Instead, the rotation tensor $\underline{\mathbf{R}}^S$ describes the rotation of material directions coinciding with the principle axes of the deformation (i.e., it maps the principle axes from the reference to the spatial configuration), which has two important implications. First, the choice of material directions that are coupled depend on the current deformation state and will in general vary in time. Second, the principle axes represent an orthonormal triad per definition, and, thus the coupling to the beam triad will not impose any constraints on the local in-plane deformation of the solid. Consequently, this solid triad variant fulfills both requirements (i) and (ii) as stated above.

Eventually, a further appealing property of the STR-POL triad shall be highlighted. Let $\theta_0 \in [-\pi, \pi]$ represent the orientation of arbitrary in-plane directors in the reference configuration defined to coincide for solid and beam according to $\underline{\mathbf{g}}_0^S(\theta_0) = \underline{\mathbf{g}}_0^B(\theta_0) = \cos(\theta_0)\underline{\mathbf{g}}_{2,0}^B + \sin(\theta_0)\underline{\mathbf{g}}_{3,0}^B$. Their push-forward is given by $\underline{\mathbf{g}}^S(\theta^S(\theta_0)) = \underline{\mathbf{F}}_n \underline{\mathbf{g}}_0^S(\theta_0)$ for the solid and $\underline{\mathbf{g}}^B(\theta^B(\theta_0)) = \underline{\mathbf{R}}^B \underline{\mathbf{g}}_0^B(\theta_0)$ for the beam, where the angles $\theta^S \in [-\pi, \pi]$ and $\theta^B \in [-\pi, \pi]$ represent the corresponding in-plane orientations in the deformed configuration (see Appendix B for a detailed definition). Since in-plane shear deformation is permissible for the solid but not for the beam, the orientations $\theta^S(\theta_0)$ and $\theta^B(\theta_0)$ cannot be identical for all $\theta_0 \in [-\pi, \pi]$ and arbitrary deformation states. However, as demonstrated in Appendix B, when coupling the beam triad to the STR-POL triad according to (5.28), the beam directors $\underline{\mathbf{g}}^B(\theta^B(\theta_0))$ represent the orientation of the solid directors $\underline{\mathbf{g}}^S(\theta^S(\theta_0))$ in an average sense such that the following L_2 -norm is minimized:

$$\int_{-\pi}^{\pi} (\theta^S(\theta_0) - \theta^B(\theta_0))^2 d\theta_0 \rightarrow \min. \quad \text{for } \underline{\Lambda}^B = \underline{\Lambda}_{\text{POL}}^S. \quad (5.29)$$

In conclusion, STR-POL is an obvious choice for the solid triad with many favorable properties, e.g., it represents the average orientation of material solid directions in a L_2 -optimal manner. However, it requires the calculation of the square root of a tensor, and more importantly, for latter variation and linearization procedures also the first and second derivatives of the tensor square root with respect to the solid degrees of freedom. This results in considerable computational costs, since this operation has to be performed at local Gauss point level. Therefore, alternative solid triad definitions will be proposed in the following that can be computed more efficiently, while still being able to represent global system responses with sufficient accuracy.

5.2.3. Alternative solid triad definitions

All solid triad variants considered in the following rely on the non-orthonormal solid directors \underline{g}_2^S and \underline{g}_3^S according to (5.19), their normalized counterparts

$$\underline{g}'_i := \frac{\underline{g}_i^S}{\|\underline{g}_i^S\|} \quad \text{for } i = 2, 3 \quad (5.30)$$

and the corresponding normal vector \underline{n} according to (5.22). Based on these definitions, three different variants will be exemplified in the following.

5.2.3.1. Fixed single solid director

In the first variant, denoted as STR-DIR_{2/3}, the orientation of one single solid director, either \underline{g}'_2 or \underline{g}'_3 , is fixed to the solid triad, cf. Figure 5.2(b). The choice which solid material direction to couple is arbitrary. Therefore, two variants will be distinguished:

$$\underline{\Lambda}_{\text{DIR}_2}^S = [\underline{n}, \underline{g}'_2, \underline{n} \times \underline{g}'_2] \quad (5.31)$$

$$\underline{\Lambda}_{\text{DIR}_3}^S = [\underline{n}, \underline{g}'_3 \times \underline{n}, \underline{g}'_3], \quad (5.32)$$

Since the variant STR-DIR_{2/3} does not fulfill the requirement (i) as stated above, it will only be considered for comparison reasons in the 2D verification examples in Section 5.4.

5.2.3.2. Fixed average solid director

In order to solve this problem, i.e., to define a solid triad that is symmetric with respect to the base vectors \underline{g}'_2 and \underline{g}'_3 , an alternative variant denoted as STR-AVG is proposed, which relies on the average of the directors \underline{g}'_2 and \underline{g}'_3 , cf. Figure 5.2(c):

$$\underline{g}_{\text{AVG}}^S = \frac{\underline{g}'_2 + \underline{g}'_3}{\|\underline{g}'_2 + \underline{g}'_3\|}. \quad (5.33)$$

With this average vector the solid triad can be constructed as:

$$\underline{\Lambda}_{\text{AVG}}^S = \underline{R} \left(-\frac{\pi}{4} \underline{n} \right) \underline{\Lambda}_{\text{AVG,ref}}^S \quad (5.34)$$

with

$$\underline{\Lambda}_{\text{AVG,ref}}^S = [\underline{n}, \underline{g}_{\text{AVG}}^S, \underline{n} \times \underline{g}_{\text{AVG}}^S]. \quad (5.35)$$

The rotation tensor $\underline{R}(-(\pi/4)\underline{n})$ in (5.34) represents a "back-rotation" of the constructed reference triad $\underline{\Lambda}_{\text{AVG,ref}}^S$ by an angle of $-\pi/4$ to ensure that the resulting solid triad aligns with the beam triad in the reference configuration according to (5.16). In Section 5.4, it will be shown numerically that the variant STR-AVG, similar to the variant STR-POL, fulfills both requirements (i) and (ii) stated above.

Remark 5.4. Theoretically, an additive director averaging procedure such as (5.33) can result in a singularity if the underlying vectors are anti-parallel, i.e., $\underline{g}'_2 = -\underline{g}'_3$. However, since the associated material directors are orthogonal in the reference configuration, i.e., $\underline{g}_{2,0}^T \underline{g}_{3,0} = 0$, and shear angles smaller than $\pi/2$ can be assumed, this singularity will not be relevant for practical applications.

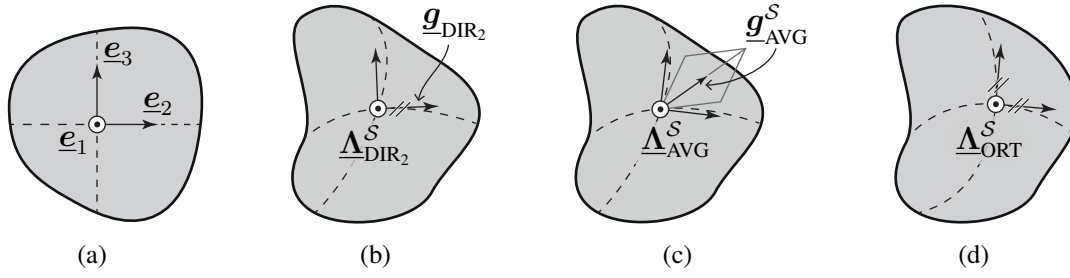


Figure 5.2.: Illustration of various solid triad definitions for an exemplary 2D problem setting. For simplicity it is assumed that the beam reference triad aligns with the Cartesian frame $\underline{e}_1, \underline{e}_2, \underline{e}_3$, i.e., $\underline{\Lambda}_0^B = \underline{I}$. Reference configuration (a), STR-DIR₂ (b), STR-AVG (c) and STR-ORT (d). Figure is taken from the author's article [138], permissions granted under the Creative Commons (CC BY) license.

5.2.3.3. Fixed orthogonal solid material directions

In the last considered solid triad definition, both material directors \underline{g}'_2 and \underline{g}'_3 are coupled to the solid triad simultaneously. This variant enforces that the directors \underline{g}'_2 and \underline{g}'_3 remain orthogonal to each other, and thus it is denoted as STR-ORT, indicated by a subscript $(\cdot)_{\text{ORT}}$. The STR-ORT variant is realized by applying the rotational coupling constraints (5.2) twice, once with $\underline{\Lambda}_{\text{DIR}_2}^S$ according to (5.31) and once with $\underline{\Lambda}_{\text{DIR}_3}^S$ according to (5.32).

Opposed to the other triad definitions in this section, this version additionally imposes a constraint on the solid displacement field by enforcing all in-plane shear strain components to vanish at the coupling point. In Section 5.4, it will be demonstrated that this over-constrained solid triad definition can lead to severe shear locking effects, i.e., requirement (ii) from Section 5.2.1 is not satisfied. Thus, also this variant will only be considered for comparison reasons in the 2D verification examples in Section 5.4.

5.2.4. Variation of the solid rotation vector

In the coupling contributions to the weak form (5.8) and (5.10) the multiplicative rotation vector variation $\delta \underline{\theta}^S$ (spin vector) of a solid rotation vector $\underline{\psi}^S$ arises. The spin vector is work-conjugated with the coupling moments, i.e., it is required to calculate the virtual work of a moment acting on the solid in a variationally consistent manner. In contrast to the beam spin vector $\delta \underline{\theta}^B$, which represents the multiplicative variation of primal degrees of freedom in the finite element discretization of the geometrically exact Simo–Reissner beam theory and is discretized directly, no such counterpart exists for the solid field. Therefore, it is assumed that the solid spin vector can be stated as a function of a set of generalized solid degrees of freedom \mathbf{d} (which will later be identified as nodal position vectors in the context of a finite element discretization) and their variations $\delta \mathbf{d}$. The additive variation of the solid rotation vector $\underline{\psi}^S(\mathbf{d})$ then reads

$$\delta \underline{\psi}^S = \frac{\partial \underline{\psi}^S(\mathbf{d})}{\partial \mathbf{d}} \delta \mathbf{d}. \quad (5.36)$$

The multiplicative and additive variations are related via (2.16), which gives the spin vector associated with the solid triad as a function of the generalized solid degrees of freedom:

$$\delta \underline{\theta}^S = \underline{T}^{-1}(\underline{\psi}^S(\mathbf{d})) \frac{\partial \underline{\psi}^S(\mathbf{d})}{\partial \mathbf{d}} \delta \mathbf{d}. \quad (5.37)$$

Remark 5.5. Alternatively, the solid spin vector can be expressed by the variations of the corresponding solid triad basis vectors \underline{g}_i^S and their variations $\delta \underline{g}_i^S$, cf. [96, 99]:

$$\begin{aligned} \delta \underline{\theta}^S &= \left(\delta \underline{g}_2^{S^T} \underline{g}_3^S \right) \underline{g}_1^S + \left(\delta \underline{g}_3^{S^T} \underline{g}_1^S \right) \underline{g}_2^S + \left(\delta \underline{g}_1^{S^T} \underline{g}_2^S \right) \underline{g}_3^S \\ &= \left((\underline{g}_1^S \otimes \underline{g}_3^S) \frac{\partial \underline{g}_2^S}{\partial \mathbf{d}} + (\underline{g}_2^S \otimes \underline{g}_1^S) \frac{\partial \underline{g}_3^S}{\partial \mathbf{d}} + (\underline{g}_3^S \otimes \underline{g}_2^S) \frac{\partial \underline{g}_1^S}{\partial \mathbf{d}} \right) \delta \mathbf{d}. \end{aligned}$$

This formulation for the solid spin vector is equivalent to the one in (5.37), but only contains the solid triad basis vectors and their variations. Therefore, this definition of the solid spin vector is better suited for solid triads constructed via their basis vector. Especially in the implementation of the finite element formulation, it is advantageous to avoid the computation and inversion of the transformation matrix in (5.37). Nonetheless, in the remainder of this chapter, the solid spin vector as defined in (5.37) is used to improve readability of the equations.

5.3. Spatial discretization

In this section, two different methods to discretize the rotational coupling terms are presented. For the rotational coupling terms it is advantageous to derive the discretized coupling terms on element pair level, i.e., the rotational coupling terms arising from the interaction of a single beam element (f) and a single solid element (e). In the following, the superscript (e, f) represents a quantity defined on element pair level. The total contribution to the weak form can then be calculated as the sum of all individual pair contributions, i.e.,

$$\delta \Pi_{(\cdot),h}^{\mathcal{R}} = \sum_{e=1}^{n_{\text{el}}^S} \sum_{f=1}^{n_{\text{el}}^B} \delta \Pi_{(\cdot),h}^{\mathcal{R}(e,f)}. \quad (5.38)$$

Here, n_{el}^B and n_{el}^S are the number of beam and solid elements, respectively. Furthermore, all integration is performed over $\Gamma_{c,h}^{(e,f)} = \Omega_h^{B(f)} \cap \Omega_h^{S(e)}$, which is the discretized coupling domain between a single beam and solid finite element. With the employed beam finite element interpolation, each beam element carries 9 rotational degrees of freedom, cf. Section 2.3.2.2. The number of solid degrees of freedom per solid element depends on the chosen element type and will be denoted by $n_{\text{dof}}^{(e)}$. To improve readability, any dependency on element parameter coordinates will not be stated explicitly.

5.3.1. Gauss point-to-segment coupling of cross-section rotations

Evaluating the variation of the total coupling potential (5.8) based on the discretized solid position field and beam cross-section rotation field as presented in the last section yields the discrete

variation of the coupling potential:

$$\delta\Pi_{\epsilon,h}^{\mathcal{R}(e,f)} = \epsilon^{\mathcal{R}} \int_{\Gamma_{c,h}^{(e,f)}} \left(\underline{\mathbf{T}}^{-1}(\underline{\psi}_h^S) \frac{\partial \underline{\psi}_h^S}{\partial \mathbf{d}^{S(e)}} \delta \mathbf{d}^{S(e)} - \mathbf{L}^{(f)} \delta \boldsymbol{\theta}^{\mathcal{B}(f)} \right)^T \underline{\psi}_{\mathcal{SB},h} \, ds. \quad (5.39)$$

This integral is evaluated numerically via a Gauss–Legendre quadrature, resulting in a Gauss point-to-segment (GPTS) coupling scheme. From a mechanical point of view this can be interpreted as a weighted enforcement of the rotational constraints at each integration point along the beam, i.e., a Gauss point-to-segment type coupling:

$$\delta\Pi_{\epsilon,h}^{\mathcal{R}(e,f)} \approx \epsilon^{\mathcal{R}} \sum_{i=1}^{n_{\text{GP}}^{\mathcal{R}}} \left[\left(\underline{\mathbf{T}}^{-1}(\underline{\psi}_h^S) \frac{\partial \underline{\psi}_h^S}{\partial \mathbf{d}^{S(e)}} \delta \mathbf{d}^{S(e)} - \mathbf{L}^{(f)} \delta \boldsymbol{\theta}^{\mathcal{B}(f)} \right)^T \underline{\psi}_{\mathcal{SB},h} \right]_{\xi^{\mathcal{B}} = \tilde{\xi}_i^{\mathcal{B}}} \tilde{w}_i, \quad (5.40)$$

where $n_{\text{GP}}^{\mathcal{R}}$ is the number of Gauss–Legendre points, $\tilde{\xi}_i^{\mathcal{B}}$ is the beam element parameter coordinate for Gauss–Legendre point i with the corresponding weight \tilde{w}_i . Again, in order to improve the readability of the remaining equations in this subsection, the explicit indication of the evaluation at the Gauss–Legendre points will be omitted in the following. The previous equation can now be stated in matrix form as

$$\delta\Pi_{\epsilon,h}^{\mathcal{R}(e,f)} \approx \begin{bmatrix} \delta \boldsymbol{\theta}^{\mathcal{B}(f)T} & \delta \mathbf{d}^{S(e)T} \end{bmatrix} \sum_{i=1}^{n_{\text{GP}}^{\mathcal{R}}} \tilde{w}_i \begin{bmatrix} \mathbf{f}_{\theta,\text{GP}}^{\mathcal{R}(e,f)} \\ \mathbf{f}_{s,\text{GP}}^{\mathcal{R}(e,f)} \end{bmatrix} = \begin{bmatrix} \delta \boldsymbol{\theta}^{\mathcal{B}(f)T} & \delta \mathbf{d}^{S(e)T} \end{bmatrix} \begin{bmatrix} \mathbf{r}_{\theta,\text{GP}}^{\mathcal{R}(e,f)} \\ \mathbf{r}_{s,\text{GP}}^{\mathcal{R}(e,f)} \end{bmatrix}. \quad (5.41)$$

Therein, the abbreviations $\mathbf{f}_{\theta,\text{GP}}^{\mathcal{R}(e,f)} \in \mathbb{R}^9$ and $\mathbf{f}_{s,\text{GP}}^{\mathcal{R}(e,f)} \in \mathbb{R}^{n_{\text{dof}}^{(e)}}$ for the generalized Gauss point coupling forces on the rotational beam element degrees of freedom and the generalized solid element degrees of freedom, respectively, have been introduced:

$$\begin{aligned} \mathbf{f}_{\theta,\text{GP}}^{\mathcal{R}(e,f)} &= -\epsilon^{\mathcal{R}} \mathbf{L}^{(f)T} \underline{\psi}_{\mathcal{SB},h} \\ \mathbf{f}_{s,\text{GP}}^{\mathcal{R}(e,f)} &= \epsilon^{\mathcal{R}} \left(\frac{\partial \underline{\psi}_h^S}{\partial \mathbf{d}^{S(e)}} \right)^T \underline{\mathbf{T}}^{-T}(\underline{\psi}_h^S) \underline{\psi}_{\mathcal{SB},h}. \end{aligned} \quad (5.42)$$

Furthermore, $\mathbf{r}_{\theta,\text{GP}}^{\mathcal{R}(e,f)} \in \mathbb{R}^9$ and $\mathbf{r}_{s,\text{GP}}^{\mathcal{R}(e,f)} \in \mathbb{R}^{n_{\text{dof}}^{(e)}}$ are the beam and solid coupling residual vectors. Employing a Newton–Raphson algorithm to solve the global system of nonlinear equations, a linearization of the residual vectors with respect to the element degrees of freedom is required, which reads:

$$\begin{bmatrix} \Delta \mathbf{r}_{\theta,\text{GP}}^{\mathcal{R}(e,f)} \\ \Delta \mathbf{r}_{s,\text{GP}}^{\mathcal{R}(e,f)} \end{bmatrix} = \sum_{i=1}^{n_{\text{GP}}^{\mathcal{R}}} \tilde{w}_i \begin{bmatrix} \frac{\partial \mathbf{f}_{\theta,\text{GP}}^{\mathcal{R}(e,f)}}{\partial \underline{\psi}_h^{\mathcal{B}}} \underline{\mathbf{T}}(\underline{\psi}_h^{\mathcal{B}}) \tilde{\mathbf{I}}^{(f)} & \frac{\partial \mathbf{f}_{\theta,\text{GP}}^{\mathcal{R}(e,f)}}{\partial \mathbf{d}^{S(e)}} \\ \frac{\partial \mathbf{f}_{s,\text{GP}}^{\mathcal{R}(e,f)}}{\partial \underline{\psi}_h^{\mathcal{B}}} \underline{\mathbf{T}}(\underline{\psi}_h^{\mathcal{B}}) \tilde{\mathbf{I}}^{(f)} & \frac{\partial \mathbf{f}_{s,\text{GP}}^{\mathcal{R}(e,f)}}{\partial \mathbf{d}^{S(e)}} \end{bmatrix} \begin{bmatrix} \Delta \boldsymbol{\theta}^{\mathcal{B}(f)} \\ \Delta \mathbf{d}^{S(e)} \end{bmatrix}. \quad (5.43)$$

Therein, the transformation matrix $\underline{\mathbf{T}}(\underline{\psi}_h^{\mathcal{B}})$ appears, since the linearization is performed with respect to the multiplicative rotation increments $\Delta \boldsymbol{\theta}^{\mathcal{B}(f)}$. Furthermore, the generalized shape function matrix $\tilde{\mathbf{I}}^{(f)}$ follows from the interpolation of the multiplicative rotation increments,

cf. (2.43). The previously derived matrices and vectors are all defined on beam-to-solid element pair level. Since no additional degrees of freedom are introduced, the pair-wise contributions can simply be assembled and added to the global linear system of equations. The Gauss point-to-segment coupling approach is presented here to illustrate how the rotational coupling conditions can be enforced in a point-wise manner. However, in Chapter 4 it is shown that a Gauss point-to-segment coupling approach leads to spurious contact locking for embedded one-dimensional beams in three-dimensional solid volumes. Therefore, this approach will not be investigated further in the remainder of this thesis, but a mortar-type coupling is proposed instead.

5.3.2. Mortar-type coupling of cross-section rotations

Employing a mortar-type coupling approach, the rotational Lagrange multiplier field $\underline{\lambda}^{\mathcal{R}}$ introduced in Section 5.1.2 is also approximated with a finite element interpolation, cf. [17, 110, 150]. The rotational Lagrange multiplier field is defined along the beam centerline and accordingly its finite element approximation is defined along the beam finite element and reads as follows:

$$\underline{\lambda}_h^{\mathcal{R}(f)} = \sum_{j=1}^{n^{\mathcal{R}(f)}} \Phi_j^{\mathcal{R}(f)}(\xi^{\mathcal{B}}) \hat{\underline{\lambda}}_j^{\mathcal{R}(f)} = \Phi^{\mathcal{R}(f)}(\xi^{\mathcal{B}}) \hat{\underline{\lambda}}^{\mathcal{R}(f)}, \quad (5.44)$$

where $n^{\mathcal{R}(f)}$ is the number of Lagrange multiplier nodes on beam element (f) , $\Phi_j^{\mathcal{R}(f)}$ is the shape function for the local node j and $\hat{\underline{\lambda}}_j^{\mathcal{R}(f)} \in \mathbb{R}^3$ is the rotational Lagrange multiplier at node j . Furthermore, $\Phi^{\mathcal{R}(f)} \in \mathbb{R}^{3 \times 3n^{\mathcal{R}(f)}}$ is the element-wise assembled Lagrange multiplier shape function matrix for a beam element and $\hat{\underline{\lambda}}^{\mathcal{R}(f)} \in \mathbb{R}^{3n^{\mathcal{R}(f)}}$ is the vector with all corresponding discrete rotational Lagrange multiplier values per beam element. As indicated by the dependency on beam parameter coordinate $\xi^{\mathcal{B}}$, the Lagrange multiplier field is defined along the beam centerline. However, there is no requirement that the Lagrange multiplier shape functions are identical to the beam centerline shape functions, or even that the number of beam nodes matches the number of Lagrange multiplier nodes. A more thorough discussion on the choice of Lagrange multiplier shape functions is given at the end of this section.

When inserting the finite element interpolations, the discretized variation of the coupling constraints (5.10) reads

$$\delta W_{\lambda,h}^{\mathcal{R}(e,f)} = \delta \hat{\underline{\lambda}}^{\mathcal{R}(f)\text{T}} \int_{\Gamma_{c,h}^{(e,f)}} \underbrace{\Phi^{\mathcal{R}(f)\text{T}} \psi_{\mathcal{SB},h}}_{\mathbf{f}_{\lambda}^{\mathcal{R}(e,f)}} ds = \delta \hat{\underline{\lambda}}^{\mathcal{R}(f)\text{T}} \mathbf{g}^{\mathcal{R}(e,f)}. \quad (5.45)$$

Therein, the abbreviations $\mathbf{f}_{\lambda}^{\mathcal{R}(e,f)} \in \mathbb{R}^{3n^{\mathcal{R}(f)}}$ and $\mathbf{g}^{\mathcal{R}(e,f)} \in \mathbb{R}^{3n^{\mathcal{R}(f)}}$ represent the integrand of the pair constraint equations and the residual of the pair constraints equations, respectively. The discretized virtual work of the coupling forces (5.11) reads

$$-\delta W_{c\theta,h}^{(e,f)} = \begin{bmatrix} \delta \boldsymbol{\theta}^{\mathcal{B}(f)\text{T}} & \delta \mathbf{d}^{\mathcal{S}(e)\text{T}} \end{bmatrix} \underbrace{\begin{bmatrix} \int_{\Gamma_{c,h}^{(e,f)}} \mathbf{f}_{\theta}^{\mathcal{R}(e,f)} ds \\ \int_{\Gamma_{c,h}^{(e,f)}} \mathbf{f}_s^{\mathcal{R}(e,f)} ds \end{bmatrix}}_{\begin{bmatrix} \mathbf{r}_{\theta}^{\mathcal{R}(e,f)} \\ \mathbf{r}_s^{\mathcal{R}(e,f)} \end{bmatrix}}. \quad (5.46)$$

Therein, the abbreviations $\mathbf{f}_\theta^{\mathcal{R}(e,f)} \in \mathbb{R}^9$ and $\mathbf{f}_s^{\mathcal{R}(e,f)} \in \mathbb{R}^{n_{\text{dof}}^{(e)}}$ represent the integrand of the beam and solid element coupling forces, i.e.,

$$\begin{aligned}\mathbf{f}_\theta^{\mathcal{R}(e,f)} &= \mathbf{L}^{(f)\top} \underline{\mathbf{T}}^\top(\underline{\psi}_{SB,h}) \Phi^{\mathcal{R}(f)} \hat{\lambda}^{\mathcal{R}(f)}, \\ \mathbf{f}_s^{\mathcal{R}(e,f)} &= \frac{\partial \underline{\psi}_h^S}{\partial \mathbf{d}^{S(e)}} \underline{\mathbf{T}}^{-\top}(\underline{\psi}_h^S) \underline{\mathbf{T}}^\top(\underline{\psi}_{SB,h}) \Phi^{\mathcal{R}(f)} \hat{\lambda}^{\mathcal{R}(f)}.\end{aligned}\quad (5.47)$$

Furthermore, $\mathbf{r}_\theta^{\mathcal{R}(e,f)} \in \mathbb{R}^9$ and $\mathbf{r}_s^{\mathcal{R}(e,f)} \in \mathbb{R}^{n_{\text{dof}}^{(e)}}$ are the beam and solid coupling residual vectors, respectively. Again, a linearization of the residual contributions with respect to the discrete beam-to-solid pair degrees of freedom is required for the Newton–Raphson algorithm. The linearization reads:

$$\text{Lin} \left(\begin{bmatrix} \mathbf{r}_\theta^{\mathcal{R}(e,f)} \\ \mathbf{r}_s^{\mathcal{R}(e,f)} \\ \mathbf{g}^{\mathcal{R}(e,f)} \end{bmatrix} \right) = \begin{bmatrix} \mathbf{0} \\ \mathbf{0} \\ \mathbf{g}^{\mathcal{R}(e,f)} \end{bmatrix} + \begin{bmatrix} \mathbf{Q}_{ss}^{\mathcal{R}(e,f)} & \mathbf{Q}_{s\theta}^{\mathcal{R}(e,f)} & \mathbf{Q}_{s\lambda}^{\mathcal{R}(e,f)} \\ \mathbf{Q}_{\theta s}^{\mathcal{R}(e,f)} & \mathbf{Q}_{\theta\theta}^{\mathcal{R}(e,f)} & \mathbf{Q}_{\theta\lambda}^{\mathcal{R}(e,f)} \\ \mathbf{Q}_{\lambda s}^{\mathcal{R}(e,f)} & \mathbf{Q}_{\lambda\theta}^{\mathcal{R}(e,f)} & \mathbf{0} \end{bmatrix} \begin{bmatrix} \Delta \theta^{\mathcal{B}(f)} \\ \Delta \mathbf{d}^{S(e)} \\ \hat{\lambda}^{\mathcal{R}(f)} \end{bmatrix}. \quad (5.48)$$

Therein, the abbreviations $\mathbf{Q}_{(\cdot)(\cdot)}^{\mathcal{R}(e,f)}$ for the stiffness matrices of the pair-wise coupling terms have been introduced, i.e.,

$$\begin{bmatrix} \mathbf{Q}_{ss}^{\mathcal{R}(e,f)} & \mathbf{Q}_{s\theta}^{\mathcal{R}(e,f)} & \mathbf{Q}_{s\lambda}^{\mathcal{R}(e,f)} \\ \mathbf{Q}_{\theta s}^{\mathcal{R}(e,f)} & \mathbf{Q}_{\theta\theta}^{\mathcal{R}(e,f)} & \mathbf{Q}_{\theta\lambda}^{\mathcal{R}(e,f)} \\ \mathbf{Q}_{\lambda s}^{\mathcal{R}(e,f)} & \mathbf{Q}_{\lambda\theta}^{\mathcal{R}(e,f)} & \mathbf{0} \end{bmatrix} = \int_{\Gamma_{c,h}^{(e,f)}} \begin{bmatrix} \frac{\partial \mathbf{f}_\theta^{\mathcal{R}(e,f)}}{\partial \underline{\psi}_h^{\mathcal{B}}} \underline{\mathbf{T}}(\underline{\psi}_h^{\mathcal{B}}) \tilde{\mathbf{I}}^{(f)} & \frac{\partial \mathbf{f}_\theta^{\mathcal{R}(e,f)}}{\partial \mathbf{d}^{S(e)}} & \frac{\partial \mathbf{f}_\theta^{\mathcal{R}(e,f)}}{\partial \hat{\lambda}^{\mathcal{R}(f)}} \\ \frac{\partial \mathbf{f}_s^{\mathcal{R}(e,f)}}{\partial \underline{\psi}_h^{\mathcal{B}}} \underline{\mathbf{T}}(\underline{\psi}_h^{\mathcal{B}}) \tilde{\mathbf{I}}^{(f)} & \frac{\partial \mathbf{f}_s^{\mathcal{R}(e,f)}}{\partial \mathbf{d}^{S(e)}} & \frac{\partial \mathbf{f}_s^{\mathcal{R}(e,f)}}{\partial \hat{\lambda}^{\mathcal{R}(f)}} \\ \frac{\partial \mathbf{f}_\lambda^{\mathcal{R}(e,f)}}{\partial \underline{\psi}_h^{\mathcal{B}}} \underline{\mathbf{T}}(\underline{\psi}_h^{\mathcal{B}}) \tilde{\mathbf{I}}^{(f)} & \frac{\partial \mathbf{f}_\lambda^{\mathcal{R}(e,f)}}{\partial \mathbf{d}^{S(e)}} & \mathbf{0} \end{bmatrix} ds. \quad (5.49)$$

As in the GPTS case, the previously derived vectors and matrices are all defined on beam-to-solid element pair level. However, in this case additional unknowns have been introduced, i.e., the rotational Lagrange multipliers $\hat{\lambda}^{\mathcal{R}(f)}$. In practice, all derivatives explicitly stated in (5.46) and (5.48) are evaluated using forward automatic differentiation (FAD), cf. [78], using the Sacado software package [121], which is part of the Trilinos project [143].

The local pair-wise residuum vectors $\mathbf{r}_\theta^{\mathcal{R}(e,f)}$, $\mathbf{r}_s^{\mathcal{R}(e,f)}$ and $\mathbf{g}^{\mathcal{R}(e,f)}$ are assembled into the global residuum vectors $\mathbf{r}_\theta^{\mathcal{R}} \in \mathbb{R}^{3n_\theta^{\mathcal{B}}}$, $\mathbf{r}_s^{\mathcal{R}} \in \mathbb{R}^{3n_s^{\mathcal{S}}}$ and $\mathbf{g}^{\mathcal{R}} \in \mathbb{R}^{3n_\lambda^{\mathcal{R}}}$, respectively. The linearization of the global rotational coupling terms reads

$$\text{Lin} \left(\begin{bmatrix} \mathbf{r}_\theta^{\mathcal{R}} \\ \mathbf{r}_s^{\mathcal{R}} \\ \mathbf{g}^{\mathcal{R}} \end{bmatrix} \right) = \begin{bmatrix} \mathbf{0} \\ \mathbf{0} \\ \mathbf{g}^{\mathcal{R}} \end{bmatrix} + \begin{bmatrix} \mathbf{Q}_{ss}^{\mathcal{R}} & \mathbf{Q}_{s\theta}^{\mathcal{R}} & \mathbf{Q}_{s\lambda}^{\mathcal{R}} \\ \mathbf{Q}_{\theta s}^{\mathcal{R}} & \mathbf{Q}_{\theta\theta}^{\mathcal{R}} & \mathbf{Q}_{\theta\lambda}^{\mathcal{R}} \\ \mathbf{Q}_{\lambda s}^{\mathcal{R}} & \mathbf{Q}_{\lambda\theta}^{\mathcal{R}} & \mathbf{0} \end{bmatrix} \begin{bmatrix} \Delta \theta^{\mathcal{B}} \\ \Delta \mathbf{d}^{\mathcal{S}} \\ \lambda^{\mathcal{R}} \end{bmatrix}, \quad (5.50)$$

where $\mathbf{Q}_{(\cdot)(\cdot)}^{\mathcal{R}}$ are the globally assembled pair-wise stiffness matrices $\mathbf{Q}_{(\cdot)(\cdot)}^{\mathcal{R}(e,f)}$, and $\lambda^{\mathcal{R}} \in \mathbb{R}^{3n_\lambda^{\mathcal{R}}}$ is the vector containing the globally assembled rotational Lagrange multipliers $\hat{\lambda}^{\mathcal{R}(f)}$.

At this point it should be pointed out that all coupling integrals are evaluated numerically using so-called segment-based integration, cf. Section 4.2.4. Therein, the beam finite element parameter space is divided into subsegments at points where the beam crosses a solid finite element face. Each subsegment is subsequently integrated using a Gauss–Legendre quadrature

with a fixed number of integration points. This leads to a highly accurate numerical integration procedure and allows for the resulting finite element coupling method to pass classical patch tests in surface-to-surface problems as well as constant stress transfer tests in beam-to-solid problems, cf. [45] and Section 4.2.4.

The choice of proper Lagrange multiplier basis functions is important for the mathematical properties of the resulting finite element discretization. The Lagrange multiplier shape functions must fulfill an inf-sup condition to guarantee stability of the mixed finite element method. This is a well-studied topic in the context of classical surface-to-surface mesh tying or contact. However, as pointed out in Section 4.2.2, beam-to-solid coupling problems diverge from the standard surface-to-surface case in some aspects. First, the discretization along the beam centerline with Hermite polynomials is unusual compared to standard (i.e., Lagrange polynomial-based) finite element discretizations. Also, the coupling can be classified as a mixed-dimensional embedded mesh problem, since there is no explicit curve in the solid domain to match the beam centerline, which can lead to stability issues [122]. Additionally, the rotational coupling considered in this chapter also differs from the standard displacement-based surface-to-surface case. A deep mathematical analysis of these properties is beyond the scope of the present thesis. However, this chapter builds upon the extensive studies and findings from Section 4.4.3, where it has been shown that a linear interpolation of the Lagrange multipliers combined with a penalty regularization leads to a stable finite element formulation of the coupled problem. Instabilities might only occur if the beam finite elements become shorter than the solid finite elements. However, this is not a mesh size relation that is within the envisioned applications for the BTSV-FULL method.

5.3.3. Combined mortar-type coupling of positions and rotations

Inserting all discretized variables into (5.4) gives the discrete nonlinear system of equations for the quasi-static BTSV-FULL problem:

$$\mathbf{r}^S(\mathbf{d}^S) + \mathbf{r}_s^V(\boldsymbol{\lambda}^V) + \mathbf{r}_s^R(\mathbf{d}^S, \boldsymbol{\psi}^B, \boldsymbol{\lambda}^R) = \mathbf{0}, \quad (5.51)$$

$$\mathbf{r}_r^B(\mathbf{d}^B, \boldsymbol{\psi}^B) + \mathbf{r}_r^V(\boldsymbol{\lambda}^V) = \mathbf{0}, \quad (5.52)$$

$$\mathbf{r}_\theta^B(\mathbf{d}^B, \boldsymbol{\psi}^B) + \mathbf{r}_\theta^R(\mathbf{d}^S, \boldsymbol{\psi}^B, \boldsymbol{\lambda}^R) = \mathbf{0}, \quad (5.53)$$

$$\mathbf{g}^V(\mathbf{d}^S, \mathbf{d}^B) = \mathbf{0}, \quad (5.54)$$

$$\mathbf{g}^R(\mathbf{d}^S, \boldsymbol{\psi}^B) = \mathbf{0}. \quad (5.55)$$

Here, the dependency of the residual contributions on the discrete unknowns is stated to illustrate the coupling connectivity introduced by each residuum vector. For improved readability, the explicit dependency of the residual contributions on the discrete unknowns will be omitted going further. The resulting BTSV-FULL global system of equations with saddle point structure reads:

$$\begin{bmatrix} \mathbf{K}_{ss}^S + \mathbf{Q}_{ss}^R & \mathbf{0} & \mathbf{Q}_{s\theta}^R & -\mathbf{M}^{V^T} & \mathbf{Q}_{s\lambda}^R \\ \mathbf{0} & \mathbf{K}_{rr}^B & \mathbf{K}_{r\theta}^B & \mathbf{D}^{V^T} & \mathbf{0} \\ \mathbf{Q}_{\theta s}^R & \mathbf{K}_{\theta r}^B & \mathbf{K}_{\theta\theta}^B + \mathbf{Q}_{\theta\theta}^R & \mathbf{0} & \mathbf{Q}_{\theta\lambda}^R \\ -\mathbf{M}^V & \mathbf{D}^V & \mathbf{0} & \mathbf{0} & \mathbf{0} \\ \mathbf{Q}_{\lambda s}^R & \mathbf{0} & \mathbf{Q}_{\lambda\theta}^R & \mathbf{0} & \mathbf{0} \end{bmatrix} \begin{bmatrix} \Delta \mathbf{d}^S \\ \Delta \mathbf{d}^B \\ \Delta \boldsymbol{\theta}^B \\ \boldsymbol{\lambda}^V \\ \boldsymbol{\lambda}^R \end{bmatrix} = \begin{bmatrix} -\mathbf{r}^S \\ -\mathbf{r}_r^B \\ -\mathbf{r}_\theta^B \\ -\mathbf{g}^V \\ -\mathbf{g}^R \end{bmatrix}. \quad (5.56)$$

It becomes clear that the global system of equations for the BTSV-FULL method is the combination of the BTSV-POS problem (4.19) and the mortar-type coupling of the beam cross-section rotations (5.50). The size of the global system of equations of the uncoupled system is extended by the total number of positional and rotational Lagrange multipliers. At this point it should be noted that due to the employed Petrov–Galerkin method the beam stiffness matrices are non-symmetric, as is the case for the rotational coupling contributions to the global stiffness matrix.

Remark 5.6. The structure of the global system of equations for BTSV-FULL (5.56) illustrates the direct coupling of the rotational degrees of freedom of the beam with the solid degrees of freedom, i.e., $\mathbf{Q}_{\theta\lambda}^{\mathcal{R}}$ and $\mathbf{Q}_{\lambda\theta}^{\mathcal{R}}$. Disregarding all other advantages of the BTSV-FULL method, this motivates it from a pure numerical point of view, as possible rigid body rotations of straight embedded fibers around their centerline are constrained, which is not the case for the BTSV-POS method (4.19).

Remark 5.7. In the BTSV-POS method, the mortar-type coupling matrices $\mathbf{D}^{\mathcal{V}}$ and $\mathbf{M}^{\mathcal{V}}$ only depend on the reference configuration, i.e., they only have to be calculated once and can be stored for the entire simulation. In the BTSV-FULL method, the (rotational) coupling terms $\mathbf{Q}_{(\cdot)(\cdot)}^{\mathcal{R}}$ depend on the current configuration, i.e., the coupling terms have to be re-evaluated in each Newton-Raphson step. However, this should not be viewed as a drawback of BTSV-FULL scheme, rather as a simplification of the BTSV-POS variant, which results from neglecting the rotational coupling terms.

5.3.4. Penalty regularization

In the present mortar-type coupling case (BTSV-FULL) the constraint equations are enforced with the Lagrange multiplier method, thus resulting in a mixed formulation. However, a direct solution of the global system (5.56) might introduce certain drawbacks, such as an increased system size compared to the uncoupled system and a generalized saddle point structure, cf. Section 2.5.2. In Chapter 4 the constraint equations have therefore been enforced using a well-known penalty regularization, which means that a relaxation of the positional coupling constraints $\mathbf{g}^{\mathcal{V}} = -\mathbf{M}^{\mathcal{V}}\mathbf{d}^{\mathcal{S}} + \mathbf{D}^{\mathcal{V}}\mathbf{d}^{\mathcal{B}} = \mathbf{0}$ in the form of $\boldsymbol{\lambda}^{\mathcal{V}} = \epsilon^{\mathcal{V}}(\mathbf{V}^{\mathcal{V}})^{-1}\mathbf{g}^{\mathcal{V}}$ is introduced. Therein, $\epsilon^{\mathcal{V}} \in \mathbb{R}^+$ is a scalar penalty parameter and $\mathbf{V}^{\mathcal{V}}$ is a scaling matrix to account for non-uniform weighting of the constraint equations, cf. Section 4.2.3 and [154]. The numerical examples in Section 4.4 show that for reasonably chosen penalty parameters the resulting violation of the constraint equations due to their relaxation does not have any impact on the accuracy of the BTSV-POS method. Therefore, the constraint enforcement of the rotational coupling equations (5.45) is also carried out with a penalty regularization. The constraint relaxation is achieved through

$$\boldsymbol{\lambda}^{\mathcal{R}} = \epsilon^{\mathcal{R}} (\mathbf{V}^{\mathcal{R}})^{-1} \mathbf{g}^{\mathcal{R}}, \quad (5.57)$$

again with a scalar penalty parameter $\epsilon^{\mathcal{R}} \in \mathbb{R}^+$ and a global scaling matrix for the rotational Lagrange multipliers $\mathbf{V}^{\mathcal{R}}$. The global scaling matrix is assembled from the nodal scaling matrices $\mathbf{V}^{\mathcal{R}[j,j]}$ for the Lagrange multiplier node j , i.e.,

$$\mathbf{V}^{\mathcal{R}[j,j]} = \int_{\Gamma_{c,h}} \Phi_j^{\mathcal{R}} \, ds \, \mathbf{I}^{3 \times 3}. \quad (5.58)$$

With the introduction of the constraint relaxation (5.57), the Lagrange multipliers $\lambda^{\mathcal{R}}$ are no longer independent degrees of freedom of the system, but a function of the beam rotations and solid displacements. Therefore, they can be eliminated from the global system of equations (5.56), which results in the condensed linear system of equations

$$\begin{bmatrix} \mathbf{A}_{ss}^{\mathcal{R}} & \mathbf{A}_{sr}^{\mathcal{R}} & \mathbf{A}_{s\theta}^{\mathcal{R}} \\ \mathbf{A}_{rs}^{\mathcal{R}} & \mathbf{A}_{rr}^{\mathcal{R}} & \mathbf{A}_{r\theta}^{\mathcal{R}} \\ \mathbf{A}_{\theta s}^{\mathcal{R}} & \mathbf{A}_{\theta r}^{\mathcal{R}} & \mathbf{A}_{\theta\theta}^{\mathcal{R}} \end{bmatrix} \begin{bmatrix} \Delta \mathbf{d}^{\mathcal{S}} \\ \Delta \mathbf{d}^{\mathcal{B}} \\ \Delta \boldsymbol{\theta}^{\mathcal{B}} \end{bmatrix} = \begin{bmatrix} \mathbf{b}_s^{\mathcal{R}} \\ \mathbf{b}_r^{\mathcal{R}} \\ \mathbf{b}_\theta^{\mathcal{R}} \end{bmatrix}. \quad (5.59)$$

Therein, the following abbreviations have been introduced for improved readability:

$$\begin{aligned} \mathbf{A}_{ss}^{\mathcal{R}} &= \mathbf{K}_{ss}^{\mathcal{S}} + \mathbf{Q}_{ss}^{\mathcal{R}} + \epsilon^{\mathcal{V}} \mathbf{M}^{\mathcal{V}^T} (\mathbf{V}^{\mathcal{V}})^{-1} \mathbf{M}^{\mathcal{V}} + \epsilon^{\mathcal{R}} \mathbf{Q}_{s\lambda}^{\mathcal{R}} (\mathbf{V}^{\mathcal{V}})^{-1} \mathbf{Q}_{\lambda s}^{\mathcal{R}} \\ \mathbf{A}_{sr}^{\mathcal{R}} &= -\epsilon^{\mathcal{V}} \mathbf{M}^{\mathcal{V}^T} (\mathbf{V}^{\mathcal{V}})^{-1} \mathbf{D}^{\mathcal{V}} \\ \mathbf{A}_{s\theta}^{\mathcal{R}} &= \mathbf{Q}_{s\theta}^{\mathcal{R}} + \epsilon^{\mathcal{R}} \mathbf{Q}_{s\lambda}^{\mathcal{R}} (\mathbf{V}^{\mathcal{V}})^{-1} \mathbf{Q}_{\lambda\theta}^{\mathcal{R}} \\ \mathbf{A}_{rs}^{\mathcal{R}} &= -\epsilon^{\mathcal{V}} \mathbf{D}^{\mathcal{V}^T} (\mathbf{V}^{\mathcal{V}})^{-1} \mathbf{M}^{\mathcal{V}} \\ \mathbf{A}_{rr}^{\mathcal{R}} &= \mathbf{K}_{rr}^{\mathcal{B}} + \epsilon^{\mathcal{V}} \mathbf{D}^{\mathcal{V}^T} (\mathbf{V}^{\mathcal{V}})^{-1} \mathbf{D}^{\mathcal{V}} \\ \mathbf{A}_{r\theta}^{\mathcal{R}} &= \mathbf{K}_{r\theta}^{\mathcal{B}} \\ \mathbf{A}_{\theta s}^{\mathcal{R}} &= \mathbf{Q}_{\theta s}^{\mathcal{R}} + \epsilon^{\mathcal{R}} \mathbf{Q}_{\theta\lambda}^{\mathcal{R}} (\mathbf{V}^{\mathcal{V}})^{-1} \mathbf{Q}_{\lambda s}^{\mathcal{R}} \\ \mathbf{A}_{\theta r}^{\mathcal{R}} &= \mathbf{K}_{\theta r}^{\mathcal{B}} \\ \mathbf{A}_{\theta\theta}^{\mathcal{R}} &= \mathbf{K}_{\theta\theta}^{\mathcal{B}} + \mathbf{Q}_{\theta\theta}^{\mathcal{R}} + \epsilon^{\mathcal{R}} \mathbf{Q}_{\theta\lambda}^{\mathcal{R}} (\mathbf{V}^{\mathcal{V}})^{-1} \mathbf{Q}_{\lambda\theta}^{\mathcal{R}} \\ \mathbf{b}_s^{\mathcal{R}} &= -\mathbf{r}_s^{\mathcal{S}} - \epsilon^{\mathcal{V}} \mathbf{M}^{\mathcal{V}^T} (\mathbf{V}^{\mathcal{V}})^{-1} \mathbf{g}^{\mathcal{V}} - \epsilon^{\mathcal{R}} \mathbf{Q}_{s\lambda}^{\mathcal{R}} (\mathbf{V}^{\mathcal{V}})^{-1} \mathbf{g}^{\mathcal{R}} \\ \mathbf{b}_r^{\mathcal{R}} &= -\mathbf{r}_r^{\mathcal{B}} - \epsilon^{\mathcal{V}} \mathbf{D}^{\mathcal{V}^T} (\mathbf{V}^{\mathcal{V}})^{-1} \mathbf{g}^{\mathcal{V}} \\ \mathbf{b}_\theta^{\mathcal{R}} &= -\mathbf{r}_\theta^{\mathcal{B}} - \epsilon^{\mathcal{R}} \mathbf{Q}_{\theta\lambda}^{\mathcal{R}} (\mathbf{V}^{\mathcal{V}})^{-1} \mathbf{g}^{\mathcal{R}}. \end{aligned} \quad (5.60)$$

As is the case in the BTSV-POS case, the penalty regularization introduces $\epsilon^{\mathcal{R}}$ as an additional system parameter. This leaves the important question on how to chose this parameter. Choosing too high penalty parameters can lead to an ill-conditioned system matrix, as well as to contact locking effects, as shown in Section 4.4.3. As already discussed in Section 4.2.3, from a mechanical point of view, it is desirable to chose penalty parameters as a function of the beam cross-section properties. The following rule of thumb can be given: the rotational parameter should be in the range of the beams Young's modulus scaled with the square of the cross-section radius, i.e., $\epsilon^{\mathcal{R}} \approx E^{\mathcal{B}} R^2$. In practice this does not lead to an unphysically large violation of the rotational coupling constraints, and contact locking has not been observed in combination with a linear interpolation of the Lagrange multiplier field.

5.4. Examples

The following numerical examples are set up using the open source beam finite element pre-processor MeshPy [137] and are simulated with the in-house parallel multi-physics research code BACI [12].

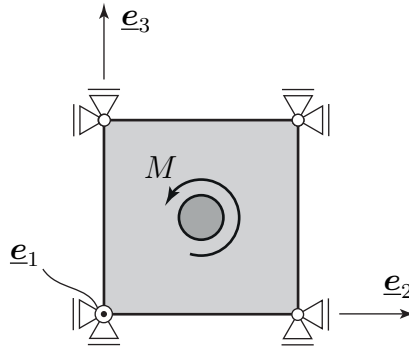


Figure 5.3.: Single element moment test – problem setup. Figure is taken from the author’s article [138], permissions granted under the Creative Commons (CC BY) license.

5.4.1. Single element moment test

The first problem setup is depicted in Figure 5.3. A straight beam is embedded inside a solid cube ($E^S = 1 \text{ N/m}^2$, $\nu^S = 0$) and the beam is loaded with a distributed torsion moment in \underline{e}_1 direction, which is constant along the beam centerline. This example is used to investigate how a moment on a beam is transferred to solid nodal forces. The cube is modeled with a single eight-noded hexahedral element and all solid degrees of freedom are fixed. A single Simo–Reissner beam finite element is used to discretize the beam. No Dirichlet boundary conditions are applied on the beam and the coupling between the beam and the solid is realized with the mortar-type BTSV-FULL method. Thus, the only interaction between the beam and the solid is the transfer of the external moment. The resulting nodal reaction forces for the various solid triad definitions introduced in Section 5.2 are depicted in Figure 5.4. Therein, the results for the STR-POL, STR-AVG and STR-ORT variants, cf. Figures 5.4(a), 5.4(d) and 5.4(e), match up to machine precision. In general, however, the solid coupling reaction forces may differ for the various definitions of the solid triad, as visible for the variants STR-DIR_{2/3} in Figures 5.4(b) and 5.4(c). This observation can be explained by the fact that the representation of a moment via nodal forces is non-unique, i.e., there is an infinite number of possible force pair combinations to achieve this. However, from a mechanical point of view, the force pairs resulting from the STR-POL, STR-AVG and STR-ORT variants seem more natural than the ones for the STR-DIR_{2/3} variants. Moreover, the former three variants result in the (unique) force pair solution if the moment is applied as a constant shear stress on the beam surface, cf. Section 3.2. Additionally, it can be observed for the STR-DIR_{2/3} variants that the choice which local solid direction is coupled to the solid triad drastically affects the result for the nodal forces.

5.4.2. Shear test

The next elementary test case is illustrated in Figure 5.5. The problem geometry is the same as in the previous example. The cube (side length $h = 1 \text{ m}$) is fixed at two bottom corner points to constrain all rigid body modes. A constant surface load $\tau = 0.001 \text{ N/mm}^2$ is applied to the surfaces of the cube, as depicted in Figure 5.5. No boundary conditions are applied to the beam. This problem illustrates how the specific solid triads affect the shear stiffness of the solid element and will be studied in two steps.

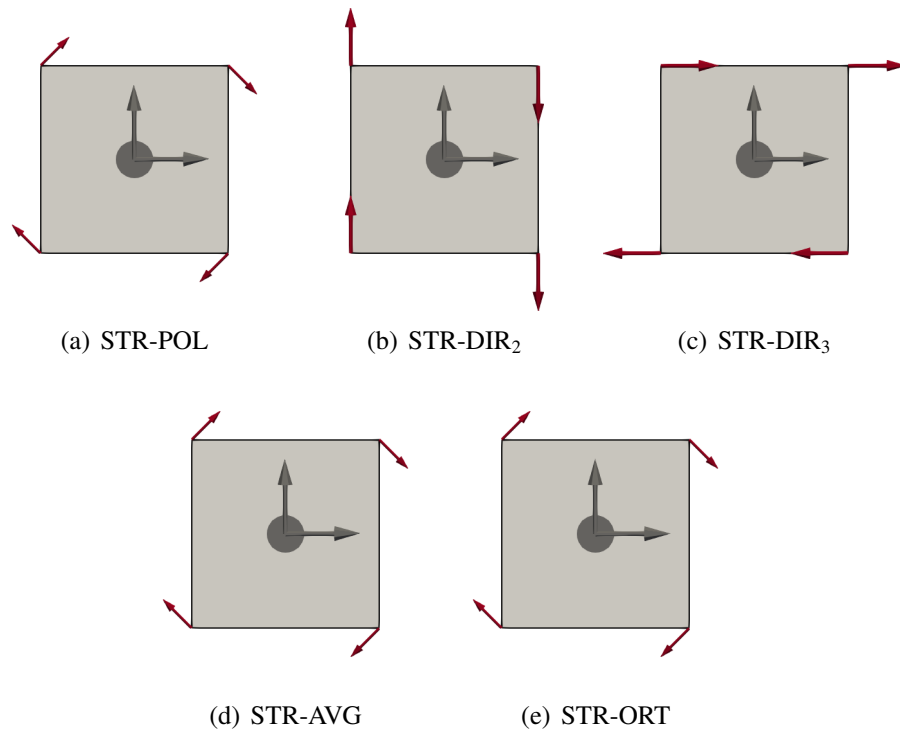


Figure 5.4.: Single element moment test – resulting nodal loads for various solid triads. Figure is taken from the author's article [138], permissions granted under the Creative Commons (CC BY) license.

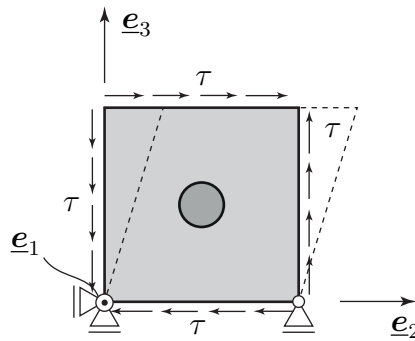


Figure 5.5.: Shear test – problem setup. Figure is taken from the author's article [138], permissions granted under the Creative Commons (CC BY) license.

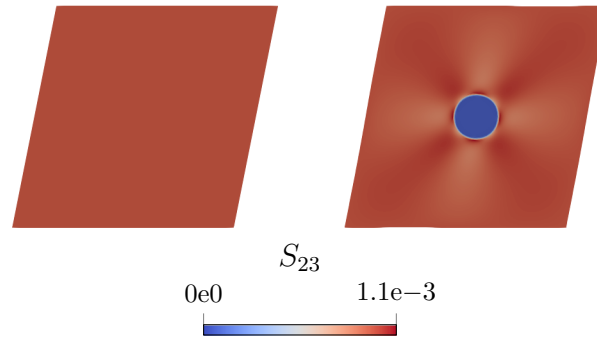


Figure 5.6.: Shear test – deformed configurations. The left figure illustrates the solution of a solid without a beam and the right figure illustrates the solution of a solid with an embedded beam (2D-3D coupling), $R = 0.1$ m. The second Piola-Kirchhoff stress S_{23} is shown in the solid. Displacements are scaled by a factor of 100. Figure is taken from the author’s article [138], permissions granted under the Creative Commons (CC BY) license.

In a first step, the impact of the local stiffening effect the beam cross-section has on the surrounding solid material is investigated. To do so, a reference solution is created by applying a full 2D-3D beam-to-solid coupling scheme, i.e., the coupling conditions are enforced on the beam surface, cf. Appendix A. For comparison purposes, a variant of this problem is simulated without the embedded beam, i.e., the pure solid shear problem. Figure 5.6 illustrates the shear stress in the solid, with and without the embedded beam, for an exemplary beam radius $R = 0.1$ m. As expected, the solution is uniform in the entire solid volume for the pure solid variant. In the 2D-3D beam-to-solid coupling variant, the embedded beam affects the solid stress and displacement fields. The overall displacement of the solid is smaller than for the variant without a beam, thus demonstrating the stiffening effects of the beam cross-section. In agreement with the fundamental modeling assumption of overlapping beam and solid domains (see Section 3.2), the solid shear stress inside the beam domain is zero. Outside of the beam domain, the solid shear stress field shows slight fluctuations due to the local constraints enforcing the 2D-3D coupling at the beam surface. However, close to the boundaries of the cube, these fluctuations become negligible and the shear stress field is quite homogeneous and therefore very similar to the pure solid shear problem.

In a second step, this problem is simulated with one single solid finite element to investigate potential shear locking effects. The coupling between beam and solid is now realized with the BTSV-FULL method and a rotational penalty parameter of $\epsilon^{\mathcal{R}} = 100$ Nm/m. In Figure 5.7, the deformed solid element and the resulting coupling reaction forces on the solid nodes are depicted for the various solid triad definitions and again for the problem without embedded beam. Due to the orthogonality constraints in the STR-ORT variant, no shear mode remains in the solid finite element, i.e., it is rigid with respect to shear deformations (in fact, small deformations can be observed due to the penalty regularization). In this example, all other solid triad definitions result in a solid displacement field matching the variant without embedded beam up to machine precision. Table 5.2 states the rigid body rotation angle $\psi^{\mathcal{B}}$ of the beam for the different solid triad variants. The rotation angle $\psi^{\mathcal{B}}$ of the beam depends on the employed solid triad variant. With the STR-DIR₂ variant the beam does not rotate at all since the orientation of the local solid

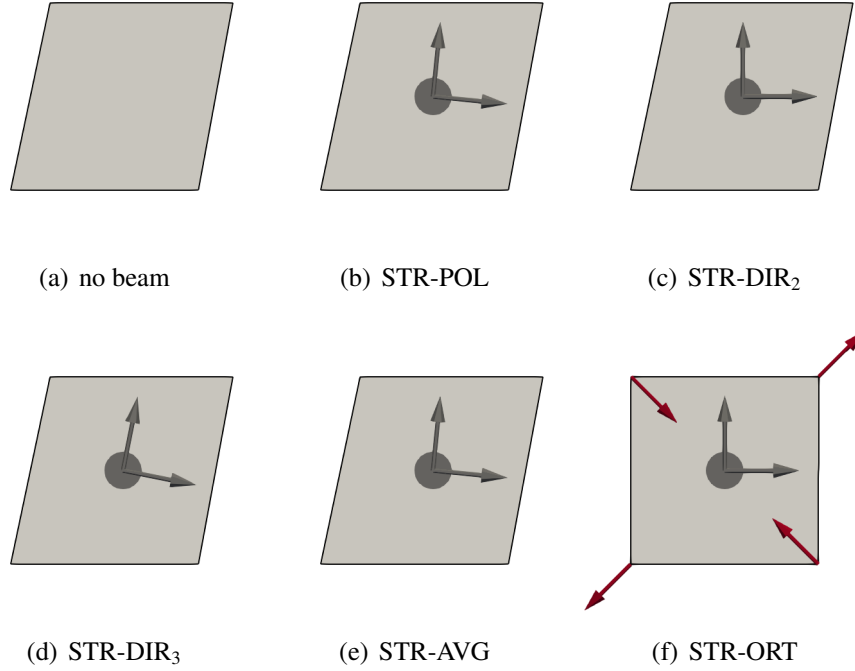


Figure 5.7.: Shear test – resulting nodal loads for various solid triads. Displacements are scaled with a factor of 100. Figure is taken from the author’s article [138], permissions granted under the Creative Commons (CC BY) license.

material fiber does not change. The STR-DIR₃ variant, on the other hand, results in the largest rotation of the beam, since the solid triad is coupled to the solid material fiber which undergoes the largest orientation change. Although they are not identical up to machine precision, the STR-POL and STR-AVG variants lead to very similar results for the rotation of the beam, i.e., roughly an average of the STR-DIR₂ and STR-DIR₃ variants.

The results show that the presented solid triads lead to either no shear stiffening effects in the solid (STR-POL, STR-DIR_{2,3} and STR-AVG) or to severe locking resulting in a complete constraining of all shear modes (STR-ORT). To assess which variant resembles best the resolved 2D-3D coupling scheme, the relative L_2 -displacement error

$$\|e\|_{L_2, \text{rel}} = \frac{\sqrt{\int_{\Omega_0^S} \|\underline{\mathbf{u}}_h^S - \underline{\mathbf{u}}_{\text{ref}}^S\|^2 dV_0}}{\sqrt{\int_{\Omega_0^S} \|\underline{\mathbf{u}}_{\text{ref}}^S\|^2 dV_0}} \quad (5.61)$$

is compared. In the results presented in the following, the reference solution is the solution obtained with a fine solid mesh and a 2D-3D coupling. Figure 5.8 illustrates $\|e\|_{L_2, \text{rel}}$ for various beam diameter to solid cube length ratios D/h . The relative error for the STR-ORT variant is almost constant 1 for all beam diameters ratios, i.e., even for beam cross-section sizes similar to the cube dimensions a full constraining of all shear modes does not accurately describe the physical coupling. For all other variants the behavior of the relative error is the same, since none of them constrain the shear deformation mode in the solid, i.e., the beam cross-sections rotate

Table 5.2.: Shear test – numerical results. Table is taken from the author’s article [138], permissions granted under the Creative Commons (CC BY) license.

solid triad	$\psi^{\mathcal{B}}$
STR-POL	-0.09899932
STR-DIR ₂	-0.00000000
STR-DIR ₃	-0.19485464
STR-AVG	-0.09742732
STR-ORT	-0.00099010

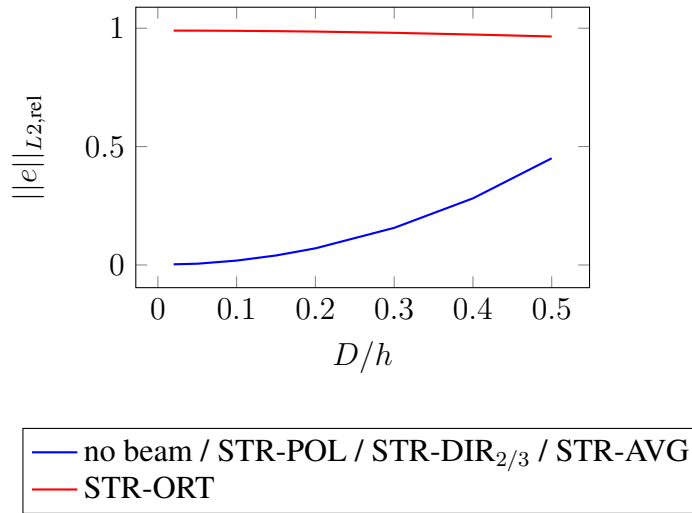


Figure 5.8.: Shear test – relative displacement error $\|e\|_{L2,rel}$ for various beam diameter to solid cube length ratios D/h . The relative error is computed with respect to the 2D-3D reference solution. The curves represent various solid triad variants. Figure is taken from the author’s article [138], permissions granted under the Creative Commons (CC BY) license.

with the solid without constraining it. For small ratios of beam radius to solid cube length the error is close to zero. For larger ratios of beam radius to solid cube length, the error increases as there is a real physical stiffening effect due to the embedded beam cross-section in the 2D-3D problem that is not captured by the 1D-3D coupling schemes. However, in the entire range of practically relevant solid mesh sizes (relative to the beam cross-section size) as illustrated in Figure 5.8, the solid triad variants that do not constrain the in-plane deformation of the solid result in a better approximation of the physical system behavior as compared to the STR-ORT triad.

5.4.3. Fiber-reinforced composite under shear loading

In this example, multiple fibers are placed inside a solid cube, cf. Figure 5.9. The solid cube has the dimensions $1\text{ m} \times 1\text{ m} \times 1\text{ m}$ and consists of a hyperelastic Saint-Venant–Kirchhoff material model ($E^{\mathcal{S}} = 1\text{ N/m}^2$, $\nu^{\mathcal{S}} = 0.0$). Embedded inside the solid cube are 5×5 fibers with a radius of 0.0125 m . All fibers point in \underline{e}_3 direction. The solid is fixed in \underline{e}_2 direction at the left boundary,

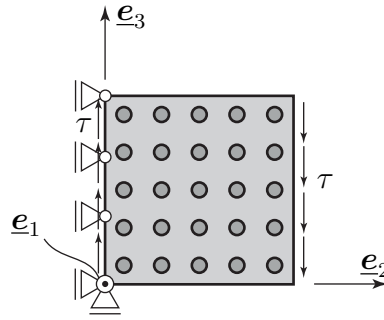


Figure 5.9.: Fiber-reinforced composite under shear loading – problem setup of 5×5 embedded fibers inside a solid cube. Figure is taken from the author’s article [138], permissions granted under the Creative Commons (CC BY) license.

and loaded with two equilibrating shear loads ($\tau = 0.01 \text{ N/m}^2$) at the left and right boundary. To constrain the remaining rigid body mode, the lower left corner point is fixed in \mathbf{e}_3 axis. The fibers are coupled to the solid via the BTSV-FULL method and no additional boundary conditions act on the fibers. The cube is meshed with $7 \times 7 \times 1$ solid *hex8* elements, and each fiber is represented by a single Simo–Reissner beam finite element. The penalty parameters for the BTSV-FULL method are $\epsilon^V = 100 \text{ N/m}^2$ and $\epsilon^R = 100 \text{ Nm/m}$. In this example, the results obtained with the BTSV-FULL method and various solid triads will be compared with a spatially converged reference solution, where the coupling between the beam surfaces and solid volume is discretized in a surface-to-volume (2D-3D) manner, i.e., the beam surface instead of the centerline is fixed to the solid, cf. Appendix A.

The resulting shear stresses are visualized in Figure 5.10. In the full 2D-3D model, there are stress concentrations at the interface between the beam surfaces and the solid. It is important to point out that the BTSV-FULL method (1D-3D), is not able to capture these stress concentrations, regardless of the employed solid triad. However, this has not been the intention of the BTSV-FULL method in the first place, but instead it has to be ensured that the far field stress in the solid is represented accurately. Figure 5.10 illustrates the shear stress results obtained with the STR-POL, STR-DIR_{2/3} and STR-AVG solid triads. In the reference solution the in-plane shear stress is positive at the top and bottom of the cube and negative in the middle. The results obtained with the STR-POL, STR-DIR_{2/3} and STR-AVG solid triads are similar to the ones obtained with 2D-3D coupling. However, the results with the STR-ORT solid triads clearly exhibit drastic shear locking effects due to the (over-) constraining of orthogonal solid directions. Table 5.3 provides the displacement at the top right corner of the cube for the 2D-3D reference solution and various types of solid triad fields, as well as the relative error. The error for the STR-ORT solid triad is six times larger than for all other solid triads. This again illustrates the unwanted locking effects introduced by the STR-ORT solid triads variant.

At this point a short recap of the first three examples for each of the investigated solid triad constructions is given to summarize their applicability in the context of the BTSV-FULL method:

STR-POL All basic consistency tests are fulfilled by this variant. However, due to the computational complexity of the polar decomposition in 3D, cf. Section 5.2.2, this variant is not used in the remaining examples presented in this chapter.

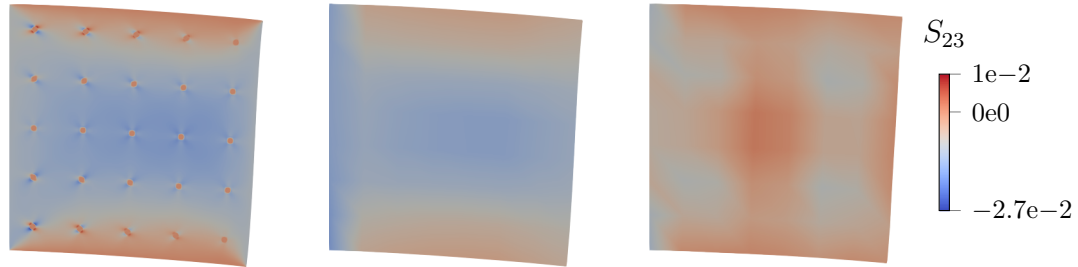


Figure 5.10.: Fiber-reinforced composite under shear loading – deformed configurations. Full 2D-3D coupling (left), STR-POL, STR-DIR_{2/3} and STR-AVG (middle), and STR-ORT (right). The second Piola-Kirchhoff stress S_{23} is shown in the solid. Figure is taken from the author’s article [138], permissions granted under the Creative Commons (CC BY) license.

Table 5.3.: Fiber-reinforced composite under shear loading – numerical results. The displacement \underline{u} at the top right corner of the cube are stated for the 2D-3D reference solution and various types of solid triad fields.

coupling type	solid triad	\underline{u} in m	$\frac{\ \underline{u} - \underline{u}_{\text{ref}}\ }{\ \underline{u}_{\text{ref}}\ }$
2D-3D (ref)	–	$[0, 0.0311342, -0.0706488]$	–
1D-3D	STR-POL, STR-DIR _{2/3} , STR-AVG	$[0, 0.0299373, -0.0681153]$	3.6282%
	STR-ORT	$[0, 0.0293469, -0.0547324]$	19.559%

STR-DIR_{2/3} The examples show that the (arbitrary) choice of the solid material direction for the construction of the solid triad can have a considerable effect on the results. Therefore, these variants will not be employed in the following. However, for comparison purposes they will be included in the spatial convergence example, cf. Section 5.4.5.

STR-AVG All basic consistency tests are fulfilled by the averaged solid triad and the results are very close to the ones obtained via the STR-POL variant, while being less expensive from a computational point of view. This variant is used in the remaining examples of this chapter.

STR-ORT This variant leads to considerable shear locking in the range of coarse solid mesh resolutions, which is exactly the range of interest for the proposed 1D-3D coupling methods. Therefore, this variant will not be used in the remainder of this chapter.

5.4.4. Constant torque transfer

This example serves as a consistency test for the BTSV-FULL method and its ability to transfer a constant torque. It is an extension of the *constant stress transfer problem* for the BTSV-POS method previously presented in Section 4.4.1. The example is inspired by classical patch tests, which are well-established tools to investigate the consistency of finite element formulations [140]. The constant torque test is depicted in Figure 5.11. It consists of a solid block Ω^S with two embedded beams Ω_1^B and Ω_2^B . The two beams occupy the same spatial position. The solid is fixed at the lower surface and no external loads are applied. One beam is loaded with a torsion load \underline{m} , and the other beam with a torsion load $-\underline{m}$, both acting along their axial direction. The magnitude of the torsion load is 10 Nm/m. Based on the space-continuous problem description, the opposing loads on the two beams cancel out each other, and in sum the two beams transfer no loads to the solid. This gives the trivial solution $\underline{u}^S = \underline{0}$ for the displacement field in the solid, cf. Section 4.4.1, and a constant solution for the beam rotations along their axis. In this test it shall be verified that this solution can also be represented in the spatially discretized setting using an arbitrarily coarse discretization. Both beams are coupled to the solid via the BTSV-FULL method. There is no direct interaction between the two beams, but all interactions are transferred through the solid domain.

The geometry and material parameters are taken from Section 4.4.1. The dimensions of the solid block are 1 m \times 1 m \times 2 m and a Saint-Venant–Kirchhoff material model ($E^S = 10 \text{ N/m}^2$, $\nu^S = 0.3$) is employed. The block is discretized with $4 \times 4 \times 7$ eight-noded, first-order hexahedral elements. The circular cross-sections of the two beams have a radius of 0.05 m, and the beam material parameters are $E^B = 100 \text{ N/m}^2$ and $\nu^B = 0$. The beams $B1$ and $B2$ are discretized with 5 and 7 Simo–Reissner beam finite elements, respectively. This results in a non-matching discretization between the two beams as well as between the beams and the solid. Coupling between the beams and the solid is realized with a linear interpolation of both the positional and rotational Lagrange multipliers. The STR-AVG solid triads are employed in this example, cf. Section 5.2.3.2. The penalty parameters are $\epsilon^V = 100 \text{ N/m}^2$ and $\epsilon^R = 100 \text{ Nm/m}$.

Figure 5.12 illustrates the results of this test. The stress in the solid and the curvature in the beam are indeed zero up to machine precision, thus matching the expected analytical solution.

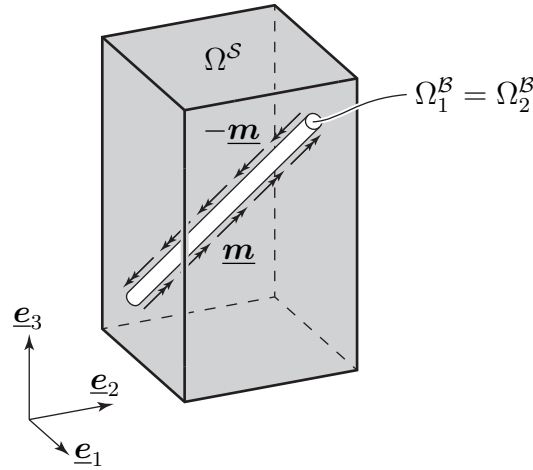


Figure 5.11.: Constant torque transfer – problem setup. Both beams Ω_1^B and Ω_2^B occupy the same spatial position. Figure is taken from the author’s article [138], permissions granted under the Creative Commons (CC BY) license.

This example illustrates the ability of the BTSV-FULL method to exactly represent a constant torsion state along the beam and the consistency of the coupling terms despite the fact that arbitrary non-matching meshes are involved.

5.4.5. Spatial convergence

This numerical example investigates the spatial convergence properties of the BTSV-FULL method under uniform mesh refinement. The problem is depicted in Figure 5.13. It consists of a solid block with the dimensions $5 \text{ m} \times 1 \text{ m} \times 1 \text{ m}$ and a Saint-Venant–Kirchhoff material model ($E^S = 10 \text{ N/m}^2$, $\nu^S = 0$). A beam (cross-section radius 0.125 m , $L = 5 \text{ m}$, $E^B = 300 \text{ N/m}^2$, $\nu^B = 0$) is embedded inside the solid block. No external loads or Dirichlet boundary conditions are applied to the beam, i.e., homogeneous Neumann boundary conditions at both ends. The right end of the block is loaded with a shear stress $\underline{\tau}$. The shear stress at point $\underline{p} = L\underline{e}_1 + y\underline{e}_2 + z\underline{e}_3$ reads

$$\underline{\tau} = (-z\underline{e}_2 + y\underline{e}_3) 0.05 \text{ N/m}^3, \quad (5.62)$$

thus resulting in a total torque of $1.65885 \cdot 10^{-2} \text{ Nm}$. The coupling between beam and solid is realized with the BTSV-FULL coupling method using linear Lagrange multiplier shape functions and the penalty parameters $\epsilon^V = 100 \text{ N/m}$ and $\epsilon^R = 100 \text{ Nm/m}$. This example can be interpreted as an adapted version of the spatial convergence problem in Section 4.4.2 to verify the scenario of rotational coupling. A similar problem is also investigated in [73]. The spatial convergence behavior of the BTSV-FULL method will be analyzed with respect to a spatially converged reference solution obtained with a 2D-3D coupling discretization, as described in Appendix A. To compare the results, the L_2 displacement error in the solid is calculated via

$$\|e\|_{L_2} = \frac{1}{V_0} \sqrt{\int_{\Omega_0^S} \|\underline{u}_h^S - \underline{u}_{\text{ref}}^S\|^2 dV_0}. \quad (5.63)$$

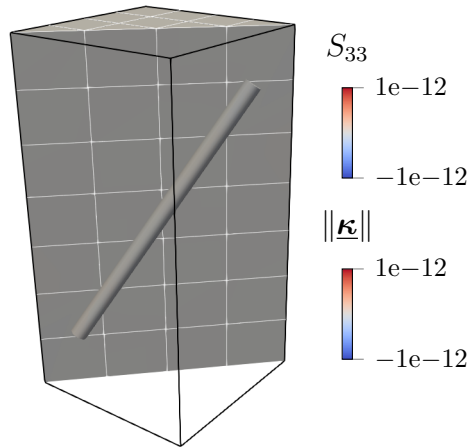


Figure 5.12.: Constant torque transfer – deformed configuration. The second Piola–Kirchhoff stress S_{33} is shown in the solid and the curvature κ in the middle of each beam element is shown in the beams. Figure is taken from the author’s article [138], permissions granted under the Creative Commons (CC BY) license.

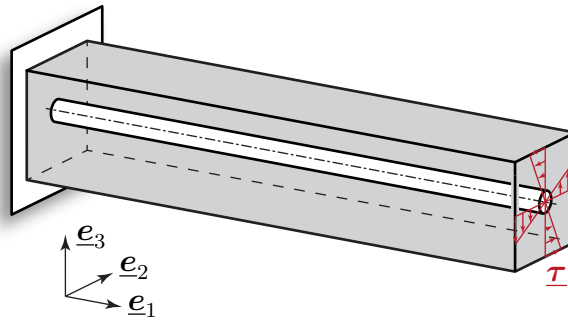


Figure 5.13.: Spatial convergence – problem setup. Figure is taken from the author’s article [138], permissions granted under the Creative Commons (CC BY) license.

Here, $V_0 = 1 \text{ m}^3$ is the solid volume in the reference configuration. It should be pointed out that the 2D-3D coupling problem does not have the same analytical solution as the BTSV-FULL problem, because the 1D-3D coupling results in a singularity in the analytical solution, cf. Section 3.2. Therefore, spatial convergence of the BTSV-FULL method towards the reference solution is not expected all the way towards the asymptotic limit of arbitrarily small solid element sizes, but only in the practically relevant regime of solid mesh sizes that are larger than the beam cross-section radius. In this regime, the singularity, i.e., the difference between the 1D-3D and 2D-3D models can not be fully resolved by the finite element solution space. This fact can be exploited to obtain reasonably accurate results with the BTSV-FULL (i.e., 1D-3D) method for the envisioned applications and practically relevant mesh resolutions.

The solution to the presented problem has a point symmetry around the \underline{e}_1 axis. Therefore, the STR-POL and STR-AVG solid triad variants coincide and give the same numerical results up to machine precision. Similarly, the results obtained with the STR-DIR_{1/2} variants match up to machine precision. Figure 5.14 shows the convergence plot for various types of solid triads as

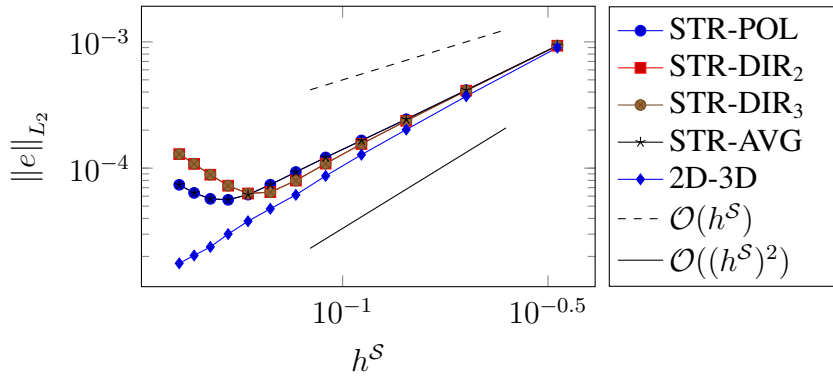


Figure 5.14.: Spatial convergence – convergence plot for various solid triads and the 2D-3D reference solution. Figure is taken from the author’s article [138], permissions granted under the Creative Commons (CC BY) license.

well as for the 2D-3D coupling approach. For coarse discretizations an excellent convergence behavior can be observed for the BTSV-FULL variants, slightly below the convergence rate of the reference 2D-3D method, but with a significantly reduced computational cost. All BTSV-FULL convergence plots exhibit a kink at a certain solid mesh resolution: the STR-DIR_{1/2} variants at around $h^S = 0.07$ m, and the STR-POL and STR-AVG variants at around $h^S = 0.06$ m. Figuratively speaking, the difference between the 1D-3D and 2D-3D coupling model becomes dominant at the kink position, since the solid element size to beam cross-section diameter ratio becomes smaller. Nevertheless, the kink only occurs when the solid element size is already smaller than the cross-section radius, which is far away from the envisioned geometric relations for the BTSV-FULL method anyways. The results confirm that for solid element sizes larger than the beam cross-section diameter, i.e., the desired and practically relevant discretization case, the results obtained with the BTSV-FULL method (1D-3D) exhibit excellent spatial convergence properties and thus give a very good approximation of the 2D-3D coupling problem.

5.4.6. Plane cantilever bending

In this example a cantilever structure modeled as a solid continuum subject to a moment load is considered. The problem is illustrated in Figure 5.15(a). The cantilever has the dimensions $5\text{ m} \times 1\text{ m}$ and consists of a Saint Venant–Kirchhoff material ($E^S = 10\text{ N/m}^2$, $\nu^S = 0$). At the left boundary all displacement components are fully constrained. A moment load $M = 0.0290888\text{ Nm}$ acts on the cantilever at the material point $\underline{\mathbf{X}}_M = [4.5, 0]^T\text{ m}$. This moment is chosen such that, if the cantilever were modeled using 1D beam theory, it should bend exactly to a quarter circle, due to a pure bending deformation in the region between the Dirichlet boundary and the applied moment. Directly imposing a conservative moment load on a solid, i.e., a Boltzmann continuum, which exhibits no rotational degrees of freedom is a non-trivial task. Standard approaches would require to model the moment as a (deformation-dependent) load/traction field distributed across an arbitrarily chosen sub-volume of the solid. A external moment is imposed on the solid structure by defining a solid triad (STR-AVG) at the application point of the moment. The nodal external forces effectively acting on the solid are obtained by projecting the moment to the solid finite element space via the discrete version of (5.37). The

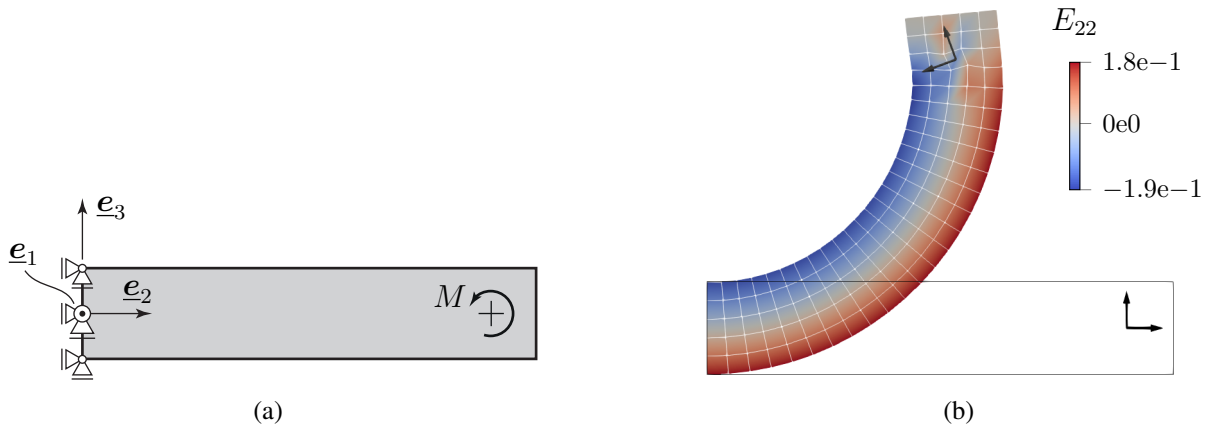


Figure 5.15.: Plane cantilever bending – problem setup (a) and the deformed configuration (b). The Green–Lagrange strains E_{22} are shown in the deformed configuration. Figure is taken from the author’s article [138], permissions granted under the Creative Commons (CC BY) license.

cantilever is discretized with 25×5 plane four-noded, first-order quadrilateral elements. In Figure 5.15(b) the deformed cantilever is illustrated. The global displacement behavior is as expected, i.e., the cantilever bends to a quarter circle. Of course, the local strain state close to the point where the external moment is applied is not meaningful in a continuum mechanics sense, since a singular moment is imposed at that point. However, according to Saint Venant’s principle, a linear stress distribution across the beam height, as expected for the pure bending of a slender beam-like structure, can be observed at a sufficient distance from the point where the moment is induced. This example illustrates that the presented rotational coupling approach is not limited to the coupling of beam cross-section orientations, but can also be used as a stand-alone feature to impose moments onto a solid domain in a variationally consistently manner. It should be pointed out that this example has only been carried out in 2D for reasons of simplicity, while the illustrated capability is available in 3D problems, too.

5.4.7. Plate with embedded beam

In this example a beam is only partially embedded inside a solid plate and loaded with a tip force. Two different geometry variants of the embedded beam are considered, cf. Figure 5.16. In variant *A* the embedded part of the beam has the shape of a quarter circle, while it is straight in variant *B*. The plate has the dimensions $1 \text{ m} \times 1 \text{ m} \times 0.1 \text{ m}$ and consists of a Saint Venant–Kirchhoff material ($E^S = 1 \text{ N/m}^2$, $\nu^S = 0.3$). The embedded Simo–Reissner beam has a cross-section radius $R = 0.025 \text{ m}$ and the material parameters are $E^B = 100 \text{ N/m}^2$ and $\nu^B = 0$. In both variants the beam is loaded with a tip load $\underline{F} = -0.0001 \text{ N } \underline{e}_3$ at the end that sticks out of the solid domain. The solid plate is fully clamped at the left and at the bottom.

The coupling of beam and solid is realized with the BTSV-FULL method and compared to the BTSV-POS method from Chapter 4, i.e., the one without rotational coupling. First-order Lagrange polynomials are employed to discretize the positional and rotational Lagrange multipliers. The penalty parameters are $\epsilon^V = 100 \text{ N/m}^2$ and $\epsilon^R = 100 \text{ Nm/m}$. The solid plate is modeled with

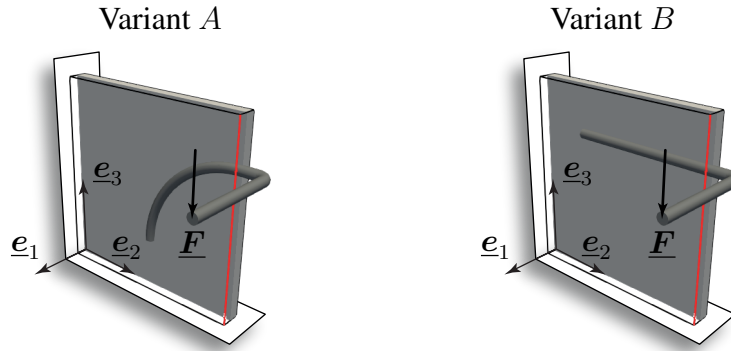


Figure 5.16.: Plate with embedded beam – problem setup for variant *A* and *B*. In variant *A* the embedded part of the beam has the shape of a quarter circle, in variant *B* it is straight. In both cases the red line indicates along which edge the results are plotted in Figure 5.19. Figure is taken from the author’s article [138], permissions granted under the Creative Commons (CC BY) license.

$1 \times 10 \times 10$ eight-noded solid-shell elements [20, 147], while the entire beam is discretized with six Simo–Reissner beam finite elements. The resulting global finite element model has 807 degrees of freedom. A full 3D model, also resolving the beam with three-dimensional solid finite elements and consisting of 90,190 second-order tetrahedra (*tet10*) elements, serves as a comparison. The discretization of the full 3D model has been chosen such that mesh convergence is guaranteed. Consequently, the full 3D model consists of 270,570 degrees of freedom.

The results for variant *A* are shown in Figure 5.17. It can be seen that the full 3D model and the new BTSV-FULL method exhibit the same overall behavior, while the beam experiences much larger deformations and the solid smaller ones in the BTSV-POS model without rotational coupling. This is due to the fact that in the full 3D problem a considerable portion of the external load is transferred from the beam to the solid via shear stresses on the beam surface, which are represented by moments in the reduced-dimensional model. Only the BTSV-FULL method is able to capture these coupling moments. Figure 5.18 shows the results for variant *B*. In this case a solution for the purely positional BTSV-POS method (i.e., only centerline position coupling) does not even exist within a quasi-static framework, since the beam has an unconstrained rigid body rotation mode around its axis of the embedded part. Again, the displacement results of the full 3D problem and the BTSV-FULL model are very close to each other. A more detailed comparison of the variants is given in Figure 5.19. Therein, the displacements along the curve indicated in Figure 5.16 are visualized. Now it also becomes clear quantitatively that the displacement results obtained with the BTSV-FULL method are very close to the ones obtained with the full 3D problem. Considering that the former reduces the number of degrees of freedom by a factor of about 330 as compared with the latter, this is a remarkable result and showcases the efficiency of the new BTSV-FULL method for challenging applications.

5.4.8. Fiber-reinforced pipe

The next numerical example is a fiber-reinforced pipe under pressure. The problem setup, illustrated in Figure 5.20(a), consists of a pipe modeled with a Neo-Hookean material law

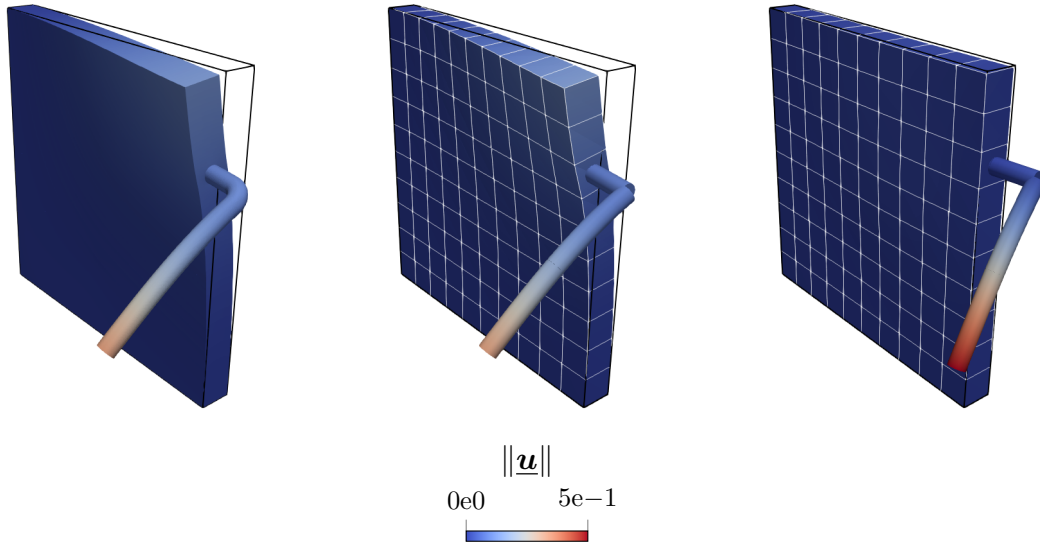


Figure 5.17.: Plate with embedded beam – deformed configurations for variant A. The left figure shows the full 3D model, the middle figure shows the BTSV-FULL model and the right figure shows the BTSV-POS model. The contour plots visualize the displacement magnitude. Figure is taken from the author’s article [138], permissions granted under the Creative Commons (CC BY) license.

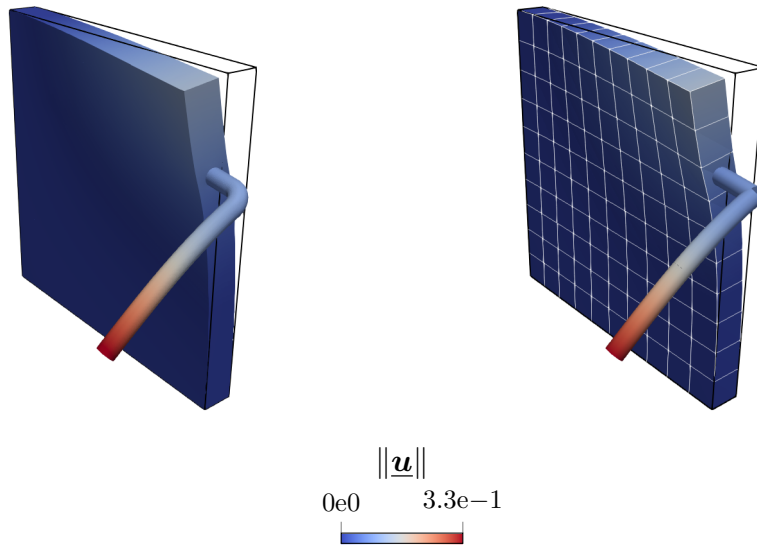


Figure 5.18.: Plate with embedded beam – deformed configurations for variant B. The left figure shows the full 3D model and the right figure shows the BTSV-FULL model. The contour plots visualize the displacement magnitude. Figure is taken from the author’s article [138], permissions granted under the Creative Commons (CC BY) license.

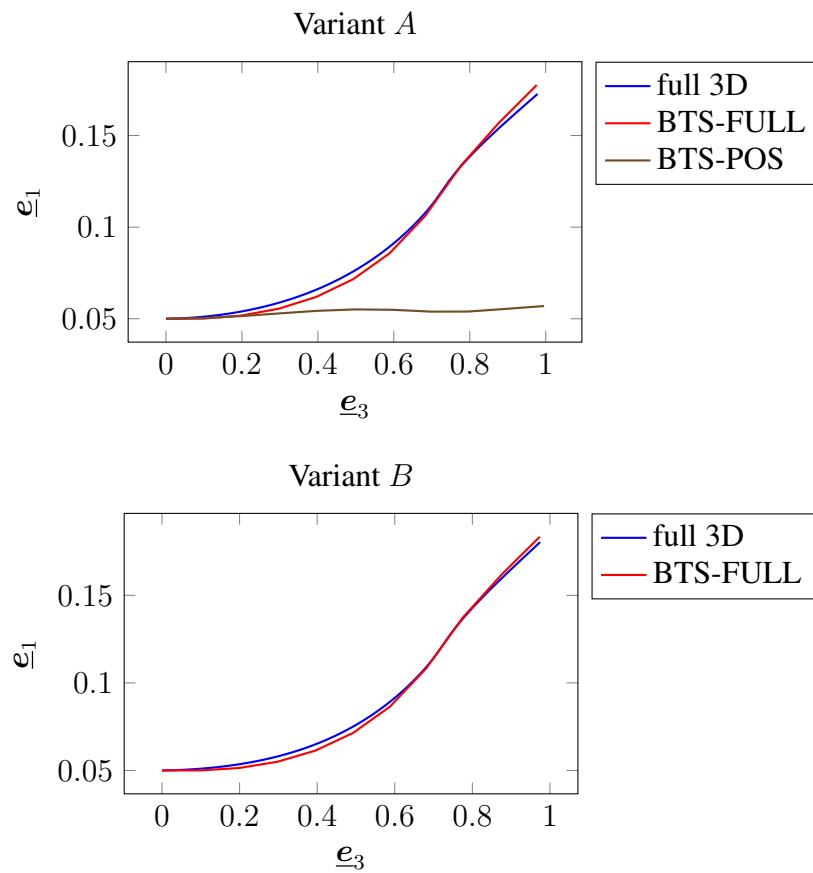


Figure 5.19.: Plate with embedded beam – deformed configurations of the edge indicated in Figure 5.16 for the two variants and for various modeling techniques. Figure is taken from the author's article [138], permissions granted under the Creative Commons (CC BY) license.

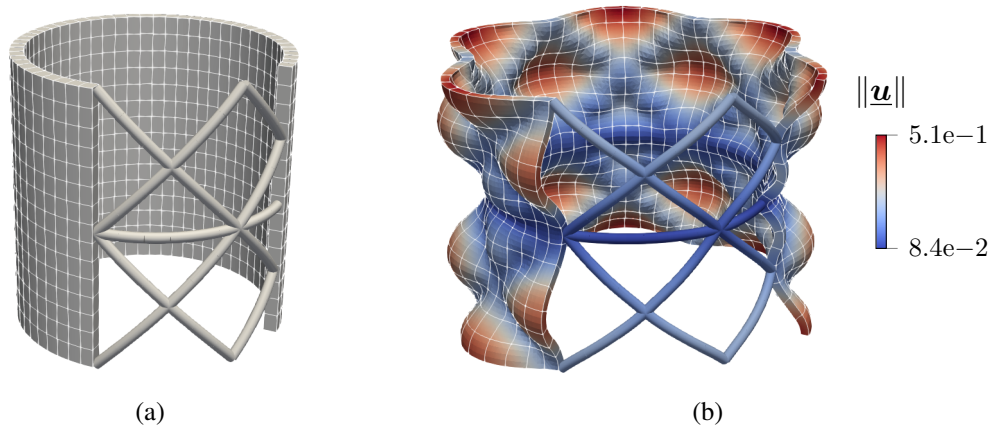


Figure 5.20.: Fiber-reinforced pipe – problem setup (a) and deformed configuration (b). The contour plot visualizes the displacement magnitude. Figure (a) is taken from the author’s article [135], permissions granted under the Creative Commons (CC BY) license.

($E^S = 10 \text{ N/m}^2$, $\nu^S = 0.3$). The pipe is 2 m long and has an inner and outer radius of 0.9 m and 1 m, respectively. It is reinforced with Simo–Reissner beams ($E^B = 1000 \text{ N/m}^2$, $\nu^B = 0$) as also shown in Figure 5.20(a). The cross-section radius of the beams is 0.04 m. The inner surface of the pipe is loaded with a Neumann surface pressure p of up to 2.5 N/m^2 . At the top and bottom, symmetry boundary conditions are applied to the pipe as well as to the beams. For further symmetry reasons, only a quarter of the depicted pipe is actually simulated with the following element numbers referring to the quarter model. Coupling between the beams and the solid is realized with the BTSV-FULL scheme approach and linear Lagrange multiplier shape functions for the positional and rotational Lagrange multipliers ($\epsilon^V = 1000 \text{ N/m}$ and $\epsilon^R = 5 \text{ Nm/m}$). The pipe is discretized with 225 C^1 -continuous isogeometric solid elements (based on second-order NURBS) and 45 Simo–Reissner beam elements.

Figure 5.20(b) shows the deformed configuration of the pipe. The expected stiffening effects of the beams onto the structure can clearly be seen. In-between the beam reinforcements, the relatively soft pipe exhibits larger displacements. Although only qualitative in nature, this example illustrates a very interesting problem class for the BTSV-FULL method. Even though all the previous derivations and examples used first-order interpolation of the solid finite elements, this example also showcases the straightforward applicability of the presented BTS interaction methods to higher-order and even C^1 -continuous solid interpolations. This allows for a coupling of beam and solid fields with the same order of interpolation continuity.

5.4.9. Twisted plate

In this final example let us consider a plate, with complex, spatially distributed fiber reinforcements in 3D, cf. Figure 5.21. The plate has the dimensions $1 \text{ m} \times 3.5 \text{ m} \times 0.1 \text{ m}$ and consists of a Neo-Hookean material ($E^S = 1 \text{ N/m}^2$, $\nu^S = 0.3$). The plate is fully clamped at the left face. The right face of the plate is rotated around the \underline{e}_2 axis with the rotation angle $\phi = [0, 2\pi]$, i.e., the plate is twisted along the \underline{e}_2 axis. Two different shapes of fibers are embedded in the plate: semicircles

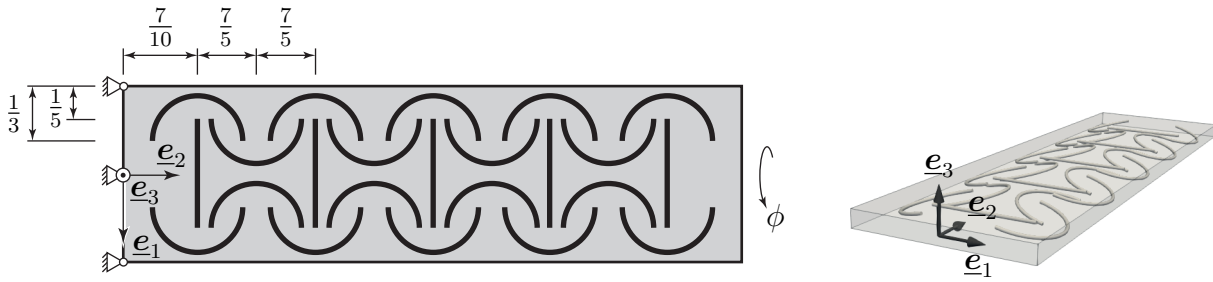


Figure 5.21.: Twisted plate – problem setup. The left figure illustrates the fiber placement in the plate, all dimensions are in m. The right figure shows a 3D view illustrating the rotation of the curved fibers around the \underline{e}_2 axis. Figure is taken from the author's article [138], permissions granted under the Creative Commons (CC BY) license.

with a radius of 0.25 m and straight lines with a length of 0.6 m. The fiber semicircles are rotated by $\pm 15^\circ$ with respect to the \underline{e}_2 axis to make the example more challenging and represent general 3D fiber-solid element intersection scenarios. The embedded fibers have a cross-section radius $R = 0.01$ m and the material parameters are $E^B = 400 \text{ N/m}^2$ and $\nu^B = 0$. The coupling of fibers and solid is realized with the BTSV-FULL method (STR-AVG solid triad, $\epsilon^V = 100 \text{ N/m}^2$ and $\epsilon^R = 1 \text{ Nm/m}$)¹. First-order Lagrange polynomials are employed to discretize the positional and rotational Lagrange multipliers. The solid plate is modeled with $10 \times 35 \times 2$ eight-noded solid-shell elements, while each fiber is discretized with four Simo–Reissner beam finite elements, thus resulting in a total of 92 beam finite elements. The displacement controlled twisting deformation of the plate is applied within 100 quasi-static load steps. At this point it should be mentioned that this example could not be solved with the BTSV-POS method, since the rigid body rotation modes of the straight fibers lead to a non-converging Newton–Raphson algorithm in the very first load step. This underlines the advantages of the mechanically consistent coupling provided by the BTSV-FULL method.

Figure 5.22 illustrates the deformed structure at various load steps. Until load step 75, the reinforced plate exhibits a more or less homogeneous twist along the \underline{e}_2 axis. From load step 75 to load step 100, the reinforced plate folds around the \underline{e}_2 axis. To assess the non-linear behavior of this structure and evaluate the global impact of the fiber-reinforcements, the fiber-reinforced plate is compared to a simple plate (same material) without any fibers. Figure 5.23 depicts the reaction moment M_2 around the \underline{e}_2 axis at the fully clamped surface of the plate with and without fiber-reinforcements. Until load step 70, the structures behave similarly. However, as expected the fiber-reinforcements lead to an increased reaction moment for the same twist angle ϕ , i.e., to a stiffer structural response. Both structures exhibit a limit point with an unstable post-critical solution, i.e., the structures would collapse if the twist is applied in a load-controlled manner. The fiber-reinforcements affect the critical point of the structure such that the instability occurs at a smaller twist angle and the critical moment is increased. This illustrates the complex influences that fiber-reinforcements may have on the global non-linear behavior of a structure.

Figure 5.24 illustrates the final configuration and shows a close-up view of the deformed embedded fibers. The maximum normal stresses in the fibers resulting from axial and bending

¹Due to a typo, the values of the penalty parameters given here differ from those in the author's article [138]. The values stated in this thesis are correct.

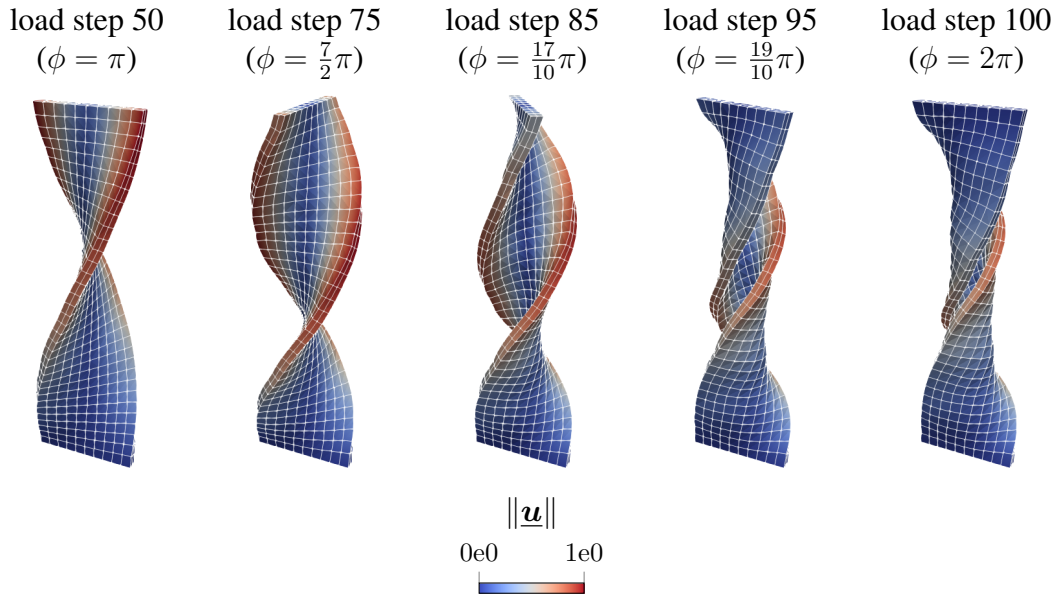


Figure 5.22.: Twisted plate – deformed configurations at various load steps. The magnitude of the displacements is shown in the solid. Figure is taken from the author’s article [138], permissions granted under the Creative Commons (CC BY) license.

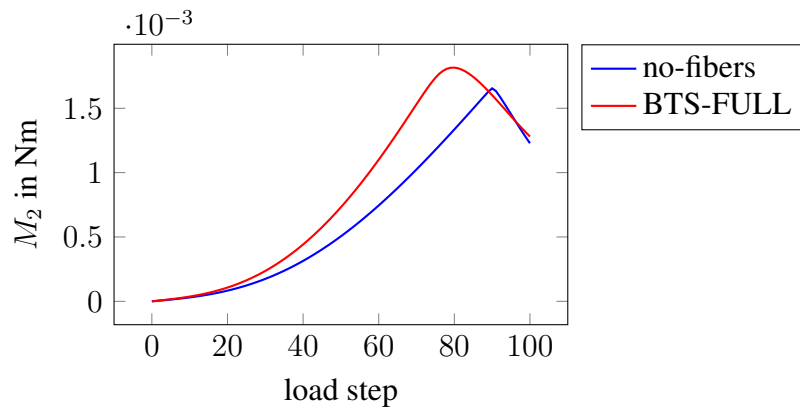


Figure 5.23.: Twisted plate – reaction moment at the fully clamped surface of the plate over the course of the simulation, with and without fiber-reinforcements. The reaction moment M_2 is the resulting moment around the \underline{e}_2 axis. Figure is taken from the author’s article [138], permissions granted under the Creative Commons (CC BY) license.

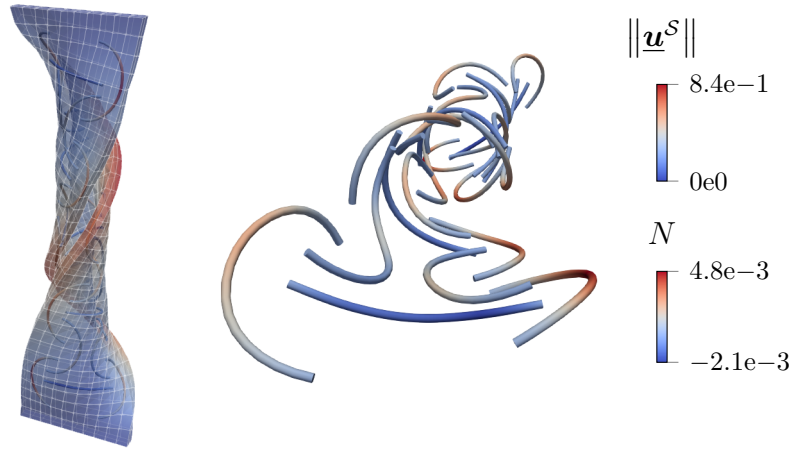


Figure 5.24.: Twisted plate – closeup of deformed configuration at load step 100. Magnitude of the displacements is visualized in the solid and the axial force N is shown in the beams. Figure is taken from the author’s article [138], permissions granted under the Creative Commons (CC BY) license.

deformations can be estimated for this example as $\approx 15 \text{ N/m}^2$ and $\approx 26 \text{ N/m}^2$ (not visualized in the figure), respectively. In the solid the maximum principal Cauchy stress is 0.578 N/m^2 (not visualized in the figure). As expected, the stresses in the stiff fibers are much larger than in the relatively soft solid matrix. To further investigate the influences of the various deformation modes of the fibers, Figure 5.25 depicts the tension, shear, torsion and bending contributions to the total internal elastic energy of the fibers over the course of the simulation. In the first few load steps, the main contributors to the internal elastic energy of the system are bending and torsion deformations, cf. right part of Figure 5.25. This can be attributed to the fact that in the beginning of the simulation the deformations of the plate mainly take place in \underline{e}_3 direction, which predominantly causes bending and torsion deformations of the fibers. As the plate is twisted further, geometrically non-linear effects materialize especially on the outer edges of the plate. The edges form helix like curves. Due to the constrained displacements in \underline{e}_3 direction at the clamped surfaces, the outside edges of the plate are stretched in \underline{e}_3 direction. This causes axial tension in the fiber semicircles at the outside. Starting at approximately load step 25, the main contribution to the internal elastic fiber energy comes from axial deformations. In the post-buckling state, the bending deformation of the plate, and therefore also of the fibers increases. This causes an increase in the internal elastic bending and torsion energy of the fibers. Moreover, shear deformations only have a minor contribution to the total internal energy of the fibers, which is expected due to the slenderness of the embedded fibers, thus motivating a future use of the BTSV-FULL method in combination with shear stiff Kirchhoff–Love beam theories [96, 97].

The considerable contributions of bending and torsional energy to the internal elastic energy of the fibers demonstrates the importance of consistently representing these modes and coupling them to the background solid material as done by the BTVS-FULL scheme. For this example, this would not be the case if simplified models for the fibers (e.g., modeled as strings without bending stiffness) or for the fiber-solid coupling (e.g., BTVS-POS) were applied.

This example also showcases the maturity of the implemented BTVS-FULL method from an algorithmic point of view. The chosen solid mesh, in combination with the tilted fiber semicircles

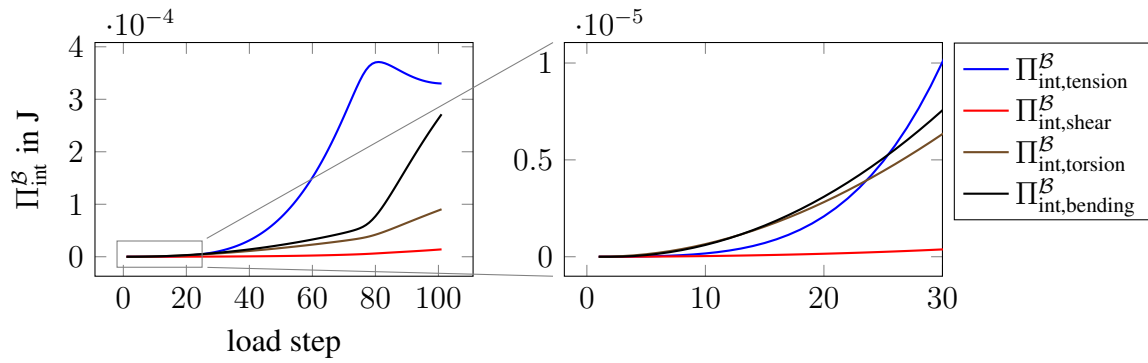


Figure 5.25.: Twisted plate – internal elastic fiber energies over the course of the simulation. The total internal elastic energy is split up in tension, shear, torsion and bending contributions. Figure is taken from the author’s article [138], permissions granted under the Creative Commons (CC BY) license.

results in complex 3D intersections between the beam finite elements and the solid finite elements, thus illustrating the robustness of the employed numerical integration algorithm. As a final example, a more complex model of a fiber-reinforced plate is considered. Therein, the dimensions of the plate are repeated 5 times in \underline{e}_1 and \underline{e}_2 direction and 3 times in \underline{e}_3 direction. The pattern and size of the fiber-reinforcements is similar to the one illustrated in Figure 5.21, however, in this case there are 3 layers of fiber-reinforcements over the thickness of the plate. This results in a total of approximately 53,000 solid finite elements and 1,800 fibers with 4 beam finite elements each, i.e., the problem size is scaled by a factor of approximately 75 compared to the previously considered plate. The deformed configuration of the plate is visualized in Figure 5.26. This further illustrates the robustness and scalability of the presented BTSV-FULL method for large-scale problems.

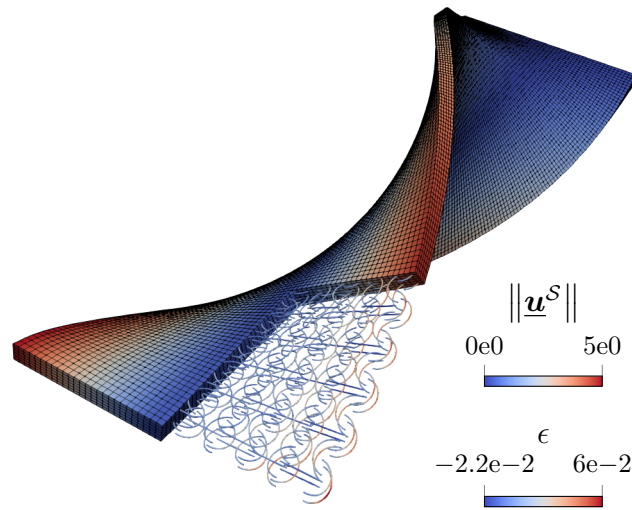


Figure 5.26.: Twisted plate – deformed configuration of a plate with an increased complexity. The applied rotation at the end of the plate is $\phi = \pi$. The magnitude of the displacements is plotted in the solid and the axial strains ϵ are plotted in the beams. Figure is taken from the author's article [138], permissions granted under the Creative Commons (CC BY) license.

6. Beam-to-solid surface coupling

In this chapter, the first truly mixed-dimensional 1D-2D mortar-type coupling approach for beam-to-solid surface (BTSS) coupling problems is proposed. The fibers / beams are represented by 1D Cosserat continua embedded in 3D space, whereas the solid body is modeled as a classical 3D Boltzmann continuum. The 1D beams are coupled to the 2D surfaces (the boundaries) of the 3D continua, thus resulting in a mixed-dimensional 1D-2D coupling problem. The constraint equations are discretized with a mortar-type approach. To the best of the author's knowledge, the proposed 1D-2D mortar-type coupling approach for BTSS coupling problems describes a novel extension of the previously presented positional beam-to-solid volume (BTSV-POS, Chapter 4) and rotational beam-to-solid volume (BTSV-ROT, Chapter 5) coupling problems. Switching from a 1D-3D to a 1D-2D mixed-dimensional coupling introduces two additional surface-specific challenges: (i) The positional BTSS coupling (BTSS-POS) constraints between the beam and the solid surface depend on the surface normal vector. Especially in the discretized problem, consistent treatment of the surface normal vector can become cumbersome. Therefore, various possible simplifications of the positional coupling constraints (BTSS-POS-(\cdot)) are presented. One of the main scientific contribution of this chapter is the demonstration that, in the general case of non-matching 1D-2D interfaces, only a fully consistent handling of the surface normal vector within the positional coupling constraints fulfills fundamental mechanical properties and gives accurate results. Exact conservation of linear and angular momentum is shown for the resulting 1D-2D coupling scheme. This is the first time that exact conservation of angular momentum is shown for a surface coupling scheme with non-vanishing surface normal distance. (ii) For rotational BTSS (BTSS-ROT) coupling a suitable solid orientation field is required on the solid surface. A detailed discussion on suitable solid triad fields within a solid volume is given in Section 5.2. However, a direct application of those to solid surfaces leads to unwanted effects, i.e., the solid surface orientation depending on the deformations inside the solid volume. Therefore, the second main scientific contribution of this chapter is presented: the construction of a suitable solid surface triad field. In the remainder of this thesis, BTSS-FULL refers to positional *and* rotational BTSS coupling. Accordingly, BTSS-FULL-(\cdot) is the specific combination of the positional coupling variant BTSS-POS-(\cdot) and rotational coupling.

6.1. Problem formulation

In this chapter, a quasi-static 3D finite deformation BTSS-FULL coupling problem as shown in Figure 6.1 is considered. The BTSS-FULL method couples all six cross-section degrees of freedom of the beam to the solid surface. This is realized by coupling the positions of the beam centerline as well as the orientation of the beam cross-section to the solid surface. One advantage of a 1D-2D coupling approach solely enforced at the beam centerline is the decoupling of the positional and rotational coupling conditions, i.e., both of them can be formulated independently.

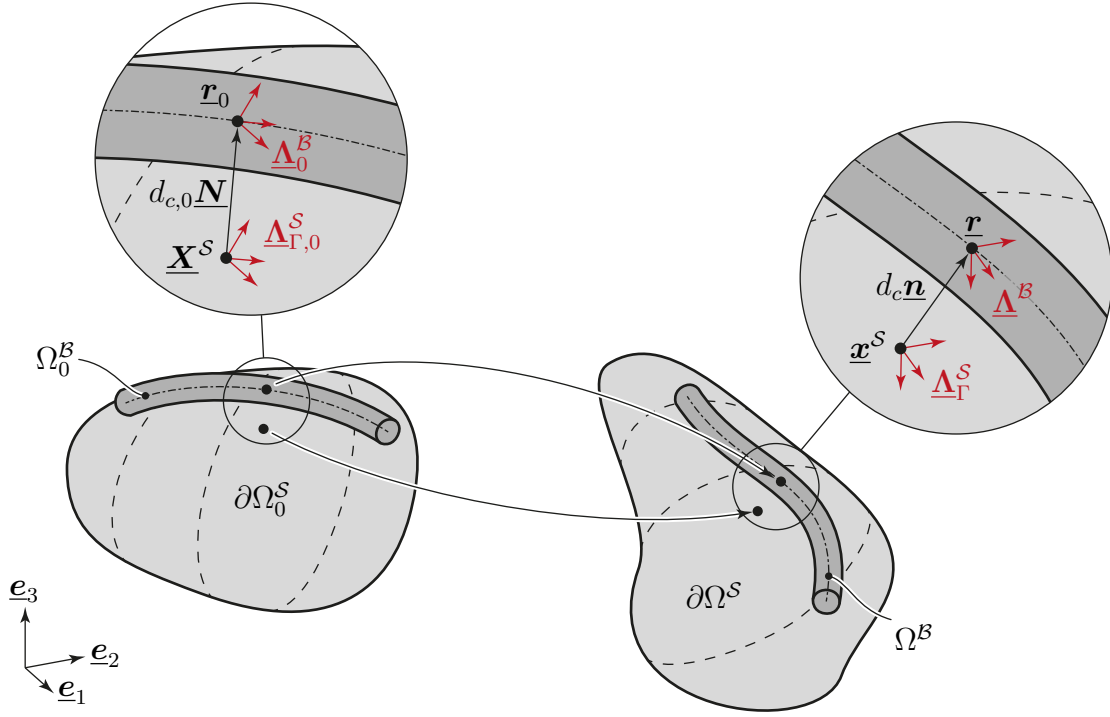


Figure 6.1.: Notation of the finite deformation BTSS coupling problem.

For embedded beam-to-solid volume (BTSV) coupling problems such an approach is presented in Chapters 4 and 5. The same general strategy is followed here for BTSS coupling problems, where two sets of coupling constraints are defined, the positional coupling constraints (BTSS-POS) and the rotational coupling constraints (BTSS-ROT). The principle of virtual work serves as basis for the employed finite element method and reads

$$\delta W^S + \delta W_{\text{SR}}^B + \delta \Pi_\lambda^U + \delta \Pi_\lambda^R = 0. \quad (6.1)$$

where δW^S and δW_{SR}^B are the virtual work of the pure solid problem and pure beam problem, respectively. Furthermore, $\delta \Pi_\lambda^U$ and $\delta \Pi_\lambda^R$ are the virtual work contributions of the positional and rotational surface coupling constraints, respectively. As was the case with the BTSV-FULL scheme presented in the previous chapter, only beam elements based on the Simo–Reissner beam theory are considered in this chapter.

Remark 6.1. In this thesis the solid surface is exclusively considered as a boundary of a three dimensional solid volume. In many of the practically relevant applications of BTSS problems, the solid's dimensions normal to the coupling surface are small compared to the overall dimensions, and therefore, the solid can be represented by a continuum mechanics shell theory. The presented BTSS coupling and contact methods in this thesis are directly applicable to beam-to-shell coupling problems, where the solid surface is modeled using shell finite elements.

Remark 6.2. In the following, the solid surface is parameterized with the two surface parameter coordinates ξ^S and η^S , introduced in the finite element formulation of the solid, cf. Section 2.3.1. To be consistent with the presented geometrically exact beam theory, cf. Section 2.2.2, the beam

centerline is parameterized with the arc-length of the undeformed beam centerline s , which can later be identified as the finite element parameter coordinate ξ^B in the discretized setting.

6.1.1. Closest point projection

In the BTSS-FULL coupling problem, cf. Figure 6.1, no requirements on the initial beam position relative to the solid surface exist. This is illustrated in Figure 6.2. Obviously, the coupling scheme has to be applicable to cases where the beam centerline curve lies on the solid surface, cf. Figure 6.2(a), and cases where the beam centerline is offset by the cross-section radius in surface normal direction, cf. Figure 6.2(b). However, also general cases, where no strict requirements on the reference placement of the beam centerline relative to the solid surface are made, are considered in the presented coupling schemes, cf. Figure 6.2(c). The only requirement considered in this chapter, is a unique closest point projection of each beam centerline point onto the solid surface. For the envisioned application cases, it can be assumed that a unique solution of the closest point projection exists in the vicinity of each beam centerline point \underline{r}_0 , cf. [76]. In order to formulate the closest point projection, the beam centerline is parameterized with the arc-length along the undeformed beam centerline $s \in \mathbb{R}$, and the solid surface is parameterized with the two surface parameter coordinates $\xi^S \in \mathbb{R}$ and $\eta^S \in \mathbb{R}$. In the reference configuration each point $\underline{r}_0(s)$ on the beam centerline is assigned a corresponding closest point $\underline{\mathbf{X}}^S(\xi_c^S, \eta_c^S)$ on the solid surface, where $\xi_c^S = \xi_c^S(s)$ and $\eta_c^S = \eta_c^S(s)$ are the surface parameter coordinates of the closest point. The closest point can be found by formulating a unilateral minimal distance problem in the reference configuration:

$$d_{c,0}(s) := \min_{\xi^S, \eta^S} d(s, \xi^S, \eta^S) = d(s, \xi_c^S, \eta_c^S) \quad (6.2)$$

with

$$d(s, \xi^S, \eta^S) = \|\underline{r}_0(s) - \underline{\mathbf{X}}^S(\xi^S, \eta^S)\|. \quad (6.3)$$

The two orthogonality conditions obtained from the minimal distance problem (6.2) read

$$\begin{aligned} \underline{\mathbf{X}}_{,\xi}^S(\xi^S, \eta^S)^T (\underline{r}_0(s) - \underline{\mathbf{X}}^S(\xi^S, \eta^S)) &= 0 \\ \underline{\mathbf{X}}_{,\eta}^S(\xi^S, \eta^S)^T (\underline{r}_0(s) - \underline{\mathbf{X}}^S(\xi^S, \eta^S)) &= 0. \end{aligned} \quad (6.4)$$

For a given beam coordinate s , these conditions can be solved for the unknown surface coordinates ξ^S and η^S . The non-trivial solution of (6.4) requires the surface directors $\underline{\mathbf{X}}_{,\xi}^S = \partial \underline{\mathbf{X}}^S / \partial \xi^S$ and $\underline{\mathbf{X}}_{,\eta}^S = \partial \underline{\mathbf{X}}^S / \partial \eta^S$ to be orthogonal to the relative vector between the surface point and the beam centerline point, i.e., this relative vector is parallel to the reference outward pointing surface normal vector $\underline{\mathbf{N}} \in \mathbb{R}^3$, i.e.,

$$\underline{r}_0(s) - \underline{\mathbf{X}}^S(\xi_c^S, \eta_c^S) = d_{c,0}(s) \underline{\mathbf{N}}(\xi_c^S, \eta_c^S), \quad (6.5)$$

with

$$\underline{\mathbf{N}}(\xi^S, \eta^S) = \frac{\underline{\mathbf{X}}_{,\xi}^S(\xi^S, \eta^S) \times \underline{\mathbf{X}}_{,\eta}^S(\xi^S, \eta^S)}{\|\underline{\mathbf{X}}_{,\xi}^S(\xi^S, \eta^S) \times \underline{\mathbf{X}}_{,\eta}^S(\xi^S, \eta^S)\|}. \quad (6.6)$$

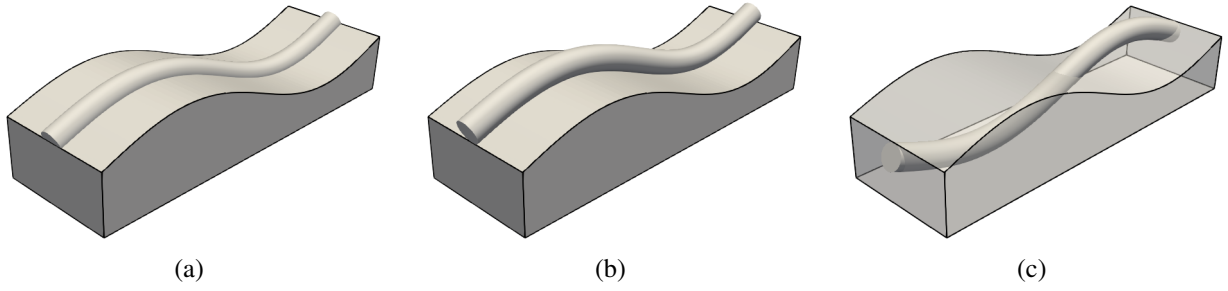


Figure 6.2.: Illustration of possible BTSS coupling problems – a curved beam on a matching curved solid surface (a), a curved beam centerline offset by the cross-section radius in surface normal direction (b) and a general non-matching case (c).

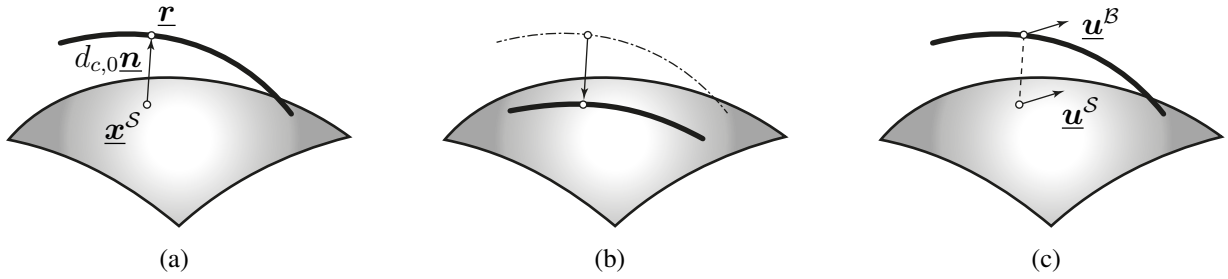


Figure 6.3.: Illustration of the three different BTSS-POS coupling variants. Consistent positional coupling (BTSS-POS-CONS) via the surface normal vector (a), forced reference configuration coupling (BTSS-POS-REF) by forcing beam centerline points to lie on the solid surface (b) and displacement coupling (BTSS-POS-DISP), where the displacement of beam centerline and solid surface are coupled (c). The BTSS-POS-REF and BTSS-POS-DISP variants are commonly used in classical surface-to-surface mesh tying problems [112].

6.1.2. Positional beam-to-solid surface coupling

In this section, three different variants of the BTSS-POS coupling constraints are presented and subsequently compared to each other in Section 6.4. The first presented variant is consistent with the kinematic relations between beam centerline and solid surface. The resulting coupling terms contain the surface normal vector, i.e., the coupling terms become non-linear. Furthermore, the second derivative of the surface normal vector is required for a consistent linearization of the problem, as required for tangent-based nonlinear solution schemes. To avoid this computationally expensive linearization, two additional variants to formulate the translational coupling constraints, commonly used in classical surface-to-surface mesh tying problems [112], will be investigated. Both of them do not require an evaluation of the current surface normal vector or its derivatives, and the resulting coupling operators only depend on the reference configuration, i.e., they are constant. The three different coupling variants are visualized in Figure 6.3.

6.1.2.1. Consistent positional coupling

The BTSS-POS coupling constraints are exclusively formulated along the beam centerline and couple the beam and solid material points associated by (6.5) to each other. For the considered variant, the surface normal distance d_c , at each beam centerline point, shall be constant over the simulation (pseudo) time, i.e., $d_c \equiv d_{c,0}$. Therefore, the coupling equations in the current configuration can be formulated as

$$\underline{\mathbf{r}}(s) - \underline{\mathbf{x}}^S(\xi_c^S, \eta_c^S) - d_{c,0}(s) \underline{\mathbf{n}}(\xi_c^S, \eta_c^S) = \underline{\mathbf{0}} \quad \text{on} \quad \Gamma_c. \quad (6.7)$$

The current normal vector is defined in analogy to the reference normal vector (6.6), i.e.,

$$\underline{\mathbf{n}}(\xi_c^S, \eta_c^S) = \frac{\underline{\mathbf{x}}_{,\xi}^S(\xi_c^S, \eta_c^S) \times \underline{\mathbf{x}}_{,\eta}^S(\xi_c^S, \eta_c^S)}{\|\underline{\mathbf{x}}_{,\xi}^S(\xi_c^S, \eta_c^S) \times \underline{\mathbf{x}}_{,\eta}^S(\xi_c^S, \eta_c^S)\|}, \quad (6.8)$$

with the current surface directors $\underline{\mathbf{x}}_{,\xi}^S = \partial \underline{\mathbf{x}}^S / \partial \xi^S$ and $\underline{\mathbf{x}}_{,\eta}^S = \partial \underline{\mathbf{x}}^S / \partial \eta^S$. The constraints (6.7) are enforced along the one-dimensional coupling domain $\Gamma_c \subseteq \Omega_0^B$ between the beam centerline and the solid surface, i.e., the part of the beam that is coupled to the solid surface. In the following considerations, the explicit dependency on the beam and solid parameter coordinates will mostly be omitted for improved readability.

In the remainder of this thesis, the positional coupling constraints (6.7) will be referred to as the *consistent* (BTSS-POS-CONS) surface coupling variant. The name refers to the fact, that the coupling definition is consistent with the kinematic relations between solid surface and beam centerline, cf. Figure 6.3(a). Furthermore, it will be shown that this variant leads to vanishing constraint forces in the (undeformed) reference configuration and exact conservation of linear and angular momentum in the discretized coupled system, cf. Section 6.3.4.1.

The Lagrange multiplier method is used to weakly enforce the coupling constraints (6.7). Therefore, a Lagrange multiplier vector field $\underline{\lambda}^U(s) \in \mathbb{R}^3$, defined along the beam centerline, is introduced. The total Lagrange multiplier potential reads:

$$\delta \Pi_\lambda^U = \int_{\Gamma_c} \underline{\lambda}^{UT} (\underline{\mathbf{r}} - \underline{\mathbf{x}}^S - d_{c,0} \underline{\mathbf{n}}) \, ds. \quad (6.9)$$

Variation of the Lagrange multiplier potential leads to the constraint contribution to the weak form,

$$\delta \Pi_\lambda^U = \underbrace{\int_{\Gamma_c} \delta \underline{\lambda}^{UT} (\underline{\mathbf{r}} - \underline{\mathbf{x}}^S - d_{c,0} \underline{\mathbf{n}}) \, ds}_{\delta W_\lambda^U} + \underbrace{\int_{\Gamma_c} \underline{\lambda}^{UT} (\delta \underline{\mathbf{r}} - \delta \underline{\mathbf{x}}^S - d_{c,0} \delta \underline{\mathbf{n}}) \, ds}_{-\delta W_c^U}. \quad (6.10)$$

Therein, δW_λ^U and δW_c^U are the variational form of the coupling constraints and the virtual work of the generalized coupling forces $\underline{\lambda}^U$, respectively. It is well-known from the geometrically exact beam theory that the variation of the centerline position $\delta \underline{\mathbf{r}}$ is work-conjugated with the resulting point-wise beam centerline load. Therefore, the generalized coupling forces $\underline{\lambda}^U$ can be directly interpreted as the coupling line load acting on the beam centerline. On the solid side, the variation of the solid displacement $\delta \underline{\mathbf{x}}^S$ is work conjugated with a point load acting on the solid, i.e., the generalized coupling forces also act as a line load on the solid. Additionally, the

term $d_{c,0}(\underline{\lambda}^u)^T \delta \underline{n}$ arises, which represents a point-wise moment contribution of the coupling line load acting on the solid surface. If the beam centerline exactly lies on the beam surface, i.e., $d_{c,0} \equiv 0$, cf. Figure 6.2(a), the BTSS-POS-CONS method (in the space continuous form) is identical to the BTSSV-POS method, cf. Chapter 4. The drawback of the BTSS-POS-CONS variant is that for general scenarios the weak form contains the surface normal vector variation, thus requiring the second derivatives of the surface normal vector for a consistent linearization of $\delta \underline{n}$, as required for tangent-based nonlinear solution schemes. Furthermore, the positional coupling operators become non-linear, i.e., they depend on the current configuration.

Remark 6.3. In the considered cases of BTSS coupling, $d_{c,0} = R/2$ is an obvious physical choice for the surface normal distance, i.e., the beam is offset of the surface by half of the cross-section radius, cf. Figure 6.2(b). However, even in cases where there is no physical motivation for a non-vanishing surface normal distance, cf. Figure 6.2(c), it can be beneficiary to employ the consistent positional coupling constraints (6.7). For example: if the continuous geometry description of beam and solid does not match, e.g., due to an incompatibility in the employed modeling software, not accounting for the resulting surface normal distance can lead to non-physical results, cf. Section 6.4.

6.1.2.2. Forced reference configuration coupling

The considered 1D-2D line-to-surface coupling constraints are very similar to the ones in classical 2D-2D surface-to-surface coupling problems, cf. [41, 103, 112]. The main difference is that in the surface-to-surface case the space continuous interfaces are usually matching, i.e., the normal distance vanishes and the coupling constraints (6.7) can be simplified to

$$\underline{r} - \underline{x}^S = \underline{0} \quad \text{on} \quad \Gamma_c. \quad (6.11)$$

This type of positional coupling constraint will be referred to as the *forced reference configuration* surface coupling (BTSS-POS-REF). The Lagrange multiplier coupling contributions to the global weak form read

$$\delta W_{\lambda, \text{REF}}^u = \int_{\Gamma_c} \delta \underline{\lambda}^{uT} (\underline{r} - \underline{x}^S) \, ds \quad (6.12)$$

$$-\delta W_{c, \text{REF}}^u = \int_{\Gamma_c} \underline{\lambda}^{uT} (\delta \underline{r} - \delta \underline{x}^S) \, ds. \quad (6.13)$$

In this case, the surface normal vector is not contained in the resulting coupling equations, simplifying the numerical evaluation of the coupling terms. However, the coupling constraints (6.11) in the reference configuration are only fulfilled if the beam centerline lies exactly on the solid surface, i.e., $d_{c,0} \equiv 0$. If the beam centerline is not a subset of the solid surface, the coupling constraints (6.11) will lead to non-vanishing virtual work contributions in the reference configuration, i.e., initial stresses and deformations in the unloaded coupled system. In other words, the BTSS-POS-REF coupling conditions force the beam centerline to exactly lie on the solid surface, which is illustrated in Figure 6.3(b).

6.1.2.3. Displacement coupling

Another alternative coupling approach in surface-to-surface mesh tying is to directly couple the displacements instead of the positions in (6.11). This variant will be referred to as the *displacement* surface coupling (BTSS-POS-DISP). The BTSS-POS-DISP coupling constraints read,

$$\underline{\mathbf{u}}^B - \underline{\mathbf{u}}^S = \underline{\mathbf{0}} \quad \text{on} \quad \Gamma_c, \quad (6.14)$$

with the beam centerline displacement $\underline{\mathbf{u}}^B = \underline{\mathbf{r}} - \underline{\mathbf{r}}_0$. The Lagrange multiplier coupling contributions to the global weak form are

$$\delta W_{\lambda, \text{DISP}}^{\mathcal{U}} = \int_{\Gamma_c} \delta \underline{\boldsymbol{\lambda}}^{\mathcal{U}^T} (\underline{\mathbf{u}}^B - \underline{\mathbf{u}}^S) \, ds \quad (6.15)$$

$$-\delta W_{c, \text{DISP}}^{\mathcal{U}} = \int_{\Gamma_c} \underline{\boldsymbol{\lambda}}^{\mathcal{U}^T} (\delta \underline{\mathbf{u}}^B - \delta \underline{\mathbf{u}}^S) \, ds. \quad (6.16)$$

As is the case for the BTSS-POS-REF variant, the normal vector does not appear in the coupling constraints. In this case, the coupling conditions are always fulfilled in the reference configuration, no matter if the initial geometries of beam centerline and solid surface are matching or not. In [112] it is demonstrated, that displacement coupling (6.14) can lead to a coupling formulation that does not conserve angular momentum. This can be shown by inserting a constant virtual rotation $\delta \underline{\boldsymbol{\phi}}$, i.e., $\delta \underline{\mathbf{u}}^B = \delta \underline{\boldsymbol{\phi}} \times \underline{\mathbf{r}}$ and $\delta \underline{\mathbf{u}}^S = \delta \underline{\boldsymbol{\phi}} \times \underline{\mathbf{x}}^S$, into (6.16). To guarantee conservation of angular momentum the resulting virtual work has to vanish, cf. [57, 84, 112]. This gives the condition for conservation of angular momentum

$$\int_{\Gamma_c} (\delta \underline{\boldsymbol{\phi}} \times (\underline{\mathbf{r}} - \underline{\mathbf{x}}^S))^T \underline{\boldsymbol{\lambda}}^{\mathcal{U}} \, ds = 0. \quad (6.17)$$

This condition is only fulfilled if $\underline{\mathbf{r}} = \underline{\mathbf{x}}^S$, i.e., for matching interfaces. For general configurations of the beam and the solid, i.e., when the beam centerline is offset in surface normal direction, conservation of angular momentum is violated by the BTSS-POS-DISP variant. This can also be interpreted from a mechanical point of view: displacement coupling of two points (a point on the beam centerline and the corresponding projection point on the solid surface) that do not coincide in the reference configuration, cf. Figure 6.3(c), leads to a non-physical coupling moment which violates the conservation of angular momentum.

6.1.3. Rotational beam-to-solid surface coupling

Rotational beam-to-solid volume (BTSSV-ROT) coupling between an embedded geometrically exact beam with a Boltzmann continuum is presented in Chapter 5. There, it is shown that constraining the relative rotation (pseudo-) vector $\underline{\boldsymbol{\psi}}_{SB}$ between the current beam triad $\underline{\mathbf{A}}^B$ and a suitable solid triad $\underline{\mathbf{A}}^S$ along the beam centerline leads to an objective coupling scheme. This is in accordance to general cross-section interaction laws within the geometrically exact beam theory, cf. [94]. This type of rotational coupling scheme can also be adopted and extended for the presented case of BTSS coupling problems. The general approach is the same as in Chapter 5, but instead of a solid volume triad field, a suitable solid *surface* triad field has to be constructed. This

construction is presented in Section 6.2. The rotational coupling constants constrain the relative rotation vector between the beam triad and a corresponding solid surface triad $\underline{\Lambda}_\Gamma^S$, i.e.,

$$\underline{\psi}_{SB} = \underline{0} \quad \text{on} \quad \Gamma_c, \quad (6.18)$$

with

$$\underline{\psi}_{SB} = \text{rv}(\underline{\Lambda}_\Gamma^S \underline{\Lambda}^{BT}). \quad (6.19)$$

The Lagrange multiplier method is used to weakly enforce the rotational coupling constraints. The corresponding weak form has been derived and thoroughly discussed in Chapter 5 and will not be stated here.

6.2. Surface triad field

The rotational coupling conditions (6.18) constrain the relative rotation vector $\underline{\psi}_{SB}$ between the beam cross-section triad $\underline{\Lambda}^B$ and a corresponding solid surface triad $\underline{\Lambda}_\Gamma^S$. The solid is modeled as a Boltzmann continuum, i.e., it does not have any rotational degrees of freedom. Therefore, a suitable solid surface triad field has to be constructed as a function of the solid deformation field. The construction of solid triad fields is thoroughly discussed and analyzed in Section 5.2. There, two important attributes of the constructed triad field are identified: (i) The solid triad field has to be invariant with respect to an arbitrary rigid body rotation, such that the rotational coupling constraints (6.18) lead to an objective discrete coupling formulation. (ii) The resulting solid triad field should not constrain shear deformations in the beam cross-section plane, as this can result in spurious stiffening / locking effects of the coupled system. It is shown in Appendix B that the rotation tensor obtained via a polar decomposition of the (in-plane projection of the) solid deformation gradient fulfills both aforementioned properties and represents the solid material directors in an L_2 -optimal manner. Furthermore, a slightly modified construction of the solid triad is presented that fixes an averaged solid material director to the solid triad. In practice, this modified variant gives very similar results compared to the solid triad obtained from the polar decomposition and also fulfills both aforementioned properties. Moreover, this variant avoids the computationally expensive evaluation of the polar decomposition (and its second derivatives) at Gauss-point level. This section presents an extension of this solid triad definition to end up with a solid triad definition that is suitable for BTSS coupling problems

For the solid volume triads in Section 5.2 the solid deformation gradient \underline{F} was used. In theory, the solid volume triad definitions from Section 5.2 can be applied to the considered BTSS problem, where the solid deformation gradient is evaluated at the solid surface. However, in this case the surface triad field would not only depend on the surface deformation, but also on deformation inside the solid volume. This is illustrated in Figure 6.4, where the solid exhibits deformations inside the solid volume, while the surface geometry stays the same. The solid deformation gradient at the solid surface changes due to the deformation of material fibers inside the solid volume. However, from an intuitive physical point of view the *orientation* of the solid surface does not change. Therefore, a different approach is proposed in this section, where the resulting solid surface triad is constructed directly based on the surface kinematics, i.e., the two surface basis vectors and the surface normal vector.

The proposed construction of the surface triad is based on a material director $\underline{\tilde{g}}$ lying on the solid surface, in combination with the surface normal vector. The obvious and intuitive choice for this solid material director is the intersection between the beam cross-section plane and the solid surface tangent plane in the reference configuration, cf. Figure 6.5, which reads

$$\underline{\tilde{g}}_0 = \frac{\underline{N} \times \underline{g}_{1,0}^B}{\|\underline{N} \times \underline{g}_{1,0}^B\|}. \quad (6.20)$$

Theoretically, this definition of the solid material director can result in a singularity if the beam cross-section and the surface tangent plane are parallel to each other. However, since this would mean that the beam centerline is normal to the solid surface, this singularity will not be relevant for practical applications. The solid surface triad in the reference configuration can subsequently be constructed based on the solid material director and the solid surface normal vector, i.e.,

$$\underline{\tilde{\Lambda}}_{\Gamma,0}^S = [\underline{\tilde{g}}_0, \underline{N}, \underline{\tilde{g}}_0 \times \underline{N}]. \quad (6.21)$$

The solid material director in the current configuration $\underline{\tilde{g}}$ is calculated by applying the push-forward operator \underline{F} to the material director in the reference configuration, i.e., $\underline{\tilde{g}} = \underline{F} \underline{\tilde{g}}_0 / \|\underline{F} \underline{\tilde{g}}_0\|$. The previously mentioned dependency of the deformation gradient on deformations inside the solid volume does not affect this projection, as $\underline{\tilde{g}}_0$ lies within the solid surface, i.e., the projection only depends on the in-plane components of \underline{F} . With the current solid material director, the surface triad in the current configuration can be constructed in analogy to (6.21), i.e.,

$$\underline{\tilde{\Lambda}}_{\Gamma}^S = [\underline{\tilde{g}}, \underline{n}, \underline{\tilde{g}} \times \underline{n}]. \quad (6.22)$$

In a final step, the actual surface triad used for evaluation of the coupling terms has to be offset by a constant rotation, such that the rotational constraint equations (6.19) are fulfilled in the reference configuration. The final surface triad reads,

$$\underline{\Lambda}_{\Gamma}^S = \underline{\tilde{\Lambda}}_{\Gamma}^S \left(\underline{\tilde{\Lambda}}_{\Gamma,0}^S \right)^T \underline{\Lambda}_0^B. \quad (6.23)$$

With this definition, it is straight-forward to show that the surface triad in the reference configuration is equal to the beam reference triad, i.e., $\underline{\Lambda}_{\Gamma,0}^S = \underline{\Lambda}_0^B$ and therefore, the rotational coupling constraints are fulfilled (by definition) in the reference configuration. It can be shown that the surface triad definition (6.23) is invariant with respect to a superposed rigid body rotation, thus fulfilling requirement (i) stated above. Furthermore, since the surface triad is constructed based on a single material director $\underline{\tilde{g}}$ and the surface normal vector, a constraining of shear deformations on the solid surface can not occur. Therefore, the presented solid surface triad also fulfills requirement (ii).

Remark 6.4. To ensure a unique closest point projection in the spatially discretized problem, an averaged C^0 -continuous surface normal field is presented in Section 6.3.1. Due to the averaging procedure, the resulting averaged normal is not point-wise orthogonal to the solid surface, cf. Figure 6.6. With the definition of the surface triad (6.22), this would result in a non-orthonormal tensor $\underline{\Lambda}_{\Gamma}^S \notin SO^3$. Therefore, the actual point-wise orthogonal normal vector on the surface, not the averaged normal vector, is used in the evaluation of the surface triad.

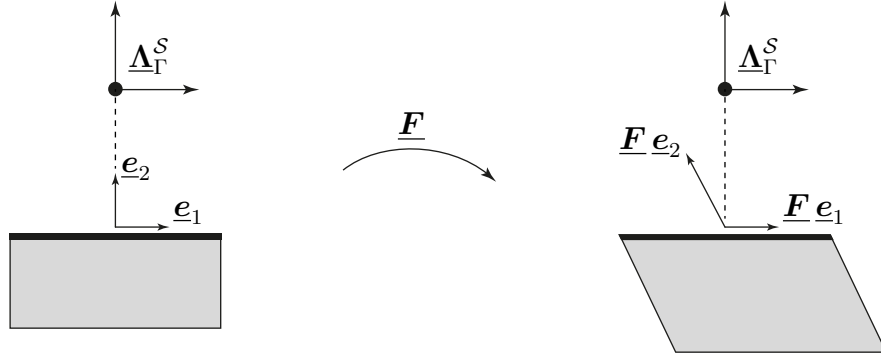


Figure 6.4.: Illustration of the influence of out of plane solid deformations on the solid deformation gradient at the solid surface.

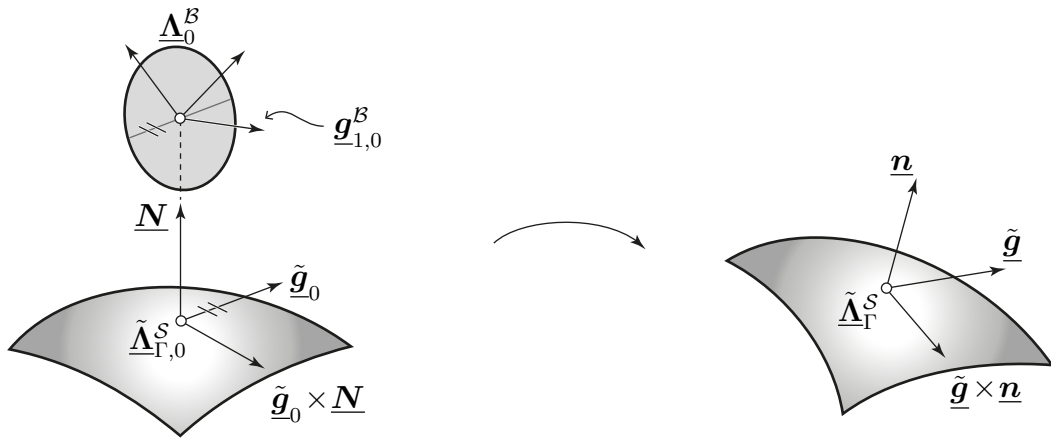


Figure 6.5.: Construction of the solid surface triad.

6.3. Spatial discretization

The spatial discretization of the BTSS coupling scheme is exclusively based on the finite element method. In Section 2.3.1 it is assumed, that the solid parameter coordinates are chosen such that the third parameter coordinate ζ^S is constant at the solid surface, i.e., the solid surface $\partial\Omega_{0,h}^S$ can be parameterized with only the first two solid parameter coordinates ξ^S and η^S . The kinematics of the solid surface only depend on the finite element nodes on the surface. The spatial interpolation of the solid surface is given by

$$\underline{\mathbf{X}}_h^S = \sum_{k=1}^{n_\Gamma^S} N_k(\xi^S, \eta^S) \underline{\hat{\mathbf{X}}}_k^S \quad (6.24)$$

$$\underline{\mathbf{u}}_h^S = \sum_{k=1}^{n_\Gamma^S} N_k(\xi^S, \eta^S) \underline{\hat{\mathbf{d}}}_k^S \quad (6.25)$$

$$\delta \underline{\mathbf{u}}_h^S = \sum_{k=1}^{n_\Gamma^S} N_k(\xi^S, \eta^S) \delta \underline{\hat{\mathbf{d}}}_k^S, \quad (6.26)$$

where, n_Γ^S is the number of solid surface nodes.

6.3.1. Evaluation of solid surface normal field

The closest point projection (6.2) of a point along the beam centerline to the solid surface requires a C^0 -continuous normal field to guarantee a unique solution. If the solid discretization is based on isogeometric solid elements with higher order continuity, then the surface normal field can be directly calculated from the kinematic description of the discretized surface. The resulting surface normal field is at least C^0 -continuous and a unique closest point projection can be guaranteed. If a standard C^0 -continuous Lagrangian finite element interpolation is employed in the solid domain, the surface normal field obtained from the kinematic description of the discretized surface is not continuous. This can result in an undefined closest point projection. However, the BTSS coupling scheme presented in this chapter is also applicable to such discretizations. This is achieved by constructing a C^0 -continuous normal field based on averaged nodal normal vectors, as is common in surface-to-surface problems, cf. [109, 154].

The main idea behind the construction of an averaged surface normal field is illustrated in Figure 6.6. An averaged nodal normal is defined at each surface node k as

$$\underline{\mathbf{n}}_{\text{AVG},k} = \frac{\sum_{e=1}^{n_{\text{adj},k}} \underline{\mathbf{n}}_k^{(e)}}{\left\| \sum_{e=1}^{n_{\text{adj},k}} \underline{\mathbf{n}}_k^{(e)} \right\|}, \quad (6.27)$$

where $\underline{\mathbf{n}}_k^{(e)}$ is the outward pointing surface normal vector at element (e) , evaluated at node k . Furthermore, $n_{\text{adj},k}$ represents the number of adjacent faces at node k . The final normal vector field is then defined via a FE interpolation, i.e.,

$$\underline{\mathbf{n}}_h(\xi^S, \eta^S) = \frac{\sum_{k=1}^{n_\Gamma^S} N_k(\xi^S, \eta^S) \underline{\mathbf{n}}_{\text{AVG},k}}{\left\| \sum_{k=1}^{n_\Gamma^S} N_k(\xi^S, \eta^S) \underline{\mathbf{n}}_{\text{AVG},k} \right\|}. \quad (6.28)$$

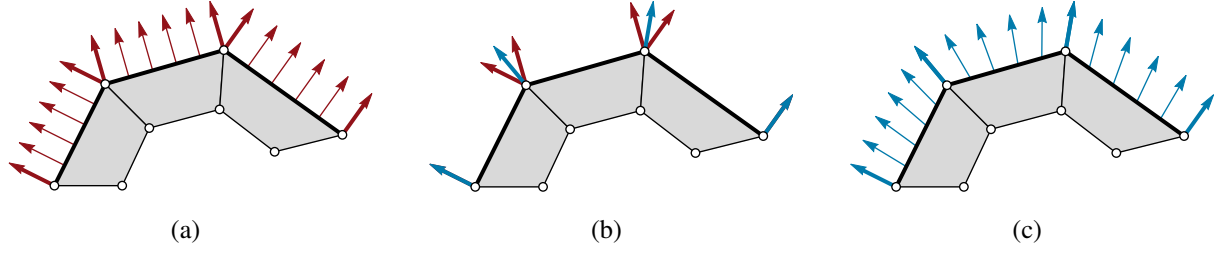


Figure 6.6.: Illustration of the constructed C^0 -continuous surface normal field, for an exemplary planar problem with three elements. Discontinuous standard surface normal field based on the finite element surface kinematics (a), averaged nodal normals (b) and C^0 -continuous interpolated averaged nodal normal field (c).

Such a surface normal field is guaranteed to be C^0 -continuous, i.e., it mimics a C^1 -continuous surface interpolation. However, this procedure increases the computational effort required to evaluate the normal field and its derivatives. Additionally, the connectivity between element degrees of freedom is increased, as the normal on a solid face element depends on the degrees of freedom of the adjacent faces.

6.3.2. Mortar-type coupling of beam-to-solid surface normal distance

Similar to the BTSV-POS method, a mortar-type coupling approach for all three positional coupling variants is employed, i.e., the Lagrange multiplier field $\underline{\lambda}^{\mathcal{U}}$ introduced in Section 6.1.2 is also interpolated with finite element shape functions, cf. Chapter 4 and [17, 109, 150]. The discrete Lagrange multiplier field is defined along the discretized beam centerline. Its finite element interpolation reads

$$\underline{\lambda}_h^{\mathcal{U}} = \sum_{j=1}^{n^{\mathcal{U}}} \Phi_j^{\mathcal{U}}(\xi^{\mathcal{B}}) \hat{\underline{\lambda}}_j^{\mathcal{U}}, \quad (6.29)$$

where $n^{\mathcal{U}}$ is the total number of Lagrange multiplier nodes, $\Phi_j^{\mathcal{U}}$ is the Lagrange multiplier shape function of the node j , and $\hat{\underline{\lambda}}_j^{\mathcal{U}} \in \mathbb{R}^3$ is the Lagrange multiplier at node j . Although defined along the beam centerline, there is no requirement for the Lagrange multiplier shape functions to match the shape functions used for interpolation of the beam centerline. Even the number of nodes can differ, i.e., $n^{\mathcal{U}} \neq n^{\mathcal{B}}$.

The choice of Lagrange multiplier basis functions is important for the mathematical properties of the resulting discretized system. Generally speaking, the Lagrange multiplier interpolations must fulfill an inf-sup condition to guarantee stability of the mixed finite element method. We circumvent the inf-sup stability condition by employing a penalty regularized Lagrange multiplier approach. Detailed discussions regarding this topic can be found in Chapter 4 for the purely positional coupling BTSV-POS and in Chapter 5 for rotational coupling BTSV-ROT. The extensive studies and discussions in these chapters show, that a linear interpolation of the Lagrange multipliers combined with a node-wise weighted penalty regularization generally leads to a stable finite element formulation of the coupled problem. Instabilities might only occur if the beam

finite elements become significantly shorter than the solid finite elements. However, as discussed in Chapter 3, such BTS element size ratios are typically not relevant for the envisioned scope of applications.

6.3.2.1. Consistent positional coupling

Inserting the finite element interpolations into the first term of (6.10) yields the discrete variation of the BTSS-POS-CONS coupling constraints,

$$\begin{aligned} \delta W_{\lambda,h}^{\mathcal{U}} = & \sum_{l=1}^{n^{\mathcal{B}}} \sum_{j=1}^{n^{\mathcal{U}}} \delta \hat{\underline{\lambda}}_j^{\mathcal{U}T} \underbrace{\int_{\Gamma_{c,h}} \Phi_j^{\mathcal{U}} \mathbf{H}_l \, ds}_{\mathbf{D}^{\mathcal{U}[j,l]}} \hat{\mathbf{x}}_l^{\mathcal{B}} - \sum_{k=1}^{n_{\Gamma}^{\mathcal{S}}} \sum_{j=1}^{n^{\mathcal{U}}} \delta \hat{\underline{\lambda}}_j^{\mathcal{U}T} \underbrace{\int_{\Gamma_{c,h}} \Phi_j^{\mathcal{U}} N_k \, ds}_{\mathbf{M}^{\mathcal{U}[j,k]}} \mathbf{I}^{3 \times 3} \hat{\underline{\mathbf{x}}}_k^{\mathcal{S}} \\ & - \sum_{j=1}^{n^{\mathcal{U}}} \delta \hat{\underline{\lambda}}_j^{\mathcal{U}T} \underbrace{\int_{\Gamma_{c,h}} \Phi_j^{\mathcal{U}} d_{c,0} \underline{\mathbf{n}}_h \, ds}_{\mathbf{q}^{\mathcal{U}[j]}} \end{aligned} \quad (6.30)$$

Here, two local matrices with mass matrix-like structure can be identified: $\mathbf{D}^{\mathcal{U}[j,l]} \in \mathbb{R}^{3 \times 6}$ and $\mathbf{M}^{\mathcal{U}[j,k]} \in \mathbb{R}^{3 \times 3}$, i.e., the so-called mortar matrices. Furthermore, the abbreviation $\mathbf{q}^{\mathcal{U}[j]} \in \mathbb{R}^3$ is introduced, referring to the integral of the surface normal distance weighted with the Lagrange multiplier shape function of the Lagrange multiplier node j . Again, inserting the finite element interpolations into the second term of (6.10) yields the discrete virtual work of the coupling forces,

$$\begin{aligned} \delta W_{c,h}^{\mathcal{U}} = & \sum_{l=1}^{n^{\mathcal{B}}} \sum_{j=1}^{n^{\mathcal{U}}} \left(\mathbf{D}^{\mathcal{U}[j,l]} \delta \hat{\underline{\mathbf{d}}}_l^{\mathcal{B}} \right)^T \hat{\underline{\lambda}}_j^{\mathcal{U}} - \sum_{k=1}^{n_{\Gamma}^{\mathcal{S}}} \sum_{j=1}^{n^{\mathcal{U}}} \left(\mathbf{M}^{\mathcal{U}[j,k]} \delta \hat{\underline{\mathbf{d}}}_k^{\mathcal{S}} \right)^T \hat{\underline{\lambda}}_j^{\mathcal{U}} \\ & - \sum_{k=1}^{n_{\Gamma}^{\mathcal{S}}} \sum_{j=1}^{n^{\mathcal{U}}} \left(\underbrace{\int_{\Gamma_{c,h}} d_{c,0} \underline{\mathbf{n}}_h \Phi_j^{\mathcal{U}} \, ds}_{-\mathbf{Q}_{\lambda_s}^{\mathcal{U}[j,k]} \delta \hat{\underline{\mathbf{d}}}_k^{\mathcal{S}}} \right)^T \hat{\underline{\lambda}}_j^{\mathcal{U}} \end{aligned} \quad (6.31)$$

where the abbreviation $\mathbf{Q}_{\lambda_s}^{\mathcal{U}[j,k]} = -\partial \mathbf{q}^{\mathcal{U}[j]} / \partial \hat{\underline{\mathbf{d}}}_k^{\mathcal{S}}$ is introduced. With equations (6.30) and (6.31) the global virtual work of the coupling contributions reads

$$\delta \Pi_{\lambda,h}^{\mathcal{U}} = \begin{bmatrix} \delta \mathbf{d}^{\mathcal{S}T} & \delta \mathbf{d}^{\mathcal{B}T} & \delta \lambda^{\mathcal{U}T} \end{bmatrix} \begin{bmatrix} (-\mathbf{M}^{\mathcal{U}} + \mathbf{Q}_{\lambda_s}^{\mathcal{U}})^T \lambda^{\mathcal{U}} \\ \mathbf{D}^{\mathcal{U}T} \lambda^{\mathcal{U}} \\ \mathbf{D}^{\mathcal{U}} \mathbf{x}^{\mathcal{B}} - \mathbf{M}^{\mathcal{U}} \mathbf{x}^{\mathcal{S}} - \mathbf{q}^{\mathcal{U}} \end{bmatrix}. \quad (6.32)$$

Here, $\mathbf{D}^{\mathcal{U}} \in \mathbb{R}^{3n^{\mathcal{V}} \times 6n^{\mathcal{B}}}$, $\mathbf{M}^{\mathcal{U}} \in \mathbb{R}^{3n^{\mathcal{V}} \times 3n^{\mathcal{S}}}$, $\mathbf{q}^{\mathcal{U}} \in \mathbb{R}^{3n^{\mathcal{V}} \times 1}$ and $\mathbf{Q}_{\lambda_s}^{\mathcal{U}} \in \mathbb{R}^{3n^{\mathcal{V}} \times 3n^{\mathcal{S}}}$ are the globally assembled matrices and vector of the previously defined local ones. The following residual vectors can be identified in (6.32)

$$\begin{bmatrix} \mathbf{r}_s^{\mathcal{U}} \\ \mathbf{r}_r^{\mathcal{U}} \\ \mathbf{g}^{\mathcal{U}} \end{bmatrix} = \begin{bmatrix} (-\mathbf{M}^{\mathcal{U}} + \mathbf{Q}_{\lambda_s}^{\mathcal{U}})^T \lambda^{\mathcal{U}} \\ \mathbf{D}^{\mathcal{U}T} \lambda^{\mathcal{U}} \\ \mathbf{D}^{\mathcal{U}} \mathbf{x}^{\mathcal{B}} - \mathbf{M}^{\mathcal{U}} \mathbf{x}^{\mathcal{S}} - \mathbf{q}^{\mathcal{U}} \end{bmatrix}. \quad (6.33)$$

Here, $\mathbf{r}_s^{\mathcal{U}}$ and $\mathbf{r}_r^{\mathcal{U}}$ are the coupling residual force vectors acting on the solid and beam degrees of freedom, respectively, and $\mathbf{g}^{\mathcal{U}}$ is the residual vector of the constraint equations. A linearization of the coupling residuum vectors with respect to the discrete degrees of freedom is required for the Newton–Raphson algorithm employed to solve the nonlinear system of equations resulting from the discretization process. The linearization of the positional coupling contributions reads:

$$\text{Lin} \left(\begin{bmatrix} \mathbf{r}_s^{\mathcal{U}} \\ \mathbf{r}_r^{\mathcal{U}} \\ \mathbf{g}^{\mathcal{U}} \end{bmatrix} \right) = \begin{bmatrix} \mathbf{0} \\ \mathbf{0} \\ \mathbf{g}^{\mathcal{U}} \end{bmatrix} + \begin{bmatrix} \mathbf{Q}_{ss}^{\mathcal{U}} & \mathbf{0} & -\mathbf{M}^{\mathcal{U}\text{T}} + (\mathbf{Q}_{\lambda s}^{\mathcal{U}})^{\text{T}} \\ \mathbf{0} & \mathbf{0} & \mathbf{D}^{\mathcal{U}\text{T}} \\ -\mathbf{M}^{\mathcal{U}} + \mathbf{Q}_{\lambda s}^{\mathcal{U}} & \mathbf{D}^{\mathcal{U}} & \mathbf{0} \end{bmatrix} \begin{bmatrix} \Delta \mathbf{d}^{\mathcal{S}} \\ \Delta \mathbf{d}^{\mathcal{B}} \\ \lambda^{\mathcal{U}} \end{bmatrix}, \quad (6.34)$$

where the abbreviation $\mathbf{Q}_{ss}^{\mathcal{U}} = \partial ((\mathbf{Q}_{\lambda s}^{\mathcal{U}})^{\text{T}} \lambda^{\mathcal{U}}) / \partial \mathbf{d}^{\mathcal{S}}$ is introduced. In practice, all integrals are numerically evaluated using segment-based integration along the beam centerline, which avoids integration over discontinuities, cf. Section 4.2.4 and [45]. Each subsegment is integrated using Gauss–Legendre quadrature with a fixed number of integration points for all coupling terms, which is required to ensure conservation of linear and angular momentum, cf. Section 6.3.4.1. Segment-based integration yields an accurate numerical evaluation of the coupling integrals and allows for the resulting coupling scheme to pass patch test-like problems, cf. Section 4.4.1. Furthermore, all derivatives explicitly stated in the discrete equations are evaluated using forward automatic differentiation (FAD), cf. [78], using the Sacado software package [121], which is part of the Trilinos project [143].

6.3.2.2. Forced reference configuration coupling

By neglecting the normal distance $d_{c,0}$, the BTSS-POS-REF variant of the positional coupling conditions (6.11) simplifies the coupling equations (6.7), such that the surface normal vector does not appear in the coupling equations anymore. The discrete coupling terms for the BTSS-POS-REF variant read

$$\begin{bmatrix} \mathbf{r}_s^{\mathcal{U}} \\ \mathbf{r}_r^{\mathcal{U}} \\ \mathbf{g}^{\mathcal{U}} \end{bmatrix}_{\text{REF}} = \begin{bmatrix} -\mathbf{M}^{\mathcal{U}\text{T}} \lambda^{\mathcal{U}} \\ \mathbf{D}^{\mathcal{U}\text{T}} \lambda^{\mathcal{U}} \\ \mathbf{D}^{\mathcal{U}} \mathbf{x}^{\mathcal{B}} - \mathbf{M}^{\mathcal{U}} \mathbf{x}^{\mathcal{S}} \end{bmatrix}. \quad (6.35)$$

It becomes clear, that the constraint equations in the reference configuration are only fulfilled if $\mathbf{D}^{\mathcal{U}} \mathbf{x}^{\mathcal{B}} - \mathbf{M}^{\mathcal{U}} \mathbf{x}^{\mathcal{S}} = \mathbf{0}$, where $\mathbf{x}^{\mathcal{B}} \in \mathbb{R}^{n^{\mathcal{B}}}$ and $\mathbf{x}^{\mathcal{S}} \in \mathbb{R}^{n^{\mathcal{S}}}$ are the global vectors containing the nodal reference positions (and tangents), respectively. If the condition is not fulfilled in the reference configuration, this coupling variant leads to initial (coupling) stresses in the system. The influence of the initial stresses within the BTSS-POS-DISP variant is analyzed in Section 6.4. The linearization of the coupling terms (6.35) reads

$$\text{Lin} \left(\begin{bmatrix} \mathbf{r}_s^{\mathcal{U}} \\ \mathbf{r}_r^{\mathcal{U}} \\ \mathbf{g}^{\mathcal{U}} \end{bmatrix}_{\text{REF}} \right) = \begin{bmatrix} \mathbf{0} \\ \mathbf{0} \\ \mathbf{g}^{\mathcal{U}} \end{bmatrix}_{\text{REF}} + \begin{bmatrix} \mathbf{0} & \mathbf{0} & -\mathbf{M}^{\mathcal{U}\text{T}} \\ \mathbf{0} & \mathbf{0} & \mathbf{D}^{\mathcal{U}\text{T}} \\ -\mathbf{M}^{\mathcal{U}} & \mathbf{D}^{\mathcal{U}} & \mathbf{0} \end{bmatrix} \begin{bmatrix} \Delta \mathbf{d}^{\mathcal{S}} \\ \Delta \mathbf{d}^{\mathcal{B}} \\ \lambda^{\mathcal{U}} \end{bmatrix}. \quad (6.36)$$

6.3.2.3. Displacement coupling

Another alternative positional coupling variant is the BTSS-POS-DISP variant (6.14). Therein, the normal distance between the beam and the solid surface is neglected and the displacements

are directly coupled to each other. The discrete coupling terms for the BTSS-POS-DISP variant read:

$$\begin{bmatrix} \mathbf{r}_s^{\mathcal{U}} \\ \mathbf{r}_r^{\mathcal{U}} \\ \mathbf{g}^{\mathcal{U}} \end{bmatrix}_{\text{DISP}} = \begin{bmatrix} -\mathbf{M}^{\mathcal{U}^T} \boldsymbol{\lambda}^{\mathcal{U}} \\ \mathbf{D}^{\mathcal{U}^T} \boldsymbol{\lambda}^{\mathcal{U}} \\ \mathbf{D}^{\mathcal{U}} \mathbf{d}^{\mathcal{B}} - \mathbf{M}^{\mathcal{U}} \mathbf{d}^{\mathcal{S}} \end{bmatrix}. \quad (6.37)$$

In this case, the coupling constraints are fulfilled in the reference configuration and there are no initial stresses in the system. However, this variant violates the conservation of angular momentum. Again, the influence of this violation within the BTSS-POS-DISP variant is analyzed in Section 6.4. The linearization of the coupling terms (6.37) reads

$$\text{Lin} \left(\begin{bmatrix} \mathbf{r}_s^{\mathcal{U}} \\ \mathbf{r}_r^{\mathcal{U}} \\ \mathbf{g}^{\mathcal{U}} \end{bmatrix}_{\text{DISP}} \right) = \begin{bmatrix} \mathbf{0} \\ \mathbf{0} \\ \mathbf{g}^{\mathcal{U}} \end{bmatrix}_{\text{DISP}} + \begin{bmatrix} \mathbf{0} & \mathbf{0} & -\mathbf{M}^{\mathcal{U}^T} \\ \mathbf{0} & \mathbf{0} & \mathbf{D}^{\mathcal{U}^T} \\ -\mathbf{M}^{\mathcal{U}} & \mathbf{D}^{\mathcal{U}} & \mathbf{0} \end{bmatrix} \begin{bmatrix} \Delta \mathbf{d}^{\mathcal{S}} \\ \Delta \mathbf{d}^{\mathcal{B}} \\ \boldsymbol{\lambda}^{\mathcal{U}} \end{bmatrix}. \quad (6.38)$$

Remark 6.5. A very similar problem occurs for surface-to-surface mesh tying problems, in the case of general curved interfaces. To guarantee conservation of angular momentum a mesh initialization procedure is performed, cf. [112]. The mesh initialization slightly relocates the reference position of the slave nodes (in the case of BTS problems, the beam nodes) $\mathbf{X}^{\mathcal{B}}$, such that the (non-linear) condition $\mathbf{D}^{\mathcal{U}} \mathbf{X}^{\mathcal{B}} - \mathbf{M}^{\mathcal{U}} \mathbf{X}^{\mathcal{S}} = \mathbf{0}$ is fulfilled. For the presented BTSS-POS method, such a mesh initialization would mean that both presented simplifications BTSS-POS-REF and BTSS-POS-DISP are identical. However, in the surface-to-surface case the space continuous interfaces are usually matching, thus the mesh initialization of the discretized system only marginally affects the overall solution. This is not the case for BTSS coupling problems. For example, in many situations it is sensible for the beam centerline to be offset of the coupling surface in surface normal direction, cf. Figure 6.2(b). In such cases, the mesh initialization procedure of the beams reference configuration might lead to a drastically different system behavior.

Remark 6.6. If the discretized beam centerline lies exactly on the discretized solid surface, the three presented variants of the global system equations (6.34), (6.36) and (6.38) are all identical, i.e., $\mathbf{Q}_{\lambda^{\mathcal{S}}}^{\mathcal{U}} = \mathbf{0}$ and $\mathbf{D}^{\mathcal{U}} \mathbf{X}^{\mathcal{B}} - \mathbf{M}^{\mathcal{U}} \mathbf{X}^{\mathcal{S}} = \mathbf{0}$. However, with the employed Lagrange polynomial interpolation for the solid finite elements and the third-order Hermitian interpolation for the beam finite elements, a matching mesh for beam and solid surface discretizations is only possible in case of planar solid surfaces. Furthermore, in this special case, the positional surface coupling variants would also be equal to the BTSV-POS method Chapter 4, as the problem can also be interpreted as a volume coupling problem, where the beam is directly embedded at the boundary of the solid volume, i.e., the solid surface. There, the beam would lie at a face of the solid (volume) finite element parameter space, i.e., the limit case for BTSV coupling.

6.3.3. Combined mortar-type coupling

In this section the global system for the BTSS-FULL problem is assembled and subsequently regularized. The BTSS-FULL problem consists of the following individual parts: the uncoupled beam and solid problem, the positional coupling (BTSS-POS) and the rotational coupling (BTSS-ROT). The rotational coupling between beam cross-section and solid surface (BTSS-ROT) is

entirely based on the BTSV-ROT coupling method presented in Chapter 5. In Section 6.3.2 three different variants of BTSS-POS are presented: BTSS-POS-CONS, BTSS-POS-REF and BTSS-POS-DISP. Depending on the employed variant, the corresponding BTSS-FULL problem is referred to as BTSS-FULL-CONS, BTSS-FULL-REF and BTSS-FULL-DISP. BTSS-FULL-CONS is the most general of the presented variants, i.e., the equations for the other variants are more or less simplifications thereof. In Section 6.4 BTSS-FULL-CONS will be identified as the superior variant, with respect to the accuracy of the results. Therefore, and for the sake of brevity, the following derivations are only presented for the fully coupled and consistent BTSS-FULL-CONS variant.

Inserting all discretized variables into (6.1) gives the discrete nonlinear system of equations for the quasi-static BTSS-FULL problem:

$$\mathbf{r}^S(\mathbf{d}^S) + \mathbf{r}_s^U(\mathbf{d}^S, \lambda^U) + \mathbf{r}_s^R(\mathbf{d}^S, \psi^B, \lambda^R) = \mathbf{0}, \quad (6.39)$$

$$\mathbf{r}_r^B(\mathbf{d}^B, \psi^B) + \mathbf{r}_r^U(\lambda^U) = \mathbf{0}, \quad (6.40)$$

$$\mathbf{r}_\theta^B(\mathbf{d}^B, \psi^B) + \mathbf{r}_\theta^R(\mathbf{d}^S, \psi^B, \lambda^R) = \mathbf{0}, \quad (6.41)$$

$$\mathbf{g}^U(\mathbf{d}^S, \mathbf{d}^B) = \mathbf{0}, \quad (6.42)$$

$$\mathbf{g}^R(\mathbf{d}^S, \psi^B) = \mathbf{0}. \quad (6.43)$$

Here, the dependency of the residual contributions on the discrete unknowns is stated to illustrate the coupling connectivity introduced by each residuum vector. For improved readability, the explicit dependency of the residual contributions on the discrete unknowns will be omitted going further. The resulting BTSS-FULL global system of equations with saddle point structure reads:

$$\begin{bmatrix} \mathbf{K}_{ss}^S + \mathbf{Q}_{ss}^U + \mathbf{Q}_{ss}^R & \mathbf{0} & \mathbf{Q}_{s\theta}^R & -\mathbf{M}^{UT} + (\mathbf{Q}_{\lambda s}^U)^T & \mathbf{Q}_{s\lambda}^R \\ \mathbf{0} & \mathbf{K}_{rr}^B & \mathbf{0} & \mathbf{D}^{UT} & \mathbf{0} \\ \mathbf{Q}_{\theta s}^R & \mathbf{0} & \mathbf{K}_{\theta\theta}^B + \mathbf{Q}_{\theta\theta}^R & \mathbf{0} & \mathbf{Q}_{\theta\lambda}^R \\ -\mathbf{M}^U + \mathbf{Q}_{\lambda s}^U & \mathbf{D}^U & \mathbf{0} & \mathbf{0} & \mathbf{0} \\ \mathbf{Q}_{\lambda s}^R & \mathbf{0} & \mathbf{Q}_{\lambda\theta}^R & \mathbf{0} & \mathbf{0} \end{bmatrix} \begin{bmatrix} \Delta \mathbf{d}^S \\ \Delta \mathbf{d}^B \\ \Delta \theta^B \\ \lambda^U \\ \lambda^R \end{bmatrix} = \begin{bmatrix} -\mathbf{r}^S \\ -\mathbf{r}_r^B \\ -\mathbf{r}_\theta^B \\ -\mathbf{g}^U \\ -\mathbf{g}^R \end{bmatrix}. \quad (6.44)$$

Remark 6.7. The global solid displacement vector \mathbf{d}^S also contains degrees of freedom not related to the solid surface, i.e., the number of total solid nodes n^S is larger than the number of solid surface nodes n_Γ^S . However, a split up of the solid degrees of freedom into surface and *inner* volume degrees of freedom is not introduced for improved readability and compatibility with the previous chapters.

6.3.4. Penalty regularization

Enforcing the coupling conditions with Lagrange multipliers results in a mixed formulation, i.e., the Lagrange multipliers are additional global unknowns, thus yielding a global system with a saddle point-type structure (6.44). A direct solution of this global system introduces certain drawbacks, e.g., an increased system size and possible linear solver issues due to the saddle point-type structure, cf. Section 2.5.2. A weighted penalty regularization has proven to be an efficient and reasonably accurate approach to circumvent the aforementioned drawbacks for BTS coupling problems, cf. Chapters 4 and 5. Therefore, the resulting global system (6.44) will also

be approximated with a penalty regularization. For the rotational coupling constraints the same penalty relaxation as in (5.57) will be employed, i.e., $\lambda^{\mathcal{R}} = \epsilon^{\mathcal{R}} (\mathbf{V}^{\mathcal{R}})^{-1} \mathbf{g}^{\mathcal{R}}$. For the BTSS-POS constraints a similar relaxation as the one for the BTSV-POS constraints (4.20) is employed,

$$\lambda^{\mathcal{U}} = \epsilon^{\mathcal{U}} (\mathbf{V}^{\mathcal{U}})^{-1} \mathbf{g}^{\mathcal{U}}. \quad (6.45)$$

Again, $\epsilon^{\mathcal{U}} \in \mathbb{R}^+$ is a scalar penalty parameter and $\mathbf{V}^{\mathcal{U}}$ is a global diagonal scaling matrix. The global scaling matrix is assembled from the nodal scaling matrices $\mathbf{V}^{\mathcal{U}[j,j]}$ for Lagrange multiplier node j , i.e.,

$$\mathbf{V}^{\mathcal{U}[j,j]} = \int_{\Gamma_{c,h}} \Phi_j^{\mathcal{U}} \, ds \, \mathbf{I}^{3 \times 3}. \quad (6.46)$$

The penalty regularization of the BTSS-FULL problem introduces two additional system parameters, $\epsilon^{\mathcal{U}}$ and $\epsilon^{\mathcal{R}}$. This leaves the important question on how to choose these two parameters, which is discussed in Sections 4.2.3 and 5.3.4 for the positional and rotational penalty parameter, respectively. There, the following recommendations choosing the two penalty parameters are given: the positional penalty parameter should be in the range of the beams Young's modulus, i.e., $\epsilon^{\mathcal{U}} \approx E^{\mathcal{B}}$, and the rotational parameter should be in the range of the beams Young's modulus scaled with the square of the cross-section radius, i.e., $\epsilon^{\mathcal{R}} \approx E^{\mathcal{B}} R^2$. This is also applicable to the present case of BTSS-FULL coupling.

The relaxation of the penalty constraints defines the Lagrange multipliers as functions of the displacements, i.e., they are no longer independent degrees of freedom of the system and can be condensed from the global system of equations (6.44):

$$\begin{bmatrix} \mathbf{A}_{ss}^{\mathcal{U}} & \mathbf{A}_{sr}^{\mathcal{U}} & \mathbf{A}_{s\theta}^{\mathcal{U}} \\ \mathbf{A}_{rs}^{\mathcal{U}} & \mathbf{A}_{rr}^{\mathcal{U}} & \mathbf{A}_{r\theta}^{\mathcal{U}} \\ \mathbf{A}_{\theta s}^{\mathcal{U}} & \mathbf{A}_{\theta r}^{\mathcal{U}} & \mathbf{A}_{\theta\theta}^{\mathcal{U}} \end{bmatrix} \begin{bmatrix} \Delta \mathbf{d}^{\mathcal{S}} \\ \Delta \mathbf{d}^{\mathcal{B}} \\ \Delta \theta^{\mathcal{B}} \end{bmatrix} = \begin{bmatrix} \mathbf{b}_s^{\mathcal{U}} \\ \mathbf{b}_r^{\mathcal{U}} \\ \mathbf{b}_\theta^{\mathcal{U}} \end{bmatrix}. \quad (6.47)$$

Therein, the following abbreviations have been introduced for improved readability:

$$\begin{aligned} \mathbf{A}_{ss}^{\mathcal{U}} &= \mathbf{K}_{ss}^{\mathcal{S}} + \mathbf{Q}_{ss}^{\mathcal{U}} + \mathbf{Q}_{ss}^{\mathcal{R}} + \epsilon^{\mathcal{U}} (-\mathbf{M}^{\mathcal{U}} + \mathbf{Q}_{\lambda s}^{\mathcal{U}})^{\mathsf{T}} (\mathbf{V}^{\mathcal{U}})^{-1} (-\mathbf{M}^{\mathcal{U}} + \mathbf{Q}_{\lambda s}^{\mathcal{U}}) \\ &\quad + \epsilon^{\mathcal{R}} \mathbf{Q}_{s\lambda}^{\mathcal{R}} (\mathbf{V}^{\mathcal{R}})^{-1} \mathbf{Q}_{\lambda s}^{\mathcal{R}} \\ \mathbf{A}_{sr}^{\mathcal{U}} &= \epsilon^{\mathcal{U}} (-\mathbf{M}^{\mathcal{U}} + \mathbf{Q}_{\lambda s}^{\mathcal{U}})^{\mathsf{T}} (\mathbf{V}^{\mathcal{U}})^{-1} \mathbf{D}^{\mathcal{U}} \\ \mathbf{A}_{s\theta}^{\mathcal{U}} &= \mathbf{Q}_{s\theta}^{\mathcal{R}} + \epsilon^{\mathcal{R}} \mathbf{Q}_{s\lambda}^{\mathcal{R}} (\mathbf{V}^{\mathcal{R}})^{-1} \mathbf{Q}_{\lambda\theta}^{\mathcal{R}} \\ \mathbf{A}_{rs}^{\mathcal{U}} &= \epsilon^{\mathcal{U}} \mathbf{D}^{\mathcal{U}\mathsf{T}} (\mathbf{V}^{\mathcal{U}})^{-1} (-\mathbf{M}^{\mathcal{U}} + \mathbf{Q}_{\lambda s}^{\mathcal{U}}) \\ \mathbf{A}_{rr}^{\mathcal{U}} &= \mathbf{K}_{rr}^{\mathcal{B}} + \epsilon^{\mathcal{U}} \mathbf{D}^{\mathcal{U}\mathsf{T}} (\mathbf{V}^{\mathcal{U}})^{-1} \mathbf{D}^{\mathcal{U}} \\ \mathbf{A}_{r\theta}^{\mathcal{U}} &= \mathbf{K}_{r\theta}^{\mathcal{B}} \\ \mathbf{A}_{\theta s}^{\mathcal{U}} &= \mathbf{Q}_{\theta s}^{\mathcal{R}} + \epsilon^{\mathcal{R}} \mathbf{Q}_{\theta\lambda}^{\mathcal{R}} (\mathbf{V}^{\mathcal{R}})^{-1} \mathbf{Q}_{\lambda s}^{\mathcal{R}} \\ \mathbf{A}_{\theta r}^{\mathcal{U}} &= \mathbf{K}_{\theta r}^{\mathcal{B}} \\ \mathbf{A}_{\theta\theta}^{\mathcal{U}} &= \mathbf{K}_{\theta\theta}^{\mathcal{B}} + \mathbf{Q}_{\theta\theta}^{\mathcal{R}} + \epsilon^{\mathcal{R}} \mathbf{Q}_{\theta\lambda}^{\mathcal{R}} (\mathbf{V}^{\mathcal{R}})^{-1} \mathbf{Q}_{\lambda\theta}^{\mathcal{R}} \\ \mathbf{b}_s^{\mathcal{U}} &= -\mathbf{r}^{\mathcal{S}} - \epsilon^{\mathcal{U}} (-\mathbf{M}^{\mathcal{U}} + \mathbf{Q}_{\lambda s}^{\mathcal{U}})^{\mathsf{T}} (\mathbf{V}^{\mathcal{U}})^{-1} \mathbf{g}^{\mathcal{U}} - \epsilon^{\mathcal{R}} \mathbf{Q}_{s\lambda}^{\mathcal{R}} (\mathbf{V}^{\mathcal{R}})^{-1} \mathbf{g}^{\mathcal{R}} \\ \mathbf{b}_r^{\mathcal{U}} &= -\mathbf{r}_r^{\mathcal{B}} - \epsilon^{\mathcal{U}} \mathbf{D}^{\mathcal{U}\mathsf{T}} (\mathbf{V}^{\mathcal{U}})^{-1} \mathbf{g}^{\mathcal{U}} \\ \mathbf{b}_\theta^{\mathcal{U}} &= -\mathbf{r}_\theta^{\mathcal{B}} - \epsilon^{\mathcal{R}} \mathbf{Q}_{\theta\lambda}^{\mathcal{R}} (\mathbf{V}^{\mathcal{R}})^{-1} \mathbf{g}^{\mathcal{R}}. \end{aligned} \quad (6.48)$$

6.3.4.1. Conservation properties

In this section, the proposed BTSS-POS-CONS scheme shall be analyzed with respect to conservation of linear and angular momentum. In the context of surface-to-surface problems this has been discussed in detail, e.g., [110, 112–114]. For surface-to-surface coupling (mesh tying) problems it has been shown, that linear momentum and angular momentum are conserved by the semi-discrete mesh tying formulation, cf. [112]. However, the proposed mixed-dimensional BTSS-POS-CONS scheme differs in two important aspects from classical surface-to-surface coupling problems: (i) The coupling constraints are formulated with the current positions instead of the displacements, and, more importantly, contain the surface normal vector. (ii) The nodal degrees of freedom for the beam nodes contain the positions as well as the centerline tangents. Therefore, a discussion on conservation of linear and angular momentum of BTSS-POS-CONS is given in the following. In the following considerations the BTSS-POS-CONS variant is analyzed, as the implications for the BTSS-POS-REF variant can be directly obtained by applying the respective simplifications. In the case of the BTSS-POS-DISP variant, it is shown in Section 6.3.2.2 that already the space continuous coupling terms do not conserve angular momentum.

As discussed in [112], conservation of linear momentum can be guaranteed if the discretized virtual work of the coupling forces vanishes for a constant virtual displacement $\delta \underline{\mathbf{u}} \neq \underline{\mathbf{0}}$. In that case, the nodal displacement weighting functions become $\delta \underline{\mathbf{d}}_k^S = \delta \underline{\mathbf{u}}$, $k = 1, \dots, n_\Gamma^S$ and $\delta \underline{\mathbf{d}}_{r,l}^B = \delta \underline{\mathbf{u}}$, $l = 1, \dots, n^B$. Since the virtual displacement is constant, the variation of the beam centerline tangents vanishes, i.e., $\delta \underline{\mathbf{d}}_{t,l}^B = \underline{\mathbf{0}}$, $l = 1, \dots, n^B$. Insertion into (6.31) yields

$$\sum_{j=1}^{n^U} \left(\sum_{l=1}^{n^B} \left(\mathbf{D}^{U[j,l]} \begin{bmatrix} \delta \underline{\mathbf{u}} \\ \underline{\mathbf{0}} \end{bmatrix} \right)^T - \sum_{k=1}^{n_\Gamma^S} \left(\mathbf{M}^{U[j,k]} \delta \underline{\mathbf{u}} \right)^T - \int_{\Gamma_{c,h}} d_{c,0} \delta \underline{\mathbf{n}}_h \Phi_j^U ds \right) \hat{\underline{\mathbf{x}}}_j^U = 0. \quad (6.49)$$

The variation of the surface normal vector vanishes for a constant virtual displacement field, i.e., $\delta \underline{\mathbf{n}}_h = \underline{\mathbf{0}}$. Furthermore, since $\delta \underline{\mathbf{u}}$ is non-zero, the condition (6.49) is only satisfied if

$$\left(\sum_{l=1}^{n^B} \int_{\Gamma_{c,h}} \Phi_j^U H_l^r ds - \sum_{k=1}^{n_\Gamma^S} \int_{\Gamma_{c,h}} \Phi_j^U N_k ds \right) \hat{\underline{\mathbf{x}}}_j^U = \underline{\mathbf{0}}. \quad (6.50)$$

With the partition of unity property of H_l^r and N_k , i.e., $\sum_{l=1}^{n^B} H_l^r = 1$ and $\sum_{k=1}^{n_\Gamma^S} N_k = 1$, the condition for conservation of linear momentum further simplifies to

$$\sum_{j=1}^{n^U} \left(\int_{\Gamma_{c,h}} \Phi_j^U ds - \int_{\Gamma_{c,h}} \Phi_j^U ds \right) = 0. \quad (6.51)$$

Obviously this property is fulfilled if the integrals are evaluated exactly. In the case of numerical integration the property is fulfilled if the same numerical integration procedure is used for both integrals. At this point it is important to point out that the two integrals originally arise from the evaluation of $\mathbf{D}^{U[j,l]}$ and $\mathbf{M}^{U[j,k]}$. As mentioned in Section 6.3.2, both integrals use the same segment-based integration scheme with a fixed number of Gauss-points. Therefore, the condition (6.51) is fulfilled, i.e., the discrete BTSS-POS-CONS scheme exactly conserves linear momentum.

In a similar fashion, conservation of angular momentum can be guaranteed, if the virtual work of the coupling forces vanishes for a constant virtual rotation $\delta \underline{\phi} \neq \underline{0}$ (for simplicity, the origin is assumed to be the center of the virtual rotation). With that assumption, the nodal virtual displacements of solid and beam are $\delta \hat{\underline{d}}_k^S = \delta \underline{\phi} \times \hat{\underline{x}}_k^S$, $k = 1, \dots, n_\Gamma^S$ and $\delta \hat{\underline{d}}_{r,l}^B = \delta \underline{\phi} \times \hat{\underline{r}}_l$, $l = 1, \dots, n^B$. In a similar fashion, the variation of the nodal beam tangent vectors reads $\delta \hat{\underline{d}}_{t,l}^B = \delta \underline{\phi} \times \hat{\underline{t}}_l$, $l = 1, \dots, n^B$, cf. [99]. Insertion into (6.31) yields

$$\begin{aligned} \sum_{j=1}^{n_\Gamma} \left(\sum_{l=1}^{n^B} \left((\delta \underline{\phi} \times \hat{\underline{r}}_l)^T \int_{\Gamma_{c,h}} \Phi_j^\mathcal{U} H_l^r ds + (\delta \underline{\phi} \times \hat{\underline{t}}_l)^T \int_{\Gamma_{c,h}} \Phi_j^\mathcal{U} H_l^t ds \right) \right. \\ \left. - \sum_{k=1}^{n_\Gamma^S} (\delta \underline{\phi} \times \hat{\underline{x}}_k^S)^T \int_{\Gamma_{c,h}} \Phi_j^\mathcal{U} N_k ds - \int_{\Gamma_{c,h}} d_{c,0} \delta \underline{n}_h^T \Phi_j^\mathcal{U} ds \right) \hat{\underline{\lambda}}_j^\mathcal{U} = 0. \end{aligned} \quad (6.52)$$

In the case of a constant virtual rotation, the variation of the normal vector can be expressed by $\delta \underline{n}_h = \delta \underline{\phi} \times \underline{n}_h$. Since $\delta \underline{\phi}$ is non-zero, the condition (6.52) is only fulfilled if

$$\begin{aligned} \sum_{j=1}^{n_\Gamma} \left(\sum_{l=1}^{n^B} \left(\overbrace{\int_{\Gamma_{c,h}} \Phi_j^\mathcal{U} H_l^r ds \hat{\underline{r}}_l + \int_{\Gamma_{c,h}} \Phi_j^\mathcal{U} H_l^t ds \hat{\underline{t}}_l}^{\mathbf{D}^{\mathcal{U}[j,l]} \hat{\underline{x}}_l^B} \right) \right. \\ \left. - \sum_{k=1}^{n_\Gamma^S} \underbrace{\int_{\Gamma_{c,h}} \Phi_j^\mathcal{U} N_k ds}_{\mathbf{M}^{\mathcal{U}[j,k]}^T} \hat{\underline{x}}_k^S - \underbrace{\int_{\Gamma_{c,h}} d_{c,0} \underline{n}_h \Phi_j^\mathcal{U} ds}_{\mathbf{q}^{\mathcal{U}[j]}} \right) \times \hat{\underline{\lambda}}_j^\mathcal{U} = 0. \end{aligned} \quad (6.53)$$

This condition can be reformulated and written in global form

$$\mathbf{D}^\mathcal{U} \mathbf{x}^B - \mathbf{M}^\mathcal{U} \mathbf{x}^S - \mathbf{q}^\mathcal{U} = \underline{0}. \quad (6.54)$$

These are simply the coupling constraints for BTSS-POS-CONS, i.e., if the coupling constraints, cf. last row in (6.32), are fulfilled, the coupling scheme preserves angular momentum. In the present thesis, the coupling constraints are enforced with a node-wise weighted penalty regularization, which results in a violation of the coupling constraints. However, the resulting regularized problem still preserves angular momentum. To demonstrate this, let us state the penalty regularization for a Lagrange multiplier at node j :

$$\hat{\underline{\lambda}}_j^\mathcal{U} = \epsilon^\mathcal{U} \left(\int_{\Gamma_{c,h}} \Phi_j^\mathcal{U} ds \mathbf{I}^{3 \times 3} \right)^{-1} \left(\sum_{l=1}^{n^B} \mathbf{D}^{\mathcal{U}[j,l]} \hat{\underline{x}}_l^B - \sum_{k=1}^{n_\Gamma^S} \mathbf{M}^{\mathcal{U}[j,k]} \hat{\underline{x}}_k^S - \mathbf{q}^{\mathcal{U}[j]} \right). \quad (6.55)$$

When inserting (6.55) into (6.53) it is obvious that the condition for conservation of angular momentum is also fulfilled for the regularized problem, as the cross product of two parallel vectors vanishes.

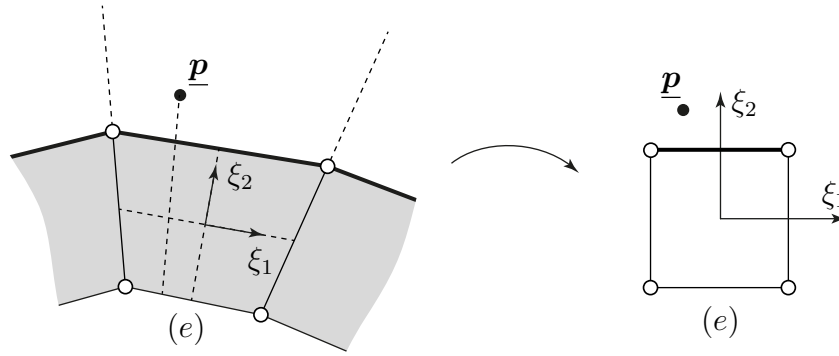


Figure 6.7.: Projection of point \underline{p} to the parameter space of the solid finite element (e) with BTSV-POS-X. For illustrative purposes a 2D example is shown.

6.3.5. Extended beam-to-solid volume coupling

The main difference between the proposed BTSS-POS-CONS coupling procedure and the BTSV-POS method, cf. Chapter 4, is a term accounting for the normal distance between the beam and the solid surface. The discretization of this term introduces rather complex coupling terms, which require the evaluation of an averaged surface normal field. An alternative to the BTSS-POS-CONS method is to use an extended version of the BTSV-POS scheme proposed in Chapter 4, which shall be denoted as the *extended* positional beam-to-solid volume coupling (BTSV-POS-X) scheme in the following. The idea of this BTSV-POS-X scheme is to simply project points on the beam centerline to an extended solid parameter space, i.e., projections that lie outside of the solid volume are still admissible. Thus, no closest point projection with the surface normal field is required. This is exemplarily illustrated in Figure 6.7. The point \underline{p} is projected to the parameter space of the solid finite element (e) , and although the ξ_2 coordinate of the projection point lies outside of the solid finite element domain the projection will still be used in the evaluation of \mathbf{M}^u . There are no coupling terms dependent on the surface normal distance in this case, i.e., the resulting linearized system of equations is equal to (6.36) and (6.38). At first glance this approach might seem very appealing as there is no need for evaluating the surface normal vector and its derivatives. Furthermore, basically the same implementation as in BTSV-POS problems can be used. However, there are two significant drawbacks of this approach: (i) The projection of the beam centerline points onto the solid surface is highly dependent on the solid finite element mesh. Figure 6.8 illustrates cases where the BTSV-POS-X method fails. In Figure 6.8(a) the solid finite elements are distorted in negative normal direction of the coupling surface, such that a unique projection is not possible in the shaded areas. (ii) The BTSV-POS-X method only works well for grid-like hexahedral meshes of the solid surface, unstructured hexahedral meshes or tetrahedral meshes lead to problems due to non-unique projections, cf. Figure 6.8(b). Additionally, the proposed BTSS-POS-CONS method can be directly applied to structural shell finite element models, whereas the BTSV-POS-X method requires that the solid is discretized with 3D solid finite elements. Therefore, the BTSV-POS-X method will not be investigated further in this thesis.



Figure 6.8.: Cautionary cases for BTSV-POS-X. Distorted elements in negative normal direction of the solid surface (a). General tetrahedral mesh (b). Gray areas indicate where a projection to the solid surface fails. For illustrative purposes a 2D example is shown.

6.4. Examples

The following numerical examples are set up using the open source beam finite element preprocessor MeshPy [137] and are simulated with the in-house parallel multi-physics research code BACI [12].

6.4.1. Constant stress transfer

In this first example the ability of the BTSS-FULL coupling method to transfer a constant stress state is investigated. This example is inspired by classical patch tests for solid mechanics, cf. [140]. Similar examples are presented in Section 4.4.1 for the BTSV-POS method and in Section 5.4.4 for the BTSV-FULL method. Figure 6.9 illustrates the problem setup. It consists of a solid block Ω^S ($E^S = 1 \text{ N/m}^2$, $\nu^S = 0$) with the dimensions $1 \text{ m} \times 1 \text{ m} \times 1.2 \text{ m}$. The center of the bottom face is located at the origin of the coordinate system. No external loads are applied to the solid and the bottom face is fixed in all spatial directions. At the top face the solid surface is coupled to two beams Ω_1^B and Ω_2^B ($R = 0.05 \text{ m}$, $E^B = 100 \text{ N/m}^2$, $\nu^B = 0$). The two beams share the same spatial position and are loaded with opposing line loads in \underline{e}_3 direction. The magnitude of the line loads is $t = 0.025 \text{ N/m}$. The opposing line loads on the beams cancel each other out, i.e., the resulting analytical solution of the space continuous problem is $\underline{u} = \underline{0}$. Both beams are coupled to the solid domain, there is no direct interaction between the beams, and all loads are transferred through the solid domain via the BTSS-FULL coupling method. This example shall verify the ability of the three proposed BTSS-FULL variants, i.e., BTSS-FULL-CONS, BTSS-FULL-REF and BTSS-FULL-DISP, to exactly represent this analytical solution using an arbitrary coarse discretization, i.e., the ability of the coupling method to transfer a constant stress state across non-matching mixed-dimensional interface meshes.

The solid block is discretized with first- and second-order hexahedral finite elements (*hex8*, *hex20* and *hex27*) as well as first- and second order tetrahedral finite elements (*tet4* and *tet10*). The beams *B1* and *B2* are discretized with 5 and 7 Simo–Reissner beam finite elements, respectively. This results in a non-matching mixed-dimensional interface discretization between the beams and the solid. The Lagrange multipliers for positional and rotational coupling are discretized using first-order Lagrange polynomials and regularized using penalty parameters of $\epsilon^U = 100 \text{ N/m}^2$ and $\epsilon^R = 0.1 \text{ Nm/m}$. The results for various coupling variants and *hex8* elements are illustrated in Figure 6.10. It can be seen that for all considered variants, the second Piola-Kirchhoff stress S_{33} in the solid and the curvature κ in the beam elements are zero up to machine precision, thus

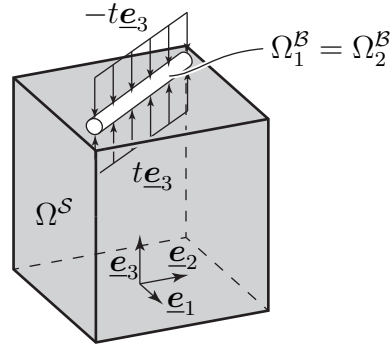


Figure 6.9.: Constant stress transfer – problem setup. Both beams Ω_1^B and Ω_2^B occupy the same spatial position.

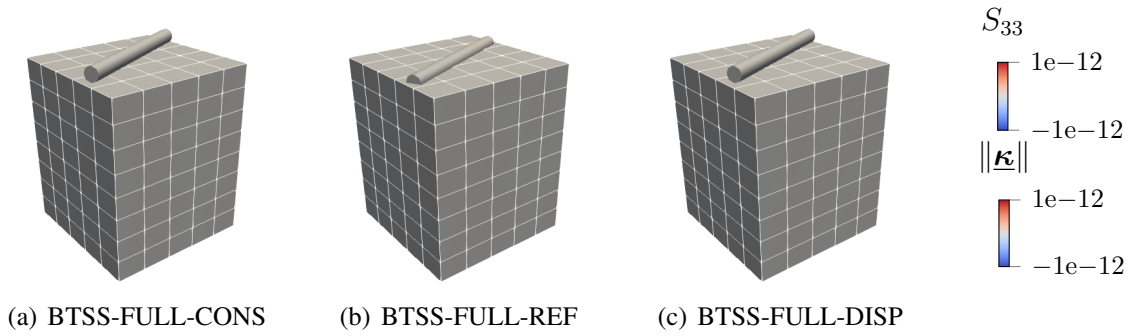


Figure 6.10.: Constant stress transfer – results for straight beams and various coupling variants. The solids are discretized with *hex8* solid finite elements. The second Piola-Kirchhoff stress S_{33} is shown in the solid and the curvature κ at the middle of each beam element. Note that both beams Ω_1^B and Ω_2^B occupy the same spatial domain in the undeformed reference configuration.

exactly representing the analytical solution. However, the displacement of the two beams in the BTSS-FULL-REF variant does not vanish, as the beam centerline is forced to lie on the solid surface, i.e., in this example the beams show an offset in negative \underline{e}_3 -direction by a distance of R . The results of the constant stress transfer test for the various solid element types are visualized in Figure 6.11. There, the coupling is realized with the BTSS-FULL-CONS variant. It can be seen, that for all considered solid element types, the stress in the solid and the curvature in the beams match the analytical solution up to machine precision. This illustrates that the BTSS-FULL-CONS coupling variant is able to exactly represent a constant stress state between a straight beam and a planar solid surface for general non-matching discretizations. The results obtained with BTSS-FULL-DISP exactly match the results obtained with BTSS-FULL-CONS. In case of the BTSS-FULL-REF variant, the beams displacement is not zero, but the constant stress state can still be transferred exactly.

To make the constant stress transfer test more demanding, the previously presented example is now modified such that a position field $\underline{\mathbf{X}}^S$ on the top surface of the solid is defined by $\underline{\mathbf{X}}^S = i\underline{\mathbf{e}}_1 + j\underline{\mathbf{e}}_2 + f(i, j)\underline{\mathbf{e}}_3$ for $i, j \in [-0.5, 0.5]$, with $f(i, j) = \frac{5}{4} - i^2 - j^2$, i.e., a curved surface is generated. The centerlines of the two beams are offset by the beam radius in surface normal

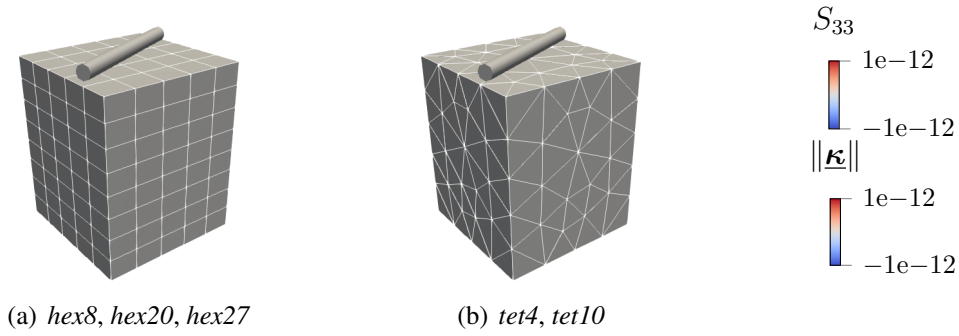


Figure 6.11.: Constant stress transfer – results for straight beams and various solid finite element discretizations. The coupling is modeled with the BTSS-FULL-CONS coupling variant. The second Piola-Kirchhoff stress S_{33} is shown in the solid and the curvature κ at the middle of each beam element. Note that both beams Ω_1^B and Ω_2^B occupy the same spatial domain in the undeformed reference configuration.

direction. Otherwise, all parameters are the same as in the previous example. Because of the specific choice of surface curvature, the employed beam centerline interpolation with third-order Hermitian polynomials is not able to exactly represent the space continuous reference geometry of the beam centerline. This results in a discretization error of the beam centerline interpolation and slightly different arc lengths of the two beams. In order for the resultants of the two line loads to still be in equilibrium with each other, the load t on beam $B2$ is scaled with a factor of 0.9995346 to account for the different beam lengths. Figure 6.12 illustrates the results of the constant stress transfer test for the curved solid surface and the various coupling variants. It can clearly be seen that the results for BTSS-FULL-REF do not match the analytical solution. This is because the beam is forced to lie on the solid surface. In case of the planar coupling surface this could be achieved by a rigid body translation of the beams onto the solid surface. However, in case of the curved solid surface, a rigid body translation of the beams can not fulfill the positional coupling equations for BTSS-FULL-REF, this also requires a deformation of the beams and the solid, and thus results in a failing constant stress transfer test. The results for the BTSS-FULL-CONS and BTSS-FULL-DISP variant are more or less equal to each other. Figure 6.13 illustrates the results for the BTSS-FULL-CONS variant in combination with various solid finite element types. Note the different scaling of the contour plots in Figure 6.12 compared to Figure 6.13. It can be observed that even for the BTSS-FULL-CONS (and also the BTSS-FULL-DISP) variant, the analytical solution is not reproduced up to machine precision as the results show a non-vanishing stress state in the solid and a non-vanishing curvature in the beams. However, these non-zero stress and curvature values, respectively, are introduced by the discretization error of the initial geometry, i.e., the inability of the beam finite elements to exactly represent the curvature of the initial geometry, and are orders of magnitude smaller than the discretization errors associated with deformation states in typical application scenarios (and the error introduced by the BTSS-FULL-REF variant). It can be concluded that the discretization error for arbitrarily curved beam centerlines within the BTSS-FULL-CONS and BTSS-FULL-DISP methods can be neglected as compared to the overall discretization error.

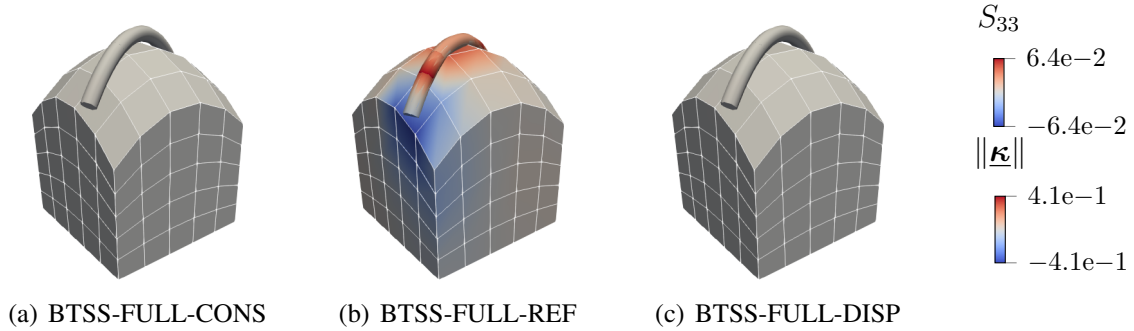


Figure 6.12.: Constant stress transfer – results for curved beams and various coupling variants. The solids are discretized with *hex8* solid finite elements. The second Piola-Kirchhoff stress S_{33} is shown in the solid and the curvature κ at the middle of each beam element. Note that both beams Ω_1^B and Ω_2^B occupy the same spatial domain in the undeformed reference configuration.

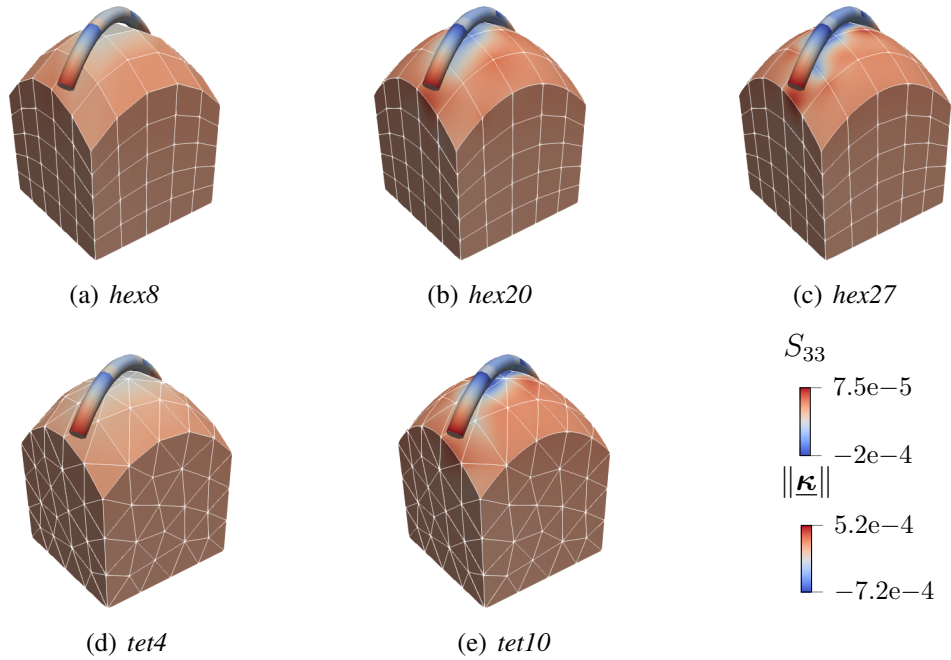


Figure 6.13.: Constant stress transfer – results for curved beams and various solid finite element discretizations. The coupling is modeled with the BTSS-FULL-CONS coupling variant. The second Piola-Kirchhoff stress S_{33} is shown in the solid and the curvature κ at the middle of each beam element. Note that both beams Ω_1^B and Ω_2^B occupy the same spatial domain in the undeformed reference configuration.



Figure 6.14.: Half-pipe with helix-shaped beam – problem setup. The left figure shows a 3D view of the problem and the right figure shows a cut through the $\underline{e}_2 - \underline{e}_3$.



Figure 6.15.: Half-pipe with helix-shaped beam – finite element discretization of the beam-to-solid mesh (left) and full 3D mesh (right).

6.4.2. Half-pipe with helix-shaped beam

In this example, a helix-shaped beam is coupled to the outer surface of a solid half-pipe, cf. Figure 6.14. This example is introduced to further compare the three surface coupling types discussed in Section 6.3.2. The solid half-pipe with length $L = 1$ m has an outer radius $r_a = 1$ m and inner radius $r_i = 0.8$ m. The pipe is modeled using a compressible Neo-Hookean material law ($E^S = 1$ N/m², $\nu^S = 0$). The solid is coupled to a helix-shaped beam with a radius $r_b = 1.05$ m and a pitch of 2 m. The beam has a cross-section radius $R = 0.1$ m, Young's modulus $E^B = 50$ N/m² and Poisson's ratio $\nu^B = 0$. With the chosen geometric dimensions, the beam centerline does not exactly lie on the outer surface of the solid half-pipe, but is offset by a normal distance of 0.05 m. On one side of the half-pipe, a concentrated force $\underline{F} = 0.0004$ N \underline{e}_3 is applied to the tip of the beam. On the other side, the solid is fixed in all spatial directions.

Coupling between the beam and the solid is realized with the three BTSS-FULL coupling variants ($\epsilon^U = 10$ N/m², $\epsilon^R = 1$ Nm/m). First-order Lagrange polynomials are employed to discretize both the positional and the rotational Lagrange multipliers. The left part of Figure 6.15 illustrates the finite element discretization of the 1D-2D model. The pipe is modeled with $2 \times 12 \times 4$ finite elements in radial, tangential and \underline{e}_2 direction, respectively. Eight-noded solid shell elements are employed, cf. [20, 147]. The beam is discretized using 10 Simo–Reissner beam finite elements. In the present example, the beam cross-sections penetrate the solid coupling surface. Therefore, it is possible to discretize this example with a full 3D finite element mesh, where the beam itself is also modeled using 3D finite elements, cf. the right part of Figure 6.15. The full 3D model is discretized with 50,480 second-order tetrahedra (*tet10*) elements. Consequently, the full 3D model consists of 226,383 degrees of freedom. The discretization of the full 3D model has been chosen such that mesh convergence is guaranteed and it can be used as a reference solution to assess the quality of the results obtained with the three BTSS-FULL variants.

Table 6.1.: Half-pipe with helix-shaped beam – numerical results for the unloaded problem ($\underline{F} = \underline{0}$). The total internal elastic energy (including penalty coupling energy) Π_{int} and the beam tip displacement \underline{u}^B are stated.

coupling type	Π_{int} in $\text{J} \cdot 10^{-4}$	\underline{u}^B in m
full 3D	0.00000	[0.0, 0.0, 0.0]
BTSS-FULL-CONS	0.00000	[0.0, 0.0, 0.0]
BTSS-FULL-REF	3.37499	[0.24411, -0.37493, -0.03631]
BTSS-FULL-DISP	0.00000	[0.0, 0.0, 0.0]

Figure 6.16 visualizes the deformed configurations for the unloaded ($\underline{F} = \underline{0}$) structure. Since no pre-stressing or prescribed initial deformations are applied to the structure, the analytical displacement field for the unloaded structure vanishes. The BTSS-FULL-REF variant exhibits non-vanishing displacements, cf. Figure 6.16(c). This is because the coupling constraints in the reference configuration are only fulfilled by the BTSS-FULL-REF variant (6.11), if the beam centerline lies exactly on the solid surface, which is not the case in this example. The coupling conditions thus force the beam centerline to lie on the solid surface. This in turn leads to an artificial pre-stressing of the system as both the beam and the solid are deformed in order to fulfill the coupling constraints in the unloaded reference configuration. All other BTSS-FULL coupling variants and the full 3D solution exhibit vanishing displacements up to machine precision as expected. A quantitative comparison of the variants is given in Table 6.1. As discussed above, only the BTSS-FULL-REF variant has a non-zero internal elastic energy Π_{int} (including the penalty coupling potential) and beam tip displacement \underline{u}^B for the unloaded state. Figure 6.17 visualizes the deformed configurations for the loaded structure. It can be seen that the BTSS-FULL-CONS variant closely resembles the full 3D reference solution. The two other variants, BTSS-FULL-REF and BTSS-FULL-DISP, exhibit a different solution than the full 3D model. Again, quantitative comparisons of the variants are given in Tables 6.2 and 6.3. The results for the BTSS-FULL-REF and BTSS-FULL-DISP show a large discrepancy with respect to the reference solution. For the BTSS-FULL-REF variant, this can easily be explained since already the initial (unloaded) configuration does not match the reference solution. For the BTSS-FULL-DISP variant, this discrepancy illustrates that the simplified coupling conditions are not able to accurately describe the coupling between the beam and the solid surface if the discretized beam centerline does not exactly lie within the discretized solid surface in the reference configuration. Furthermore, the balance of internal and external moments around the origin shows that the conservation of angular momentum is not fulfilled by the BTSS-FULL-DISP variant, cf. Table 6.2. Finally, the internal elastic energy and the beam tip displacement obtained with the BTSS-FULL-CONS variant are very close to the reference solution, which is a remarkable feature considering the much simpler spatial discretization of the mixed-dimensional problem.

Recapitulatory, after the first two examples it can be stated that both presented simplifications of the BTSS-FULL conditions, BTSS-FULL-REF and BTSS-FULL-DISP, are not suitable for general purpose BTSS coupling problems. Only the BTSS-FULL-CONS variant with a consistent handling of the surface normal vector, and its derivatives, passes the constant stress transfer tests and gives accurate and usable results. Therefore, only the consistent variant will be used in the

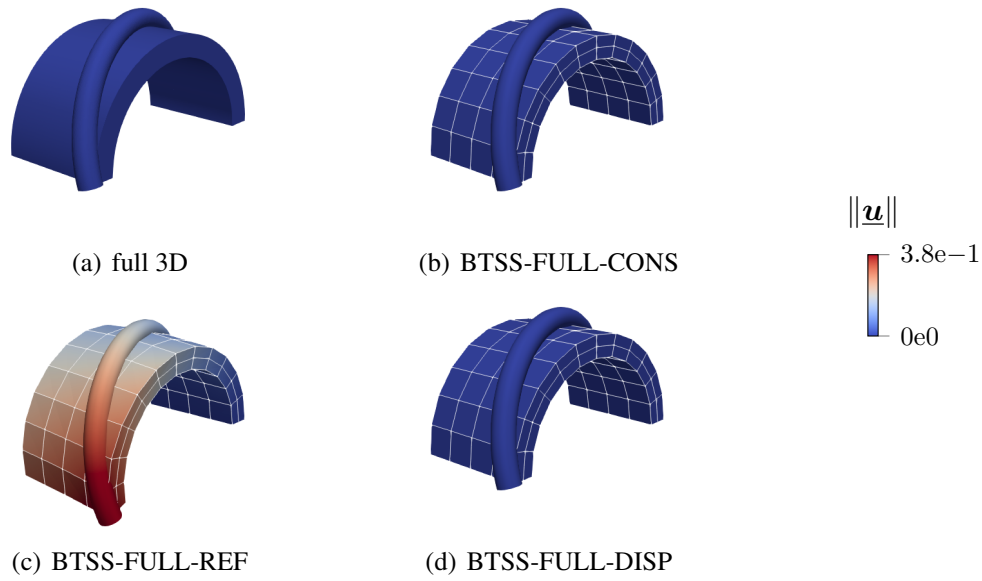


Figure 6.16.: Half-pipe with helix-shaped beam – deformed configurations for the unloaded problem ($\underline{F} = \underline{0}$). The results for the various coupling schemes are shown and the contour plots visualize the displacement magnitude.

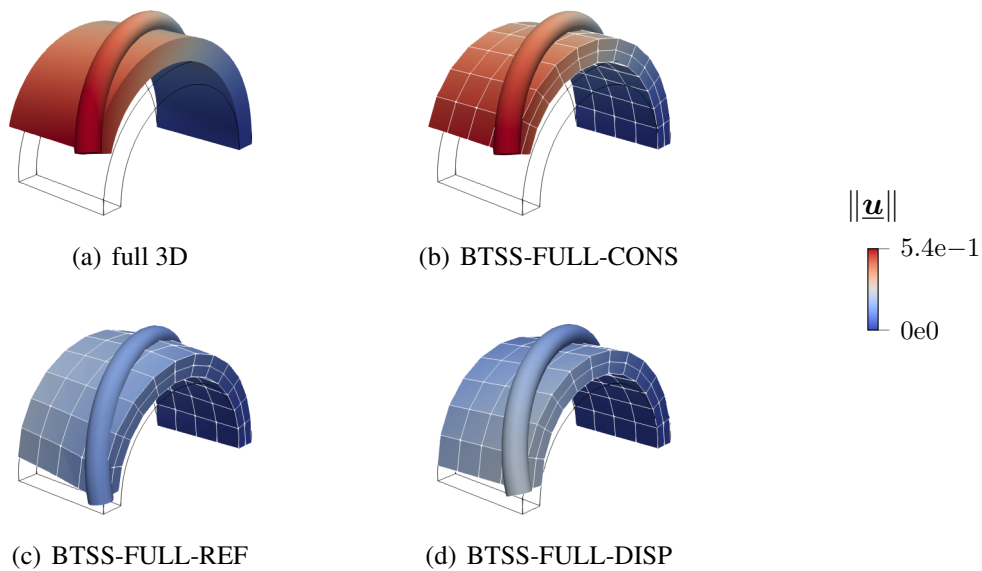


Figure 6.17.: Half-pipe with helix-shaped beam – deformed configurations for the loaded problem. The results for the various coupling schemes are shown and the contour plots visualize the displacement magnitude.

Table 6.2.: Half-pipe with helix-shaped beam – numerical results for energy and balance of moments. The total internal elastic energy (including penalty coupling energy) Π_{int} , the total energy errors, and the normalized sum of internal and external moments are stated.

coupling type	Π_{int} in $\text{J} \cdot 10^{-4}$	$\frac{\ \Pi_{\text{int}} - \Pi_{\text{int,full3D}}\ }{\ \Pi_{\text{int,full3D}}\ }$	$\frac{\ \Sigma(\underline{\mathbf{M}}_{\text{int}} + \underline{\mathbf{M}}_{\text{ext}})\ }{\ \underline{\mathbf{F}}\ l}$
full 3D	1.14109	–	0.0000
BTSS-FULL-CONS	1.12581	1.3392%	0.0000
BTSS-FULL-REF	4.39811	285.4301%	0.0000
BTSS-FULL-DISP	4.74429	58.4232%	126.5426

Table 6.3.: Half-pipe with helix-shaped beam – numerical displacements results. The beams tip displacement $\underline{\mathbf{u}}^{\mathcal{B}}$ and the relative tip displacement errors are stated.

coupling type	$\underline{\mathbf{u}}^{\mathcal{B}}$ in m	$\frac{\ \underline{\mathbf{u}}^{\mathcal{B}} - \underline{\mathbf{u}}_{\text{full3D}}\ }{\ \underline{\mathbf{u}}_{\text{full3D}}\ }$
full 3D	[-0.08411, 0.55495, -0.00476]	–
BTSS-FULL-CONS	[-0.08077, 0.54627, -0.00883]	1.8088%
BTSS-FULL-REF	[0.05225, 0.10224, -0.02442]	84.3041%
BTSS-FULL-DISP	[-0.03799, 0.22497, 0.05944]	60.4513%

remainder of this contribution to model the positional coupling between beam and solid surface.

6.4.3. Supported plate

In this example the importance of coupling both positions *and* rotations within the BTSS coupling scheme is demonstrated. This is achieved by comparing the BTSS-FULL-CONS (including rotational coupling) and BTSS-POS-CONS (without rotational coupling) coupling schemes to each other. The problem consists of a plate and a straight beam serving as a strut, cf. Figure 6.18. The plate is loaded with a surface load $\underline{\mathbf{f}} = 0.0002 \text{ N/m}^2 \underline{\mathbf{e}}_3$ at the bottom surface. The dimensions of the plate are $3 \text{ m} \times 1 \text{ m} \times 0.1 \text{ m}$ and it is modeled using a compressible Neo-Hookean material law ($E^{\mathcal{S}} = 1 \text{ N/m}^2$, $\nu^{\mathcal{S}} = 0$). On the opposite face of the surface load, the plate is reinforced by a straight beam with circular cross-section ($R = 0.075 \text{ m}$, $E^{\mathcal{B}} = 100 \text{ N/m}^2$ and $\nu^{\mathcal{B}} = 0$). The beam centerline is parallel to the $\underline{\mathbf{e}}_1$ axis and offset from the solid surface by a distance of R in surface normal direction, i.e., the beam cross-section exactly touches the solid surface. In $\underline{\mathbf{e}}_2$ direction, the beam centerline is offset by a distance of 0.35 m with respect to the middle of the plate. At the right end, both solid and beam are fully clamped. Apart from that, no displacement boundary conditions are applied to the system.

A full 3D reference solution is computed, where the plate as well as the beam are fully resolved with 3D solid finite elements. In this reference solution, the connection between the beam and the plate, i.e., the weld line, has to be modeled. For the mixed-dimensional BTSS-FULL coupling scheme a rigid connection between the beam and the solid surface is assumed, cf. Section 3.2.2. Figure 6.19 shows the fully resolved connection (weld line) between the beam and the plate which

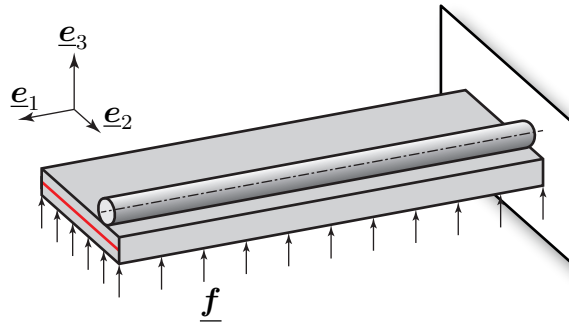


Figure 6.18.: Supported plate – problem setup. The red line indicates the material line for which the results are plotted in Figure 6.21.

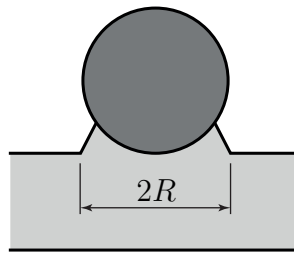


Figure 6.19.: Supported plate – modeled weld line between the beam and the plate in the full 3D reference solution.

has a total width of $2R$. The weld line between beam and solid is assumed to be made up of the solid material and resembles a sufficiently stiff connection between the beam surface and the solid surface to align with the modeling assumptions of the mixed-dimensional model. The full model is discretized with first-order hexahedral (*hex8*) elements, thus resulting in roughly 125,000 elements and 450,000 degrees of freedom to obtain mesh convergence.

In the 1D-2D BTSS coupling problems, the coupling between the beam and the solid surface is realized with first-order Lagrange polynomials as shape functions for the rotational and the positional Lagrange multipliers ($\epsilon^U = 100 \text{ N/m}^2$, $\epsilon^R = 0.1 \text{ Nm/m}$). The plate is modeled with $30 \times 10 \times 1$ eight-noded solid shell elements, cf. [20, 147]. The beam is discretized using 10 Simo–Reissner beam finite elements. The total number of degrees of freedom for the BTSS coupling problem is only 2,175.

Figure 6.20 visualizes the deformed configurations for the various models. The full 3D reference solution as well as the 1D-2D BTSS-FULL-CONS solution including rotational coupling behave very similarly, i.e., the plate is bent upwards and the strut stiffens the plate, cf. Figures 6.20(a) and 6.20(b). The BTSS-POS-CONS variant without rotational coupling, however, exhibits much larger deformations. In that case, the rotational movement of the plate is not coupled to the rotations of the supporting beam, i.e., the torsional stiffness of the beam is not directly coupled to the solid plate, thus resulting in an overall softer structural behavior, cf. Figure 6.20(c). This clearly underlines the importance of including rotational coupling for BTSS coupling problems to fully capture all relevant stiffening effects. A more detailed comparison of the variants is given in Figure 6.21, where the displacements along the curve indicated in Figure 6.18 are visualized. Now it also becomes clear quantitatively that the displacement results

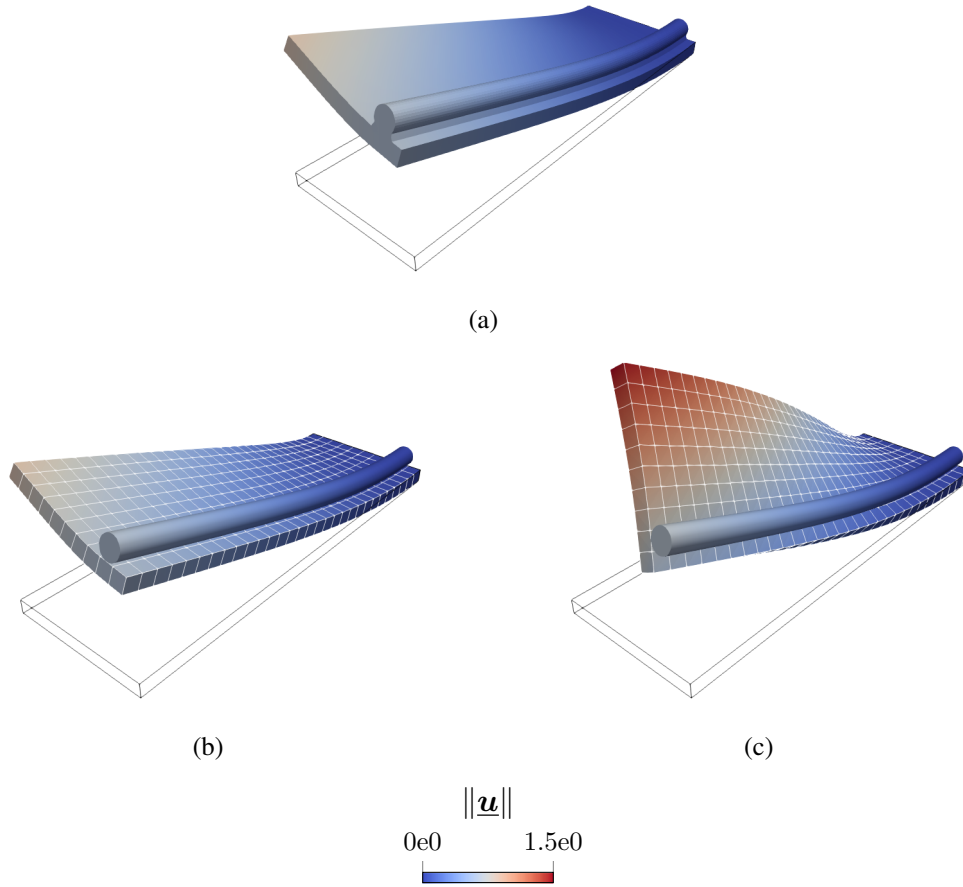


Figure 6.20.: Supported plate – deformed configurations for various modeling techniques. Full 3D model (a), BTSS-FULL-CONS (with rotational coupling) (b) and BTSS-POS-CONS (without rotational coupling) (c). The contour plots visualize the displacement magnitude.

obtained with the BTSS-POS-CONS variant without rotational coupling are unphysical due to the underestimated overall stiffness of the structure. Furthermore, the full 3D model and the BTSS-FULL-CONS model exhibit almost matching displacement curves. Considering that the latter reduces the number of degrees of freedom by a factor of about 200 as compared with the former, this is a remarkable result and showcases the efficiency of the BTSS-FULL-CONS coupling method for reinforced plate applications.

6.4.4. Stented elastic artery

This final example is designed to give an outlook towards real-life applications and the applicability of the proposed BTSS coupling approach to more complex coupling scenarios. This is motivated by the fact that in [139] a general one-dimensional vascular stent model was found to be in good agreement with the results of a fully resolved three-dimensional simulation presented in [156], at a fraction of the degrees of freedoms. In this example, the suitability of the proposed

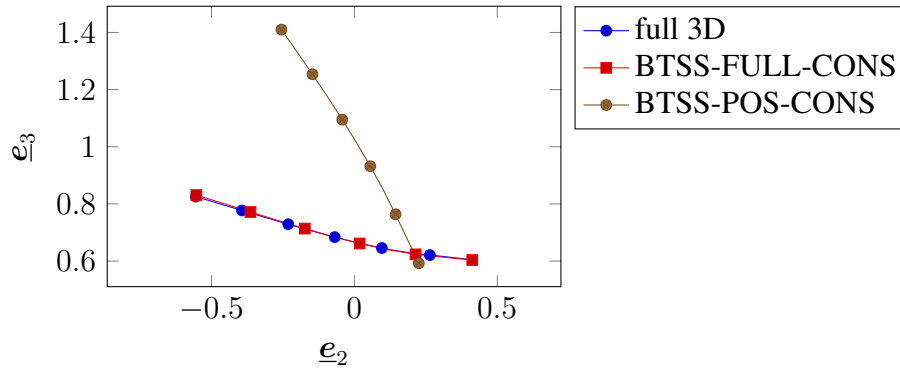


Figure 6.21.: Supported plate – deformed configurations of the material line indicated in Figure 6.18 for various modeling techniques.

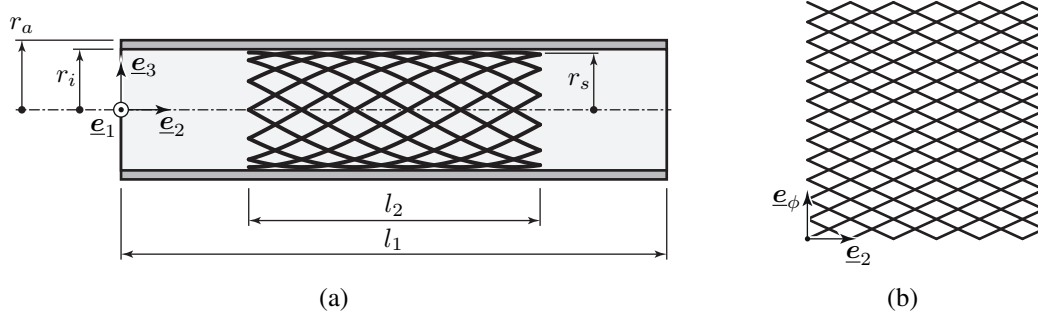


Figure 6.22.: Stented elastic artery – problem setup. Geometric configuration of the stent and artery (a), and unwrapped stent geometry (b).

BTSS-FULL coupling approach in the context of vascular angioplasty is investigated. The present example is inspired by the well-known fluid-structure interaction (FSI) benchmark problem of a pressure wave traveling through an elastic tube (artery), that was originally proposed in [48], to validate the suitability of FSI algorithms for blood flow simulations. The presented BTSS-FULL coupling approach is employed to capture the effect of a diamond-shaped stent on the behavior of the overall system.

Figure 6.22(a) illustrates the problem setup. As in the original benchmark problem, a constant pulse p_{in} is applied for $3 \cdot 10^{-3}$ s at the fluid inlet. Besides the pulse, zero traction conditions are applied to the fluid inflow as well as outflow boundary, on the left and right end of the pipe, respectively. Both ends of the pipe are assumed to be clamped. The beam centerline geometry depicted in Figure 6.22(b) is wrapped around a cylinder with a radius of $r_s = r_i - R$, i.e., the stent perfectly fits into the pipe up to an offset the size of the beam radius. In addition to the BTSS-FULL problem introduced in Section 5.1, this example contains a fluid, modeled as Newtonian with a constant dynamic viscosity η_F , and a density ρ_F , using the incompressible Navier-Stokes equations. The fluid is coupled to the solid via classical surface-coupled FSI [75] in a partitioned manner aided by a matrix free Newton Krylov method [83] to accelerate convergence. Classical no-slip conditions are enforced on the FSI boundary. Since FSI problems are necessarily transient, the BTSS-FULL problem is enhanced by a Generalized- α Lie group time integration

Table 6.4.: Stented elastic artery – problem parameters.

Geometry	r_i	0.0125 m
	r_a	0.01375 m
	r_s	0.01246 m
	l_1	0.15 m
	l_2	0.06 m
Beam	E_B	$9 \cdot 10^8 \text{ N/m}^2$
	ρ_B	7800 kg/m^3
	ν_B	0.3
	R	0.0004 m
Solid	E_S	$3 \cdot 10^5 \text{ N/m}^2$
	ρ_S	1200 kg/m^3
	ν_S	0.3
Fluid	p_{in}	500 N/m^2
	ρ_F	1000 kg/m^3
	η_F	0.003 kg/(ms)

method, for all structural degrees of freedom [29, 30]. Here, the parameters are chosen to obtain a fully implicit scheme, and a time step size $\Delta t = 10^{-4} \text{ s}$ is used. To the fluid field, a classical second-order accurate Generalized- α time integration scheme, with the same time step size as for the structure field, is applied [70]. A detailed analysis of the effect of different time integration parameters on the original benchmark problem can be found in [91]. The mortar-type BTSS-FULL-CONS method is applied using linear shape functions for the Lagrange multiplier field and the penalty parameters $\epsilon^V = 10^9 \text{ N/m}^2$ and $\epsilon^R = 10^2 \text{ Nm/m}$. The stent and pipe are discretized with 264 Simo–Reissner beam elements and 2,880 solid shell elements, respectively. For the fluid, 22,800 streamline upwind Petrov–Galerkin (SUPG) stabilized Q1-Q1 fluid elements with an additional div-grad stabilization term [124] are employed. All dimensions and material parameters of the problem setup are summarized in Table 6.4.4.

Figures 6.23(a) to 6.23(c) depict the deformed problem (scaled with a factor of 15) after 0.01 s, 0.016 s, and 0.024 s. It is evident, that the wall displacement caused by the pressure wave in the stiffer stented region in Figure 6.23 is smaller than in the unstented region. Figure 6.24 illustrates the fluid velocity v_2 in channel direction along the pipe’s centerline. The fluid velocity plot demonstrates that the maximum fluid velocity increases slightly while traveling through the stented region.

While the change of compliance in the artery, and thus also its effect on the fluid flow, could also be modeled by a simpler homogenized approach, the proposed approach allows to quantify the forces interchanged on the coupling interface. Figures 6.25(a) and 6.25(c) show the coupling interactions, i.e., the line loads exerted on the beam system by the surface. In general, it can be observed, that the interaction is highest at the ends of the stent, i.e., at the transition between a compliant and a very stiff region. This is particularly notable in Figure 6.25(b), where the pressure wave is right at the transition between the unstented and stented region. Furthermore,

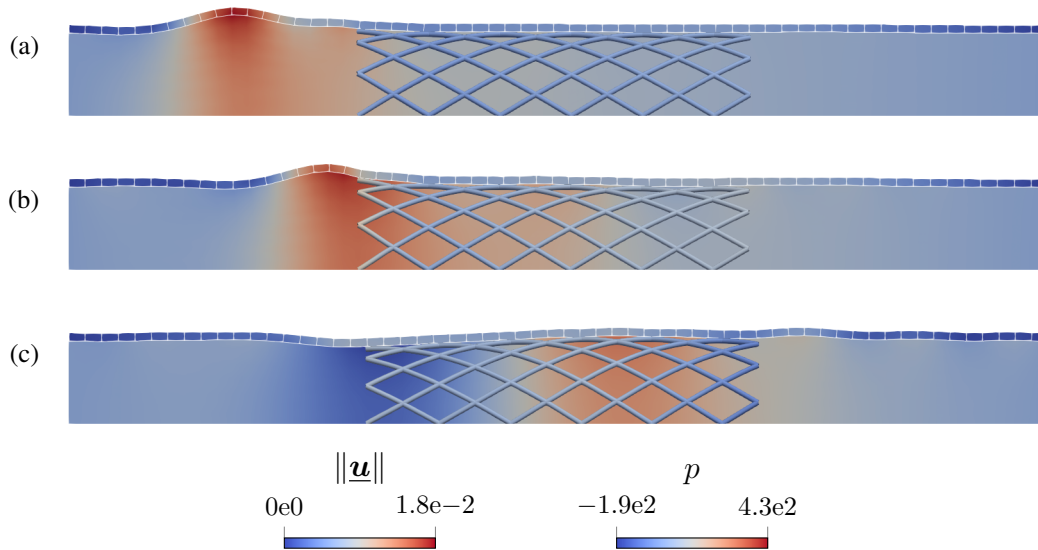


Figure 6.23.: Stented elastic artery – deformed configurations at various simulation times. The snapshots are taken at $t = 0.01$ s (a), $t = 0.016$ s (b) and $t = 0.024$ s (c) respectively. The norm of the displacements is shown in the solid and the pressure is shown in the fluid. The displacements are scaled with a factor of 15.

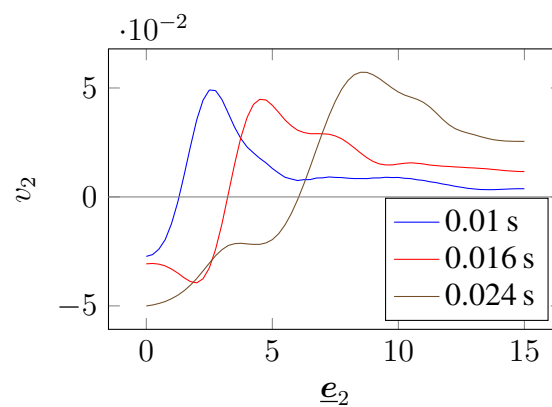


Figure 6.24.: Stented elastic artery – plot of the fluid velocity v_2 in channel direction along the centerline of the pipe.

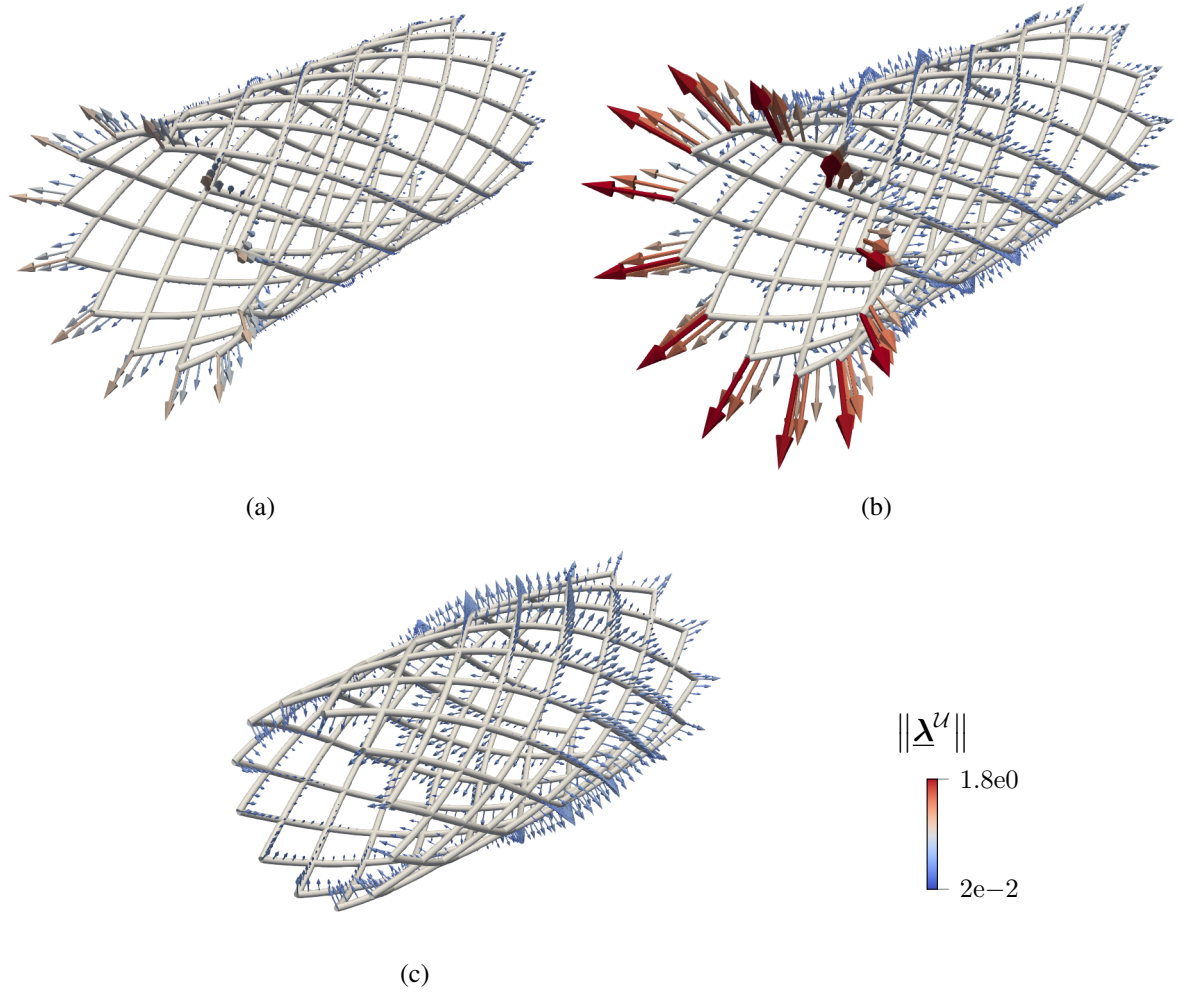


Figure 6.25.: Stented elastic artery – negative coupling line loads for beam-to-solid surface coupling at various simulation times. The snapshots are taken at $t = 0.01$ s (a), $t = 0.016$ s (b) and $t = 0.024$ s (c) respectively. Five values are visualized along each beam element and only the positional coupling loads are shown.

dividing the 1D coupling loads by the beam diameter results in an approximation of the interaction stresses between the beam and the artery. The absolute maximum normal and shear stresses can be estimated for this example as $1.8179 \cdot 10^3 \text{ N/m}^2$ and $1.28899 \cdot 10^3 \text{ N/m}^2$ (not visualized in the figures), respectively. The sign for the normal stresses is positive, therefore, this is a tensile stress between the beam and the solid surface.

It is evident, that the shown example is still a long way from the complexity of simulating real-life stenting procedures. Using BTSS coupling, instead of frictional BTSS contact, prevents the investigation of real-life phenomena such as stent migration. Nevertheless, because of growth and remodeling of the artery, coupling between the stent and the artery is a valid assumption in many patient-specific cases. Also, direct interactions between the stent and the fluid flow are not considered in this example. In any case, the presented simulation results have shown that the proposed BTSS-FULL coupling approach can generally be used for geometrically complex

beam systems such as stent geometries. The ability to capture important phenomena, such as changes in compliance and its effect on the blood flow as well as the distribution of the interaction forces, which may provide insight into the long-term success of vascular angioplasty, has been demonstrated.

7. Beam-to-solid surface contact

The main focus of this thesis lies in the development of BTS coupling, i.e., mesh tying, schemes. Nevertheless, a unilateral contact formulation between 1D beams and 2D solid surfaces will be presented in this chapter, i.e., beam-to-solid surface contact (BTSSC). This is the obvious next step in the development of a general purpose mixed-dimensional BTS interaction framework. In the previous sections, the constraint equations are weakly enforced using a Lagrange multiplier approach and subsequently discretized with a (penalty regularized) mortar-type finite element method. Recently, the mortar method has been successfully applied in the context of beam-to-beam contact problems, cf. [28, 142]. While the development of such mortar-type contact schemes for BTS problems is subject of ongoing research, the presented BTSSC scheme is directly based on a space continuous penalty potential. The qualitative and quantitative results obtained in Section 7.2 demonstrate the maturity of the presented penalty-based BTSSC scheme.

7.1. Problem formulation

In this section a BTSSC formulation is presented, that formulates the contact conditions as a line constraint along the entire beam, i.e., a line-to-surface contact scheme. This can be viewed as an extension to the beam-to-surface (BTSS) coupling scheme presented in Chapter 6. Furthermore, in some aspects, the line-to-surface contact scheme closely resembles beam-to-beam line contact formulations presented in [93, 95, 100].

7.1.1. Contact kinematics

All contact models considered in this chapter are based on the assumptions of frictionless contact, circular beam cross-sections with a radius R and small shear deformations of the contacting beams. With these assumptions, the contact terms can be completely described by the positional field of the beam centerline. The contact conditions in the line-to-surface scheme are fulfilled for each point $\underline{r}(s)$ along the beam centerline. Consequently, the corresponding point on the solid surface is obtained by formulating a unilateral minimal distance problem in the current configuration:

$$d_{ul}(s) := \min_{\xi^S, \eta^S} d(s, \xi^S, \eta^S) = d(s, \xi_c^S, \eta_c^S) \quad (7.1)$$

with

$$d(s, \xi^S, \eta^S) = \|\underline{r}(s) - \underline{x}^S(\xi^S, \eta^S)\|. \quad (7.2)$$

As with the BTSS coupling formulation, it can be assumed that this closest point projection has a unique solution for the envisioned applications. The two orthogonality conditions obtained from

the minimal distance problem (7.1) read

$$\begin{aligned}\underline{\mathbf{x}}_{,\xi}^S(\xi^S, \eta^S)^T (\underline{\mathbf{r}}(s) - \underline{\mathbf{x}}^S(\xi^S, \eta^S)) &= 0 \\ \underline{\mathbf{x}}_{,\eta}^S(\xi^S, \eta^S)^T (\underline{\mathbf{r}}(s) - \underline{\mathbf{x}}^S(\xi^S, \eta^S)) &= 0.\end{aligned}\quad (7.3)$$

For a given beam coordinate s , these conditions can be solved for the unknown surface coordinates ξ^S and η^S . The non-trivial solution of (7.3) requires the surface directors $\underline{\mathbf{x}}_{,\xi}^S = \partial \underline{\mathbf{x}}^S / \partial \xi^S$ and $\underline{\mathbf{x}}_{,\eta}^S = \partial \underline{\mathbf{x}}^S / \partial \eta^S$ to be orthogonal to the relative vector between the surface point and beam centerline point, i.e., this relative vector is parallel to the outward pointing surface normal vector $\underline{\mathbf{n}} \in \mathbb{R}^3$,

$$\underline{\mathbf{r}}(s) - \underline{\mathbf{x}}^S(\xi_c^S, \eta_c^S) = d_{ul}(s) \underline{\mathbf{n}}(\xi_c^S, \eta_c^S). \quad (7.4)$$

A left multiplication of (7.4) with $\underline{\mathbf{n}}^T$ leads to the following definition of the minimal distance function,

$$d_{ul}(s) = \underline{\mathbf{n}}(\xi_c^S, \eta_c^S)^T (\underline{\mathbf{r}}(s) - \underline{\mathbf{x}}^S(\xi_c^S, \eta_c^S)). \quad (7.5)$$

In the next step, a *gap* function, i.e., the minimal distance between a point on the circumference of the circular beam cross-section and the solid surface, is defined as

$$g(s) = d_{ul}(s) - R. \quad (7.6)$$

This definition can be written as a simple subtraction of scalar values due to the previously mentioned assumption of small shear deformations in the beam, i.e., the solid surface normal vector lies within the beam cross-section plane. The gap function has to fulfill the non-penetration condition

$$g(s) \geq 0 \quad \forall s, \quad (7.7)$$

i.e., the closest distance between a point on the beam surface and the solid surface has to be larger or equal to zero as penetrations are prohibited.

7.1.2. Variational formulation and finite element discretization

The contact constraint enforcement in the BTSSC scheme is based on a space continuous penalty potential, similar to beam-to-beam line contact [93, 95, 100], i.e.,

$$\Pi_\epsilon^C = \int_{\Omega_0^B} \tilde{\Pi}_\epsilon^C(s) \, ds \quad \text{with} \quad \tilde{\Pi}_\epsilon^C(s) = \frac{\epsilon^C}{2} \langle g(s) \rangle^2 \quad (7.8)$$

where $\epsilon^C \in \mathbb{R}^+$ is a scalar penalty parameter and

$$\langle x \rangle = \begin{cases} x, & x \leq 0 \\ 0, & x > 0 \end{cases}. \quad (7.9)$$

Variation of the penalty potential (7.8) yields the contact contributions to the weak form,

$$\delta \Pi_\epsilon^C = \epsilon^C \int_{\Omega_0^B} \langle g(s) \rangle \delta g(s) \, ds, \quad (7.10)$$

with the variation of the gap function, cf. Appendix C,

$$\delta g(s) = (\delta \underline{\mathbf{r}}(s) - \delta \underline{\mathbf{x}}^S(\xi_c^S, \eta_c^S))^T \underline{\mathbf{n}}(s). \quad (7.11)$$

From the virtual work expression (7.10) the contact force $\underline{\mathbf{f}}^C(s)$ acting on the beam centerline can be identified as

$$\underline{\mathbf{f}}^C(s) = f(s) \underline{\mathbf{n}}(s) \quad \text{with} \quad f(s) = -\epsilon^C \langle g(s) \rangle. \quad (7.12)$$

Here f is a scalar penalty law, i.e., the contact force dependent on the gap function. A more detailed discussion on various variants of the penalty law is given in Section 7.1.3. Adding the variation of the penalty potential to the virtual work of the beam and the solid yields the total virtual work of the BTSSC problem

$$\delta W^S + \delta W_{(\cdot)}^B + \delta \Pi_\epsilon^C = 0 \quad (7.13)$$

To ensure a unique closest point projection, a C^0 -continuous surface normal field is required. Therefore, the C^0 -continuous averaged surface normal field from Section 6.3.1 is employed in combination with the presented BTSSC scheme. The discretized contact contributions to the weak form can be obtained by inserting the finite element interpolations from Section 2.3 into (7.10), i.e.,

$$\delta \Pi_{\epsilon,h}^C = \sum_{l=1}^{n^B} \delta \hat{\mathbf{d}}_l^B \underbrace{\int_{\Gamma_{c,h}} \epsilon^C \langle g(\xi^B) \rangle \mathbf{H}_l^T \underline{\mathbf{n}}_h \, ds}_{\mathbf{r}_r^{C[l]}} - \sum_{k=1}^{n^S} \delta \hat{\mathbf{d}}_k^S \underbrace{\int_{\Gamma_{c,h}} \epsilon^C \langle g(\xi^B) \rangle N_k^T \underline{\mathbf{n}}_h \, ds}_{-\mathbf{r}_s^{C[k]}}, \quad (7.14)$$

where the abbreviations $\mathbf{r}_r^{C[l]}$ and $\mathbf{r}_s^{C[k]}$, describing the nodal BTSSC forces on a beam and solid node, respectively, have been introduced. Accordingly, the contact contributions to the global force vector are \mathbf{r}_r^C and \mathbf{r}_s^C , i.e., the BTSSC residual vectors. Finally, the global linearized system of equations can be given as

$$\begin{bmatrix} \mathbf{K}_{ss}^S + \mathbf{K}_{ss}^C & \mathbf{K}_{sr}^C \\ \mathbf{K}_{rs}^C & \mathbf{K}_{rr}^B + \mathbf{K}_{rr}^C \end{bmatrix} \begin{bmatrix} \Delta \mathbf{d}^S \\ \Delta \mathbf{d}^B \end{bmatrix} = \begin{bmatrix} -\mathbf{r}_s^S - \mathbf{r}_s^C \\ -\mathbf{r}_r^B - \mathbf{r}_r^C \end{bmatrix}, \quad (7.15)$$

with the contact contributions to the global tangent stiffness matrix $\mathbf{K}_{ss}^C = \partial \mathbf{r}_s^C / \partial \mathbf{d}^S$, $\mathbf{K}_{sr}^C = \partial \mathbf{r}_s^C / \partial \mathbf{d}^B$, $\mathbf{K}_{rs}^C = \partial \mathbf{r}_r^C / \partial \mathbf{d}^S$ and $\mathbf{K}_{rr}^C = \partial \mathbf{r}_r^C / \partial \mathbf{d}^B$. The presented (frictionless) BTSSC scheme only depends on the positional beam centerline degrees of freedom, therefore no rotational degrees of freedom are stated in (7.15). All derivatives in the discrete equations (7.15) are evaluated using forward automatic differentiation (FAD), cf. [78], using the Sacado software package [121], which is part of the Trilinos project [143].

Remark 7.1. The enforcement of the contact constraints via the presented penalty potential (7.8) inevitably results in a violation of the non-penetration condition (7.7). In the case of BTSSC, it can be argued that this penetration is physical, as it can be interpreted as the in-plane deformation of the beam cross-section. Obviously, this requires the penalty parameter to be a function of the material and geometric properties of the beam. However, a thorough derivation and analysis of this relation is beyond the scope of the present thesis. The interested reader is referred to [98, 100] for a detailed discussion on this topic in the context of beam-to-beam contact.

Remark 7.2. To avoid spurious locking effects, as observed in Chapter 4, the integrals in (7.14) are evaluated using element-based integration without boundary segmentation. This will result in a violation of suitable BTSSC constant stress transfer tests. Nevertheless, the results in Section 7.2 demonstrate that the presented BTSSC scheme can still be employed to obtain physically accurate results.

Remark 7.3. The inclusion of frictional contact phenomena between the beam and the solid surface introduces contact terms acting on the rotational degrees of freedom of the beam. This is because the frictional contact forces act at the contact point between the beam cross-section and the solid surface, which lies on the circumference of the beam cross-section. The frictional forces are perpendicular to the surface normal vector, therefore, a projection of the frictional forces onto the beam centerline results in a contact moment. A variationally consistent description of this contact moment introduces coupling terms dependent on the rotational degrees of freedom. However, this is conceptually different and should not be confused with rotational (BTSS) coupling introduced in Chapter 5 and section 6.1.3, where the orientation of the beam cross-section is coupled to a suitable solid surface triad, thus resulting in rotational coupling terms. In the case of frictional BTS contact, no rotations are coupled. Instead, the rotational coupling terms arise because of the previously described projection of the friction forces onto the beam centerline.

7.1.3. Penalty laws

In this section two different types of penalty laws f will be presented. Both are directly adapted from line-to-line beam-to-beam contact, cf. [98]. The penalty law (7.12) derived from the penalty potential (7.8) is a linear penalty law,

$$f(g) = \begin{cases} -\epsilon^c g, & g \leq 0 \\ 0, & g > 0. \end{cases} \quad (7.16)$$

In practical applications, it is common to use a regularized penalty law that allows for a smooth contact force transition between active and inactive contact. Such a regularization usually improves the behavior of the nonlinear solver and the time integration scheme, cf. [98]. The employed quadratically regularized penalty law in this thesis is directly adopted from [98] and reads

$$f(g) = \begin{cases} \frac{\epsilon^c}{2} (\bar{g} - 2g), & g \leq 0 \\ \frac{\epsilon^c}{2\bar{g}} (\bar{g} - g)^2, & 0 < g \leq \bar{g} \\ 0, & g > \bar{g}. \end{cases} \quad (7.17)$$

Here, $\bar{g} \in \mathbb{R}^+$ defines the (positive) value of the gap function, where the first contact force arises, cf. Figure 7.1. The corresponding integrand of the total penalty potential is

$$\tilde{\Pi}_\epsilon^c(g) = \begin{cases} \frac{\epsilon^c}{6} (-3\bar{g}^2 + 3g\bar{g} - \bar{g}^2), & g \leq 0 \\ \frac{\epsilon^c}{6\bar{g}} (\bar{g} - g)^3, & 0 < g \leq \bar{g} \\ 0, & g > \bar{g}. \end{cases} \quad (7.18)$$

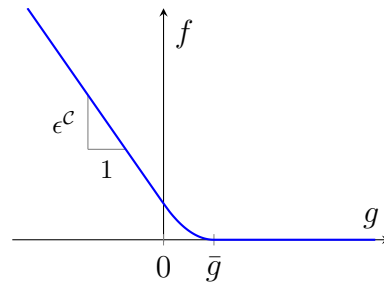


Figure 7.1.: Visualization of the quadratically regularized penalty law. Figure is adapted from [98].

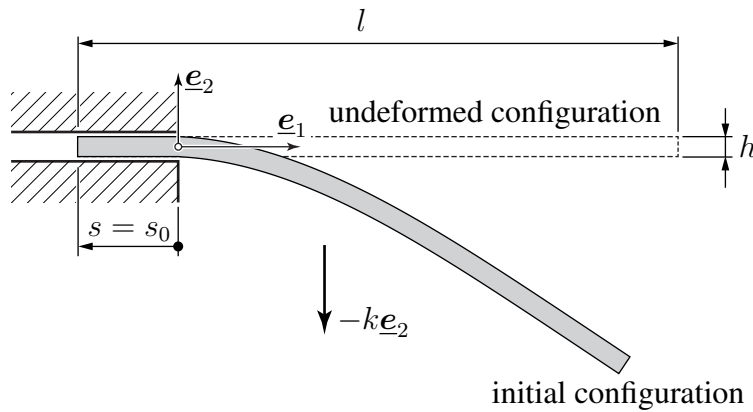


Figure 7.2.: Sliding spaghetti problem – problem setup. Figure adapted from the author’s article [134], permissions granted under the Creative Commons (CC BY) license.

7.2. Numerical examples

7.2.1. Sliding spaghetti problem

In this example, a variant of the sliding spaghetti problem is considered, cf. [32, 66, 67, 134]. The name of this example stems from the simple experiment almost everybody has performed at some point, sucking a cooked noodle into ones mouth. The problem considered in this example is an adapted version of the sliding spaghetti problem presented in [134]. Figure 7.2 depicts the problem setup and Table 7.1 states the geometric and material properties of the problem. It consists of an initially straight beam subject to a constant body load k in negative \underline{e}_2 -direction. The left end of the beam is placed in a rigid guide and is initially retracted by a distance $s = s_0$. Over the course of the quasi-static simulation, the beam is further retracted into the guide until the retracted distance $s = s_{\text{end}}$. Even in the static case, this is a challenging problem for numerical (contact) algorithms as it includes large deformations and an inherently large relative sliding motion between the guide and the beam.

The beam is discretized with 250 equidistant Simo–Reissner beam finite elements. Although the beam has a high slenderness ratio, it is important to include shear flexibility, as the shear deformations within the guide result in a rotation of the beam cross-section at the opening of the guide. Neglection of this shear deformation, e.g., by employing Kirchhoff–Love or Euler–

Table 7.1.: Sliding spaghetti problem – geometric and material properties, cf. [134].

total beam length	l	6 m
beam width	b	1 m
beam height	h	0.2 m
Young's modulus	E^B	10^7 N/m^2
Poisson's ratio	ν^B	0
body load	k	1000 N/m^3
initially retracted length	s_0	0.5 m
final retracted length	s_{end}	5.5 m

Bernoulli beam finite elements, leads to a vanishing rotation at the guide and inaccurate results, cf. [134]. The prescribed displacement s is applied to the left end of the beam via a Dirichlet boundary condition. All displacements and rotations are constrained at the left end of the beam. The top and bottom parts of the guide are modeled with one eight-noded hexahedral element (*hex8*) each. The height of the resulting guide is equal to the height of the beam. To represent the rigid guide, both solid elements are fully constrained. The contact between the beam and guide is modeled with the penalty-based BTSSC scheme (linear penalty law with $\epsilon^C = 10^{10} \text{ N/m}^2$ and $n_{\text{GP}} = 6$). A sufficiently large penalty parameter is chosen, to accurately represent the rigid guide for comparison purposes. The solution of this problem is performed in two stages: first, the body load is applied to the undeformed configuration with 5 incremental load steps. In the second stage, the left end of the beam is retracted with 50 load steps until $s = s_{\text{end}}$.

The results obtained with the BTSSC method are compared to results obtained with the sliding-beam-formulation (SBF), cf. [66, 67, 134, 146]. Within the SBF, a coordinate transformation is introduced, which maps the region of the beam inside the guide and the region of the beam outside the guide to constant intervals. The contact conditions, i.e., constrained displacement in \underline{e}_2 direction inside the guide and unconstrained outside the guide, can then be directly applied to the transformed intervals, as the boundary conditions are constant for each interval of the transformed system. In [134], the SBF model of the sliding spaghetti problem was successfully compared to 1D beam and 3D solid finite element models using the commercial finite element solver ABAQUS [39]. The finite element discretization of the SBF model is setup as described in [134] and a total of 240 beam finite elements are used to discretize both intervals, which guarantees a spatially converged solution. The SBF is implemented and simulated with the open source simulation software HOTINT [49].

A detailed comparison between the results obtained with the BTSSC method and the SBF is given in Figure 7.3, where the tip trajectory of the right part tip of the beam is plotted over the course of the retraction process. It becomes clear, that the displacement results obtained with the two methods are very close to each other. This is a remarkable result, considering the fundamentally different modeling approach of both methods. Furthermore, this illustrates that the presented BTSSC method is able to accurately model the considered version of the sliding spaghetti problem. Finally, to illustrate the deformation of the sliding spaghetti problem, various configurations of the beam during the retraction process are shown in Figure 7.4.

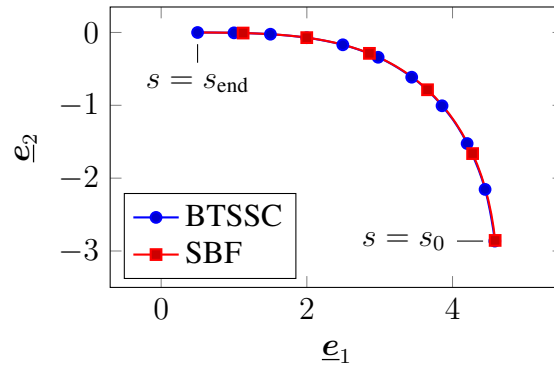


Figure 7.3.: Sliding spaghetti problem – trajectories of the right hand tip of the beam over the course of the retraction process for the BTSSC method and the SBF. The lower right part of the curves represent the initial configuration, the upper left part represents the retracted configuration.

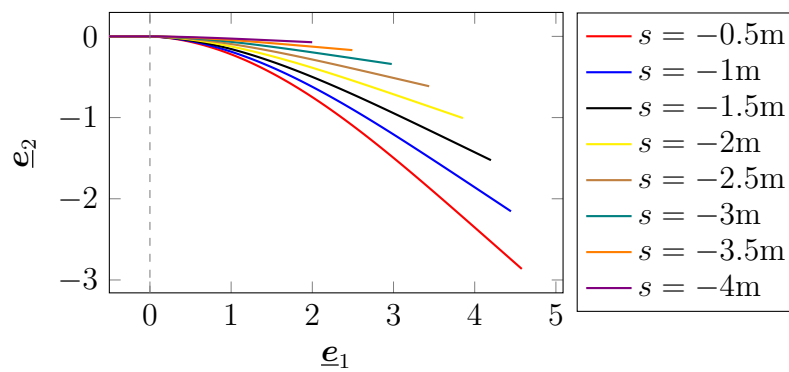


Figure 7.4.: Sliding spaghetti problem – deformed configurations at various retraction stages.

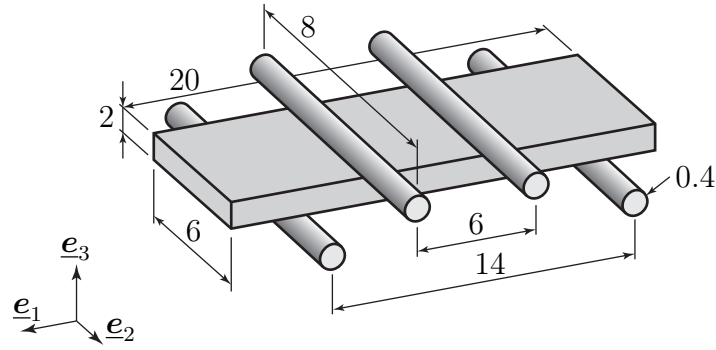


Figure 7.5.: Four-point bending test – problem setup. All given dimensions are in m.

7.2.2. Four-point bending test

In this example, finite deformation contact of a four-point bending test is analyzed. The bending specimen (Saint-Venant–Kirchhoff material model, $E^S = 1 \text{ N/m}^2$, $\nu^S = 0.3$) is placed between two straight beams on the bottom and two straight beams on the top ($E^B = 5 \text{ N/m}^2$, $\nu^B = 0$). In the reference configuration, the beams exactly touch the solid, i.e., the initial gap between the beams surface and solid surface is zero. All beams are fully constrained at both ends. Additionally, the ends of the two upper beams are moved downwards via a prescribed displacement by a distance of 3 m in negative \underline{e}_3 -direction. The geometric relations of the problem are illustrated in Figure 7.5. The four-point bending test is a commonly used test case in material sciences, since the (idealized) specimen exhibits pure bending between the two upper beams. In most real life applications, the indenters can be considered rigid relative to the specimen. However, the chosen ratio of indenter (beam) Young’s modulus to specimen (solid) Young’s modulus in this example is only 5, i.e., the flexibility of the beams has an effect on the overall solution to the problem, thus presenting a more challenging problem for the employed contact algorithm.

The problem has two planes of symmetry, the \underline{e}_1 – \underline{e}_3 plane and the \underline{e}_2 – \underline{e}_3 plane. Therefore, only a quarter of the problem is actually modeled and symmetry boundary conditions are applied accordingly. The quarter of the specimen is discretized using $30 \times 9 \times 3$ eight-noded hexahedral elements (*hex8*). Each (half) beam is modeled using 4 Simo–Reissner beam finite elements. The contact interaction between the beams and the solid is realized with the penalty-based BTSSC scheme (quadratically regularized penalty law, $\epsilon^c = 10 \text{ N/m}^2$, $g_0 = 0.001 \text{ m}$, $n_{GP} = 6$). The displacement of the upper beams is applied in 10 equidistant static load steps. Due to the non-zero value of g_0 , the rigid body mode of the solid in \underline{e}_3 direction does not lead to numerical issues, as there is already a contact contribution to the global tangent stiffness matrix in the initial time step, eliminating all rigid body modes.

The final deformed configuration of the four-point bending problem is visualized in Figure 7.6. The expected behavior of the specimen can clearly be observed. Furthermore, due to the low relative stiffness, the indenters also exhibit visible deformations under the resulting contact forces. Two detailed visualizations of the quarter model of the problem are illustrated in Figure 7.7. In Figure 7.7(a) the second Piola–Kirchhoff stress S_{11} is visualized in the solid. Even in this large deformation configuration, the specimen exhibits an almost constant bending state between the two upper indenters. Furthermore, a deformation of the rectangular cross-section of the specimen

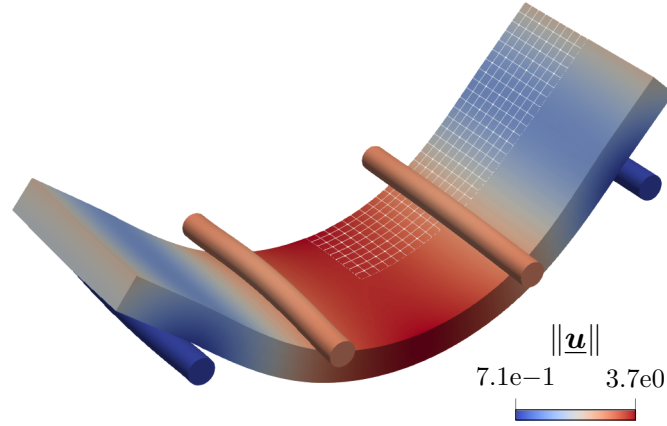


Figure 7.6.: Four-point bending test – deformed configuration. The contour plot visualizes the displacement magnitude. Note that only a quarter of the problem is actually meshed, due to the symmetry of the problem.

can be observed. This is due to the non-zero Poisson's ratio in the solid. The upper part of the specimen is compressed in \underline{e}_1 -direction and thus extends in \underline{e}_2 -direction. The opposite occurs on the bottom side of the specimen, resulting in the deformation of the specimen cross-section. The resulting second Piola–Kirchhoff stress S_{22} is about one quarter of the magnitude of the S_{11} stress, cf. Figure 7.7(b). Furthermore, the bending moment in the beams is visualized in Figure 7.7(a) and Figure 7.7(b), for the moment in \underline{e}_1 and \underline{e}_3 -direction, respectively. In this example frictionless contact is considered, i.e., the contact forces are normal on the solid surface, thus explaining the larger bending moment in \underline{e}_1 -direction. Figure 7.8 visualizes the contact forces acting on the beams surface. One can observe that, due to the bending of the indenters as well as the aforementioned deformation of the solid cross-section, the contact zones do not span over the full width of the specimen, but only form towards the edge of the specimen.

7.2.3. Dynamic simulation of a tennis shot

In this last and probably most demanding numerical example, the dynamic impact of a tennis ball on a tennis racket is simulated. The geometry and material parameters of this example are inspired by [5–7] to closely resemble the real life application. The main geometric dimensions of the racket are visualized in Figure 7.9(a). It consists of an elliptic frame with elliptic cross-section. The frame is connected to the handle via two connectors which also have the same elliptic cross-section. The whole racket frame is modeled using a Saint-Venant–Kirchhoff material model (Young's modulus $E_R^S = 5 \cdot 10^{10}$ N/m², Poisson's ratio $\nu_R^S = 0.3$). The density $\rho_R^S = 553.1$ kg/m³ is chosen such that $m_R^S = 0.3$ kg, where m_R^S is the mass of the racket. The string bed of the racket consists of 17 horizontal and 16 vertical strings (Young's modulus $E^B = 2 \cdot 10^{10}$ N/m², density $\rho^B = 1100$ kg/m³). Each string has a circular cross-section with radius $R = 6.5 \cdot 10^{-4}$ m. The strings are strung in a way that the top and bottom strings switch between two adjacent intersections, cf. Figure 7.9(b). Finally, the tennis ball itself is modeled as a hollow sphere with an outer radius $r_a = 0.03333$ m and thickness $t_B = 0.003663$ m, and is described by a Neo-Hookean material law (Young's modulus $E_B^S = 5 \cdot 10^7$ N/m², Poisson's ratio $\nu_B^S = 0.3$,

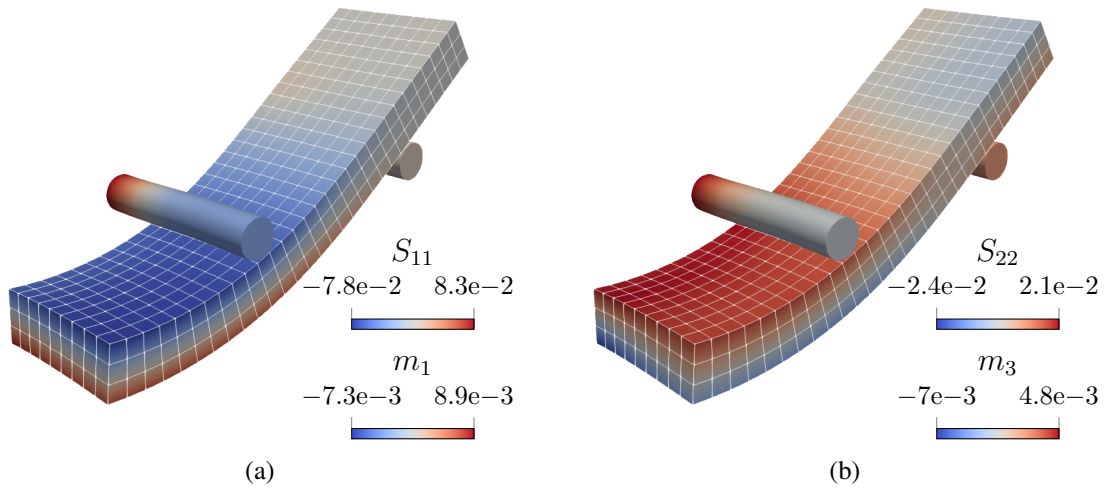


Figure 7.7.: Four-point bending test – quarter view of the deformed configuration. The contour plots once visualize the second Piola-Kirchhoff stress S_{11} in the solid and the beam bending moment m_1 in the beam (a) and once the second Piola-Kirchhoff stress S_{22} in the solid and the beam bending moment m_3 in the beam (b).

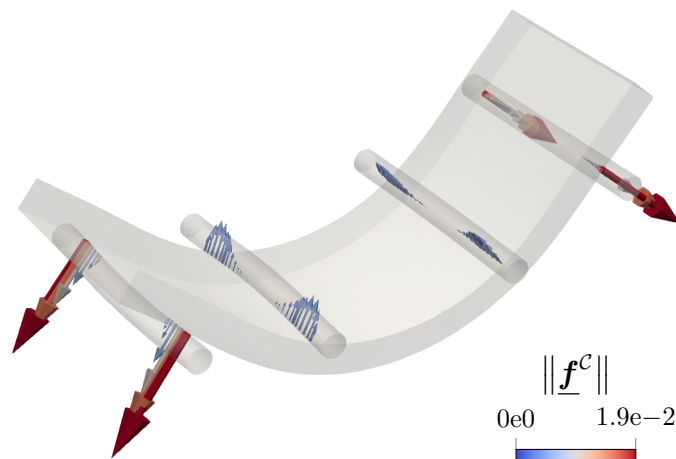


Figure 7.8.: Four-point bending test – deformed configuration with the contact forces \underline{f}^c acting on the beams. The contact forces are visualized for each Gauss point along the beam centerlines.

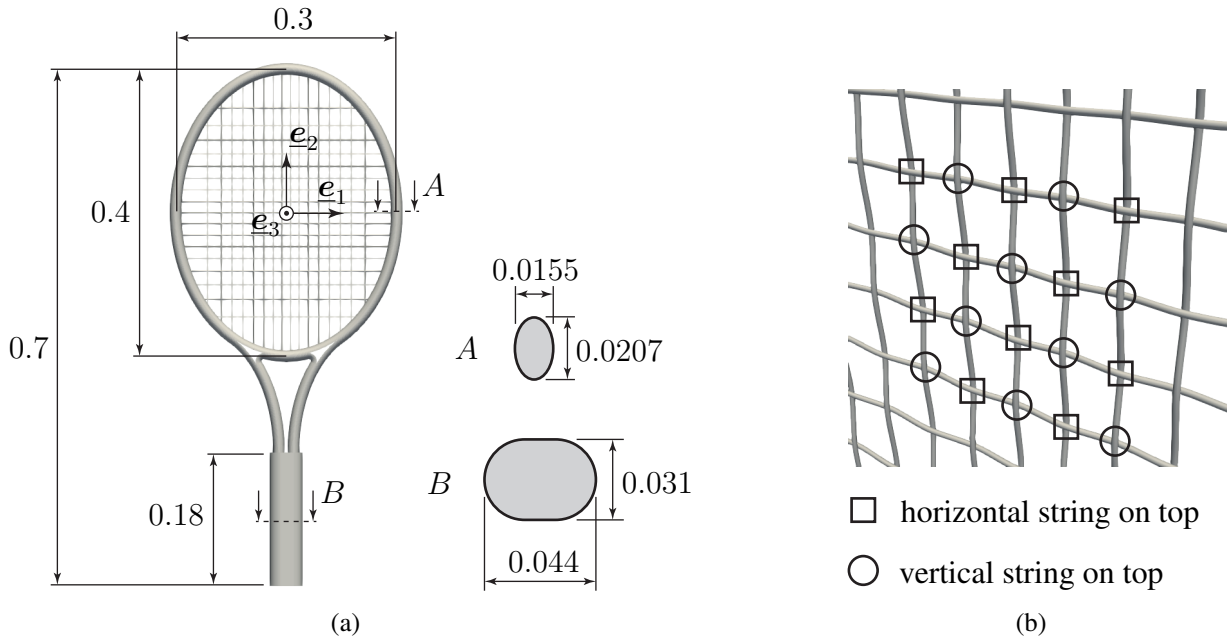


Figure 7.9.: Dynamic simulation of a tennis shot – problem setup. Geometric relations of the racket (a) and detailed illustration of the string webbing (b). All given dimensions are in m.

density $\rho_B^S = 882 \text{ kg/m}^3$). The density of the ball is chosen such that $m_B^S = 0.04 \text{ kg}$. The center of the ball is initially located at the spatial position $\underline{\mathbf{p}} = 0.03655 \text{ m } \mathbf{e}_3$.

Each string is discretized using 40 torsion-free beam finite elements, which are straight in the undeformed configuration. The racket is discretized using 20,738 eight-noded hexahedral (*hex8*) solid finite elements and the ball is modeled with 2,198 eight-noded solid-shell elements [20, 147, 148]. All in all, the total number of degrees of freedom for the system is 98,538. A number of different beam-to-(\cdot) interactions occur during the simulation. The interaction between the strings themselves is modeled with the all-angle beam contact (ABC) beam-to-beam (BTB) contact scheme, cf. [95, 100]. In the present example, only point-to-point beam-to-beam contact interactions occur. A quadratically regularized penalty law, similar to the one presented in Section 7.1.3, with $\epsilon_{\text{BTB}} = 7.2 \cdot 10^5 \text{ N/m}$ and $g_{0,\text{BTB}} = 5 \cdot 10^{-5} \text{ m}$ is employed. The connection of the strings with the racket frame is modeled with positional beam-to-solid volume (BTSV-POS) coupling and a linear interpolation of Lagrange multipliers, $\epsilon^V = 10^{10} \text{ N/m}^2$. Furthermore, the interaction of the strings with the ball is modeled with the penalty-based BTSSC scheme (quadratically regularized penalty law, $\epsilon^C = 2 \cdot 10^8 \text{ N/m}^2$, $g_0 = 5 \cdot 10^{-5} \text{ m}$, $n_{\text{GP}} = 6$).

Over the course of the whole simulation, the bottom face of the racket handle is clamped in all directions. The initial configuration of the racket is pre-stressed, as the strings have to be under tension and interwoven with each other to produce a stiff string bed. This pre-stressed configuration is achieved in three separate stages:

1. In this first stage, the axial tension of the strings is applied via non-zero Dirichlet conditions. The undeformed straight strings are pre-stressed with an axial force of 400 N and 250 N for the horizontal and vertical strings, respectively. This is realized by applying a prescribed

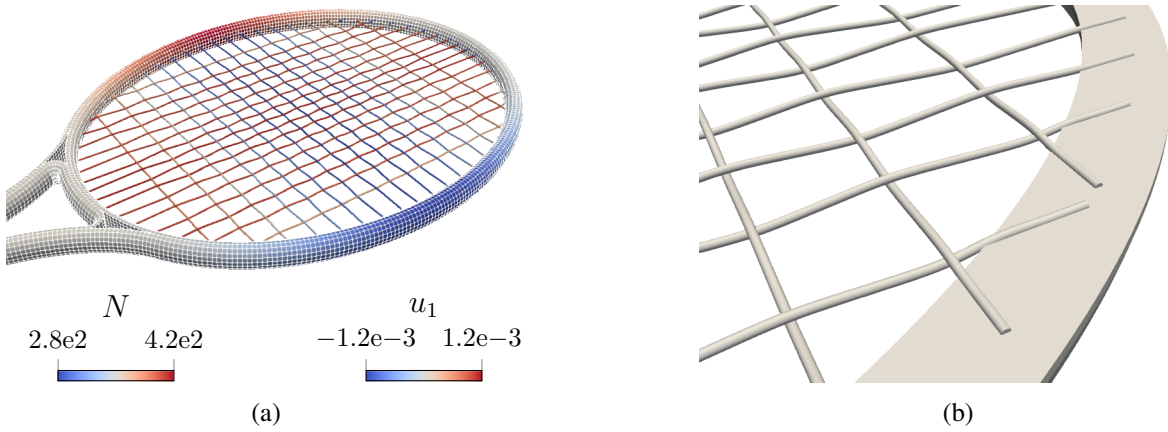


Figure 7.10.: Dynamic simulation of a tennis shot – pre-stressed initial configuration of the racket. Subfigure (a) shows the complete string bed, where the contour plot shows the normal force N in the strings and the \underline{e}_1 component of the displacement u_1 in the racket. Subfigure (b) shows a close up of the BTSV-POS coupling between the strings and the racket frame

Dirichlet displacement, in axial direction, at both ends of each string. Neither beam-to-beam contact or BTSV-POS coupling is activated during this stage. One quasi-static load step is preformed in this stage.

2. In the second stage, BTSV-POS coupling is activated between the strings and the racket frame, while the Dirichlet conditions from stage 1 on the strings are still active. Furthermore, the topology of the string bed depicted in Figure 7.9(b) is achieved by applying Dirichlet conditions to the beam nodes closest to each intersection point between the strings. The magnitude of this Dirichlet condition is chosen such that no two beams penetrate each other. Again, one quasi-static load step is preformed in this stage.
3. In the final pre-stressing stage, beam-to-beam contact is activated and the Dirichlet conditions from stages 1 and 2 are removed, thus resulting in the final pre-stressed racket frame. To achieve a converging Newton–Raphson iteration, the Dirichlet conditions are replaced by Neumann boundary conditions with matching nodal forces. These Neumann loads are linearly reduced to zero within 20 quasi-static load steps.

The resulting pre-stressed initial configuration of the racket is shown in Figure 7.10. Even though the prescribed tension in the horizontal strings is larger than in the vertical ones, in the pre-stressed state it can be observed that the vertical strings are under higher tension. This is due to the deformation of the frame itself, which reduces the tension in the horizontal strings and increases the tension in the vertical strings, cf. Figure 7.10(a). A close up of the BTSV-POS coupling between the strings and the racket frame is illustrated in Figure 7.10(b).

The previously described pre-stressed initial configuration serves as the initial configuration for the dynamic simulation of the racket. The racket is at rest, i.e., zero initial velocity, while the ball has a uniform initial velocity $\dot{\underline{u}}_0 = -30 \text{ m/s } \underline{e}_3$. A dynamic simulation of the transient system evolution along a total simulation time of $t \in [0 \text{ ms}, 5 \text{ ms}]$ is performed. Time discretization

is based on the standard generalized- α scheme with a time step $\Delta t = 0.005$ ms and a spectral radius $\rho_\infty = 1$. The standard generalized- α scheme for vector spaces, cf. [35], can be employed since the torsion-free beam elements do not carry any rotational degrees of freedom. Time deformed configurations at various simulation times are illustrated in Figure 7.11. The impact of the ball on the string bed leads to a large compression of the ball. At around $t = 1.5$ ms the velocity in \underline{e}_3 -direction of the ball is roughly zero, i.e., the movement in direction of the racket is stopped and the ball will be reflected from this point on. This is also the time, where the string bed exhibits the largest local deformations. Large parts of the balls kinetic energy are converted into elastic deformations of the ball and the string bed. Until around $t = 3$ ms, the elastic deformations are again converted into kinetic energy of the ball. The time evolution of the averaged ball velocity in \underline{e}_3 -direction $\bar{u}_3 = \int_{\Omega_B} \dot{u}_3 dV_0/V_0$, is plotted in Figure 7.12. It can be seen that the return velocity is more or less constant from around $t = 3$ ms on, which coincides with the time, where the ball and the string bed are not in contact any more. The ratio of impact to return velocity is roughly $3/2$, the "lost" kinetic energy is converted into kinetic and elastic energy of the racket frame and string bed. For illustrative purposes, Figure 7.13 visualizes a photo-realistic rendering of the present example at $t = 1.5$ ms, generated with the open source visualization software Blender [22].

Obviously, this problem does not include some important effects of the real physical problem, such as the nonlinear behavior of the ball due to compression of the enclosed gas, cf. [51], or the friction between several strings as well as strings and the ball. Nevertheless, the results demonstrate the robustness of the BTSSC method and also showcase the immense potential of employing and combining beam-to-(\cdot) interactions for real life applications.

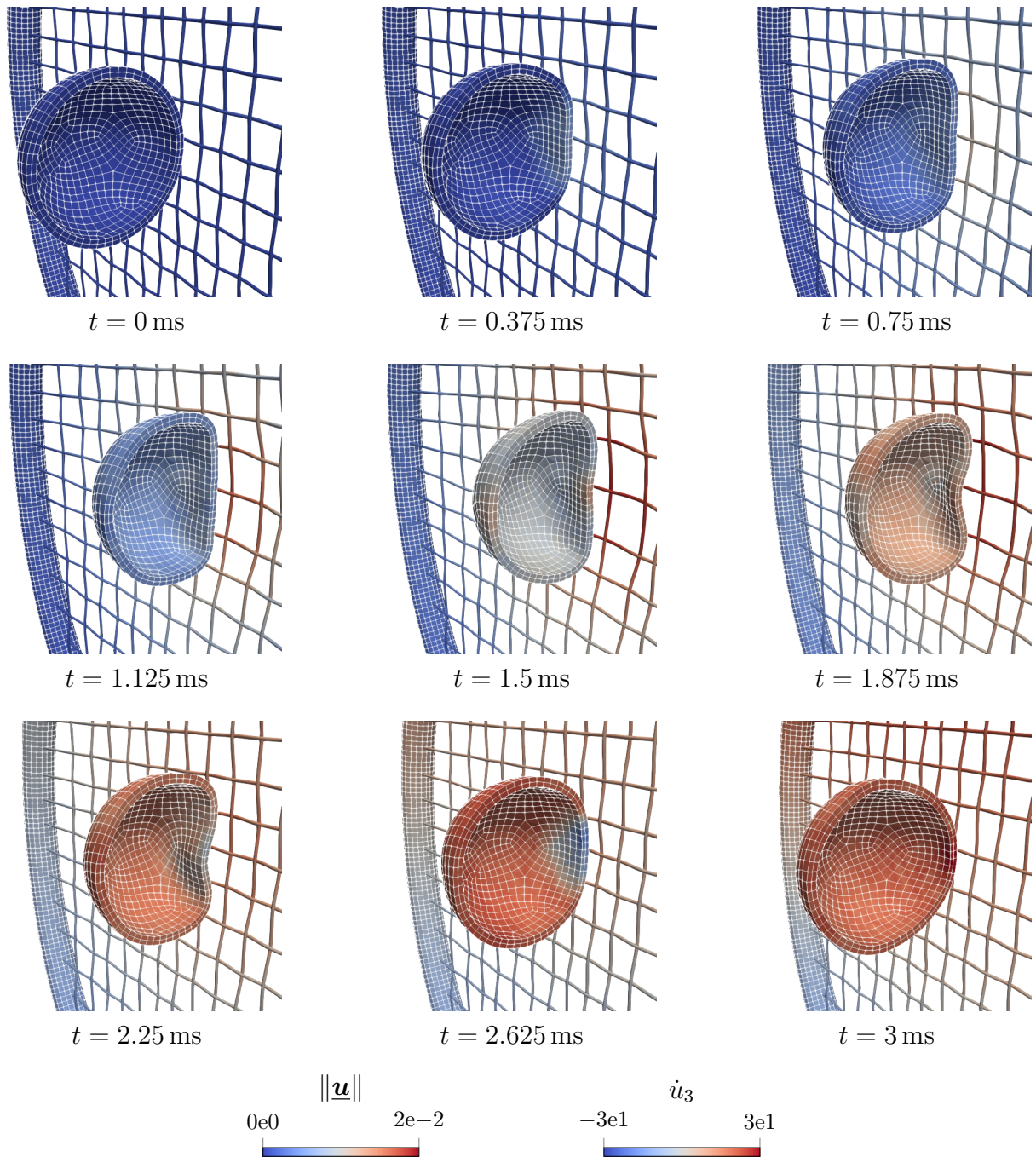


Figure 7.11.: Dynamic simulation of a tennis shot – deformed configurations of tennis ball and racket at various time steps. For visualization purposes only half of the ball is shown. The contour plots visualize the displacement magnitude in the racket and the strings, and the \underline{e}_3 -component of the velocity in the ball.

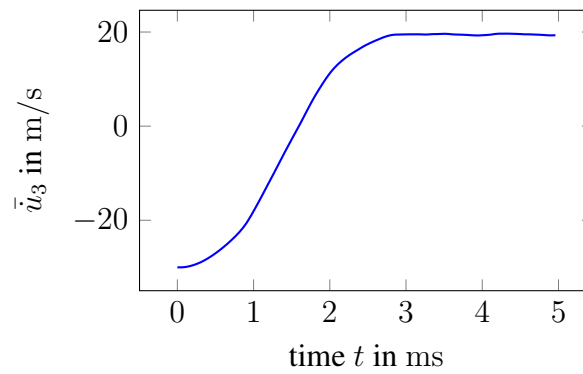


Figure 7.12.: Dynamic simulation of a tennis shot – average velocity of the tennis ball in \underline{e}_3 -direction over the course of the simulation.



Figure 7.13.: Dynamic simulation of a tennis shot – photo-realistic rendering of the tennis ball and racket at $t = 1.5$ ms.

8. Summary and outlook

8.1. Summary of achievements

In this thesis, numerical solution methods for beam-to-solid (BTS) problems were investigated. Within the developed BTS interaction framework, the beams were exclusively modeled as 1D Cosserat continua based on the geometrically exact beam theory, thus resulting in a mixed-dimensional interaction problem between the 1D beams and the 3D solids.

Firstly, new modeling techniques for the coupling of 1D Cosserat continua embedded in 3D Boltzmann continua have been proposed (BTSV-POS). The position of the beam centerline was coupled to the underlying solid matrix. Two different finite element-based coupling schemes have been introduced: a Gauss point-to-segment (GPTS) and an embedded mortar-type approach. The resulting constraint equations of both schemes are enforced via a penalty approach, and in the case of the mortar-type approach, the penalty regularization was performed in a weighted node-wise manner. For the mortar-type method, various discrete Lagrange multiplier bases were investigated. Moreover, various numerical integration methods of the coupling terms were compared. Several numerical experiments were conducted to assess the behavior of the various schemes regarding the choice of the penalty parameter and the numerical integration of the coupling terms. For relevant physical application scenarios of the BTSV-POS method, i.e., relatively slender and stiff fibers compared to the surrounding matrix material, the validity of the fundamental modeling assumption of 1D-3D coupling was confirmed, and its optimal spatial convergence behavior was shown numerically. Overall, the embedded mortar-type discretization with linear interpolation of the discrete Lagrange multiplier basis proves to be the better modeling choice due to its superior robustness regarding the choice of the penalty parameter, the beam element to solid element length ratio, and its optimal spatial convergence properties. Furthermore, the results underline the importance of an accurate numerical integration of the coupling terms as provided only by carefully chosen segmentation schemes. The subsequently developed coupling schemes are largely based on these fundamental findings.

Secondly, a 1D-3D coupling scheme has been proposed to fully embed 1D Cosserat beams into 3D Boltzmann continua. Full embedding of fibers inside volumes is characterized by six constraint equations at each point along the fiber centerline, namely three positional constraints and three rotational constraints, thus resulting in a full, mechanically consistent coupling between the 1D beams and the 3D continuum (BTSV-FULL). Deriving the full 1D-3D coupling on the beam centerline from a 2D-3D coupling on the beam surface via a Taylor series expansion of the solid displacement field would require to fully couple the deformed solid directors with the undeformable beam cross-section triad. It is demonstrated that such an approach, which suppresses all in-plane deformation modes of the solid at the coupling point, might result in severe locking effects in the practically relevant regime of relatively coarse solid mesh sizes. Therefore, a suitable triad field must be defined in the 3D Boltzmann continuum that only represents solid

material directions in an average sense without constraining them. It has been shown that the rotational part of the polar decomposition of the (in-plane projection of the) solid deformation gradient is a natural choice, since it represents the average orientation of material directions of the 3D continuum in a L_2 -optimal manner. Additionally, several other solid triad definitions have been presented, which allow for a more efficient numerical evaluation. The existing BTSV-POS coupling methods for the positional degrees of freedom have been extended for the coupling of rotational degrees of freedom, all within the theory of large rotations. The coupling equations were again discretized using a mortar-type approach and enforced using a weighted penalty regularization. Based on elementary numerical test cases, it was demonstrated that a consistent spatial convergence behavior can be achieved and potential locking effects can be avoided, if the proposed BTSV-FULL scheme is combined with a suitable solid triad definition. Furthermore, numerical experiments were conducted to show the applicability of the proposed method to real-life engineering applications.

Thirdly, a 1D-2D mixed-dimensional coupling method to consistently couple 1D Cosserat beams to 2D surfaces of 3D Boltzmann continua has been presented (BTSS-FULL). Therein, similar to the BTSV-FULL scheme, all local degrees of freedom along the beam centerline are coupled to the solid surface. Three different variants of the positional coupling constraints were investigated. One of them, the *consistent* variant requires the expensive evaluation of the current surface normal field. The other two variants are commonly used in surface-to-surface mesh tying problems. Numerical examples have shown that only the consistent positional coupling constraints, i.e., with inclusion of the surface normal vector, lead to physically correct results and fulfill basic mechanical consistency properties, such as conservation of angular momentum. The existing coupling methods for the rotational degrees of freedom in the BTSV-FULL scheme were used in the BTSS-FULL scheme. This required the construction of a suitable surface triad field on the 2D surface of the 3D Boltzmann continuum. The Lagrange multiplier method was again used to enforce the positional and rotational coupling constraints, which were discretized with a mortar-type approach. Numerical examples illustrate the importance of positional *and* rotational coupling via a practically motivated example. A multi-physics simulation, inspired by models of stented arteries, has demonstrated the BTSS-FULL scheme's suitability for complex beam geometries.

Finally, a 1D-2D mixed-dimensional frictionless contact method between 1D Cosserat beams to 2D surfaces of 3D Boltzmann continua has been presented (BTSSC). In contrast to the previously described mortar-type coupling schemes, that have been developed within this thesis, the presented BTSSC scheme is based on a GPTS approach. Although future research on BTSSC is required, numerical experiments have been presented to demonstrate the applicability of the proposed method to real-life engineering applications.

In summary, it can be stated that a mixed-dimensional interaction framework between 1D Cosserat beams and 3D Boltzmann continua has been developed and successfully applied to multiple examples relevant for real-life applications.

8.2. Outlook and future work

Although substantial progress towards a truly general purpose mixed-dimensional simulation framework for BTS interaction problems has been made, there is still room for improvements.

Future work on the presented BTS interaction framework can be split up into four main categories:

Applications Throughout this thesis, the presented numerical examples illustrate possible application scenarios for the presented BTS interaction methods, as well as the maturity of the developed code framework to deal with complex problems. The obvious next step is to apply the developed algorithms to actual real life engineering and biomedical problems. For example, ongoing work focuses on the modeling of fiber-reinforced concrete, based on actual computed tomography (CT) scans of existing specimens. Furthermore, patient specific simulations and optimizations for abdominal aortic aneurysm repair are also part of ongoing research. Future work will also focus on applying the developed BTSV coupling schemes to optimize the placement of steel reinforcement in concrete beams.

Interaction physics The primary focus of this thesis is the development and analysis of coupling (mesh tying) algorithms for BTS problems. The previous chapter gave a short outlook on frictionless unilateral BTSSC. Although the presented approach already shows a remarkable maturity, further investigations into the contact constraint discretization techniques are required. Moreover, the extension to frictional BTSSC is an important aspect of future research to enable the capture of complex real life interface effects in BTSSC problems. Another topic of interest is the use of the developed BTSV coupling schemes for the analysis of progressive damage and failure phenomena in fiber-reinforced materials, such as fiber pull-out.

Model assumptions The presented BTSV coupling schemes are based on true 1D-3D mixed-dimensional interactions, i.e., the interaction terms are evaluated exclusively along the 1D beam centerline. As discussed in detail, this allows for accurate results of the overall system response. Instead of evaluating the coupling along the 1D beam centerline, the coupling can also be evaluated on the surface of the embedded beam, i.e., a 2D-3D coupling approach. The beam is still modeled as a 1D Cosserat continuum. This thesis outlines two approaches (penalty and Lagrange multiplier) for 2D-3D beam-to-volume coupling problems. The penalty based 2D-3D coupling scheme is employed to obtain reference solutions for the spatial convergence examples. A topic of interest for future research is the combination of such true 1D-3D and 2D-3D coupling within a unified BTS coupling approach. This would allow the use of 2D-3D coupling along with a refined solid mesh only in domains where high resolution of solid stress fields is of interest, and using the proposed, highly efficient 1D-3D coupling approach in the remaining problem domain. Moreover, a combination of the developed schemes with concepts allowing for a consistent coupling of the beam ends with the solid domain are also considered as a promising future research direction.

Algorithmic and numerical properties Based on the work presented in this thesis, further extensions of the interaction discretization should be considered. This includes direct solution of the mixed-formulation problem, i.e., abolishing the penalty regularization and directly solving the coupled BTS problem including Lagrange multipliers. This will also very likely require the construction of an inf-sup stable Lagrange multiplier interpolation, similar to 3D-3D embedded mesh methods. Another important aspect that was beyond the scope of the present thesis is the development of iterative linear solvers and preconditioning schemes for BTS interaction problems. This includes the penalty regularized system

considered in this thesis, as well as the system with saddle point structure directly arising from discretizing the variational mixed-formulation.

The listed aspects above should not be viewed as shortcomings of the presented BTS interaction schemes, but rather as promising extensions of the application range, or improvements of numerical properties and computational performance. To recapitulate, this thesis presents a BTS interaction framework combining the long history of beam theory with classical 3D continuum mechanics. The presented theoretical considerations and numerical examples throughout this thesis lead to the conclusion that this framework can become an important tool in various fields of science, engineering and biomechanics.

A. Full 2D-3D coupling for beam-to-volume coupling problems

In the example sections for BTSV-POS and BTSV-FULL the truly 1D-3D coupling methods are compared to reference solutions obtained with a 2D-3D coupling approach. For the sake of completeness, the kinematic coupling constraints for the employed 2D-3D coupling approach are stated in this appendix. The 2D-3D coupling constraints read

$$\underline{r} + \underline{r}_{\text{CS}} - \underline{x}^S = \underline{0} \quad \text{on} \quad \Gamma_{c,2\text{D-3D}}. \quad (\text{A.1})$$

Therein, $\Gamma_{c,2\text{D-3D}}$ is the 2D-3D coupling surface, i.e., the part of the beam surface that lies within the solid volume. Furthermore, $\underline{r}_{\text{CS}} \in \mathbb{R}^3$ is the cross-section position vector, i.e., the vector that points from the cross-section centroid to the cross-section perimeter. The cross-section position vector can be expressed by the current beam triad basis vectors \underline{g}_2^B and \underline{g}_3^B , or via the cross-section rotation tensor $\underline{\Lambda}^B$ and the Cartesian basis vectors \underline{e}_2 and \underline{e}_3 , i.e.,

$$\underline{r}_{\text{CS}} = \alpha \underline{g}_2^B + \beta \underline{g}_3^B = \underline{\Lambda}^B (\alpha \underline{e}_2 + \beta \underline{e}_3). \quad (\text{A.2})$$

Therein, $\alpha \in \mathbb{R}$ and $\beta \in \mathbb{R}$ are the beam cross-section coordinates, i.e., they parametrize the beam cross-section.

A.1. Constraint enforcement strategies

In the following, two methods to enforce the 2D-3D coupling conditions (A.1) are presented, once with a Lagrange multiplier method and once with a quadratic penalty potential.

A.1.1. Penalty potential

The quadratic penalty potential reads

$$\Pi_{\epsilon,2\text{D-3D}} = \frac{\epsilon_{2\text{D-3D}}}{2} \int_{\Gamma_{c,2\text{D-3D}}} \left(\underline{r} + \underline{r}_{\text{CS}} - \underline{x}^S \right)^T \left(\underline{r} + \underline{r}_{\text{CS}} - \underline{x}^S \right) dA_0. \quad (\text{A.3})$$

Here, $\epsilon_{2\text{D-3D}} \in \mathbb{R}$ is a scalar penalty parameter. Variation of the penalty potential gives the following contributions to the weak form:

$$\begin{aligned} \delta \Pi_{\epsilon,2\text{D-3D}} = \int_{\Gamma_{c,2\text{D-3D}}} & \underbrace{\delta \underline{r}^T \epsilon_{2\text{D-3D}} \left(\underline{r} + \underline{r}_{\text{CS}} - \underline{x}^S \right)}_{\underline{f}_{2\text{D-3D}}} + \underbrace{\delta \underline{\theta}^{B^T} \epsilon_{2\text{D-3D}} \left(\underline{S}(\underline{r}_{\text{CS}}) \left(\underline{r} - \underline{x}^S \right) \right)}_{\underline{m}_{2\text{D-3D}}} \\ & + \underbrace{\delta \underline{x}^{S^T} \epsilon_{2\text{D-3D}} \left(-\underline{r} - \underline{r}_{\text{CS}} + \underline{x}^S \right)}_{-\underline{f}_{2\text{D-3D}}} dA_0. \end{aligned} \quad (\text{A.4})$$

Therein, the coupling force \underline{f}_{2D-3D} , acting on the beam centerline and solid, can be identified. Furthermore, \underline{m}_{2D-3D} is the coupling moment acting on the beam cross-section. This demonstrates the projection of purely positional coupling constraints (on the surface of the beam) onto the beam centerline, and illustrates the arising rotational coupling terms in a 2D-3D coupling approach.

A.1.2. Lagrange multiplier potential

The 2D-3D coupling conditions (A.1) can also be enforced with a Lagrange multiplier method. A Lagrange multiplier vector field $\underline{\lambda}_{2D-3D} \in \mathbb{R}^3$ is therefore defined on the coupling surface $\Gamma_{c,2D-3D}$. The total Lagrange multiplier potential for the 2D-3D coupling reads

$$\Pi_{\lambda,2D-3D} = \int_{\Gamma_{c,2D-3D}} \underline{\lambda}_{2D-3D}^T (\underline{r} + \underline{r}_{CS} - \underline{x}^S) dA_0. \quad (A.5)$$

The variation of the total Lagrange multiplier potential gives the following contributions to the weak form:

$$\begin{aligned} \delta \Pi_{\lambda,2D-3D} = \int_{\Gamma_{c,2D-3D}} & \left(\delta \underline{\lambda}_{2D-3D}^T (\underline{r} + \underline{r}_{CS} - \underline{x}^S) + \delta \underline{r}^T \underline{\lambda}_{2D-3D} \right. \\ & \left. + \delta \underline{\theta}^B \underline{S}(\underline{r}_{CS}) \underline{\lambda}_{2D-3D} - \delta \underline{x}^S \underline{\lambda}_{2D-3D} \right) dA_0. \end{aligned} \quad (A.6)$$

Again, this showcases the projection onto the beam centerline, in this case of the Lagrange multiplier field $\underline{\lambda}_{2D-3D}$, i.e., the coupling surface tractions on the beam surface.

A.2. Constraint discretization strategy for full 2D-3D coupling

In this section the discretization of the full 2D-3D coupling constraints is presented. Only the version based on the variation of the penalty potential (A.4) is presented, as this was the actual method used to obtain the reference results.

A.2.1. Gauss point-to-segment approach for full 2D-3D coupling

Evaluating the variation of the total coupling potential (A.4) on the basis of the discretized solid position field and beam cross-section rotation field yields the discrete variation of the 2D-3D coupling potential:

$$\begin{aligned} \delta \Pi_{\epsilon,2D-3D,h} = \epsilon_{2D-3D} \int_{\Gamma_{2D-3D,h}} & \left(\underline{H} \delta \underline{d}^B + \underline{S}(\underline{L} \delta \underline{\theta}^B) \underline{\Lambda}_h^B (\alpha \underline{e}_2 + \beta \underline{e}_3) - \underline{N} \delta \underline{d}^S \right)^T \\ & \left(\underline{H} \underline{d}^B + \underline{\Lambda}_h^B (\alpha \underline{e}_2 + \beta \underline{e}_3) - \underline{N} \underline{d}^S \right) dA_0. \end{aligned} \quad (A.7)$$

Therein, $\Gamma_{2D-3D,h}$ is the discrete beam surface. It is important to point out that the beam surface is not directly discretized. It is an analytical surface defined by the discretized beam centerline,

the beam cross-section orientations and the beam cross-section geometry. Equation (A.7) can be stated in matrix form as

$$\begin{aligned} \delta \Pi_{\epsilon, 2D-3D, h} &= \begin{bmatrix} \delta \mathbf{d}^S & \delta \mathbf{d}^B & \delta \boldsymbol{\theta}^B \end{bmatrix} \begin{bmatrix} \int_{\Gamma_{2D-3D, h}} \mathbf{f}_{c, 2D-3D}^S dA_0 \\ \int_{\Gamma_{2D-3D, h}} \mathbf{f}_{c, r, 2D-3D}^B dA_0 \\ \int_{\Gamma_{2D-3D, h}} \mathbf{f}_{c, \theta, 2D-3D}^B dA_0 \end{bmatrix} \\ &= \begin{bmatrix} \delta \mathbf{d}^S & \delta \mathbf{d}^B & \delta \boldsymbol{\theta}^B \end{bmatrix} \begin{bmatrix} \mathbf{r}_{c, 2D-3D}^S \\ \mathbf{r}_{c, r, 2D-3D}^B \\ \mathbf{r}_{c, \theta, 2D-3D}^B \end{bmatrix}, \end{aligned} \quad (\text{A.8})$$

with the generalized point-wise 2D-3D coupling forces

$$\begin{aligned} \mathbf{f}_{c, 2D-3D}^S &= \epsilon_{2D-3D} \left(\mathbf{N}^T \mathbf{N} \mathbf{d}^S - \mathbf{N}^T \mathbf{H} \mathbf{d}^B - \mathbf{N}^T \underline{\Lambda}_h^B (\alpha \mathbf{e}_2 + \beta \mathbf{e}_3) \right), \\ \mathbf{f}_{c, r, 2D-3D}^B &= \epsilon_{2D-3D} \left(-\mathbf{H}^T \mathbf{N} \mathbf{d}^S + \mathbf{H}^T \mathbf{H} \mathbf{d}^B + \mathbf{H}^T \underline{\Lambda}_h^B (\alpha \mathbf{e}_2 + \beta \mathbf{e}_3) \right), \\ \mathbf{f}_{c, \theta, 2D-3D}^B &= \epsilon_{2D-3D} \left(-\mathbf{L}^T \underline{\mathbf{S}} (\underline{\Lambda}_h^B (\alpha \mathbf{e}_2 + \beta \mathbf{e}_3)) \mathbf{N} \mathbf{d}^S + \mathbf{L}^T \underline{\mathbf{S}} (\underline{\Lambda}_h^B (\alpha \mathbf{e}_2 + \beta \mathbf{e}_3)) \mathbf{H} \mathbf{d}^B \right). \end{aligned} \quad (\text{A.9})$$

Furthermore, $\mathbf{r}_{c, 2D-3D}^S$, $\mathbf{r}_{c, r, 2D-3D}^B$ and $\mathbf{r}_{c, \theta, 2D-3D}^B$ are the local residual vectors. Again, a linearization of the residual contributions with respect to the discrete beam-to-solid pair degrees of freedom is required for the Newton–Raphson algorithm. The linearization reads¹:

$$\begin{aligned} \text{Lin} \left(\begin{bmatrix} \mathbf{r}_{c, 2D-3D}^S \\ \mathbf{r}_{c, r, 2D-3D}^B \\ \mathbf{r}_{c, \theta, 2D-3D}^B \end{bmatrix} \right) &= \begin{bmatrix} \mathbf{r}_{c, 2D-3D}^S \\ \mathbf{r}_{c, r, 2D-3D}^B \\ \mathbf{r}_{c, \theta, 2D-3D}^B \end{bmatrix} \\ &+ \int_{\Gamma_{2D-3D, h}} \begin{bmatrix} \frac{\partial \mathbf{f}_{c, 2D-3D}^S}{\partial \mathbf{d}^S} & \frac{\partial \mathbf{f}_{c, 2D-3D}^S}{\partial \mathbf{d}^B} & \frac{\partial \mathbf{f}_{c, 2D-3D}^S}{\partial \psi_h^B} \underline{\mathbf{T}}(\psi_h^B) \tilde{\mathbf{I}} \\ \frac{\partial \mathbf{f}_{c, r, 2D-3D}^B}{\partial \mathbf{d}^S} & \frac{\partial \mathbf{f}_{c, r, 2D-3D}^B}{\partial \mathbf{d}^B} & \frac{\partial \mathbf{f}_{c, r, 2D-3D}^B}{\partial \psi_h^B} \underline{\mathbf{T}}(\psi_h^B) \tilde{\mathbf{I}} \\ \frac{\partial \mathbf{f}_{c, \theta, 2D-3D}^B}{\partial \mathbf{d}^S} & \frac{\partial \mathbf{f}_{c, \theta, 2D-3D}^B}{\partial \mathbf{d}^B} & \frac{\partial \mathbf{f}_{c, \theta, 2D-3D}^B}{\partial \psi_h^B} \underline{\mathbf{T}}(\psi_h^B) \tilde{\mathbf{I}} \end{bmatrix} dA_0 \begin{bmatrix} \Delta \mathbf{d}^S \\ \Delta \mathbf{d}^B \\ \Delta \boldsymbol{\theta}^B \end{bmatrix}. \end{aligned} \quad (\text{A.10})$$

The local contributions (A.8) and (A.10) to the global residual and the stiffness matrix, respectively, can be assembled in a straightforward manner and will not be stated here for the sake of brevity. As in the BTSV-FULL mortar-type coupling, all derivatives explicitly stated in (A.10) are evaluated using forward automatic differentiation (FAD).

In practice, all integrals presented in this section are evaluated using a Gauss-point-to-segment (GPTS) approach as illustrated in Figure A.1. At each Gauss–Legendre point $\tilde{\xi}_i^B$ along the beam centerline, multiple equally spaced coupling points (illustrated with the symbol ‘ \times ’ in Figure A.1) are defined along the circumference of the corresponding cross-section. Mechanically speaking, each coupling point is tied to the underlying solid via a linear penalty constraint.

¹In the author’s article [138] there is a typo in this formulae. The version stated here is correct.

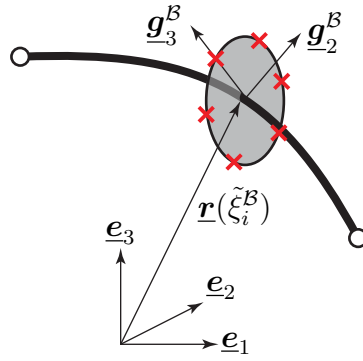


Figure A.1.: Illustration of the discrete coupling points for 2D-3D coupling along a single cross-section. Figure is taken from the author's article [138], permissions granted under the Creative Commons (CC BY) license.

B. L2-optimality for the polar decomposition of the deformation gradient

In the following, a proof shall be given for (5.29). First, an angle $\theta_0 \in [-\pi, \pi]$ is defined that represents the orientation of arbitrary in-plane directors in the reference configuration defined to coincide for solid and beam according to $\underline{g}_0^S(\theta_0) = \underline{g}_0^B(\theta_0) = \cos(\theta_0)\underline{g}_{2,0}^B + \sin(\theta_0)\underline{g}_{3,0}^B$. The push-forward to the spatial configuration is given by $\underline{g}_S = \underline{F}_n \underline{g}_0^S(\theta_0)$ for the solid and $\underline{g}^B = \underline{R}^B \underline{g}_0^B(\theta_0)$ for the beam. As stated in Section 5.2.1, it is a desirable property of the (to be defined) solid triad and therefore also of the beam triad that the base vectors \underline{g}_2^B and \underline{g}_3^B lie in the \underline{n} -plane, i.e., the plane spanned by the solid base vectors \underline{g}_2^S and \underline{g}_3^S . Thus, in analogy to (5.26) as stated for the solid, it is assumed that the total rotation of the beam cross-section \underline{R}^B is split in a multiplicative manner into two successive rotations

$$\underline{R}^B = \underline{R}_{2D}^B \underline{R}_n \quad (\text{B.1})$$

where \underline{R}_n describes the 3D rotation from $\underline{\Lambda}_0^B$ to $\underline{\Lambda}$, and \underline{R}_{2D}^B the quasi-2D rotation from $\underline{\Lambda}$ to $\underline{\Lambda}^B$. Thus, after push-forward to the intermediate configuration defined by \underline{R}_n the corresponding directors of solid and beam still coincide:

$$\bar{\underline{g}}^S(\theta_0) = \bar{\underline{g}}^B(\theta_0) = \underline{R}_n \underline{g}_{B,0}(\theta_0) = \cos(\theta_0) \bar{\underline{g}}_2 + \sin(\theta_0) \bar{\underline{g}}_3. \quad (\text{B.2})$$

In the following, the material and spatial principle axes associated with the polar decomposition (5.27) of the in-plane deformation gradient \underline{F}_{2D} are denoted as \underline{G}_{P2} and \underline{G}_{P3} as well as $\underline{g}_{P2} = \underline{R}_{2D}^S \underline{G}_{P2}$ and $\underline{g}_{P3} = \underline{R}_{2D}^S \underline{G}_{P3}$. Since the principle axes \underline{G}_{P_i} and the orthonormal base vectors $\bar{\underline{g}}_i$ are related by quasi-2D rotations with respect to the normal vector \underline{n} , the directors in (B.2) can alternatively be stated as

$$\bar{\underline{g}}^S(\theta_0) = \bar{\underline{g}}^B(\theta_0) = \cos(\tilde{\theta}_0) \underline{G}_{P2} + \sin(\tilde{\theta}_0) \underline{G}_{P3}, \quad (\text{B.3})$$

where $\tilde{\theta}_0 = \theta_0 - \theta_{\text{diff}}$ is defined via the constant offset value θ_{diff} describing the rotation from $\bar{\underline{g}}_i$ to \underline{G}_{P_i} . The final beam cross-section triad follows from the second (quasi-2D) rotation $\underline{R}_{2D}^B = \underline{R}(\theta_{2D}^B \underline{n})$ from $\bar{\underline{g}}_i$ to \underline{g}_i^B described by the scalar rotation angle θ_{2D}^B . In a similar fashion the (quasi-2D) rotation $\underline{R}_{2D}^S = \underline{R}(\theta_{2D}^S \underline{n})$ from \underline{G}_{P_i} to \underline{g}_{P_i} is described by the scalar rotation angle θ_{2D}^S . Due to the 2D-nature of these rotations, the beam director \underline{g}^B in the spatial configuration can be derived from (B.3) according to:

$$\underline{g}^B(\theta_0) = \cos(\tilde{\theta}_0 + \theta_{2D}^B - \theta_{2D}^S) \underline{g}_{P2} + \sin(\tilde{\theta}_0 + \theta_{2D}^B - \theta_{2D}^S) \underline{g}_{P3}. \quad (\text{B.4})$$

Let the principle stretch ratios associated with the in-plane deformation gradient \underline{F}_{2D} be denoted as λ_2 and λ_3 . Then, the solid director $\underline{g}^S = \underline{F}_n \underline{g}_0^S(\theta_0)$ in the spatial configuration can be derived according to:

$$\underline{g}^S(\theta_0) = \underline{v}_{2D} \underline{R}_{2D}^S \left(\cos(\tilde{\theta}_0) \underline{G}_{P2} + \sin(\tilde{\theta}_0) \underline{G}_{P3} \right) = \lambda_2 \cos(\tilde{\theta}_0) \underline{g}_{P2} + \lambda_3 \sin(\tilde{\theta}_0) \underline{g}_{P3}. \quad (B.5)$$

Here, the relation $\underline{g}_{P_i} = \underline{R}_{2D}^S \underline{G}_{P_i}$ and the diagonal structure $\underline{v}_{2D} = \lambda_2 \underline{g}_{P2} \otimes \underline{g}_{P2} + \lambda_3 \underline{g}_{P3} \otimes \underline{g}_{P3}$ of the spatial stretch tensor has been exploited. From (B.4) and (B.5), the orientation angles of the spatial beam and solid directors $\underline{g}^B(\theta_0)$ and $\underline{g}^S(\theta_0)$ relative to the spatial principle axis \underline{g}_{P2} can be identified according to:

$$\theta^B(\theta_0) = \tilde{\theta}_0 + \theta_{2D}^B - \theta_{2D}^S, \quad (B.6)$$

$$\theta^S(\theta_0) = \arctan \left(\frac{\lambda_3 \sin(\tilde{\theta}_0)}{\lambda_2 \cos(\tilde{\theta}_0)} \right). \quad (B.7)$$

Now, the difference between the solid director orientations and the beam director orientations, measured in the L_2 -norm, shall be minimized, i.e.,

$$\int_{-\pi}^{\pi} (\theta^B(\theta_0) - \theta^S(\theta_0))^2 d\theta_0 \rightarrow \min. \quad (B.8)$$

As necessary condition, the first derivative of the integral with respect to θ_{2D}^B has to vanish, i.e.,

$$\int_{-\pi}^{\pi} (\theta^B(\theta_0) - \theta^S(\theta_0)) d\theta_0 \doteq 0. \quad (B.9)$$

By exploiting the property $\theta^S(-\theta_0) = -\theta^S(\theta_0)$ of (B.7), it can easily be shown that (B.9) results in the requirement:

$$\theta_{2D}^B = \theta_{2D}^S \quad \Leftrightarrow \quad \underline{R}_{2D}^B = \underline{R}_{2D}^S. \quad (B.10)$$

This means that the beam directors \underline{g}_i^B have to coincide with the principle axes \underline{g}_{P_i} and, thus, the total beam triad has to satisfy $\underline{\Lambda}^B = \underline{R}_{2D}^S \underline{R}_n \underline{\Lambda}_0^B$, which is identical to the solid triad definition STR-POL according to (5.28) with the initial condition $\underline{\Lambda}_0^B = \underline{\Lambda}_0^S$. By checking the second derivative, it can easily be confirmed that this solid triad choice indeed results in a minimum of the L_2 -norm in (B.8).

C. Variation of the gap function in beam-to-solid surface contact

In this appendix, the variation of the gap function (7.6) for BTSSC shall be presented. The full definition of the gap function reads

$$g(\xi^B) = \underline{\mathbf{n}}(\xi_c^S, \eta_c^S)^T (\underline{\mathbf{r}}(\xi^B) - \underline{\mathbf{x}}^S(\xi_c^S, \eta_c^S)) - R, \quad (\text{C.1})$$

with the variation

$$\delta g(\xi^B) = \delta \underline{\mathbf{n}}^T (\underline{\mathbf{r}}(\xi^B) - \underline{\mathbf{x}}^S(\xi^B)) + \underline{\mathbf{n}}^T \delta (\underline{\mathbf{r}}(\xi^B)) - \underline{\mathbf{n}}^T \delta (\underline{\mathbf{x}}^S(\xi_c^S, \eta_c^S)). \quad (\text{C.2})$$

The first term in (C.2) can be reformulated as $\delta \underline{\mathbf{n}}^T \underline{\mathbf{n}}$. As the name suggests, the normal vector is normalized, i.e., $\underline{\mathbf{n}}^T \underline{\mathbf{n}} = 1$. Variation of this condition results in $\delta \underline{\mathbf{n}}^T \underline{\mathbf{n}} = 0$, and therefore, the first term in (C.2) vanishes. The solid parameter coordinates ξ_c^S and η_c^S are dependent on the beam parameter coordinate, thus resulting in a contribution of $\delta \xi_c^S$ and $\delta \eta_c^S$ to the total variation of the solid position $\delta(\underline{\mathbf{x}}^S)$. Inserting this total variation of the solid position into the last term in (C.2) yields (only for the last term)

$$\underline{\mathbf{n}}^T \delta (\underline{\mathbf{x}}^S(\xi_c^S, \eta_c^S)) = \underline{\mathbf{n}}^T (\delta \underline{\mathbf{x}}^S(\xi_c^S, \eta_c^S) + \underline{\mathbf{x}}_{,\xi}^S(\xi_c^S, \eta_c^S) \delta \xi_c^S + \underline{\mathbf{x}}_{,\eta}^S(\xi_c^S, \eta_c^S) \delta \eta_c^S). \quad (\text{C.3})$$

Since $\underline{\mathbf{n}}^T \underline{\mathbf{x}}_{,\xi}^S = 0$ and $\underline{\mathbf{n}}^T \underline{\mathbf{x}}_{,\eta}^S = 0$, this can be simplified to

$$\underline{\mathbf{n}}^T \delta (\underline{\mathbf{x}}^S(\xi_c^S, \eta_c^S)) = \underline{\mathbf{n}}^T \delta \underline{\mathbf{x}}^S(\xi_c^S, \eta_c^S). \quad (\text{C.4})$$

Inserting all considerations above into (C.2) gives the final variation of the gap function

$$\delta g(\xi^B) = \underline{\mathbf{n}}^T (\delta \underline{\mathbf{r}}(\xi^B) - \delta \underline{\mathbf{x}}^S(\xi_c^S, \eta_c^S)). \quad (\text{C.5})$$

Bibliography

- [1] Agarwal, B.D., Broutman, L.J., Chandrashekhara, K.: Analysis and performance of fiber composites, fourth edn. John Wiley & Sons (2017)
- [2] Akula, B.R., Vignollet, J., Yastrebov, V.A.: Stabilized MorteX method for mesh tying along embedded interfaces (2019). Preprint, <https://arxiv.org/abs/1902.04003>
- [3] Alart, P., Curnier, A.: A mixed formulation for frictional contact problems prone to Newton like solution methods. *Computer Methods in Applied Mechanics and Engineering* **92**(3), 353–375 (1991)
- [4] Alberts, B., Johnson, A., Lewis, J., Raff, M., Roberts, K., Walter, P.: Molecular biology of the cell, fifth edn. Garland Science (2008)
- [5] Allen, T., Haake, S., Goodwill, S.: Comparison of a finite element model of a tennis racket to experimental data. *Sports Engineering* **12**(2), 87–98 (2009)
- [6] Allen, T., Hart, J., Spurr, J., Haake, S., Goodwill, S.: Validated dynamic analysis of real sports equipment using finite element; a case study using tennis rackets. *Procedia Engineering* **2**(2), 3275–3280 (2010)
- [7] Allen, T.B.: Finite element model of a tennis ball impact with a racket. Dissertation, Sheffield Hallam University (2009)
- [8] Almeida, J.H.S., Bittrich, L., Jansen, E., Tita, V., Spickenheuer, A.: Buckling optimization of composite cylinders for axial compression: A design methodology considering a variable-axial fiber layout. *Composite Structures* **222**, 110928 (2019)
- [9] Antman, S.S.: Nonlinear problems of elasticity. Springer (1995)
- [10] Areias, P., Rabczuk, T.: An engineering interpretation of Nesterov’s convex minimization algorithm and time integration: application to optimal fiber orientation. *Computational Mechanics* **68**(1), 211–227 (2021)
- [11] Argyris, J.: An excursion into large rotations. *Computer Methods in Applied Mechanics and Engineering* **32**(1), 85–155 (1982)
- [12] BACI: A Comprehensive Multi-Physics Simulation Framework. <https://baci.pages.gitlab.lrz.de/website> (2021)
- [13] Bathe, K.J.: Finite element procedures, second edn. K.J. Bathe, Watertown, MA (2014)

- [14] Bauchau, O.A., Han, S., Mikkola, A., Matikainen, M.K.: Comparison of the absolute nodal coordinate and geometrically exact formulations for beams. *Multibody System Dynamics* **32**(1), 67–85 (2014)
- [15] Béchet, É., Moës, N., Wohlmuth, B.: A stable Lagrange multiplier space for stiff interface conditions within the extended finite element method. *International Journal for Numerical Methods in Engineering* **78**(8), 931–954 (2009)
- [16] Belytschko, T., Liu, W.K., Moran, B., Elkhodary, K.: *Nonlinear finite elements for continua and structures*, second edn. Wiley (2013)
- [17] Ben Belgacem, F.: The mortar finite element method with Lagrange multipliers. *Numerische Mathematik* **84**(2), 173–197 (1999)
- [18] Betsch, P., Menzel, A., Stein, E.: On the parametrization of finite rotations in computational mechanics: A classification of concepts with application to smooth shells. *Computer Methods in Applied Mechanics and Engineering* **155**(3), 273–305 (1998)
- [19] Betsch, P., Steinmann, P.: Frame-indifferent beam finite elements based upon the geometrically exact beam theory. *International Journal for Numerical Methods in Engineering* **54**(12), 1775–1788 (2002)
- [20] Bischoff, M., Ramm, E.: Shear deformable shell elements for large strains and rotations. *International Journal for Numerical Methods in Engineering* **40**(23), 4427–4449 (1997)
- [21] Bittrich, L., Spickenheuer, A., Almeida, J.H.S., Müller, S., Kroll, L., Heinrich, G.: Optimizing variable-axial fiber-reinforced composite laminates: The direct fiber path optimization concept. *Mathematical Problems in Engineering* **2019**, 8260563 (2019)
- [22] Blender Online Community - a 3D modelling and rendering package. <http://www.blender.org> (2018)
- [23] Bock, S.D., Iannaccone, F., Santis, G.D., Beule, M.D., Loo, D.V., Devos, D., Vermassen, F., Segers, P., Verheghe, B.: Virtual evaluation of stent graft deployment: A validated modeling and simulation study. *Journal of the Mechanical Behavior of Biomedical Materials* **13**, 129–139 (2012)
- [24] Boffi, D., Brezzi, F., Fortin, M.: *Mixed finite element methods and applications*, first edn. Springer (2013)
- [25] Boman, E.G., Çatalyürek, U.V., Chevalier, C., Devine, K.D.: The Zoltan and Isorropia Parallel Toolkits for Combinatorial Scientific Computing: Partitioning, Ordering and Coloring. *Scientific Programming* **20**(2), 29–150 (2012)
- [26] Bonet, J., Burton, A.J.: A simple orthotropic, transversely isotropic hyperelastic constitutive equation for large strain computations. *Computer Methods in Applied Mechanics and Engineering* **162**(1), 151–164 (1998)

-
- [27] Bonet, J., Wood, R.D.: Nonlinear continuum mechanics for finite element analysis, second edn. Cambridge University Press (2008)
- [28] Bosten, A., Cosimo, A., Linn, J., Brüls, O.: A mortar formulation for frictionless line-to-line beam contact. *Multibody System Dynamics* **54**(1), 31–52 (2022)
- [29] Brüls, O., Cardona, A.: On the use of Lie group time integrators in multibody dynamics. *Journal of Computational and Nonlinear Dynamics* **5**(3) (2010)
- [30] Brüls, O., Cardona, A., Arnold, M.: Lie group generalized- α time integration of constrained flexible multibody systems. *Mechanism and Machine Theory* **48**, 121–137 (2012)
- [31] Cardona, A., Geradin, M.: A beam finite element non-linear theory with finite rotations. *International Journal for Numerical Methods in Engineering* **26**(11), 2403–2438 (1988)
- [32] Carrier, G.F.: The spaghetti problem. *The American Mathematical Monthly* **56**(10), 669–672 (1949)
- [33] Casandjian, C., Challamel, N., Lanos, C., Hellesland, J.: Reinforced concrete beams, columns and frames. John Wiley & Sons (2013)
- [34] Chang, T.Y., Taniguchi, H., Chen, W.F.: Nonlinear finite element analysis of reinforced concrete panels. *Journal of Structural Engineering* **113**(1), 122–140 (1987)
- [35] Chung, J., Hulbert, G.M.: A time integration algorithm for structural dynamics with improved numerical dissipation: The generalized- α method. *Journal of Applied Mechanics* **60**(2), 371–375 (1993)
- [36] Cook, R.D., Malkus, D.S., Plesha, M.E., Witt, R.J.: Concepts and applications of finite element analysis, fourth edn. John Wiley & Sons (2001)
- [37] Cottrell, J., Hughes, T., Bazilevs, Y.: Isogeometric analysis: Toward integration of CAD and FEA. John Wiley & Sons (2009)
- [38] Crisfield, M.A., Jelenić, G.: Objectivity of strain measures in the geometrically exact three-dimensional beam theory and its finite-element implementation. *Proceedings of the Royal Society of London A* **455**(1983), 1125–1147 (1999)
- [39] Dassault Systèmes Simulia Corp.: Abaqus 2021 documentation (2021)
- [40] Demanget, N., Duprey, A., Badel, P., Orgéas, L., Avril, S., Geindreau, C., Albertini, J.N., Favre, J.P.: Finite element analysis of the mechanical performances of 8 marketed aortic stent-grafts. *Journal of Endovascular Therapy* **20**(4), 523–535 (2013)
- [41] Dohrmann, C.R., Key, S.W., Heinstein, M.W.: Methods for connecting dissimilar three-dimensional finite element meshes. *International Journal for Numerical Methods in Engineering* **47**(5), 1057–1080 (2000)
- [42] Dolbow, J., Harari, I.: An efficient finite element method for embedded interface problems. *International Journal for Numerical Methods in Engineering* **78**(2), 229–252 (2009)

- [43] Durville, D.: Finite element simulation of textile materials at mesoscopic scale. In: Finite element modelling of textiles and textile composites. Saint-Petersbourg, Russian Federation (2007)
- [44] Elwi, A.E., Hrudey, T.M.: Finite element model for curved embedded reinforcement. *Journal of Engineering Mechanics* **115**(4), 740–754 (1989)
- [45] Farah, P., Popp, A., Wall, W.A.: Segment-based vs. element-based integration for mortar methods in computational contact mechanics. *Computational Mechanics* **55**(1), 209–228 (2015)
- [46] Favata, A.: On the Kelvin problem. *Journal of Elasticity* **109**(2), 189–204 (2012)
- [47] Figueroa, C.A., Taylor, C.A., Yeh, V., Chiou, A.J., Zarins, C.K.: Effect of curvature on displacement forces acting on aortic endografts: A 3-dimensional computational analysis. *Journal of Endovascular Therapy* **16**(3), 284–294 (2009)
- [48] Gerbeau, J.F., Vidrascu, M.: A quasi-Newton algorithm based on a reduced model for fluid-structure interaction problems in blood flows. *ESAIM: Mathematical Modelling and Numerical Analysis* **37**(4), 631–647 (2003)
- [49] Gerstmayr, J., Dorninger, A., Eder, R., Gruber, P., Reischl, D., Saxinger, M., Schörgenhumer, M., Humer, A., Nachbagauer, K., Pechstein, A., Vetyukov, Y.: HOTINT: A script language based framework for the simulation of multibody dynamics systems. In: Proceedings of the ASME 2013 International Design Engineering Technical Conferences & Computers and Information in Engineering Conference (IDETC/CIE), Portland (OR), USA (2013)
- [50] Gomes, H.M., Awruch, A.M.: Some aspects on three-dimensional numerical modelling of reinforced concrete structures using the finite element method. *Advances in Engineering Software* **32**(4), 257–277 (2001)
- [51] Goodwill, S.R., Kirk, R., Haake, S.J.: Experimental and finite element analysis of a tennis ball impact on a rigid surface. *Sports Engineering* **8**(3), 145–158 (2005)
- [52] Grill, M.J., Eichinger, J.F., Koban, J., Meier, C., Lieleg, O., Wall, W.A.: A novel modelling and simulation approach for the hindered mobility of charged particles in biological hydrogels. *Proceedings of the Royal Society A: Mathematical, Physical and Engineering Sciences* **477**(2249), 20210039 (2021)
- [53] Hagmeyer, N., Mayr, M., Steinbrecher, I., Popp, A.: One-way coupled fluid-beam interaction: capturing the effect of embedded slender bodies on global fluid flow and vice versa. *Advanced Modeling and Simulation in Engineering Sciences* **9**(1), 9 (2022)
- [54] Hauck, S.R., Kupferthaler, A., Stelzmüller, M., Eilenberg, W., Ehrlich, M., Neumayer, C., Wolf, F., Loewe, C., Funovics, M.A.: Endovascular stent-graft repair of the ascending aorta: Assessment of a specific novel stent-graft design in phantom, cadaveric, and clinical application. *CardioVascular and Interventional Radiology* **44**(9), 1448–1455 (2021)

- [55] Hautefeuille, M., Annavarapu, C., Dolbow, J.E.: Robust imposition of Dirichlet boundary conditions on embedded surfaces. *International Journal for Numerical Methods in Engineering* **90**(1), 40–64 (2012)
- [56] Hemmler, A., Lutz, B., Reeps, C., Kalender, G., Gee, M.W.: A methodology for in silico endovascular repair of abdominal aortic aneurysms. *Biomechanics and Modeling in Mechanobiology* (2018)
- [57] Hesch, C., Betsch, P.: A mortar method for energy-momentum conserving schemes in frictionless dynamic contact problems. *International Journal for Numerical Methods in Engineering* **77**(10), 1468–1500 (2009)
- [58] Hesch, C., Betsch, P.: Transient three-dimensional domain decomposition problems: Frame-indifferent mortar constraints and conserving integration. *International Journal for Numerical Methods in Engineering* **82**(3), 329–358 (2010)
- [59] Hesch, C., Betsch, P.: Transient three-dimensional contact problems: mortar method, mixed methods and conserving integration. *Computational Mechanics* **48**(4), 461–475 (2011)
- [60] Holzapfel, G.A.: *Nonlinear solid mechanics: A continuum approach for engineering*. Wiley (2000)
- [61] Holzapfel, G.A.: *Collagen in arterial walls: Biomechanical aspects*, chap. 11, pp. 285–324. Springer US, Boston, MA (2008)
- [62] Holzapfel, G.A., Gasser, T.C., Ogden, R.W.: A new constitutive framework for arterial wall mechanics and a comparative study of material models. *Journal of elasticity and the physical science of solids* **61**(1), 1–48 (2000)
- [63] Holzinger, S., Gerstmayr, J.: *Time integration of rigid bodies modelled with three rotation parameters*. Multibody System Dynamics (2021)
- [64] Hughes, T.J.R.: *The finite element method: Linear static and dynamic finite element analysis*. Dover Publications (2000)
- [65] Hughes, T.J.R., Cottrell, J.A., Bazilevs, Y.: Isogeometric analysis: CAD, finite elements, NURBS, exact geometry and mesh refinement. *Computer Methods in Applied Mechanics and Engineering* **194**(39), 4135–4195 (2005)
- [66] Humer, A.: Dynamic modeling of beams with non-material, deformation-dependent boundary conditions. *Journal of Sound and Vibration* **332**(3), 622–641 (2013)
- [67] Humer, A., Steinbrecher, I., Vu-Quoc, L.: General sliding-beam formulation: A non-material description for analysis of sliding structures and axially moving beams. *Journal of Sound and Vibration* **480**, 115341 (2020)
- [68] Ibrahimbegović, A., Frey, F., Kožar, I.: Computational aspects of vector-like parametrization of three-dimensional finite rotations. *International Journal for Numerical Methods in Engineering* **38**(21), 3653–3673 (1995)

- [69] Irschik, H., Gerstmayr, J.: A continuum mechanics based derivation of Reissner's large-displacement finite-strain beam theory: the case of plane deformations of originally straight Bernoulli–Euler beams. *Acta Mechanica* **206**(1), 1–21 (2009)
- [70] Jansen, K., Whiting, C., Hulbert, G.: Generalized- α method for integrating the filtered Navier-Stokes equations with a stabilized finite element method. *Computer Methods in Applied Mechanics and Engineering* **190**, 305–319 (2000)
- [71] Jelenić, G., Crisfield, M.A.: Geometrically exact 3D beam theory: implementation of a strain-invariant finite element for statics and dynamics. *Computer Methods in Applied Mechanics and Engineering* **171**(1), 141–171 (1999)
- [72] Kerfriden, P., Claus, S., Mihai, I.: A mixed-dimensional CutFEM methodology for the simulation of fibre-reinforced composites. *Advanced Modeling and Simulation in Engineering Sciences* **7**(1), 18 (2020)
- [73] Khristenko, U., Schuß, S., Krüger, M., Schmidt, F., Wohlmuth, B., Hesch, C.: Multi-dimensional coupling: A variationally consistent approach to fiber-reinforced materials. *Computer Methods in Applied Mechanics and Engineering* **382**, 113869 (2021)
- [74] Klein, B., Gansicke, T.: *Leichtbau-Konstruktion*, eleventh edn. Springer Vieweg (2019)
- [75] Klöppel, T., Popp, A., Küttler, U., Wall, W.A.: Fluid–structure interaction for non-conforming interfaces based on a dual mortar formulation. *Computer Methods in Applied Mechanics and Engineering* **200**(45), 3111–3126 (2011)
- [76] Konyukhov, A., Schweizerhof, K.: On the solvability of closest point projection procedures in contact analysis: Analysis and solution strategy for surfaces of arbitrary geometry. *Computer Methods in Applied Mechanics and Engineering* **197**(33), 3045–3056 (2008)
- [77] Konyukhov, A., Schweizerhof, K.: On some aspects for contact with rigid surfaces: Surface-to-rigid surface and curves-to-rigid surface algorithms. *Computer Methods in Applied Mechanics and Engineering* **283**, 74–105 (2015)
- [78] Korelc, J., Wriggers, P.: *Automation of finite element methods*. Springer International Publishing (2016)
- [79] Kremheller, J., Vuong, A.T., Schrefler, B.A., Wall, W.A.: An approach for vascular tumor growth based on a hybrid embedded/homogenized treatment of the vasculature within a multiphase porous medium model. *International Journal for Numerical Methods in Biomedical Engineering* **35**(11) (2019)
- [80] Krenk, S.: *Non-linear modeling and analysis of solids and structures*. Cambridge University Press (2009)
- [81] Kružík, M., Roubíček, T.: *Mathematical methods in continuum mechanics of solids*. Springer Nature Switzerland (2019)
- [82] Kurrer, K.E.: *The history of the theory of structures*, second edn. Ernst & Sohn (2018)

-
- [83] Küttler, U., Wall, W.A.: Fixed-point fluid-structure interaction solvers with dynamic relaxation. *Computational Mechanics* **43**(1), 61–72 (2008)
- [84] Laursen, T.A.: *Computational contact and impact mechanics*. Springer Berlin, Heidelberg (2002)
- [85] Lé, B., Legrain, G., Moës, N.: Mixed dimensional modeling of reinforced structures. *Finite Elements in Analysis and Design* **128**, 1–18 (2017)
- [86] Leichner, A.: *Computational contact mechanics based on implicit boundary representations for voxel-based meshes*. Ph.D. thesis, Technische Universität Kaiserslautern (2019)
- [87] Leichner, A., Andrä, H., Simeon, B.: A contact algorithm for voxel-based meshes using an implicit boundary representation. *Computer Methods in Applied Mechanics and Engineering* **352**, 276–299 (2019)
- [88] Lieleg, O., Claessens, M.M.A.E., Bausch, A.R.: Structure and dynamics of cross-linked actin networks. *Soft Matter* **6**, 218–225 (2010)
- [89] Mattheij, P., Gliesche, K., Feltin, D.: Tailored fiber placement – mechanical properties and applications. *Journal of Reinforced Plastics and Composites* **17**(9), 774–786 (1998)
- [90] Mattheij, P., Gliesche, K., Feltin, D.: 3D reinforced stitched carbon/epoxy laminates made by tailored fibre placement. *Composites Part A: Applied Science and Manufacturing* **31**(6), 571–581 (2000)
- [91] Mayr, M., Klöppel, T., Wall, W.A., Gee, M.W.: A temporal consistent monolithic approach to fluid-structure interaction enabling single field predictors. *SIAM Journal on Scientific Computing* **37**(1), 30–59 (2015)
- [92] Mayr, M., Popp, A.: Scalable computational kernels for mortar finite element methods (2022). Preprint, <https://arxiv.org/abs/2202.03933>
- [93] Meier, C.: *Geometrically exact finite element formulations for slender beams and their contact interaction*. Dissertation, Technische Universität München (2016)
- [94] Meier, C., Grill, M.J., Wall, W.A.: Generalized section-section interaction potentials in the geometrically exact beam theory (2021). Preprint, <https://arxiv.org/abs/2105.10032>
- [95] Meier, C., Grill, M.J., Wall, W.A., Popp, A.: Geometrically exact beam elements and smooth contact schemes for the modeling of fiber-based materials and structures. *International Journal of Solids and Structures* **154**, 124–146 (2018)
- [96] Meier, C., Popp, A., Wall, W.A.: An objective 3D large deformation finite element formulation for geometrically exact curved Kirchhoff rods. *Computer Methods in Applied Mechanics and Engineering* **278**, 445–478 (2014)

- [97] Meier, C., Popp, A., Wall, W.A.: A locking-free finite element formulation and reduced models for geometrically exact Kirchhoff rods. *Computer Methods in Applied Mechanics and Engineering* **290**, 314–341 (2015)
- [98] Meier, C., Popp, A., Wall, W.A.: A finite element approach for the line-to-line contact interaction of thin beams with arbitrary orientation. *Computer Methods in Applied Mechanics and Engineering* **308**, 377–413 (2016)
- [99] Meier, C., Popp, A., Wall, W.A.: Geometrically exact finite element formulations for slender beams: Kirchhoff–Love theory versus Simo–Reissner theory. *Archives of Computational Methods in Engineering* **26**(1), 163–243 (2019)
- [100] Meier, C., Wall, W.A., Popp, A.: A unified approach for beam-to-beam contact. *Computer Methods in Applied Mechanics and Engineering* **315**, 972–1010 (2017)
- [101] Moës, N., Cloirec, M., Cartraud, P., Remacle, J.F.: A computational approach to handle complex microstructure geometries. *Computer Methods in Applied Mechanics and Engineering* **192**(28), 3163–3177 (2003)
- [102] Müller, K.W., Meier, C., Wall, W.A.: Resolution of sub-element length scales in Brownian dynamics simulations of biopolymer networks with geometrically exact beam finite elements. *Journal of Computational Physics* **303**, 185–202 (2015)
- [103] Park, K.C., Felippa, C.A., Rebel, G.: A simple algorithm for localized construction of non-matching structural interfaces. *Int. J. Numer. Meth. Engng.* **53**(9), 2117–2142 (2002)
- [104] Pattinson, S.W., Huber, M.E., Kim, S., Lee, J., Grunsfeld, S., Roberts, R., Dreifus, G., Meier, C., Liu, L., Hogan, N., Hart, A.J.: Additive manufacturing of biomechanically tailored meshes for compliant wearable and implantable devices. *Advanced Functional Materials* **29**(32), 1901815 (2019)
- [105] Phillips, D.V., Zienkiewicz, O.C.: Finite element non-linear analysis of concrete structures. *Proceedings of the Institution of Civil Engineers* **61**(1), 59–88 (1976)
- [106] Piegl, L., Tiller, W.: *The NURBS book*, second edn. Springer Berlin Heidelberg (1997)
- [107] Podio-Guidugli, P., Favata, A.: *Elasticity for geotechnicians: A modern exposition of Kelvin, Boussinesq, Flamant, Cerruti, Melan, and Mindlin problems*, vol. 204. Springer, Cham (2014)
- [108] Popp, A.: *Mortar methods for computational contact mechanics and general interface problems*. Dissertation, Technische Universität München (2012)
- [109] Popp, A., Gee, M.W., Wall, W.A.: A finite deformation mortar contact formulation using a primal–dual active set strategy. *International Journal for Numerical Methods in Engineering* **79**(11), 1354–1391 (2009)
- [110] Popp, A., Gitterle, M., Gee, M.W., Wall, W.A.: A dual mortar approach for 3D finite deformation contact with consistent linearization. *International Journal for Numerical Methods in Engineering* **83**(11), 1428–1465 (2010)

-
- [111] Popp, A., Wohlmuth, B.I., Gee, M.W., Wall, W.A.: Dual quadratic mortar finite element methods for 3D finite deformation contact. *SIAM Journal on Scientific Computing* **34**(4), 421–446 (2012)
 - [112] Puso, M.A.: A 3D mortar method for solid mechanics. *International Journal for Numerical Methods in Engineering* **59**(3), 315–336 (2004)
 - [113] Puso, M.A., Laursen, T.A.: A mortar segment-to-segment contact method for large deformation solid mechanics. *Computer Methods in Applied Mechanics and Engineering* **193**(6), 601–629 (2004)
 - [114] Puso, M.A., Laursen, T.A.: A mortar segment-to-segment frictional contact method for large deformations. *Computer Methods in Applied Mechanics and Engineering* **193**(45), 4891–4913 (2004)
 - [115] Puso, M.A., Laursen, T.A., Solberg, J.: A segment-to-segment mortar contact method for quadratic elements and large deformations. *Computer Methods in Applied Mechanics and Engineering* **197**(6), 555–566 (2008)
 - [116] Ranjbaran, A.: Mathematical formulation of embedded reinforcements in 3D brick elements. *Communications in Numerical Methods in Engineering* **12**(12), 897–903 (1996)
 - [117] Reissner, E.: On one-dimensional finite-strain beam theory: The plane problem. *Zeitschrift für angewandte Mathematik und Physik ZAMP* **23**(5), 795–804 (1972)
 - [118] Romero, I.: The interpolation of rotations and its application to finite element models of geometrically exact rods. *Computational Mechanics* **34**(2), 121–133 (2004)
 - [119] Romero, I.: A comparison of finite elements for nonlinear beams: the absolute nodal coordinate and geometrically exact formulations. *Multibody System Dynamics* **20**(1), 51–68 (2008)
 - [120] Rüberg, T., Cirak, F., García Aznar, J.M.: An unstructured immersed finite element method for nonlinear solid mechanics. *Advanced Modeling and Simulation in Engineering Sciences* **3**(1), 28 (2016)
 - [121] The Sacado Project Website. <https://trilinos.github.io/sacado.html> (2021)
 - [122] Sanders, J., Puso, M.A.: An embedded mesh method for treating overlapping finite element meshes. *International Journal for Numerical Methods in Engineering* **91**(3), 289–305 (2012)
 - [123] Sanders, J.D., Laursen, T.A., Puso, M.A.: A Nitsche embedded mesh method. *Computational Mechanics* **49**(2), 243–257 (2012)
 - [124] Schott, B., Rasthofer, U., Gravemeier, V., Wall, W.A.: A face-oriented stabilized Nitsche-type extended variational multiscale method for incompressible two-phase flow. *International Journal for Numerical Methods in Engineering* **104**(7), 721–748 (2015)

- [125] Setareh, M., Darvas, R.: Concrete structures, second edn. Springer Cham (2017)
- [126] Simo, J.C.: A finite strain beam formulation. The three-dimensional dynamic problem. Part I. Computer Methods in Applied Mechanics and Engineering **49**(1), 55–70 (1985)
- [127] Simo, J.C., Fox, D.D., Hughes, T.J.R.: Formulations of finite elasticity with independent rotations. Computer Methods in Applied Mechanics and Engineering **95**(2), 277–288 (1992)
- [128] Simo, J.C., Hughes, T.J.R.: Computational inelasticity. Springer (1998)
- [129] Simo, J.C., Vu-Quoc, L.: On the dynamics of flexible beams under large overall motions – The plane case: Part I. Journal of Applied Mechanics **53**(4), 849–854 (1986)
- [130] Simo, J.C., Vu-Quoc, L.: On the dynamics of flexible beams under large overall motions – The plane case: Part II. Journal of Applied Mechanics **53**(4), 855–863 (1986)
- [131] Simo, J.C., Vu-Quoc, L.: On the dynamics in space of rods undergoing large motions – A geometrically exact approach. Computer Methods in Applied Mechanics and Engineering **66**(2), 125–161 (1988)
- [132] Spickenheuer, A., Schulz, M., Gliesche, K., Heinrich, G.: Using tailored fibre placement technology for stress adapted design of composite structures. Plastics, Rubber and Composites **37**(5), 227–232 (2008)
- [133] Spurrier, R.A.: Comment on "Singularity-free extraction of a quaternion from a direction-cosine matrix". Journal of Spacecraft and Rockets **15**(4), 255–255 (1978)
- [134] Steinbrecher, I., Humer, A., Vu-Quoc, L.: On the numerical modeling of sliding beams: A comparison of different approaches. Journal of Sound and Vibration **408**, 270–290 (2017)
- [135] Steinbrecher, I., Mayr, M., Grill, M.J., Kremheller, J., Meier, C., Popp, A.: A mortar-type finite element approach for embedding 1D beams into 3D solid volumes. Computational Mechanics **66**(6), 1377–1398 (2020)
- [136] Steinbrecher, I., Popp, A.: Efficient mortar-based algorithms for embedding 1D fibers into 3D volumes. PAMM **20**(1), e202000151 (2021)
- [137] Steinbrecher, I., Popp, A.: MeshPy – A general purpose 3D beam finite element input generator. <https://compsim.gitlab.io/codes/meshpy> (2021)
- [138] Steinbrecher, I., Popp, A., Meier, C.: Consistent coupling of positions and rotations for embedding 1D Cosserat beams into 3D solid volumes. Computational Mechanics **69**(3), 701–732 (2022)
- [139] Tambača, J., Kosor, M., Čanić, S., D. Paniagua, M.D.: Mathematical modeling of vascular stents. SIAM Journal on Applied Mathematics **70**(6), 1922–1952 (2010)

-
- [140] Taylor, R.L., Simo, J.C., Zienkiewicz, O.C., Chan, A.C.H.: The patch test – A condition for assessing FEM convergence. *International Journal for Numerical Methods in Engineering* **22**(1), 39–62 (1986)
- [141] Thomson, W.: Note on the integration of the equations of equilibrium of an elastic solid. *The Cambridge and Dublin mathematical journal* **3**, 87–89 (1848)
- [142] Tomec, J., Jelenić, G.: Analysis of static frictionless beam-to-beam contact using mortar method. *Multibody System Dynamics* (2022)
- [143] The Trilinos Project Website. <https://trilinos.github.io> (2021)
- [144] Tschisgale, S., Fröhlich, J.: An immersed boundary method for the fluid-structure interaction of slender flexible structures in viscous fluid. *Journal of Computational Physics* **423**, 109801 (2020)
- [145] Vetyukov, Y.: Nonlinear mechanics of thin-walled structures: Asymptotics, direct approach and numerical analysis. *Foundations of Engineering Mechanics*. Springer (2014)
- [146] Vu-Quoc, L., Li, S.: Dynamics of sliding geometrically-exact beams: large angle maneuver and parametric resonance. *Computer Methods in Applied Mechanics and Engineering* **120**(1), 65–118 (1995)
- [147] Vu-Quoc, L., Tan, X.G.: Optimal solid shells for non-linear analyses of multilayer composites. I. Statics. *Computer Methods in Applied Mechanics and Engineering* **192**(9), 975–1016 (2003)
- [148] Vu-Quoc, L., Tan, X.G.: Optimal solid shells for non-linear analyses of multilayer composites. II. Dynamics. *Computer Methods in Applied Mechanics and Engineering* **192**(9), 1017–1059 (2003)
- [149] Wiedemann, J.: *Leichtbau: Elemente und Konstruktion*, third edn. Springer-Verlag Berlin Heidelberg (2007)
- [150] Wohlmuth, B.I.: A mortar finite element method using dual spaces for the lagrange multiplier. *SIAM Journal on Numerical Analysis* **38**(3), 989–1012 (2000)
- [151] Wriggers, P.: Finite element algorithms for contact problems. *Archives of Computational Methods in Engineering* **2**(4), 1–49 (1995)
- [152] Wriggers, P.: *Computational contact mechanics*. Springer-Verlag Berlin Heidelberg (2006)
- [153] Wriggers, P.: *Nonlinear finite element methods*. Springer-Verlag Berlin Heidelberg (2008)
- [154] Yang, B., Laursen, T.A., Meng, X.: Two dimensional mortar contact methods for large deformation frictional sliding. *International Journal for Numerical Methods in Engineering* **62**(9), 1183–1225 (2005)
- [155] Zienkiewicz, O.C., Taylor, R.L., Zhu, J.Z.: *The finite element method: Its basis and fundamentals*, seventh edn. Butterworth-Heinemann (2013)

- [156] Zunino, P., Tambača, J., Cutrí, E., Čanić, S., Formaggia, L., Migliavacca, F.: Integrated stent models based on dimension reduction: Review and future perspectives. *Annals of biomedical engineering* **44**(2), 604–617 (2015)

Supervised student thesis

name	title	type	year
Dao Viet Anh	Modellierung von Balken-, Festkörper- Interaktionen mit der Finite-Elemente-Methode	bachelor thesis	2018
Dao Viet Anh	Modellierung und Simulation von faserverstärktem Beton anhand realer 3D-Computertomografie-Scans, Master thesis	master thesis	2020
Willi Helbig	Oriented random rotations for the modelling of fiber-reinforced materiales	student project	2020
Jennifer Böltz	Algorithmic extraction of 1D curves based on CT scans of fiber-reinfoced concrete	student project	2021